Trinity College Dublin
Coláiste na Tríonóide, Baile Átha Cliath
The University of Dublin

School of Engineering

Dynamic response of Spar-type Floating Offshore Wind Turbines: Eulerian and Lagrangian approaches

Hoa Xuan Nguyen

16310914

11/03/2022

A Dissertation submitted in partial fulfilment of the requirements for the degree of Doctor Of Philosophy

Declaration

I declare that this thesis has not been submitted as an exercise for a degree at this or any other university and it is entirely my own work.

I agree to deposit this thesis in the University's open access institutional repository or allow the Library to do so on my behalf, subject to Irish Copyright Legislation and Trinity College Library conditions of use and acknowledgement.

I consent / do not consent to the examiner retaining a copy of the thesis beyond the examining period, should they so wish (EU GDPR May 2018).

Signed: _____ Date: _____

Abstract

Floating offshore wind turbines (FOWTs) are an alternative technology to harness the abundant wind energy in open sea areas. A FOWT structure consists of a floating platform, a mooring system, and a wind turbine structure (tower and Rotor-Nacelle Assembly (RNA)). The FOWT numerical model integrates the structural dynamics and hydrostatic, hydrodynamic, aerodynamic and mooring loads. The main objective of this thesis is to investigate the dynamic responses of FOWT structure with large-amplitude waves. Special efforts are also devoted to studying the effects of large-amplitude waves-current interaction and the non-linear solitary waves-structure interaction.

A coupled rigid-flexible multi-body model treats the blades, the tower as the flexible components and the platforms as rigid bodies. The model is derived with 10 degrees of freedom model to model the floating wind turbine. The equations of motions of the model based on energy formulation are derived using Euler-Lagrangian equations.

The hydrodynamic forces are evaluated using Morison's equations for a slender structure. The aerodynamic loads are estimated using the classical Blade Element Momentum (BEM) method. A dynamic mooring model is applied to determine the cable tensions of the mooring system proposed to anchor the platform to the seabed.

The hydrodynamic effects of the large-amplitude waves are evaluated through derivation of the large-amplitude waves accelerations. The numerical continuum approach was used to compute the large-amplitude wave solutions. The formulations of the flow accelerations were proposed using the results from the numerical continuum approach. The accelerations, velocity, and pressure are required to evaluate the hydrodynamic

forces and moments as a function of the platform displacements. An investigation into the flow kinematics under large-amplitude waves was carried out. Further, the FOWT responses achieved by applying large-amplitude wave theory were compared with the results of the linear wave theory. The application of large-amplitude waves significantly affected the FOWT displacement and the cable fairlead forces. The vertical displacement of the FOWT and the cable fairlead forces was observed to be most affected by the large-amplitude waves.

A new combination of the large-amplitude waves with the uniformly underlying current was also proposed in this thesis. The impact of the current with a constant strength has been evaluated in two directions: following waves or against waves. It was shown that the current significantly modifies fluid horizontal velocity profiles and affects the FOWT. In addition, the current affected the static responses and the dynamic responses of the spar and the cables. The results also provided an understanding of the interconnectedness of the large-amplitude waves amplitude and the current strength.

Finally, solitary waves were applied in the models to examine the FOWT system ability to an impulsive load. The solitary waves were considered as moving hump of water with high speed and long wavelength. Due to its high propagating speed, a short-duration response but extreme amplitude of the FOWT structure is caused by the solitary waves loads. Moreover, the interactions of the solitary waves-structure were also incorporated in the models to examine a more realistic model of a FOWT system. The interaction was represented by the modification of the stable solitary waves profiles. Therefore, a useful meshless method, Smoothed Particle Hydrodynamics (SPH), was used to capture the surface modification which is an input for a Finite Element Method approach to estimate the flow kinematics accounting for the waves-structure interaction. It was shown that including the wave-structure interaction amplified the platform displacements and the mooring forces.

Acknowledgements

I would like to express my gratitude ro my supervisor Professor Biswajit Basu for his support, encouragement and many fruitful ideas and discussions throughout my years working with him. From my first day of my PhD studies to the present day his advice and support has been invaluable.

Special thanks are directed to Dr. Lin Chen. The helpful contributions with numerical continuum model greatly improved the computational codes related to various parts of this thesis are highly appreciated.

Additional thanks go to Dr. Dinh Nguyen for his support. His comments and suggestions regarding the structural dynamic models developed in this thesis were very helpful and much appreciated.

I wish to acknowledge the entire faculty of the Department of Civil, Structural and Environmental Engineering at Trinity College Dublin for their help in building my broad understanding of the subject and in preparation of this thesis.

I am grateful to my fellow researchers for providing a relaxed and fun environment in which to work. I am especially grateful to Alejandro, John Hickey, Unnikrisnan, Saptarshi, Matthew, Himanshu, Giacomo, Shreya, Charu and Gurbir for their friendship, help and support.

This Ph.D. is dedicated to my family: my parents, my wife, Lien, and my kids, Khoa and An. Their encouragement and support has helped me through all my years at Trinity.

Contents

List of Figures

List of Tables

Nomenclature

(q, p) transformed domain variables

(u, v, w) fluid velocity

(U_c, V_c, W_c) current velocity in cable reference frame

(u_r, v_r, w_r) relative cable velocity in the local Lagrangian coordinate system

α empirical parameter

α_d normalisation parameter of kernel function

β empirical parameter

β_s structural damping coefficient

Δt time step

δ solitary wave constant phase shift

$\delta()$ Dirac delta function

δ_s unity tensor

$\eta()$ free surface profile

γ exponent parameter

$\gamma()$ vorticity function

$\hat{\varphi}$ solitary potential

κ wave number

κ_s scaling parameter for kernel length

$\mathbf{\Omega}_b$ particle body rotational velocity

a acceleration

C damping matrix of the system

$\mathbf{f}$ external volumetric force vector

$\mathbf{f}_b$ hydrostatic load

$\mathbf{f}_g$ gravitational load

$\mathbf{f}_h$ hydrodynamic load

$\mathbf{f}_m$ fair-lead tension

$\mathbf{f}_w$ wind load

$\mathbf{I}_p$ spar inertia

$\mathbf{I}_r$ rotor inertia

$\mathbf{I}_t$ tower inertia

$\mathbf{I}_{nac}$ nacelle inertia

$\mathbf{K}$ stiffness matrix of the system

$\mathbf{M}$ mass matrix of the system

$\mathbf{q}$ generalized displacement vector

$\mathbf{R_0}$ particle body center of mass

$\mathbf{r}$ particle position vector

$\mathbf{v}$ particle velocity vector

$\mathbf{V}_b$ particle body velocity

$\mathcal{T}$ total kinematic energy of the SFOWT

$\mathcal{V}$ total potential energy of the SFOWT

μ_b blade variable mass per unit length

μ_t tower distributed mass per unit length

Ω particle surrounding volumn

ω wave angular frequency

Ω_b blade speed

$\overline{D_\eta}$ physical fluid domain

ϕ initial phase

$\phi_b()$ blade mode shape

$\phi_t()$ tower mode shape function

Π_{ij}	viscous force
$\psi()$	stream function
ρ_0	reference density
ρ_i	particle density
ρ_w	water density
σ	surface stress tensor
τ	deviatoric stress tensor
θ	numerical variable
$\vec{n}$	normal unit vector
ξ	spar degree of freedom
a	wave amplitude
B	reference pressure
C	solitary wave phase velocity
c	wave speed
c_0	speed of sound at reference density
c_s	modified wave speed in SPH scheme
c_w	speed of sound from wave celerity
C_{an}	added mass coefficient
C_{db}	cable drag coefficient
C_{dn}	cable drag coefficient
C_{dt}	cable drag coefficient
c_{ij}	mean speed of sound
$C_{s,a}$	added mass coefficient
$C_{s,d}$	spar drag coefficient
d	still water depth
d_c	cable diameter
$d_{s,0}$	spar diamater above taper
$d_{s,1}$	spar diameter below taper

dn elliptic function

dp initial distance between particles

E elliptic integral

$e_t()$ piston motion

EA elastic stiffness

$f()$ arbitrary function

f_p peak frequency

g gravitational acceleration

H wave height

h distance between hub center and spar center of gravity

$H()$ laminar flow solution

$h()$ height function

h_c initial cable depth

h_d spar draft

h_s kernel length

h_t tower height

h_w wave paddle height

I_b particle body moment of inertia

I_s spar inertia about G

K elliptic integral

k average horizontal current strength

k_{sb} normalised seabed stiffness

L wave length

L_0 unstretched length of cable

l_c initial cable radius

LWT Linear wave theory

M Mach number

m particle mass

$m()$ periodic even function

M_b particle body mass

m_c mass perunit length of cable

M_n nacelle mass and rotor mass

M_p spar mass

M_r rotor mass

M_s spar mass

M_t tower mass

m_t tower mass

M_{nac} nacelle mass

N number of particles

N_s spectrum parts

p particle pressure

$P(x, z)$ fluid pressure

p_0 relative mass flux

P_{atm} atmospheric pressure

Q hydraulic head

R blade length

R_s relative particle diatance

S surface fraction

S_0 piston stroke

s_m source term in continuity equation

s_v variable resolution source term in momentum equation

T wave period

t time

v maximum speed of the fluid

V_i particle volume

v_{max} maximum fluid velocity

W	kernel function
w_0	wet weight per unit length
Z	Zeta function
z_G	gravity center location

1 Introduction

1.1 Development of floating offshore wind turbines

Climate change has become one of the biggest global challenges for humans. The body of evidence on climate change is severe, and the impact is alarming. Humans have used two-thirds of all available fossil fuel and resources [4]. There is an urgent need to limit global warming to 1,5°C compared to pre-industrial levels. A vast share of global greenhouse gas emissions are caused by energy production and use; the energy sector has become a key action area for climate change mitigation measures. The accelerated growth of renewable technologies alongside rapidly declining costs has created a dynamic shift from conventional sources of energy (coal, gas, oil, nuclear) towards renewable and more climate-friendly sources. Apart from reducing greenhouse gas emissions, the benefits of renewable power provide tremendous development opportunities for emerging economies.

For many decades, renewable energy was seen as utopian dreams of naive environmentalists that were unfeasible for meeting growing global energy demand. Nobody can foresee the impressive market growth to come. Renewal has evolved from small subsidized niches in global energy supply to robust, mature and cost-competitive energy technologies representing a substantial energy source in the energy share of many countries. Renewable energies are derived from three primary sources: the Sun, the Moon and the Earth. Energy from the Sun manifests itself in various ways ranging from solar radiation to wind and from hydro-power to biomass. Isotope decay takes place deep down the earth surface and produces geothermal heat. In addition, the moon's gravity affects the tides on earth, enabling electricity production from tidal power stations. The observable shift towards renewable electricity from conventional fossil and nuclear generation on a global scale is remarkable. Global new investment in renewable energy reached USD 1.9 trillion in 2021 [5]. Wind power capacity worldwide is now 743 GW [6], and 93 GW of new wind energy capacity is newly installed in 2020, i.e., about 53 percent year-on-year increase. The Asia-Pacific regions becoming an increasingly important in the growth of global wind power [6]. It is a sign of increased international competitive-

ness. The average capital cost of renewable technologies has been decreasing over the past years while the capacity addition continues to rise.

Wind energy is a renewable energy resource that can contribute to replacing fossil fuels in the future. Wind energy projects have been built, operated, and planned worldwide, both in lands and offshore. Compared to the in land wind turbine, FOWTs have reduced visual impact and less noise constraint. When the wind turbines are installed far from shore, it does not create the problem of noise and the visual impact on to the neighbouring area where residents live. In addition, FOWTs have higher rotor speeds; thus, they have more captured power. At sea level, the wind velocity is 20% higher, and that leads to 45-60% more power captured. The design of a single wind turbine system has been initiated many types of research in foundation design, control of the blade, and floating offshore wind turbine. For an offshore wind turbine, floater design is crucial, leading to various floater concepts. Based on the developments in the offshore oil and gas business, these floater concepts, such as spar buoys, tension leg platforms, and barges, have been investigated for their applicability to support wind turbine structures. The first floating offshore wind turbine of the Hywind project consists of a spar-type foundation supporting a 2-MW generator that was installed and tested in the North Sea in 2009 [7]. The world's first full-scale floating wind farm is deployed at the northeast coast of Scotland [8]. For the purpose of research, a spar-type floating offshore wind turbine numerical model proposed by Jonkman based on Hywind spar floater and NREL 5-MW baseline wind turbine is used by many researchers in the offshore wind field [7, 9, 10, 11].

1.2 FOWTs concepts

A FOWT structure includes a floating platform supporting the wind turbine and a mooring system anchoring to the sea bottom. The platform and the mooring lines are subjected mainly to the hydrodynamic loads, while the wind turbine and tower face the aerodynamic disturbances. The floating platform concepts inherit designs used in the offshore oil and gas industry, such as spar-type platform (SFOWT), tension-leg platform (TLPFOWT), semi-submersible platform (SMFOWT), and pontoon-type [12] (see Fig.1.1).

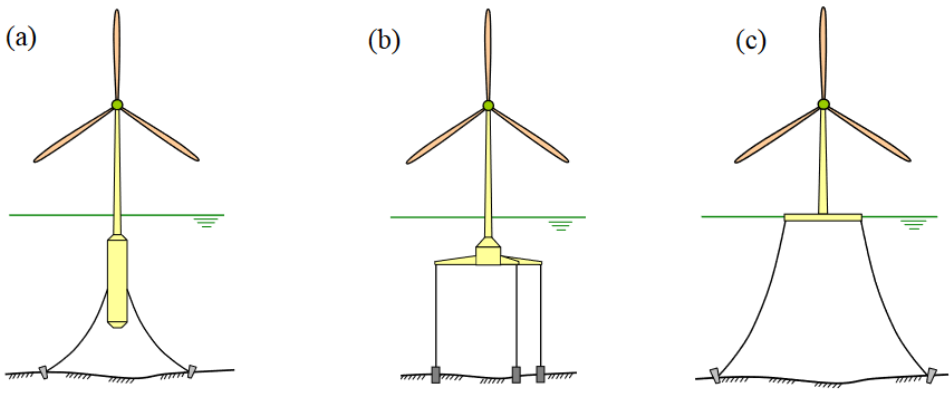

Figure 1.1: FOWT platform models: (a) SFOWT, (b) TLPFOWT, (c) SMFOWT [1].

SFOWT consists of a cylindrical floater whose draft is usually filled with ballast of water and gravel. The draft of the platform is always larger than the super-structure. At the bottom of the draft, a ballast is attached to lower the centre of gravity to be well below the centre of buoyancy. This ensures the stability of the floater and attenuates the translational and rotational motions [13]. A conventional mooring system anchors the floater in position using three catenary lines [14]. The TLPFOWT is connected with taut vertical mooring lines to the seabed. The tensioned mooring line has resulted from the suppression of buoyancy. The taut mooring system possesses high heave, roll, and pitch stiffness. The wind turbine tower is kept vertical without excessive nacelle and tower inertia forces [14, 15]. The SMFOWT consists of three large pontoons connected by steel tubular frame. It is anchored to the seabed by catenary mooring system. The design can support one to three wind turbines on each pontoon or one wind turbine at the centre as Dutch tri-floater concept [15]. The stability of the system is obtained by the high hydrostatic restoring moment from the platform's large water plane area. The barge platform is a moored wide pontoon (compared to pontoon height). This platform can be used for single or multiple wind turbine [15, 16]. In addition to the aforementioned concepts, there are several combined platform concept, i.e. tension-leg-spar concept [15]. Comparison of platforms and another concepts of FOWTs can be found in literature survey type of papers [14, 15, 17, 18]. For water depth less than 40-60 m, the monopiles or bottom-fixed jacket type foundations have been used typically. In deeper regions, the TLPFOWTs or SMFOWTs are preferred. At depths larger than 120 m, SFOWTs are used.

At these far-shore locations, the wind turbines are deployed in an energy rich area with higher ratings (5 - 10 MW), however they have to survive harsh marine conditions. Control systems are incorporated in modern wind turbines to optimise energy output and ensure safe operations. In a large wind farm, each wind turbine has their control systems while they are also constrained by the wind farm Supervisory Control And Data

Acquisition (SCADA) system.

The mooring system comprises of cables connecting the floating platform to the anchors. The system maintains the FOWT structure in position and constrain the system displacements against the environmental loads [19, 20]. The mooring system can be constructed using cables, synthetic ropes, chains, or their combinations. A recent review of mooring system can be found in [20]. The mooring systems are divided into catenary, taut-leg, and tension leg. Their material and design are calculated depending on the structure and the depth of water. The catenary mooring is slack line with part of it may lie on the seabed while other end connects to the platform. Buoys can be attached to the catenary lines to reduce the mooring weight. Clump weights can also be added to the catenary lines to enhance mooring stiffness and reduce overall fluctuations. In taut and tension leg mooring system, the lines are pre-tensioned excess the buoyancy force. The is no sag along the lines due to high tension forces. The internal forces in the tension leg mooring systems are mostly vertical so a particular anchor type is required [21].

1.3 Dynamic modelling of FOWT

Dynamic modelling of FOWT is a multidisciplinary problem combining flexible and rigid body dynamics, hydrostatics, hydrodynamics, aerodynamics, and cable mechanics. In the following, an overview of the relevant literature on the dynamics of FOWTs is presented.

There are few theoretical rigid body dynamic models of FOWTs proposed in literature. Matsukuma and Utsunomiya presented a multi-body dynamic model of SFOWT subjected to steady wind without waves [22]. The study found the influence of gyroscopic moment on the system dynamic due to the rotor spin. TLPFOWT model in wave and wind condition was developed by Wang and Sweetmn [23, 24]. Newton-Euler approach was used to develop a rigid multi-body dynamic model. Based on the OC3 concept [10], Sandner [25, 26] introduced SFOWT model considering both hydrodynamic and aerodynamic load. A three-dimensional rigid body dynamic model of a TLPFOWT was presented by Ramachandran et al. [27]. The study computed the aerodynamic effect using blade-element-momentum theory. To account for the motion of the tower fore-aft motion, the works by [25, 26, 27] used a spring-mass system on top of the tower. Nevertheless, the aforementioned research did not consider the elastic motion of flexible components and the coupling effect of the flexible-rigid body motions. Dinh [28] analysed a 5MW SFOWT of NREL model responses. The impact of coupling effect of spar-nacelle-blade on the responses of both the nacelle and the spar is significant as the wave loading is considered. Al-Solihat [29] presented a coupled rigid-flexible multi-

body model where the tower is assumed flexible. The study compared results from two models: one model has flexible tower and other model has rigid tower. The study found that the model with rigid tower under under-predict the platform yaw response and possess less damping than the model with a flexible tower. Therefore, the flexible tower is modelled in this thesis to analyse the dynamic behaviour of the flexible structure of a wind turbine more accurately. Chen [30, 31] developed a six-degrees-of-freedom (6-DOF) rigid bodies with flexible tower to investigate the effect of dynamic mooring model and wave-current impact on SFOWT. Dinh [32] also proposed semi-active algorithm for edgewise vibration control of the SFOWT. The semi-active algorithm behaves more effectively than the passive control one. In addition, Sakar et al. [33] and [34] proposed a multibody dynamic model of a SFOWT with individual blade pitch control strategies to improve the dynamic responses of the turbine.

FOWT simulation codes have also been developed to analyse the coupled dynamic response of the system [35, 36]. Aerodynamic, structural dynamic, hydrodynamic, control, and mooring dynamic are incorporated in these flexible multi-body dynamics codes depending on their capabilities, namely FAST, HAWC2, GH Bladed, 3DFloat, ADAMS, SIMO, SEASAME/DEEPC. A complete review of these codes can be found in [36]. However, lacks of the detailed theoretical dynamic models on which these codes are based in literature. These codes are being improved and new codes are developed to increase the accuracy of the dynamic models.

Mooring cables can be assumed massless springs with constant stiffness. The method might be valid for taut mooring or slack mooring with small displacement. However, this is not applicable as the structure has large displacement. Therefore, the cable can be modelled using quasi-static and dynamic cable models. The quasi-static cable model uses the equation of an elastic catenary [37, 38, 39]. Wave impacts, fluid-cable interaction, inertia forces, internal cable damping cannot be considered using this method. However, this method is considered appropriate for shallow water and low frequency restoring force [21]. In contrast, the use of dynamic cable model results in higher maximum dynamic tension, particularly for high frequency motion and in deep water regions [40, 41]. Kreuzer et al. [42] investigated the dynamic of a single mooring line including the fluid-structure interaction. A multibody system approach was applied for an 800 m steel wire. The free end of the cable has a harmonic translation displacement with frequency varying from 0.025 to 0.25 rad/s. At high frequency, the maximum dynamic tension is found two times larger than the quasi-static tension. The cable dynamic model can be computed numerically using lumped mass and finite element method [43, 44]. The cable is discretised into a system of discrete masses connected by massless springs and dampers. The cable bending and torsional stiffness are neglected. The hydrodynamic effects, fluid drag, cable-seabed interaction can be

included then the model can be solved in time domain [41]. Jeffery at al. [45] studied a taut mooring system using a linear and non-linear FEM dynamic models. Buckham et al. investigated slack cables in three dimensions including the torsion effect [46].

The wind load on the wind turbine blades is estimated using blade element momentum theory [47]. Due to increase of wind speed with respect to height, higher rotor obtains more wind energy [48]. In smooth terrain like open sea, the wind speed at the same height above the sea level is higher than that above the ground [49].

Wave loads are considered the most severe environmental load in comparison with the current and wind loads [40]. Linear Airy wave theory is usually used to characterise the wave hydrodynamics. The potential flow theory is an alternative approach to model the hydrodynamic effect assuming that the fluid is incompressible and inviscid and the flow is irrotational [19, 37]. Non-linear wave theories, namely Stokes waves, are used to estimate the drift force components [19]. Morison equation which is valid for slender structures is generally used to predict the hydrodynamic effects of the submerged part of the structure. The Morison's equation accounts for the inertia and drag forces but neglect the wave diffraction effect [37, 49, 50]. The Morison's equation can also account for the current effects and wave-current effect though vectorial addition of the fluid velocity. Therefore, the total hydrodynamic forces can be evaluated by integrating the surface pressure distribution over the wet area of the structure [37, 50]. Most of current SFOWT studies use the aforementioned approaches to model the hydrodynamics effects that are listed in the following Table 1.1.

Table 1.1: SFOWT numerical wave model

Research	Platform	Hydrodynamic theory	Wave theory	Wind load
Jonkman [10]	Spar	Potential theory and Morrison's equation	Linear wave theory	yes
Dinh et al. [28]	Spar	Morrison's equation	Linear wave theory	yes
Gao and Sweetman [11]	Spar	Morrison's equation	Linear wave theory	yes
Pham and Shin [51]	Spar combined moonpool	Morrison's equation	Linear wave theory	yes
Bredmose et al.[52]	Triple spar	Experimental study	Linear wave theory	yes

Table 1.1: SFOWT numerical wave model

Karimirad and Moan [53]	Short spar for moderate water depth	Morrison's equation	Linear wave theory	yes
Utsunomia et al. [54]	Pre-stressed concrete hybrid spar	1/22.5 model, experiment	On-site wave load	yes
Shin et al. [55]	Ring cylinders around OC3 spar	Morrison's equation	Linear wave theory	yes
Shin et al.[56]	Main OC3 spar and four wider cylinder	Potential flow theory	Linear wave theory	yes
Meng et al.[57]	Spar	Morrison's equation	Linear wave theory, current	yes
Tomasicchio et al. [58]	OC3 Spar	Experimental study	Linear wave theory	yes
Liu et al. [59]	OC3 Spar, mooring with clump masses	Potential flow theory	Linear wave theory	yes
Russo et al. [60]	OC3 Spar	Experimental study	Linear wave theory	yes
Kopperstad et al. [61]	Spar	Potential flow theory	Linear wave theory	yes
Pantusa et al. [62]	Spar	—	Linear wave theory	yes
Stewart and Muskulus [17]	Spar	—	Linear wave theory	yes
Leimeister et al. [18]	Spar	—	Linear wave theory	yes
Salic et al. [63]	Spar	—	Linear wave theory	yes
Xu and Srinil [64]	Spar	Morrison's equation	Linear wave theory	yes

Linear wave theory (LWT) linearizes the free surface boundary where the waves propagate on a homogeneous fluid layer. The assumption is that the wave height is small compared to the water depth in the deep-water regions or the wavelength in shallow water regions. LWT is convenient to replicate the random sea states and higher-order non-linear surface gravity waves for applying in design offshore structural engineering

applications. Another application of LWT is to approximate tsunami waves in the ocean. Up to now, LWT has been used in previous studies on FOWTs [65, 66, 67, 68]. However, LWT has failed to address the actual free surface. The waves of LWT have a sinusoidal wave pattern and the wave amplitudes, which are the distance from the peak or the trough to the mean water level, are equal. The physical periodic sea waves tend to have shaper crest and flatter trough [2] leading to the various distance from the waves' maxima to the mean water level, where the above mean water distance usually exceeds the maximal depression below it. Besides, LWT can not provide accurate wave kinematics above the mean water level. Faltinsen [37] had mentioned the 'higher-order error' regarding velocity and pressure distribution, especially under the wave trough. To overcome the errors with the free surface instantaneous positions, it requires extension methods [69] to estimate the wave kinematic above mean water level (MWL). The higher terms are also added lately to the first-order regular solution, called Stokes' expansion, to sharpen the crests and shallow the troughs [70]. Despite the above correction approaches, LWT possesses limitations with recreating wave amplitude and non-linear fluid properties. Linear approximations limit the application of LWT in waves of small amplitude. LWT cannot accurately simulate the moderate and large-amplitude waves, the wave kinematic, and the physical motion of the fluid particle [2, 71]. Recently, large-amplitude waves theory exist and provide an alternative steady periodic wave model accounting for the non-linear free surface as well as non-linear wave kinematics [2].

1.4 Large-amplitude wave theory

Irrotational periodic travelling waves were firstly studied by Stokes [70]. Other authors constructed the solutions related to waves of low amplitude using power series in [72, 73, 74]. For the large-amplitude irrotational waves, Krasovskii provided a proof of the existence of the steady-state waves without a hypothesis of smallness of the waves amplitude [75]. Keady and Norbury [76] extended Krasovkii's work using the method of bifurcation theory and [77, 78, 79] proved the existence of waves with stagnation points at their crest. The stagnation points have zero vertical velocity and the horizontal velocity equals the speed of the surface wave.

In reality, rotational waves exist with arbitrary distribution of vorticity, for instance, shear current with non-uniform velocity profile or surface motion of water due to wind. Hence, the irrotational flow is not an accurate assumption. Nonzero vorticity was considered by Gerstner in propagation of a periodic travelling waves in infinite depth water [**?**] in 1802. In 1934, Dubreil-Jacotin studied the existence of steady periodic water waves with general vorticity using power series. Goyon [80] and Zeidler [81] extended Dubreil-

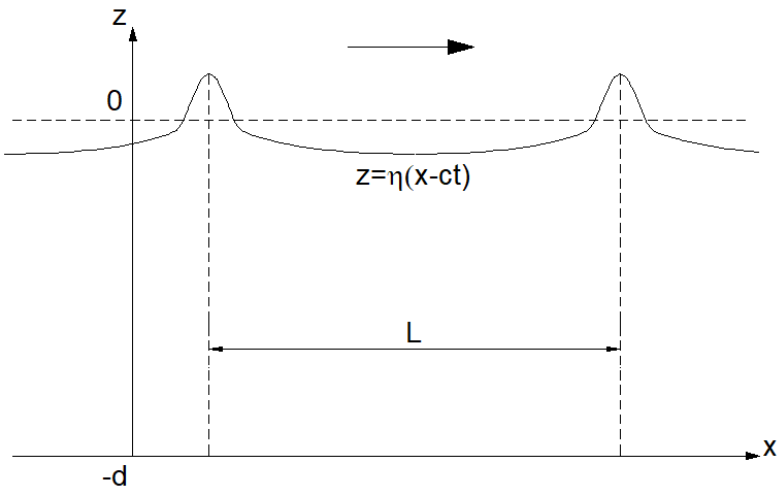

Figure 1.2: A non-linear periodic travelling wave propagates in $(x, z)-$coordinate in fixed mean water depth d with wavelength L and surface profile η (figure recreated from [2]).

Jacotin study to construct small-amplitude rotational waves. The regular waves defined in the study have one crest per wave length, constant wave speed, and a decreasing profile from crest to trough. In case of irrotational flow, Stokes [70] and Amick, Fraenkel, and Toland [82] found a limiting wave with stagnation and angle $2\pi/3$ at wave crest.

On the other hand, the linear approximation to model rotational waves results in a poor description with considerable errors shown in experimental studies [83, 84, 85, 86]. In 2004, Constantin and Strauss proved the existence of two-dimensional inviscid periodic large-amplitude regular waves with vorticity in a flow without stagnation points [87]. The authors considered wave speed, wavelength, and relative mass flux. It is worth noting that the water depth is not a constant and it varies along the bifurcation curve of solutions [87, 88, 89]. Since then, the flow properties with vorticity were studied extensively, i.e., the symmetric profile [90, 91, 92], stability [93], and real analyticity of the streamlines [94, 95, 96, 97, 98]. Moreover, the study is extended to investigate the existence of waves to flows with surface tension, with stagnation points, and discontinuous vorticity [99, 100, 101, 102, 103, 104, 105]. In addition, the numerical results in [88, 89] reveal the stagnation points occur within the fluid domain beneath the wave crest for some constant non-zero vorticities, for instance the maximum horizontal fluid velocity is on the bed under the wave crest.

Nevertheless, engineering applications are constrained by the non-constant water depth since man-made structures are usually deployed in a fixed depth water area. Henry [106, 107] proved the existence of steady periodic water waves for rotational flows with fixed depth allowing the relative flux to vary. He introduced the water depth into a modified height function while retaining the height function characteristic [87]. This

is remarkable difference from the height function in [87] where the water depth is not involved. Based on his work, the numerical model is presented in the thesis.

Large-amplitude waves travelling in flows with constant vorticity is firstly numerically solved using penalization method [108]. An alternative approach is based on numerical continuation techniques [109]. The bifurcation curve is obtained with non-laminar flows of constant vorticity and particular case of vorticity [110]. The numerical solutions is bounded by waves of maximal amplitude with a stagnation point in the flow. Ko and Strauss [88, 89] presented numerical results agreed with the analytical findings. Kalimeris [110, 111] showed that the stagnation points can occur both at the crest and at the point on the bottom beneath the wave crest. The maximum wave amplitude is obtained at the end of the bifurcation curve and the vorticity affects the shape of the streamline of the extreme waves. For cases with constant vorticity, there are also some numerical computations [112, 113, 114, 115, 116] documented in a recent survey for rotational water waves [117]. Numerical method based on conformal mapping have also been presented for waves on linear shear flow [118, 119, 120].

The aforementioned studies [87, 102] have proved the existence of large amplitude steady water waves with a general vorticity distribution in a flow with no stagnation points and in constant vorticity flows with stagnation points. These are in the global bifurcation branch of which the speed of wave c being larger than the speed of the current k. Basu [121] investigated flow qualitative properties, i.e., velocity, pressure, and surface profiles, under two-dimensional waves (irrespective of waves amplitude) and an underlying uniform current. The flow properties are found to be dependent on the relative speed of the surface waves and the average strength of the current, while the pressure field is not affected by the current. In addition, the Stokes waves and the underlying uniform current of same speed can not exist simultaneously in an irrotational flow [121].

On the other hand, as $k > c$, the flow field properties differ from the case without underlying uniform current [122, 123]. The possibility of existence of global bifurcation branch when the speed of wave c being less than the speed of the current k has recently proved by Basu [124] based on the works of Keady [76] and Basu [121]. The author sought for the solutions for two-dimensional periodic free surface waves propagating on an irrotational flow over finite depth with uniform underlying current. Basu analytical results [121] were then investigated numerically by Chen et.al. [125] and [126]. In [125], the numerical model is based on the Dubreil-Jacotin transformation [127], local bifurcation, and numerical continuation. It is worth noting that the numerical model proposed by Chen and Basu [125] is for irrotational flow.

The numerical continuation method based on Constantin and Strauss breakthrough work

[87] have been used to study the rotational flows [88, 111] providing a set of waves of the same wave length with the fixed relative mass flux. However, the water depth varies in these studies. For large-amplitude waves propagating on rotational flow in fixed depth water with arbitrary vorticity (depth varying current), Chen and Basu [126] proposed a numerical model based on Henry's formulation [106, 107]. For a fixed water depth and arbitrary current profile, Chen and Basu [126] numerical method begins with the laminar flow solution for a known vorticity distribution, arriving at a small-amplitude waves solution (local bifurcation) and shooting toward a limiting wave of the largest wave height (at stagnation point-global bifurcation).

The solutions are a family of waves of same wavelength with fixed mean water depth while allowing the corresponding wave period to vary. The numerical model captures a very interesting feature of the bifurcation diagram where the wave period decrease with the the increase of the wave amplitude. A small changes in the wave period leads to a dramatical increase of the wave amplitude along the bifurcation diagram.

The above theoretical studies have not investigated the fluid accelerations under the free surface so far. Lack of fluid acceleration limits the applications of large-amplitude waves in studying large-amplitude waves effects on structures. In addition, the investigation of large-amplitude waves-structure interaction, large-amplitude waves-current interaction are also restricted by incomplete wave kinematics. Therefore, this thesis aims to bridge these gaps. In this thesis, the fluid acceleration formulations are for the first time derived using the numerical solutions from large-amplitude wave results: either height function values or pressure results. The equivalence of these approaches is proved to ensure the accuracy of the numerical results. Including the fluid accelerations, the fluid kinematics under a large-amplitude wave are fulfilled. The hydrodynamic effects can be estimated with provided wave kinematics, and the loads from the large-amplitude waves are computed completely. Therefore, the FOWTs responses to the large-amplitude waves are investigated for the first time.

1.5 Large-amplitude wave-current interactions

For coastal and offshore structures, applications of wave and current have been included in the oil and gas industry (rigs, pipelines, ship operations), coastal structures, ecological (oxygen, sedimentological studies, wave and tidal devices, flooding). As the wave and the underlying current are coexist in an open sea, they influence each other. Wave-current interactions occur over a wide range of oceanic conditions: surface waves and barotropic tidal current, surface waves and wind-driven surge currents, wave-generated mean flow, etc.

The wave-current interactions was initially studied in 1960s [128, 129] showing changes in shape of short waves. In addition, numerical method was of interest to investigate quantitatively the interaction effects. Dalrymple [130] proposed a numerical model for waves on linear shear flow. The numerical results confirmed the changes in the surface profile due to the linear shear flow. To model finite amplitude waves on rotational flow with nonconstant vorticity, Dalrymple [131, 132] used the Dubreil-Jacotin transformation [127] and finite difference method. The numerical models results were found to be in moderate agreement with experimental results [86]. Dalrymple and Cox investigated the influence of vorticity on surface waves profiles with trigonometric and hyperbolic current profiles. Effects of opposing current and linear shear flow have been studied numerically and experimentally by Liao et.al. [133, 134] and Ma et.al. [135, 136]. Further studies on the numerical studies for time-dependent wave-current interaction and varying topology can be found in [137, 138, 139]

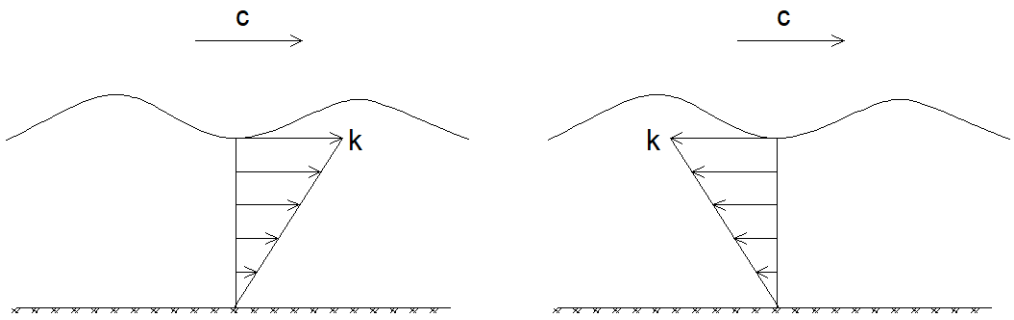

Figure 1.3: Wave-current interaction: (a) favourable current; (b) adverse current. Current strength and wave speed are represented by k and c, respectively (figure recreated from [2]).

Wave kinematics such as wave number and frequency are modified due to shoaling and refraction in the absence of energy sources and sinks. On the one hand, the wave does not influence the current field. On the other hand, the water depth and current are accounted for in the dispersion relation with wavelength changes depending on the current direction. There is also a contribution leading to the different effects of the homogeneous or inhomogeneous current and steady/unsteady flow. The linear regular wave-current interaction model proposed by Thomas [140] is based on Airy waves. The waves dispersion relation and the wave frequency are modified by the current during the propagation. Similarly, the irregular waves-current interaction is given in [141, 142]. Hedges and Lee [143] provided a derivation of an equivalent uniform current. The wave-current interaction, specifically in the vertical direction, including the bottom fiction, wave kinematics, and wave-induced mass transport were discussed by Soulsby and colleagues [144]. The authors predicted wavelength and bottom orbital velocity using a mean current approximation. Tolman treated the current as unsteady [145, 146, 147]. Burrows and Hedges [148] investigated the current impact on the wave parameters.

Hedges [149] implied the importance of taking the wave-current interaction into account as considering the recorded bottom pressure for waves [150], and calculation of wave spectra, refraction, forces on the structure and extreme waves. Wolf and Prandle [151] stated that the waves and current should be monitored simultaneously since the knowledge of either determines the other in the shallow water region. The authors noted that the waves are likely to affect tidal current in less than 50m water depth regions. In the shallower depths (less than 20m), the dramatic effect can be found as the point wave velocities are dispersive for waves with periods larger than 6s. As the wave height increase, the tidal current amplitude decreases apparently. In addition, the wave-current interaction also exists in deep water regions. The underlying current modifies not only the surface wave profile but also the wave kinematics.

The significant impacts of the waves-current interaction were practically observed [152] or numerically highlighted through the fatigue loading [153] in shallow or intermediate water depth. Turning into the deep water region, where the FOWTs are deployed, the current effects on the mooring system are extensively pronounced because of its large dimensions. Two main challenges to examine the impact of wave-current interaction on the FOWTs responses are a fully non-linear mooring model and a precisely analytical wave-current interaction model. The first issue has been overcome by the recent development of the non-linear moorings so far [154]. In mooring studies, the linear wave model has been widely used in linearized or quasi-static mooring models. Although the existence of current in the flow field is recognized and its effect is recommended to be considered in the mooring model [155], studies assessing current impact are limited in earlier studies [9, 28]. In addition, the current affects the static, dynamic, and damping response of the mooring cables [156, 157] as well as induces the static offset and possibly the dynamic responses of the overall floating platform [158]. The first way to incorporate the current effect is simply superposing the current strength and the wave in which their interaction is neglected [157].

On the other hand, the latter issue requires more attention. There is a widely used model for linearized waves and current interaction in which the wave angular frequency and the dispersion relation are modified due to the current effects [140]. Based on the solution of the regular waves model, the irregular waves-current interaction was presented by Huang et al. [142] and Tung and Huang [141]. The authors investigated the effect of current on the spectrum of irregular waves. The models were then further extended to account for the wave breaking by the direction of the underlying current [159, 160]. The models was validated with experimental studies [140, 161, 162] then they has been used to validate the numerical model [163]. The models have been used in studies of marine structure [164, 165], marine current turbines [166, 167]. The model was also used to investigate the fatigue loading of a fixed-bottom wind turbine. Chen

and Basu [168] used the above wave-current model to study the fatigue life of FOWTs. The authors then investigate the wave-current interaction on the dynamic responses of FOWTs structure recently [31], especially on mooring cables' responses.

The existence of large-amplitude waves on shear flow had been reported in numerical studies [115, 169], however it had not been proved analytically. In 2004, a rigorous work of Constantin and Strauss [123] proving the existence of the large-amplitude waves on rotational flow laid fundamental principle of large-amplitude waves theory. Subsequently, the work is extended by considering flows with discontinuous vorticity [101, 170, 171, 172, 173] investigation of flow properties [91, 92, 174], analyticity of the surface profile and streamlines [94, 96], particle trajectory [120, 174], and effects of vorticity [88, 89]. The aforementioned studies with assumption that the propagating speed of the waves larger than the speed of the current has been extended by Basu and his colleagues. The properties of the irrotational flow with underlying current was studied, particularly for the case where the current strength is larger than the surface waves speed [121, 175, 176]. Subsequently, Basu [124, 177] proved the existence of the large-amplitude waves propagating on the surface of an irrotational flow with underlying uniform current. The author further proposed the flow force function to reformulate the irrotational periodic gravity water wave problem in [178]. Following the work of Basu [124], a numerical method has been established for solving large-amplitude travelling on underlying current [125, 126].

In this thesis, the proposed numerical continuation approach [126] is used for computing large-amplitude waves, based on emerging formulation for fixed mean-depth of water [106, 107].

1.6 Solitary wave-structure interactions

There are many existing studies on solitary waves and solitary waves' impact on offshore structures. In the flow field, the presence of a structure distorts free surface and the flow motion. The flow properties consequently possess an impacted profile compared to permanently analytical wave models. Therefore, the computation of the structure responses should consider the modification of the surface water such as the green water, the breaking water, and overtopping water. In this thesis, a hybrid approach is introduced to study the interaction of FOWTs and solitary waves.

A tsunami is generated by earthquakes, landslides, volcano eruptions and other mechanisms such as the earth's crust movements. A substantial and sudden displacement of a massive amount of water is created at the places where these natural events happen. The wave speed can reach speeds of about 805 km/h [179], and the wave retains its

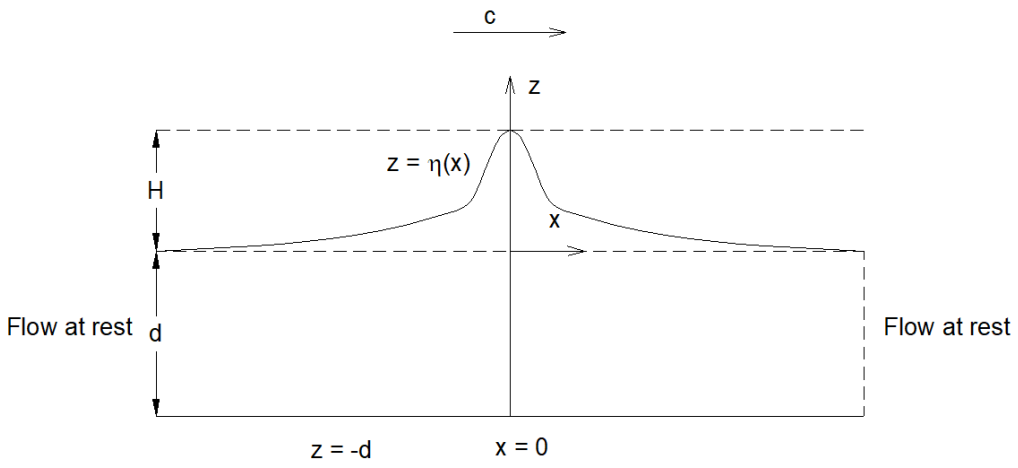

Figure 1.4: A solitary wave (figure recreated from [2]) propagating in x-direction with wave speed c, wave height H, surface profile η, over water depth d.

energy as it travels across the ocean [180]. At the source of the wave and during its propagation, the wave amplitude is small (1-2m), while the wavelength is much longer than the local water depth (3-10 km). A tsunami with 7.7m height water run-up was observed in particular on Biak Island [181]. Once the waves approach the shore, the shore bathymetry, i.e. reduction of water depth and lope of beach, affect the wave pattern. The wave height change dramatically, especially for the following wave in a series of waves which is always stronger and higher than the first wave [179]. The water level can rise about 3m - 30m. Following the waves is the high energy flood which can travel inland by 300 m or more, stripping the nearshore buildings, damaging properties, and causing the lost of lives. In 1775, a tsunami killed 60000 people in Portugal, Spain, and North Africa. A tsunami associated with an earthquake in the South China sea killed 40000 people. A tsunami by Indonesia's Krakatoa volcano eruption made 36500 life lost in 1883. In 2004, the most devastating Indian Ocean tsunami in the south Java sea killed 200000 people. According to the U.S National Oceanic and Atmospheric Administration (NOAA), most tsunami have been observed in the Pacific ocean so far [179].

Solitary waves usually have smaller wave heights in the open sea, and they almost have no impact on floating devices. It leads to the fact that solitary waves' influence in the open sea is not as severe as in the shoreline. Nevertheless, the high phase speed of the wave will have a significant effect on the subsurface structure, especially for offshore wind turbines having large foundations with a broad shape or deep draft. Therefore, solitary wave impacts requires to be investigated carefully.

Research on solitary wave-structure interaction can be divided into three main topics: the wave run-up [182, 183], interaction of solitary wave and fixed structures [184, 185, 186, 187], and interaction of wave with floating and/or flexible structures [188].

Recently, Cui *et.al.* examined the responses and mooring system of a scaled model of a floating platform [189]. Cai et.al. used the observation data of internal soliton near Dongsha Islands to estimate the horizontal velocity and acceleration in the vertical sections (along the length of the monopile) to compute the force and torque on a fixed cylindrical pile [190, 191].

Apart from the surface solitary waves, internal solitary waves simultaneously attract researchers and engineers, especially their impact on floating devices. The internal solitary waves exist in deep water regions with a larger amplitude than the solitary surface waves. Zhang *et.al.* compared forces and moments on the spar and semi-submersible platform under the internal solitary wave, and surface waves [192]. The internal wave amplitude is -140 m while the surface wave height is 7.7 m and 12.2 m. They concluded that the Morison equations are an accurate method for estimating Korteweg-de Vries (KdV) internal wave loading for spar and semi-submersible platforms. In addition, the author found that the thickness of the water layer relates to the horizontal wave load and moment. The results showed that the internal solitary wave had a much large wave amplitude. Therefore, its wave forces on platforms are smaller than that of the surface waves. However, they should not be ignored. Experimental studies were conducted in Shanghai Jiao Tong University to investigate wave load on the spar platform by Huang *et.al.* [193]. The author suggested an empirical formula to determine drag and inertia coefficients for Morison equations. The results showed that the forces increase as the wave approaches the spar, horizontal and vertical forces reach their trough and crest as the wave recently passes by the structure. Wang and Zhou [194] investigated the scaling effect of internal solitary wave loads on spar platforms. They found that the direct scale of horizontal force would lead to overestimating the prototype while the vertical force was applicable directly.

The phenomenon of the waves overtopping offshore structures and propagating over a structure's deck is known as a green water event [195, 196]. The green water can alter the hydrodynamic loads and damage the integrity of floating structure [197]. Greco *et.al.* [198] classified the green water events into three main types: the dam-break, the plunging-dam-break, and the hammer-fist types. The study of green water is necessary to predict the waver propagation over the structures and estimate induced loads. Physical tests are preferred to obtain information on flow evolution [199, 200, 201, 202] using the image-based measurement in simplified experiments [203] in terms of the water elevations [204, 205, 206, 207]. In terms of the structure width, the spar-type FOWT is considered a slender structure, the incoming solitary waves approach the structure, but a hump of water does not overtop the body. Due to wave-structure interaction, the water elevation alters at the vicinity of the structure. It means that the wave shape is not analytically stable as to be assumed by the theoretical model. Although studies

on solitary waves have been of interest to researchers for decades; however, there are limited studies considering fluid-structure interaction's effect on the FOWT structures.

Numerical wave simulation has been performed using a variety of methods. To solve the Navier-Stoke equations, the Lagrangian and the Eulerian are the two approaches. The Eulerian approach has been applied to study waves for decades and is considered mature. Nevertheless, the Eulerian method still faces the challenge of simulating large deformations and violent surface interactions which require special meshing technique on the surface boundary. On the other hand, the Lagrangian approach is naturally suited for large deformation problems [1] since it requires no special treatment for monitoring and recreating free surface. Because of these, the SPH which is a Lagrangian method has received attention from scientists and engineers.

In the literature, there has been many studies on wave simulation using SPH [208, 209]. SPH, which was released in 1994 [209] for fluid dynamics, is investigated and proved its applicability in wave simulation, wave-structure interaction, astrophysics, hydrodynamics, soil mechanics and biomechanics, etc. In hydrodynamic study, there are many studies have been carried on using SPH for wave-structure interaction [210, 211, 212], basic flow problems [213], multi-phase flow [214], flow in machine-a pump [215, 216]. The method is receiving attentions from many researchers to improve the method accuracy and to apply the method to new engineering problems. Lind et al. proposed Incompressible Smoothed Particle Hydrodynamics (ISPH) method to stabilize wave propagation along an open channel [217]. Altomare et al. reported a comprehensive study of wave generation and wave absorption using Weakly Compressible Smoothed Particle Hydrodynamics (WCSPH) [210, 211, 212]. Omidvar et al. identified the disadvantage of artificial viscosity that affects water surface representation [218]. Chang et al. proposed a new SPH method where generated wave properties agreed well with the Second order Stokes' wave [219]. Recently, Verbrugghe et al. coupled Finite Volume Method (FVM) and the DualSPHysics code [220] to simulate non-linear wave in a large domain [221]. In the above studies, the properties of the modelled wave, which are the surface amplitude, pressure, and velocity field, are studied and validated with the results from analytical methods and experimental simulations. However, the distributions and profiles of pressure and velocity field beneath the surface within the fluid domain are not completely examined. The previous studies mostly focused on the pressure or velocity at a specific position under generated wave. Hence, the objective of this thesis is to investigate the ability of SPH to simulate numerical waves, waves'kinematics, and the wave-structure interaction.

In addition to the analytical study of the FOWTs's responses to the large amplitude waves, the thesis proposes a hybrid approach to investigate the impact of wave-structure interaction on FOWTs specifically solitary waves. Recent analytical studies do not

account for the surface changes that means neglecting the structure-wave interaction. Since FOWTs in the fluid domain is an obstacle to the propagating waves, the solitary wave's shape will be modified accordingly due to interaction. The change in surface profiles represents the modification of the fluid kinematics that should be taken into account.

We propose a hybrid algorithm to calculate wave kinematics under modified non-linear surface waves. The code is first applied to compute solitary wave kinematics with an permanent free surface. Then, the solutions are compared with the analytical results for validation. Following the validation of the computational code, non-linear solitary wave-structure interaction surface are studied; their velocity, accelerations profiles, and pressure distribution are derived from the free surface profile obtained from SPH simulations in which the solitary waves-FOWT interaction is modelled to obtain the modified surface profile. Wave kinematics resulting from the modified surface profile is then used to investigate the impact of solitary waves on FOWTs.

In this thesis, SPH method is applied to model the large amplitude wave and the soaring phenomenon as the solitary wave interacting with the structure. By capturing the soaring water profile, the vertical velocity component at the free surface is calculated. The Laplace equation of the vertical velocity component is then solved numerically for the vertical velocity within the fluid domain. Based on the solutions, we can recover the fluid kinematics within the fluid domain. By that, the fluid-structure interaction is accounted for as the solitary wave is considered in FOWT study.

1.7 Motivation of this thesis

The aim of this thesis is to investigate the structural dynamic behaviour of SFOWT to non-linear wave effects. Particular emphasis will be placed on studying SFOWT responses in large-amplitude waves. This work is of topical research interest for design of modern offshore wind turbines.

As the wind turbines are deployed further from the shore, they are subjected to vibrations induced by external aerodynamic loading, gravity loading, wave loading, current loading, mooring loading, and their interactions. The large-amplitude regular waves affect the mechanical components of the turbine and induce fatigue in the wind turbine components which may lead to the structural/mechanical damage. Therefore, there is a crucial requirement for understanding the large-amplitude wave effects and this in turn could lead to a significant improvement in the operational efficiency and lifespan of a wind turbine.

Theoretical models for the wind turbine will be developed in this thesis using an Euler-

Lagrangian approach. The model accounts for the dynamic behaviour of blades, tower, floater and their interactions. The effect of mooring system will also be accounted for.

Aerodynamic loads are calculated using the BEM. Large-amplitude waves theory has not been used for exploring before. Large-amplitude wave acceleration formulations are derived using modified height function and fluid pressure. The hydrodynamic effects will be computed using the Morison equations for structural load estimations.

The effect of the currents will also be studied. The fluid kinematics under the large-amplitude waves will be modified by the existence of the current, their modification will also be investigated and the performance of the FOWT will be analysed.

Finally, this thesis will aim to accurately model the interaction of the solitary waves and the wind turbine structure by accounting for the effect of solitary waves-structure interaction. A hybrid approach combining the advantages of SPH and the FEM has been proposed and investigated.

1.8 Organisation and aim of the thesis

This thesis has seven chapters following this chapter, including an introduction (Chapter 1) and conclusion (Chapter 7).

Chapter 1 provides a detailed review of the literature relevant to the topics dealt with throughout the thesis. The current state-of-the-art research in the area of wind turbine dynamics is presented. Particular emphasis is placed on non-linear waves and application of large-amplitude waves theory. The non-linear wave-current interactions is introduced with a particular emphasis on flow kinematics and thus the SFOWT responses. In addition, SFOWT responses to solitary waves are discussed.

Chapter 2 introduces the Euler-Lagrangian structural dynamic spar-type floating offshore wind turbine models and presents their formulations. The dynamic mooring model is used to simulate mooring loads and cable forces. Large amplitude non-linear water wave theory based formulation for investigating the impact on FOWT is derived. Large-amplitude wave kinematics are used to compute wave accelerations. The hydrodynamic loads are computed using Morison' equations. SFOWT responses to soly large-amplitude regular waves are investigated.

Chapter 3 describes the wave-current loading applied to the wind turbine models. Current effects are described and simulated by modifying the flow kinematics. Both spar hydrodynamic loads and mooring dynamic loads are updated and accounted for the current effects. Numerical simulations are performed on the models developed in Chapter 2.

In Chapter 4 solitary wave impact are studied with a view to investigate the significant impulse SFOWT responses that may develop. The dynamic responses of the whole system including the mooring system is considered.

Chapter 5 introduces SPH, a mesh-less method, to model the numerical waves. First, the fundamental of SPH is introduced. Then, a qualitative study is carried out to examine numerical wave kinematics compared to the exact results from non-linear large-amplitude wave theory. The numerical results prove the applicability of SPH to simulate the numerical wave tank, surface profiles of waves, and fluid kinematics.

Chapter 6 proposes a new approach for the calculation of the solitary waves kinematics taking the free surface of the waves-structure interaction into account. A FEM model is proposed and developed to solve for fluid dynamic within the fluid domain. Realistic loading representative of solitary waves-FOWT structure interaction is applied to the structure and the dynamic responses of the SFOWT are examined and compared to the non-interaction solitary waves results.

Chapter 7 concludes the thesis. The work that has been carried out in this thesis is summarized and conclusions that can be drawn from this study are presented. Suggestions are also made for areas requiring further research.

2 Dynamic response of FOWTs under large-amplitude waves

2.1 Introduction

The impact of large-amplitude waves on the FOWT responses and the cable fairlead forces have been analysed. The proposed formulation incorporates the recently developed theory of regular large-amplitude non-linear wave to study the FOWT responses. Significant differences between the large-amplitude wave kinematics and the linear wave kinematics exist.

For the purpose of investigation, a detail offshore wind turbine model with the relevant degrees of freedom is developed using the Euler-Lagrangian stationary principle. The blade and tower vibrations are coupled in the edge-wise direction (across-wind). The spar motions are in three dimensions, both linear and angular.

2.2 Large amplitude regular waves

2.2.1 Governing equations

Two-dimensional periodic large-amplitude waves propagating over a uniform water depth is considered. The water depth is fixed. The formulation of the gravity water wave problem is outlined here. The equations are first reformulated using a stream function applying Dubreil-Jacotin semi-hodograph [127] and finally transformed to the modified height form [106].

The Cartesian $(x, z)-$coordinates are used to represent the governing equations. The depth of the water is denoted by d, and the still water level is located at $z = 0$. So, the bottom is at $z = -d$. The wave period is assumed to be $2L$. The equation of the

free surface, $\eta(x,t)$, is $z=\eta(t,x)$ with

$$\int_{-L}^{L}\eta(x,t_0)dx=0. \tag{2.1}$$

The wave speed is denoted by $c>0$. The fluid velocity field takes the form $(u(x-ct,z),w(x-ct,z))$ or transferring to a moving frame of reference. The surface profile in the moving frame is obtained by $\eta(x-ct)$ and is unknown. Since the wave speed is assumed constant, the problem becomes a time-independent problem in the moving frame. The fluid domain is denoted by $\overline{D_\eta}=\{(x,z)\in\mathbf{R}^2:-d\leq z\leq\eta(x)\}$. The conservation of mass equation is given by

$$u_x+w_z=0, \tag{2.2}$$

with a constant fluid density, and the Euler's equation is given by

$$\begin{cases}(u-c)u_x+wu_z=-P_x\\(u-c)w_x+ww_z=-P_z-g,\end{cases} \tag{2.3}$$

where $P(x,z)$ is the pressure distribution function and g is the acceleration due to gravity. The fluid (water) is inviscid.

The boundary conditions include two surface conditions and one for the bottom. At the surface, the fluid particles always stay on the free boundary leading to the kinematic boundary condition. The condition states the relation between the vertical velocity component and the horizontal component and is expressed as $w=(u-c)\eta_x$ on $z=\eta(x)$. In addition, the dynamic boundary condition states that the pressure at the surface complies with $P=P_{atm}$ on $z=\eta(x)$ neglecting the surface tension. Here, P_{atm} is the constant atmospheric pressure. The bottom bed is considered impermeable. Thus, the kinematic boundary condition at the bottom states $w=0$ on $z=-d$.

The horizontal velocity component is assumed such that $u<c$, where c is the wave speed, throughout the fluid domain. The assumption ensures that no weak-stagnation points exist in the fluid domain. The wave peak and the wave trough are located at $x=0$ and $x=\pm L$, respectively. The flow vorticity is given by $\omega=w_x-u_z$.

We define a stream function $\psi(x,z)$, with $\psi_z=u-c,\psi_x=-w$. We also assume $\psi=0$ on $z=\eta(x)$ at the free surface. Hence, at the bottom, $z=-d$, $\psi=-p_0$, with

$$p_0=\int_{-d}^{\eta(x)}(u(x,z)-c)dz<0. \tag{2.4}$$

At a specific height z, the streamlines of the fluid motion with period of $2L$ are given

by

$$\psi(x,z) = -p_0 + \int_{-d}^{z} (u(x,s) - c)ds. \tag{2.5}$$

The relation of the stream function and the vorticity in a stream function-vorticity (see [123]) is deduced

$$\Delta\psi = \omega. \tag{2.6}$$

Let

$$\tilde{\Gamma}(p) = \int_0^p p_0\gamma(s)ds, \tag{2.7}$$

where, γ is the vorticity function and $p = -\psi$ on the flat bottom. The hydraulic head from Bernoulli's law is given as follows

$$Q = \frac{(u-c)^2 + w^2}{2} + g(z+d) + P - \left(\frac{\psi}{p_0}\right), \tag{2.8}$$

which is constant throughout the domain $\overline{D_\eta}$. The governing equations and boundary conditions in a stream function formulation are

$$\Delta\psi = \omega \qquad \text{in } -d < z < \eta(x), \tag{2.9a}$$

$$|\nabla\psi|^2 + 2g(z+d) = Q \qquad \text{on } z = \eta(x), \tag{2.9b}$$

$$\psi = 0 \qquad \text{on } z = \eta(x), \tag{2.9c}$$

$$\psi = -p_0 \qquad \text{on } z = -d. \tag{2.9d}$$

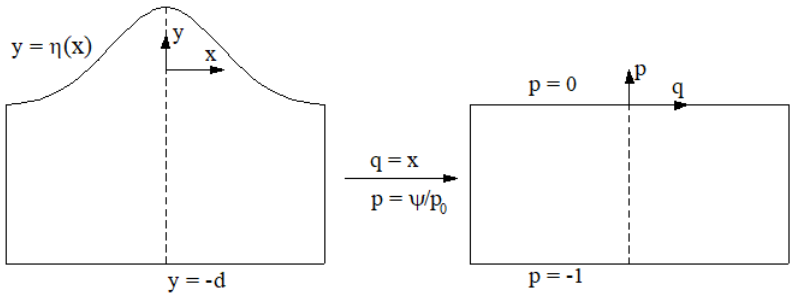

Figure 2.1: The semi-hodograph transform.

The governing equations are now reformulated using the modified height function [106] applying semi-hodograph transform [127]. The two new variables, (q, p), are related to the physical domain by $q = x, p = \psi(x,z)/p_0$ as shown in Fig.2.1. Now, the unknown free surface problem is transformed into a rectangular domain $\overline{R} = \mathbf{R} \times [-1, 0]$ and z becomes a function of new variables $z = z(q,p)$. In the transformed domain, the

modified height function is given by

$$h(q,p) = \frac{z}{d} - p. \tag{2.10}$$

The height function value takes the water depth into account, this is the main difference from the approach in Constantin [87]. There are two main characteristics of the height function, they are

$$\int_{-\pi}^{\pi} h(q,0)dq = 0 \text{ and } h(q,-1) = 0. \tag{2.11}$$

In addition, the derivatives from the two domain are related by

$$\begin{aligned} \partial_x &= \frac{\psi_x}{p_0}\partial_p + \partial_q, \qquad \partial_z = \frac{\psi_z}{p_0}\partial_p, \\ \partial_p &= \frac{p_0}{u-c}\partial_z = \frac{p_0}{\psi_z}\partial_z, \qquad \partial_q = \partial_x + \frac{w}{u-c}\partial_z = \partial_x - \frac{\psi_x}{\psi_z}\partial_z. \end{aligned} \tag{2.12}$$

The new system of equations in the transformed domain are given as follows

$$\begin{aligned} \left(\frac{1}{d^2} + h_q^2\right) h_{pp} - 2h_q(h_p+1)h_{pq} + (h_p+1)^2 h_{qq} + \frac{\gamma(p)}{p_0}(h_p+1)^3 = 0, \\ \text{in } -1 < p < 0, \\ \frac{1}{d^2} + h_q^2 + \frac{(h_p+1)^2}{p_0^2}[2gd(h+1) - Q] = 0, \qquad p = 0, \\ h = 0, \qquad p = -1. \end{aligned} \tag{2.13}$$

The height function, h, is even and periodic in q with period of 2π. The mass flux remains constant for each h, $p_0 = p_0^{(h)}$. The assumption of the horizontal velocity being smaller than the wave speed, $u < c$, is equivalent to $h_p + 1 > 0$.

2.2.2 Numerical scheme

Following the works by Constantin [2], and others [89, 111, 125], a numerical scheme is introduced in this section. Since the physical dimension for the problem concerned is large, modelling the physical domain would be costly. A scaled model is an alternative approach to save the computational cost. Constantin [2] suggested a scaled model with

$$\begin{aligned} \bar{\eta} = \kappa\eta, \quad \bar{c} = c, \quad \bar{u} = u, \quad \bar{w} = w, \quad \bar{P} = P, \quad \bar{x} = \kappa x, \quad \bar{z} = \kappa z, \\ \bar{t} = \kappa t, \quad \bar{g} = \kappa^{-1} g, \quad \bar{\gamma} = \kappa^{-1}\gamma, \quad \bar{d} = \kappa d \end{aligned} \tag{2.14}$$

where $\kappa = \frac{2\pi}{L}$ is the wave number, and L is the wavelength. The numerical model becomes $[-\pi, \pi] \times [-1, 0]$ [106, 107]. Since the waves are symmetrical about the crest,

the computational domain will be a half of the scaled model [91, 92]. The discretised domain using finite difference scheme [89, 125], $[0, \pi]\times[-1, 0]$, is shown in Fig.2.2 where vertical nodes and horizontal nodes are denoted by by $j = 1, 2, ..., J$ and $i = 1, 2, 3, ..., I$, respectively. The distance between the vertical nodes and that of horizontal nodes are Δp and Δq, respectively.

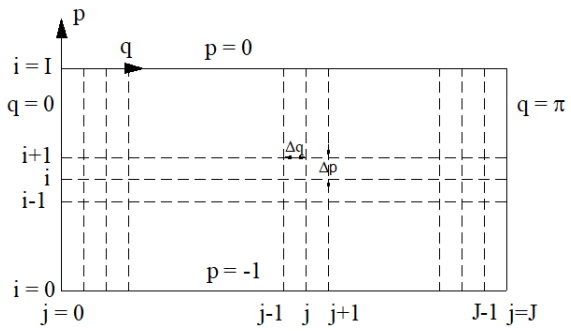

Figure 2.2: Mesh grids.

There are $(I+1)\times(J+1)$ nodes in the finite difference scheme and thus $(I+1)\times(J+1)$ unknowns for h values. The derivatives of the h function are determined by applying the central difference scheme for middle nodes and the forward and backward schemes for the boundary nodes as appropriate. Details of the h-derivatives are listed below.

Derivatives h_{pp} and h_{qq}

The second derivatives h_{pp} at boundaries $p = -1$ and $p = 0$ are given as follow

$$\begin{aligned} h_p|_{i=0,j} &\approx \frac{h_{1,j} - h_{0,j}}{\Delta p_0} \\ h_{pp}|_{i=0,j} &\approx \frac{\frac{h_{2,j}-h_{0,j}}{\Delta p_0+\Delta p_1} - \frac{h_{1,j}-h_{0,j}}{\Delta p_0}}{\Delta p_0} \\ &\approx \frac{h_{2,j}}{\Delta p_0(\Delta p_0 + \Delta p_1)} - \frac{h_{1,j}}{\Delta^2 p_0} + \frac{h_{0,j}}{\Delta^2 p_0(\Delta p_0 + \Delta p_1)/\Delta p_1} \end{aligned} \tag{2.15}$$

$$\begin{aligned} h_p|_{i=I,j} &\approx \frac{h_{I,j} - h_{I-1,j}}{\Delta p_I} \\ h_{pp}|_{i=I,j} &\approx \frac{\frac{h_{I,j}-h_{I-1,j}}{\Delta p_I} - \frac{h_{I,j}-h_{I-2,j}}{\Delta p_I+\Delta p_{I-1}}}{\Delta p_I} \\ &\approx \frac{h_{I-2,j}}{\Delta p_I(\Delta p_{I-1} + \Delta p_I)} - \frac{h_{I-1,j}}{\Delta^2 p_I} + \frac{h_{I,j}}{\Delta^2 p_I(\Delta p_{I-1} + \Delta p_I)/\Delta p_{I-1}} \end{aligned} \tag{2.16}$$

$$
\begin{aligned}
h_p|_{i,j} &\approx \frac{h_{i+1,j} - h_{i-1,j}}{\Delta p_i + \Delta p_{i-1}} \\
h_{pp}|_{i,j} &\approx \frac{\frac{h_{i+1,j}-h_{i,j}}{\Delta p_i} - \frac{h_{i,j}-h_{i-1,j}}{\Delta p_{i-1}}}{(\Delta p_i + \Delta p_{i-1})/2} \\
&\approx \frac{h_{i+1,j}}{\Delta p_i(\Delta p_{i-1} + \Delta p_i)/2} - \frac{h_{i,j}}{\Delta p_i \Delta p_{i-1}/2} + \frac{h_{i-1,j}}{\Delta p_{i-1}(\Delta p_{i-1} + \Delta p_i)/2}
\end{aligned} \tag{2.17}
$$

The second derivatives h_{qq} are given as

$$
\begin{aligned}
h_q|_{i,j=1} &\approx \frac{h_{i,2} - h_{i,1}}{\Delta q_1} \\
h_{qq}|_{i,j=1} &\approx \frac{\frac{h_{i,3}-h_{i,1}}{\Delta q_2+\Delta q_1} - \frac{h_{i,2}-h_{i,1}}{\Delta q_1}}{\Delta q_1} \\
&\approx \frac{h_{i,3}}{\Delta q_1(\Delta q_1 + \Delta q_2)} - \frac{h_{i,2}}{\Delta^2 q_1} + \frac{h_{i,1}}{\Delta^2 q_1(\Delta q_1 + \Delta q_2)/\Delta q_2}
\end{aligned} \tag{2.18}
$$

$$
\begin{aligned}
h_q|_{i,j=J} &\approx \frac{h_{i,J} - h_{i,J-1}}{\Delta q_J} \\
h_{qq}|_{i,j=J} &\approx \frac{\frac{h_{i,J}-h_{i,J-1}}{\Delta q_J} - \frac{h_{i,J}-h_{i,J-2}}{\Delta q_J+\Delta q_{J-1}}}{\Delta q_J} \\
&\approx \frac{h_{i,J-2}}{\Delta q_J(\Delta q_J + \Delta q_{J-1})} - \frac{h_{i,J-1}}{\Delta^2 q_J} + \frac{h_{i,J}}{\Delta^2 q_J(\Delta q_{J-1} + \Delta q_J)/\Delta p_{J-1}}
\end{aligned} \tag{2.19}
$$

$$
\begin{aligned}
h_q|_{i,j} &\approx \frac{h_{i,j+1} - h_{i,j-1}}{\Delta q_j + \Delta q_{j-1}} \\
h_{qq}|_{i,j} &\approx \frac{\frac{h_{i,j+1}-h_{i,j}}{\Delta q_j} - \frac{h_{i,j}-h_{i,j-1}}{\Delta q_{j-1}}}{(\Delta q_j + \Delta q_{j-1})/2} \\
&\approx \frac{h_{i,j+1}}{\Delta q_i(\Delta q_{j-1} + \Delta q_j)/2} - \frac{h_{i,j}}{\Delta q_j \Delta q_{j-1}/2} + \frac{h_{i,j-1}}{\Delta q_{j-1}(\Delta q_{j-1} + \Delta q_j)/2}
\end{aligned} \tag{2.20}
$$

Derivatives h_{pq}

The expression are as follows

$$
h_{pq}|_{i,j} \approx \frac{\frac{h_{i+1,j+1}-h_{i+1,j-1}}{\Delta q_j+\Delta q_{j-1}} - \frac{h_{i-1,j+1}-h_{i-1,j-1}}{\Delta q_j+\Delta q_{j-1}}}{(\Delta p_i + \Delta p_{i-1})} \approx \frac{h_{i+1,j+1} - h_{i+1,j-1} - h_{i-1,j+1} + h_{i-1,j-1}}{(\Delta q_{j-1} + \Delta q_j)(\Delta p_i + \Delta p_{i-1})} \tag{2.21}
$$

$$h_{pq}|_{i,j=1} \approx \frac{\frac{h_{i+1,2}-h_{i+1,1}}{\Delta q_1} - \frac{h_{i-1,2}-h_{i-1,1}}{\Delta q_1}}{(\Delta p_i + \Delta p_{i-1})} \approx \frac{h_{i+1,2} - h_{i+1,1} - h_{i-1,2} + h_{i-1,1}}{\Delta q_1(\Delta p_i + \Delta p_{i-1})} \tag{2.22}$$

$$h_{pq}|_{i,j=J} \approx \frac{\frac{h_{i+1,J}-h_{i+1,J-1}}{\Delta q_J} - \frac{h_{i-1,J}-h_{i-1,J-1}}{\Delta q_J}}{(\Delta p_i + \Delta p_{i-1})} \approx \frac{h_{i+1,J} - h_{i+1,J-1} - h_{i-1,J} + h_{i-1,J-1}}{(\Delta q_j)(\Delta p_i + \Delta p_{i-1})} \tag{2.23}$$

$$h_{pq}|_{i=I,j} \approx \frac{\frac{h_{I,j+1}-h_{I-1,j+1}}{\Delta p_I} - \frac{h_{I,j-1}-h_{I-1,j-1}}{\Delta p_I}}{(\Delta q_J + \Delta q_{J-1})} \approx \frac{h_{I,j+1} - h_{I-1,j+1} - h_{I,j-1} + h_{I-1,j-1}}{\Delta p_I(\Delta q_J + \Delta q_{J-1})} \tag{2.24}$$

$$h_{pq}|_{i=0,j} \approx \frac{\frac{h_{1,j+1}-h_{0,j+1}}{\Delta p_1} - \frac{h_{1,j-1}-h_{0,j-1}}{\Delta p_1}}{(\Delta q_j + \Delta q_{j-1})} \approx \frac{h_{1,j+1} - h_{0,j+1} - h_{1,j-1} + h_{0,j-1}}{\Delta p_1(\Delta q_{j-1} + \Delta q_j)} \tag{2.25}$$

At four corners

$$h_{pq}|_{0,0} \approx \frac{\frac{h_{1,1}-h_{1,0}}{\Delta q_1} - \frac{h_{0,1}-h_{0,0}}{\Delta q_1}}{\Delta p_1} \approx \frac{h_{1,1} - h_{1,0} - h_{0,1} + h_{0,0}}{\Delta p_1 \Delta q_1} \tag{2.26}$$

$$h_{pq}|_{I,0} \approx \frac{\frac{h_{I,1}-h_{I,0}}{\Delta q_1} - \frac{h_{I-1,1}-h_{I-1,0}}{\Delta q_1}}{\Delta p_I \Delta q_1} \approx \frac{h_{I,1} - h_{I,0} - h_{I-1,1} + h_{I-1,0}}{\Delta p_I \Delta q_1} \tag{2.27}$$

$$h_{pq}|_{I,J} \approx \frac{\frac{h_{I,J}-h_{I,J-1}}{\Delta q_J} - \frac{h_{I-1,J}-h_{I-1,J-1}}{\Delta q_J}}{\Delta p_I} \approx \frac{h_{I,J} - h_{I,J-1} - h_{I-1,J} + h_{I-1,J-1}}{\Delta p_I \Delta q_J} \tag{2.28}$$

$$h_{pq}|_{0,J} \approx \frac{\frac{h_{1,J}-h_{1,J-1}}{\Delta q_J} - \frac{h_{0,J}-h_{0,J-1}}{\Delta q_J}}{\Delta p_1} \approx \frac{h_{1,J} - h_{1,J-1} - h_{0,J} + h_{0,J-1}}{\Delta p_1 \Delta q_J} \tag{2.29}$$

In this thesis, the numerical schemes applied by Chen and Basu [125] and Ko and Strauss [89] is followed. The domain is discretised with more vertical nodes than the horizontal nodes to obtain better resolution of streamlines. Substituting the derivative

approximations into the governing equations, one obtains $(I-1)\times(J-1)$ equations for intermediate nodes with indices $i = 1, 2, ..., I-1$ and $j = 1, 2, ..., J-1$; and $2(J-1)$ equations for the boundaries with $i = 0, I$ and $j = 1, 2, ..., J-1$. Because of the symmetry property at $q = 0$ and $q = 1$, there are $2(I+1)$ equations given by

$$h_{i,0} = h_{i,2}, h_{i,J-2} = h_{i,J}(i = 0, 1, 2, ..., I). \tag{2.30}$$

At the free surface, the mean water at $z = 0$, states

$$\sum_{j=1}^{J-2} \frac{1}{2}(h_{I,j} + h_{I,j+1})\Delta q_j = 0, \tag{2.31}$$

using the trapezoidal rule for numerical integration. For $(I+1)\times(J+1)+1$ unknowns, we have $(I+1)\times(J+1)+1$ equations to solve for

$$\mathbf{h} = [h_{0,0}, h_{1,0}, ..., h_{I,0}, h_{0,1}, ..., h_{I,J}\theta]^T \tag{2.32}$$

where θ can be d, p_0 or Q depending on the setup of the problem. The parameters d and Q are unknowns in the fixed flux problems [89] and [109]. In our study, d is known representing fixed depth problem while p_0 and Q vary. Then, Newton method solves the non-linear system of equations

$$\mathbf{f}(\mathbf{h}) = \mathbf{0}. \tag{2.33}$$

Refinement are performed near the surface, bottom and crest line ($q = 0$).

Numerical continuation method

Ko and Strauss [88] suggested a systematic method based on local bifurcation and numerical continuation. The solutions comprise a set of waves with varying water depth d. The solution started with the laminar flow solution and linearised wave solution. The head Q is obtained from the laminar solution. The local bifurcation is the first solution with linearised wave solution. The dispersion relation for discontinuous vorticity distribution for rotational flow has been provided by Henry [107, 222] and [223]. Regarding general vorticity, the dispersion relation is obtained with given relative mass flux [224, 225, 226]. The solution from the small-amplitude wave is used to initialize the iteration that searches for a set of waves with moderate and large amplitudes waves. Finally, the iteration is interrupted with a stagnation point representing the global bifurcation.

Following solving for Q is from the laminar flow, the numerical continuation involves following the predictor-corrector method by Amann and Kalimeris [109]. The solutions

for fixed depth, $d = const$, are

$$\mathbf{h} = [h_{0,0}, h_{1,0}, ..., h_{I,0}, h_{0,1}, ..., h_{I,J}, p_0, Q]^T. \tag{2.34}$$

An additional equation is provided to bound the solution with

$$g(\mathbf{h}) = 0, \tag{2.35}$$

for example,

$$g(\mathbf{h}) = \theta^{(n+1)} - (\theta^{(n)} + \Delta\theta) = 0, \tag{2.36}$$

where θ is a component of $\mathbf{h}$ and $\Delta\theta$ is a given continuation step. If Q is considered as the continuation parameter, that means $\theta = Q$. The superscript $^{(n)}$ denotes the obtained nth solution in the set of solution, while the super script $^{(n+1)}$ indicates the next solution. The above algorithm is implemented and solved using the open-source library Eigen [227].

Solving procedure

The solution of the non-linear system is sought with the following steps.

- Finding p_0 from the dispersion relation.

- Obtaining the solution for laminar flow $H(\lambda, p)$, and thus the linearised solution of the height function at each grid node $H(p, \lambda)+\varepsilon m(q, p)$ with ε a small value. Corresponding Q is computed.

- Using the linearised solution with p_0 and Q to initiate the Newton method. The solution scheme seeks the linearised small-amplitude wave solution for the non-linear equation of motion.

- Performing numerical continuation from linearised solution to a stagnation point where the global bifurcation occurs.

Laminar flow solution

Laminar flow solutions are not dependent on q, $H(p)$. The governing equation takes the form

$$\frac{H_{pp}}{(H_p + 1)^3} = -\frac{d^2\gamma(p)}{p_0} \text{ in } -1 < p < 0, \tag{2.37a}$$

$$[H_p(0) + 1]^2 = \frac{p_0^2}{d^2}\frac{1}{Q - 2gd[H(0) + 1]} \text{ on } p = 0, \tag{2.37b}$$

$$H = 0 \text{ on } p = -1, \tag{2.37c}$$

The bifurcation is defined as (see Constantin [87])

$$\lambda = [c - u(0,0)]^2 = \left.\frac{1}{(1+H_p^2)}\right|_{p=0}. \tag{2.38}$$

We define

$$\Gamma(p) = 2\int_0^p \frac{d^2\gamma(s)}{p_0} ds, -1 \leq p \leq 0, \tag{2.39}$$

with

$$\Gamma_{min} = min_{p\in[-1,0]}\Gamma(p) \leq 0. \tag{2.40}$$

For $\lambda > -\Gamma_{min}$, the following solution is obtained

$$\begin{aligned} H(p) &= \int_0^p \frac{ds}{\sqrt{\lambda+\Gamma(s)}} + \frac{1}{2gd}\left(Q - \frac{p_0^2}{d^2}\lambda\right) - (p+1) \\ &= \int_{-1}^p \frac{ds}{\sqrt{\lambda+\Gamma(s)}} - (p+1), -1 < p < 0. \end{aligned} \tag{2.41}$$

At the bottom boundary,

$$Q(\lambda) = 2gd\int_{-1}^0 \frac{ds}{\sqrt{\lambda+\Gamma(s)}} + \frac{p_0^2}{d^2}\lambda > 0. \tag{2.42}$$

Linearised solutions

Euler equations give the linearised solutions of the form $h(q,p) = H(p,\lambda) + \varepsilon m(q,p)$, which are then pursued, where m is a periodic even function in q and ε is a small parameter. Substituting the expression of the linearised solution, one gets

$$\frac{1}{d^2}m_{pp} + (H_p+1)^2 m_{qq} + \frac{\gamma(p)}{p_0}3(H_p+1)^2 m_p = 0 \text{ in } -1 < q < 0, \tag{2.43a}$$

$$2\frac{H_p+1}{p_0^2}m_p[2gd(H+1) - Q] + \frac{(H_p+1)^2}{p_0^2}2gdm = 0 \text{ on } p = 0, \tag{2.43b}$$

$$m = 0 \text{ on } p = -1. \tag{2.43c}$$

Define

$$a(p,\lambda) = \frac{1}{(H_p+1)} = \sqrt{\lambda+\Gamma(p)}, \text{ for } \lambda > \Gamma_{min}, \tag{2.44}$$

with $a_p = d^2\gamma(p)/(p_0 a)$. The above equations are then rewritten as

$$(a^3 m_p)_p + d^2 a m_{qq} = 0 \text{ in } -1 < p < 0, \tag{2.45a}$$

$$a^3 m_p = \frac{g d^3}{p_0^2} m \text{ on } p = 0, \tag{2.45b}$$

$$m = 0 \text{ on } p = -1. \tag{2.45c}$$

Assume that the even m-function admits Fourier expansion

$$m(q,p) = \sum_{j=0}^{\infty} M_j(p) cos(jq), \tag{2.46}$$

where,

$$M_0(q,p) = \frac{1}{2L}\int_{-L}^{L} m(q,p)dq, \tag{2.47a}$$

$$M_j(q,p) = \frac{1}{L}\int_{-L}^{L} m(q,p)cos(jq)dq, j \geq 1. \tag{2.47b}$$

The following Sturm-Liouville problems is applied for each j as

$$(a^3 M_p)_p = j^2 d^2 a M \text{ in } -1 < p < 0, \tag{2.48a}$$

$$a^3 M_p = \frac{g d^3}{p_0^2} M \text{ on } p = 0, \tag{2.48b}$$

$$M = 0 \text{ on } p = -1. \tag{2.48c}$$

The approximation of h up to the first order of ε is sufficient [109], i.e., terms up to $j = 1$ are retained.

2.2.3 Dispersion relations

The dispersion relation is required to compute the critical value of λ, denoted by λ^*. This value relates to the bifurcation point from the laminar solution to a small-amplitude wave solution. The parameter λ^* gives the corresponding critical speed of the laminar flow at the surface

$$u^* - w = \frac{p_0\sqrt{\lambda^*}}{d}. \tag{2.49}$$

For different vorticity distribution for fixed-depth simulations, corresponding dispersions relations can be derived. For irrotational flow, $a(p,\lambda) = \sqrt{\lambda}$, and the solution of the laminar flow is given by [2]

$$H(p) = \frac{p+1}{\sqrt{\lambda}} - (p+1). \tag{2.50}$$

Moreover, the solution of Sturm-Liouville for $j = 1$ is obtained as $m(q, p) = M(p)cos(q)$ with

$$M(p) = c_1 sinh\left(\frac{dp + d}{\sqrt{\lambda}}\right), \tag{2.51}$$

where $c_1 \neq 0$ is a coefficient. At $p = 0$, Eq.2.48(a) leads to the dispersion relation for irrotational flow as

$$tanh\left(\frac{d}{\sqrt{\lambda}}\right) - \frac{p_0^2}{gd^2}\lambda = 0. \tag{2.52}$$

Substituting Eq.2.49 to Eq.2.9, we get $\lambda^* = 1$. Hence, the standard dispersion relation from Eq.2.52 becomes

$$p_0 = -d\sqrt{gtanh(d)}, \tag{2.53}$$

giving p_0 for a particular d.

2.2.4 Wave kinematics

Applying finite difference scheme [89, 109, 125] following Sec.2.2.2, the value of h at each node can be obtained and is used to seek the wave kinematics in the fluid domain. We compute z using h values as follows

$$z = d[h(q, p) + p]. \tag{2.54}$$

The wave height is calculated from the height function value at the crest and the trough, as expressed by

$$H = d[h(0, 0) - h(L, 0)]. \tag{2.55}$$

The velocity field are

$$c - u = -\frac{p_0}{d(h_p + 1)}, \qquad w = \frac{p_0 h_q}{h_p + 1}. \tag{2.56}$$

One gets the total pressure as

$$P = P_{atm} + \tilde{\Gamma}(p) - gd(h + 1) - gdp - \frac{p_0^2(1/d^2 + h_q^2)}{2(h_p + 1)^2} + \frac{Q}{2}. \tag{2.57}$$

The wave speed is recovered from the average horizontal current strength, k, and the fluid velocity is given by

$$c = k - \frac{1}{L}\int_0^L [u(x, -d) - c]dx. \tag{2.58}$$

The hydrodynamic pressure is given by

$$P_{dynamic} = P_{atm} + \tilde{\Gamma}(p) - gd - \frac{p_0^2(1/d^2 + h_q^2)}{2(h_p + 1)^2}, \tag{2.59}$$

The numerical pressure is scaled up with water density ρ_w (1025 kg/m^3).

Within a wave length, the velocity profiles distribute and vary from the wave crest to the wave trough, and also depend on the depth of the fluid particles [87, 121, 124]. The horizontal velocity u follows the inequalities in

$$\begin{cases} u_z(0,z) > 0 \text{ for } z \in (-d, \eta(0)), \\ u_x(x,-d) < 0 \text{ for } x \in (0,\pi), \\ u_z(\pi,z) < 0 \text{ for } z \in (-d, \eta(\pi)). \end{cases} \tag{2.60}$$

The vertical velocity is equal to zero along three sides of the flow domain from the wave crest to the wave trough. It is given by [2, 121]

$$\begin{cases} v_z(0,z) = 0 \text{ for } z \in (-d, \eta(0)), \\ v_x(x,-d) = 0 \text{ for } x \in (0,\pi), \\ v_z(\pi,z) = 0 \text{ for } z \in (-d, \eta(\pi)). \end{cases} \tag{2.61}$$

Constantin [228] proved that the minimum pressure equalling zero along the free surface, and the maximum occurs at the bottom bed directly under the wave crest.

It is worth noting that the acceleration of the fluid has not been studied while engineering applications require these parameters for calculating the hydrodynamic forces acting on the submerged structures. Hence, this thesis derives the acceleration formulation from the provided height function results and the pressure profiles. Thus, the derivation of the acceleration fulfils the requirement to calculate the forces and makes the large-amplitude wave theory available for offshore engineering applications.

2.2.5 Fluid accelerations under large amplitude waves

The non-linear hydrodynamic force calculation requires fluid acceleration profiles to be computed. Nevertheless, no existing study investigates the acceleration distribution within the fluid domain under large amplitude waves. Therefore, we derive the acceleration formulation and prove the consistency of the formulations derived from the Euler equation (using the pressure equation) and $h-$values (by directly differentiating the fluid velocity). The complete fluid dynamics is achieved to investigate the responses of the floating structures.

Since the wave is steady, the $t-$dependent terms in Euler equation are non-existent.

On one hand, the flow acceleration's formulations are derived from the Euler equations, with relations from velocity components (Eq.2.62) and the pressure (Eq.2.63), as follow

$$\partial_x = \frac{\psi_x}{p_0}\partial_p + \partial_q, \qquad \partial_z = \frac{\psi_z}{p_0}\partial_p, \tag{2.62}$$

$$\psi_z = u - c, \qquad \psi_x = -w, \tag{2.63}$$

$$\partial_x = \frac{-w}{p_0}\partial_p + \partial_q, \qquad \partial_z = \frac{(u-c)}{p_0}\partial_p \tag{2.64}$$

$$a_x = -P_x = \frac{w}{p_0}P_p - P_q, \qquad a_z = -P_z - g = -\frac{(u-c)}{p_0}P_p - g \tag{2.65}$$

On the other hand, the acceleration components can also be obtained using the $h-$values and differentiation as follow

$$\begin{aligned}
a_x &= (u-c)u_x + wu_z \\
&= (u-c)\frac{\partial}{\partial_x}(u-c) + w\frac{\partial}{\partial_z}(u-c) \\
&= (u-c)\left(\frac{-w}{p_0}\partial_p + \partial_q\right)(u-c) + w\left(\frac{(u-c)}{p_0}\partial_p\right)(u-c) \\
&= (u-c)\frac{\partial}{\partial_q}(u-c) \\
&= \frac{p_0}{d(h_p+1)}\frac{\partial}{\partial_q}\frac{p_0}{d(h_p+1)} \\
&= \frac{p_0}{d(h_p+1)}\left(\frac{p_0}{d}\frac{-h_{pq}}{h_p+1)^2}\right) \\
&= \frac{p_0^2}{d^2}\left(\frac{-h_{pq}}{(h_p+1)^3}\right),
\end{aligned} \tag{2.66}$$

and

$$\begin{aligned}
a_z &= (u-c)w_x + ww_y \\
&= (u-c)\frac{\partial}{\partial_x}w + w\frac{\partial}{\partial_z}w \\
&= (u-c)\left(\frac{-w}{p_0}\partial_p + \partial_q\right)w + w\left(\frac{(u-c)}{p_0}\partial_p\right)w \\
&= (u-c)\frac{\partial}{\partial_q}w \\
&= \frac{p_0}{d(h_p+1)}\frac{\partial}{\partial_q}\frac{p_0 h_q}{(h_p+1)} \\
&= \frac{p_0}{d(h_p+1)}\left(p_0\frac{h_{qq}(h_p+1) - h_q h_{pq}}{(h_p+1^2)}\right) \\
&= \frac{p_0^2}{d}\left(\frac{h_{qq}(h_p+1) - h_q h_{pq}}{(h_p+1^3)}\right).
\end{aligned} \tag{2.67}$$

Recalling the pressure equation

$$P = P_{atm} + \tilde{\Gamma}(p) - gd(h+1) - gdp - \frac{p_0^2\left(1/d^2 + h_q^2\right)}{2(h_p+1)^2} + Q/2, \tag{2.68}$$

we have

$$\begin{aligned} P_p &= -gdh_p - gd - \frac{p_0^2}{2}\left(\frac{2h_q h_{qp}(h_p+1)^2 - (1/d^2+h_q^2)2h_{pp}(h_p+1))}{(h_p+1)^4}\right) \\ &= -gd(h_p+1) - p_0^2\frac{h_q h_{qp}(h_p+1) - (1/d^2+h_q^2)h_{pp}}{(h_p+1)^3}, \end{aligned} \tag{2.69}$$

$$\begin{aligned} P_q &= -gdh_q - \frac{p_0^2}{2}\left(\frac{2h_q h_{qq}(h_p+1)^2 - (1/d^2+h_q^2)2h_{pq}(h_p+1))}{(h_p+1)^4}\right) \\ &= -gdh_q - p_0^2\frac{h_q h_{qq}(h_p+1) - (1/d^2+h_q^2)h_{pq}}{(h_p+1)^3}, \end{aligned} \tag{2.70}$$

and

$$\begin{aligned} a_x &= \frac{w}{p_0}P_p - P_q \\ &= \frac{h_q}{h_p+1}\left(-gd(h_p+1) - p_0^2\frac{h_q h_{qp}(h_p+1) - h_{pp}(1/d^2+h_q^2)}{(h_p+1)^3}\right) \\ &+ \left(gdh_q + p_0^2\frac{h_q h_{qq}(h_p+1) - h_{qp}(1/d^2+h_q^2)}{(h_p+1)^3}\right) \\ &= p_0^2\left(\frac{-h_q^2 h_{qp}(h_p+1) + h_q h_{pp}(1/d^2+h_q^2)}{(h_p+1)^4} + \frac{h_q h_{qq}(h_p+1) - h_{qp}(1/d^2+h_q^2)}{(h_p+1)^3}\right) \\ &= \frac{p_0^2}{(h_p+1)^4}\left(-h_q^2 h_{qp}(h_p+1) + h_q h_{pp}(1/d^2+h_q^2) + h_q h_{qq}(h_p+1)^2 - h_{qp}(1/d^2+h_q^2)(h_p+1)\right). \end{aligned} \tag{2.71}$$

From the first equation of Eq.2.13, we get the relation

$$h_{pp}(1/d^2+h_q^2) = 2h_q h_{qp}(h_p+1) - h_{qq}(h_p+1)^2, \tag{2.72}$$

hence,

$$\begin{aligned} a_x &= \frac{p_0^2}{(h_p+1)^4}\left(-h_q^2 h_{qp}(h_p+1) + h_q h_{qq}(h_p+1)^2 - h_{qp}(1/d^2+h_q^2)(h_p+1)\right. \\ &\quad \left.+2h_q^2 h_{qp}(h_p+1) - h_q h_{qq}(h_p+1)^2\right) \\ &= \frac{p_0^2(h_p+1)}{(h_p+1)^4}\left(h_q^2 h_{qp} - h_{qp}(1/d^2+h_q^2)\right) \\ &= \frac{-p_0^2}{d^2}\frac{h_{qp}}{(h_p+1)^3} \end{aligned} \tag{2.73}$$

Similarly, a_z are proved with

$$\begin{aligned} a_z &= \frac{c-u}{p_0}P_p - g \\ &= -\frac{p_0}{d(h_p+1)}\frac{1}{p_0}\left(-gd(h_p+1) - p_0^2\frac{h_q h_{qp}(h_p+1) - h_{pp}(1/d^2+h_q^2)}{(h_p+1)^3}\right) - g \\ &= g + \frac{p_0^2}{d(h_p+1)}\left(\frac{h_q h_{qp}(h_p+1) - (1/d^2+h_q^2)h_{pp}}{(h_p+1)^3}\right) - g \\ &= \frac{p_0^2}{d(h_p+1)}\left(\frac{h_q h_{qp}(h_p+1) + (-2h_q h_{qp}(h_p+1) + h_{qq}(h_p+1)^2)}{(h_p+1)^3}\right) \\ &= \frac{p_0^2}{d(h_p+1)}\left(\frac{h_{qq}(h_p+1)^2 - h_q h_{qp}(h_p+1)}{(h_p+1)^3}\right) \\ &= \frac{p_0^2}{d}\left(\frac{h_{qq}(h_p+1) - h_q h_{qp}}{(h_p+1)^3}\right) \end{aligned} \tag{2.74}$$

The two acceleration formulations are equivalent.

There is no existing studies investigating the fluid acceleration under large-amplitude surface waves. This thesis introduces a derivation of the acceleration of large-amplitude waves. The results are then compared with the ones from the linear waves in the following sections providing understanding of the acceleration field and its distribution and variation along the water depth.

The formulations provided in this thesis provides the complete dynamics for waves. Based on the results provided in this section, the wave kinematics and the acceleration profiles can be substituted into Morison equation to determine the hydrodynamic effects.

2.2.6 Interpolation scheme

Engineering applications of large-amplitude waves require the flow properties at each time step. With linear wave theory, one can compute the fluid kinematics at a particu-

lar position by substituting the instantaneous coordinates into the wave formula. If the large-amplitude waves are applied, the method of calculating flow kinematics is different from the well-known linear approach. Finite difference schemes provide solutions; therefore, the fluid properties are attached at computational nodes within the scaled computational domain. Those properties then must be rescaled to the physical coordinates using the wave-number κ, and the water density ρ_w. The instantaneous position of the structure used to calculate the hydrodynamic loads is updated every time step; the calculated flow properties depend on the segments' coordinates and neighbouring nodes' coordinates. Hence, the instantaneous velocity and acceleration of the spar elements are determined using the interpolation scheme, which is similar to Umeyama's method [71]. The flow properties at a specific position will be interpolated from the nearby four grid nodes, as shown in Fig.2.3.

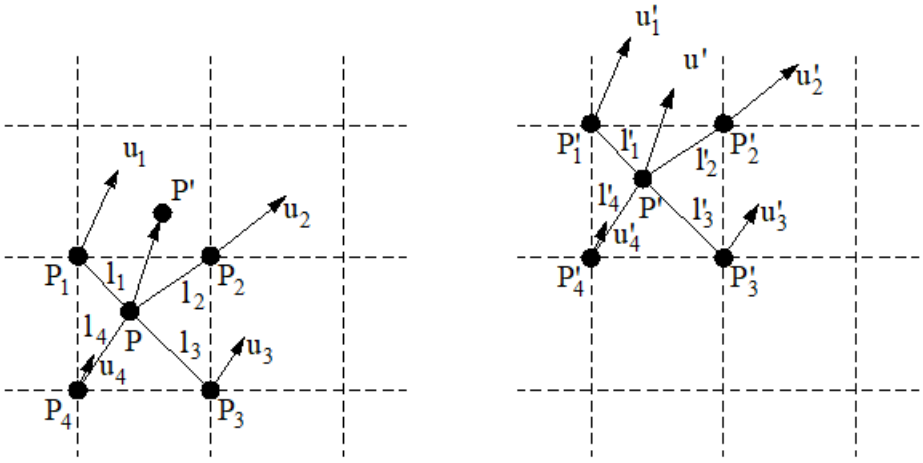

Figure 2.3: Interpolation algorithm.

The wave kinematics are provided at spatially discrete nodal points in an Eulerian scheme; the velocity, for example, is estimated as follows. The other properties are estimated following the same technique. Fig.2.3 describes the motion of a point across a general mesh of quadrilateral cells. The velocity u at point P at time step t is estimated by interpolating the neighbouring velocity values (u_1 at P_1, u_2 at P_2, u_3 at P_3, and u_4 at P_4). Then, at $t + \Delta t$, the point P moves to P' with the velocity u'. The velocities at two steps are

$$u = \frac{(u_1/l_1) + (u_2/l_2) + (u_3/l_3) + (u_4/l_4)}{(1/l_1) + (1/l_2) + (1/l_3) + (1/l_4)} \text{ at } t = t, \tag{2.75}$$

and

$$u' = \frac{(u'_1/l'_1) + (u'_2/l'_2) + (u'_3/l'_3) + (u'_4/l'_4)}{(1/l'_1) + (1/l'_2) + (1/l'_3) + (1/l'_4)} \text{ at } t = t + \Delta t. \tag{2.76}$$

2.3 Comparison between the large-amplitude waves and the linear waves

The sea states in the OC3 report [10] are chosen the reference values as the wave amplitude and wave period varies in a wide range from small, moderate to extreme conditions. An ocean engineer can select the linear waves parameters following limitation on wave steepness [229]. However, the surface profile can not reflect the actual free surface for non-linear waves as the linear wave theory is in use.

To simulate the real free surface, the linear wave theory can then be extended to model the non-linear wave surface, i.e. the second to ninth order non-linear Stoke's wave [70, 230, 231]. Stokes' waves are very convenient for computation of the wave kinematics with prescribed formulations. Second order and third order Stokes' waves are used widely in the FOWT dynamic research. However, the real free surface requires higher order Stokes' waves. In contrast, the large-amplitude wave theory generates a set of waves, and each wave has its wave amplitude, free surface profile, and corresponding wave kinematics. The large amplitude wave theory generates the wave with a strong relationship between the wave period and the wave height. A slight change in the wave period results in a significantly different wave height. The wave kinematics hence possess more extreme profiles than the linear waves.

In the following sections, wave kinematics are investigated in three cases. In the first case, the large amplitude waves have the same period as the linear waves but different wave amplitude. The second case considers a slight variation of the wave period on the bifurcation diagram, and by that, the free surface of the non-linear wave with a small variation from the linear wave period possesses a dramatic variation compared to the linear waves. Finally, the third comparison is between the linear waves of the recommended sea-state [10] with non-linear waves of intermediate points along the bifurcation curve. In these cases, the wave kinematics is monitored along with the water depth, and the free surface is compared with the linear wave solutions.

2.3.1 Large-amplitude waves solutions compared with linear waves of same wave period

Table 2.1: Regular wave properties.

Case	Wave height (m)	Wave period (s)	Wave length (m)	Water depth (m)	Wave speed (m/s)
1	1.40	6.5025	70.01	320	10.76
2	3.66	9.7014	153.48	320	15.82
3	15.24	17.0046	472.03	320	27.76

In this section, the large-amplitude waves have similar wave period to the linear waves, shown in Table 2.1. Fig.2.4 shows the bifurcation diagram for three different waves. To obtain the large-amplitude waves with the similar wave period to the linear wave, the initial solutions of the numerical procedure have to be chosen as the laminar flow (i.e., $T = 6.7$ s, 9.92 s, and 17.4 s for the three cases) and then progress sequentially. Next, we choose waves with corresponding wave heights at $T \approx 6.5$ s, 9.7 s, and 17.0 s which are $H = 5.32$ m, 10.17 m, and 32.0 m, respectively. Compared to the linear wave height, $H = 1.4$ m, 3.66 m, and 15.24 m, the large-amplitude waves possess a significantly different wave heights, seen in Fig.2.4(b,d,f). The large-amplitude waves obviously have non-linear free surface profiles with shaper crests and flatter troughs than linear waves in Fig.2.4(b,d,f). It is also worth noting that the amplitude of large-amplitude waves show dependences on the initial wave period as seen from the bifurcation diagram. If we choose different initial wave periods, that are even close to the linear wave periods, we might get dissimilar wave heights.

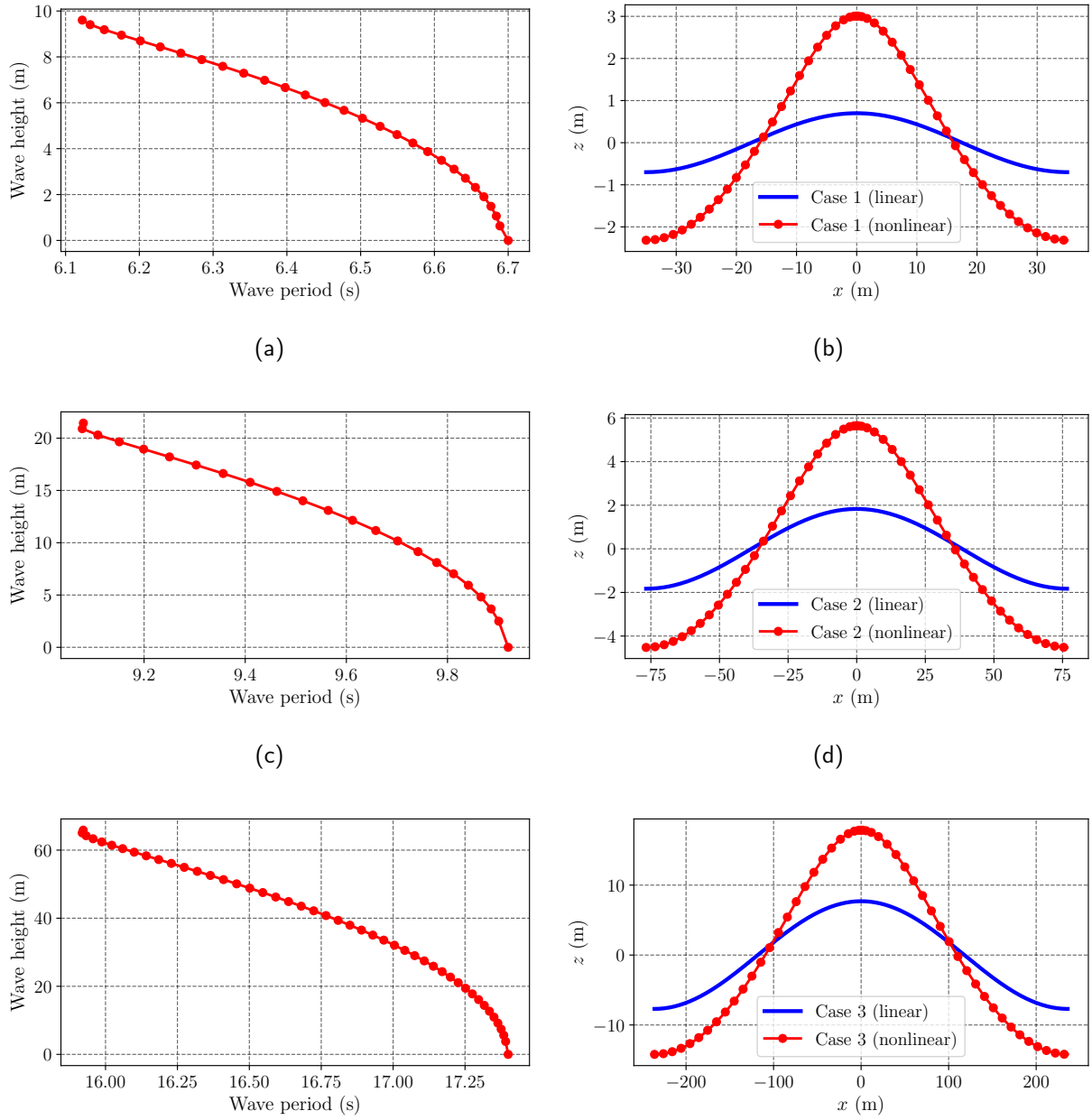

Figure 2.4: Variation of the wave height versus the wave period.

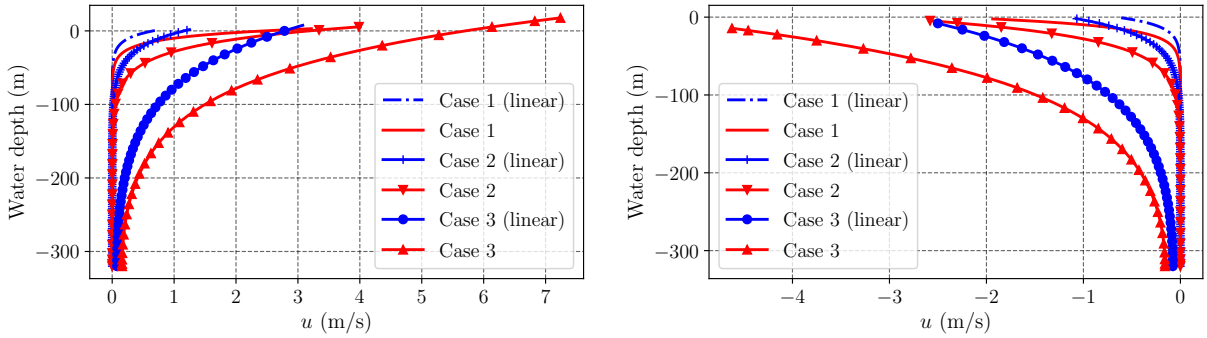

Figure 2.5: Comparison of the horizontal velocities: (left) under the crest; (right) under the trough.

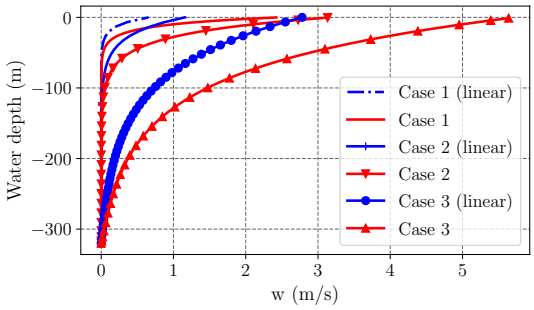

Figure 2.6: Comparison of the vertical velocity profiles.

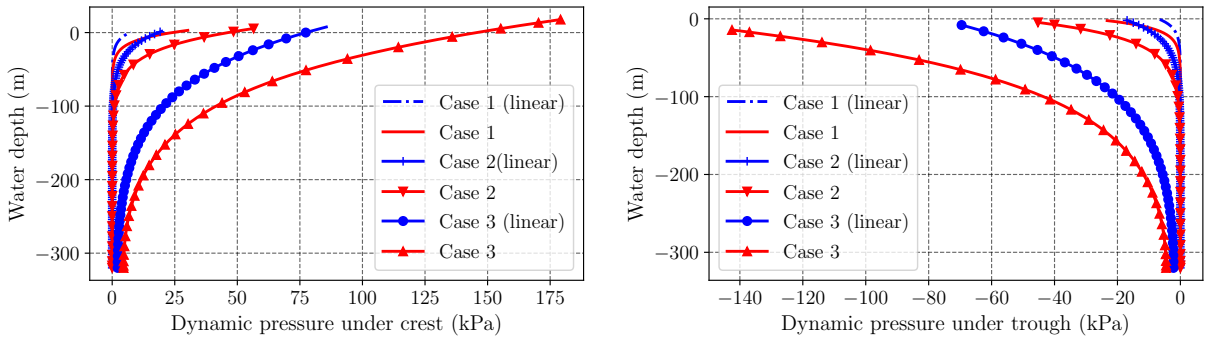

Figure 2.7: Comparison of the dynamic pressure: (left) under the crest; (right) under the trough.

Fig.2.5 to Fig.2.7 illustrate the distribution of wave velocity and pressure profiles along the water depth obtained from the two wave theories. In all cases, the non-linear waves have sharper profiles than the linear waves, particularly near free surface. Also, velocities are different as computed from the two theories, particularly near the surface.

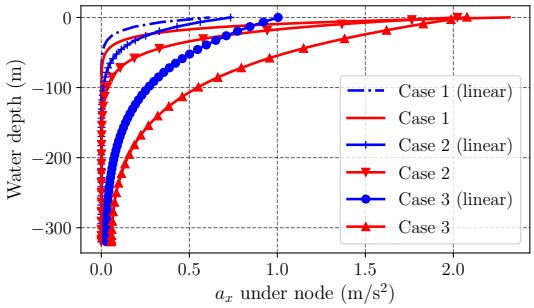

Figure 2.8: Comparison of the horizontal acceleration profiles.

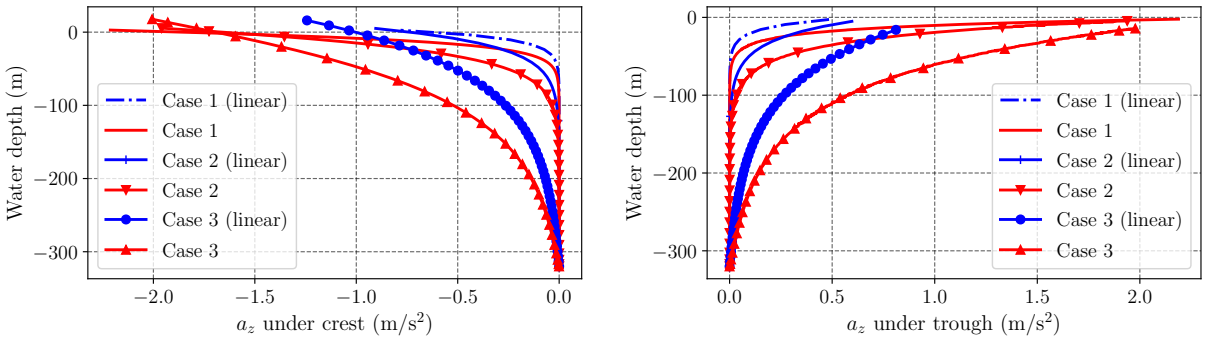

Figure 2.9: Comparison of the vertical acceleration for: (left) under the crest; (right) under the trough.

Fig.2.8 and Fig.2.9 reveal that the acceleration for the non-linear waves have remarkably larger values than that of the linear waves. The horizontal acceleration profiles are monitored under the node where the free surface profile intersects the horizontal mean water level line [37]. At the free surface, the non-linear waves accelerations are almost double the linear waves accelerations. Findings in this section show that (for a same wave period) the large-amplitude wave theory can generate a wave with significantly different wave kinematics compared to the linear wave theory. The flow forces can be calculated accordingly with the provided accelerations to estimate the dynamic responses of a FOWT.

2.3.2 Large-amplitude wave solutions compared with solutions from linear wave with slightly different wave period

In this section, the results from the two wave theories, with a slight difference in the wave period are compared. The wave parameters are presented in Table.2.2. Fig.2.10 and Fig.2.11 indicate the free surface profiles and the sensitiveness of the large-amplitude

waves amplitudes to the wave period. As shown in Fig.2.11(a,c), a very small change in the wave period leads to a considerable difference in wave height, i.e. 0.1 s corresponds to about 5 m change in the wave height.

Table 2.2: Regular linear wave and large-amplitude wave properties.

Case	Wave	Wave height (m)	Wave period (s)	Wave number (κ)	Wave speed (m/s)
1	Linear	9.14	13.60	0.0125	21.22
2	Non-linear	14.23	13.50	0.0125	21.58
3	Linear	15.2	16.97	0.0138	26.37
4	Non-linear	20.85	16.88	0.0138	26.89

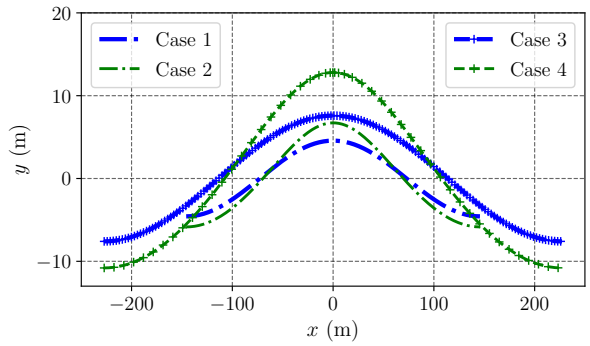

Figure 2.10: Free surface profiles of considered cases.

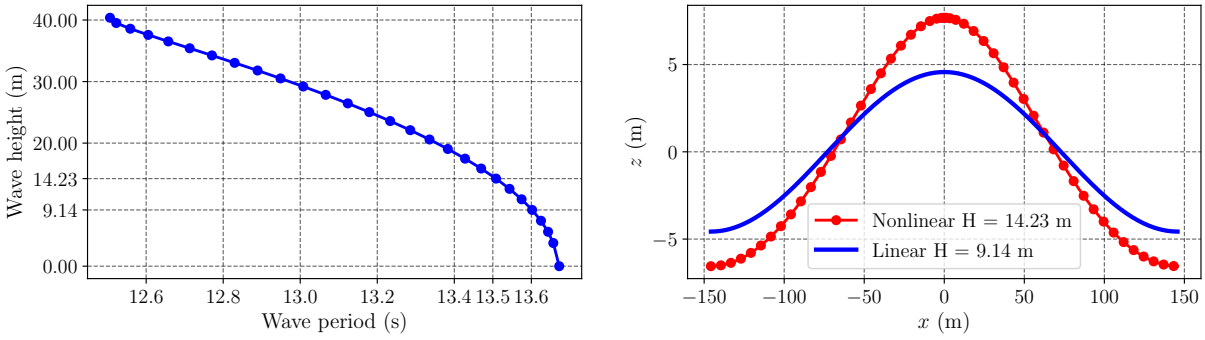

(a) (b)

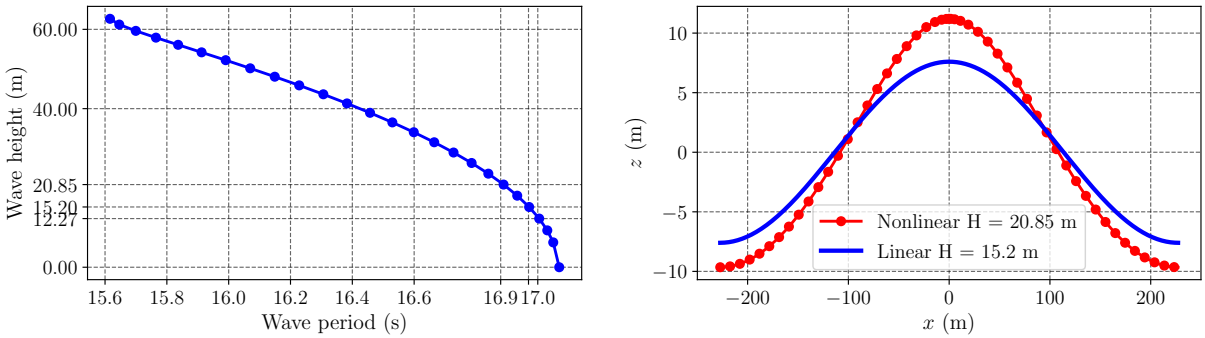

(c) (d)

Figure 2.11: (a)&(c) Bifurcation diagram; (b)&(d) Wave surface profiles.

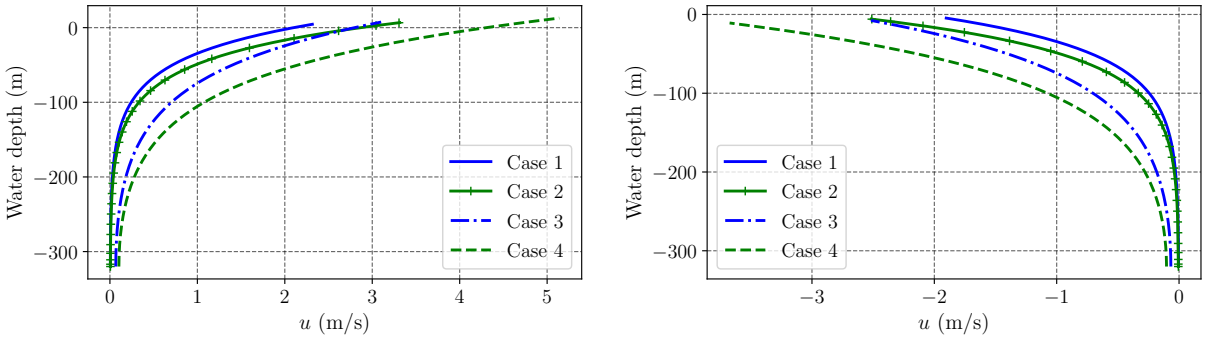

(a) (b)

Figure 2.12: Comparison of the horizontal velocity profiles.

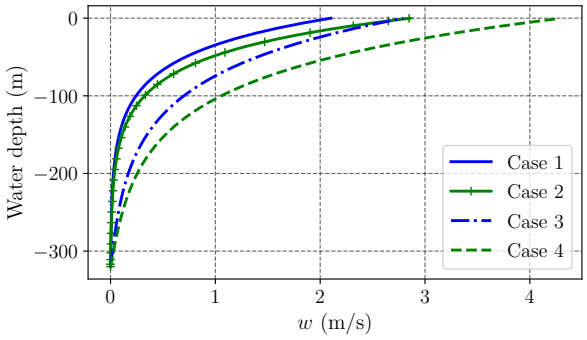

Figure 2.13: Comparison of the vertical velocity profile.

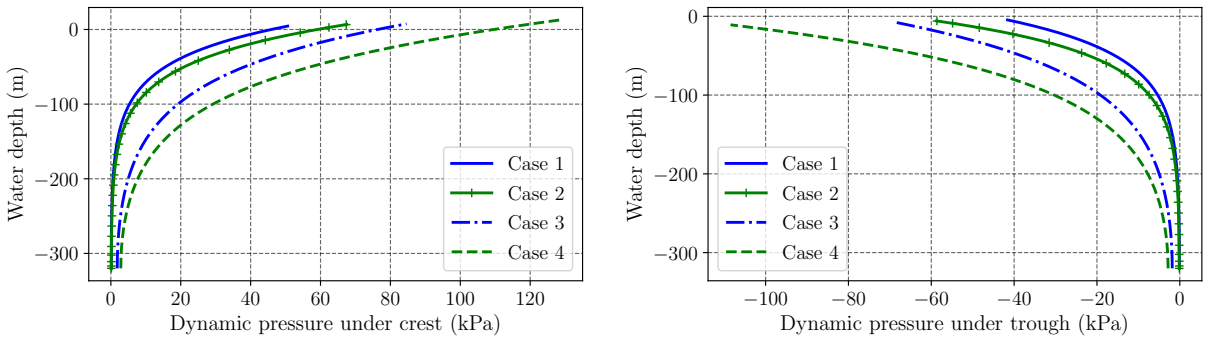

(a) (b)

Figure 2.14: Comparison of the hydrodynamic pressure profiles.

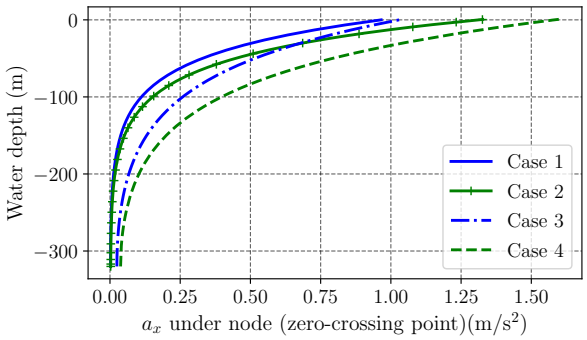

Figure 2.15: Comparison of the horizontal acceleration profiles.

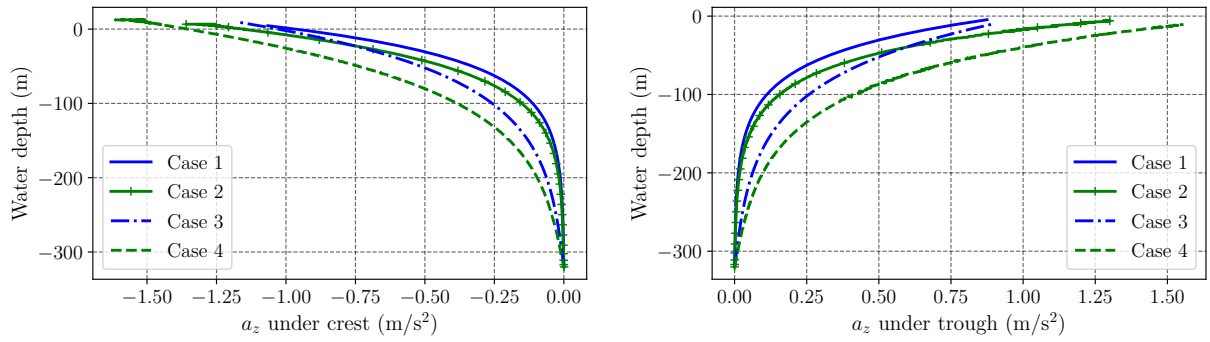

(a) (b)

Figure 2.16: Comparison of the vertical acceleration profile.

Acceleration profiles are compared in Fig.2.15 and Fig.2.16 to contrast the large-amplitude wave solutions with the linear waves results. The accelerations of the large-amplitude waves are considerably larger than that of the linear waves at the vicinity of the free surface. It is also worth noting that the discrepancy between two wave theories under the wave trough are more than that under the wave crest.

2.3.3 Large-amplitude wave solutions compared with linear waves with significantly different wave period

In this section, the sea states three, five, and eight in OC3 report [10] are chosen as the initial conditions of the numerical bifurcation curve and three sets of the large-amplitude waves are generated and are compared with the linear waves.

Table 2.3: Regular linear and non-linear wave properties.

Sea state	Linear wave height (m)	Wave period (s)	Large-amplitude wave height (m)	Wave period (s)	Wavenumber (κ)	Wave speed
3	1.40	6.5	5.50	6.27	0.095282	10.5081
5	3.66	9.7	9.25	9.51	0.042785	15.4382
8	15.24	17.0	43.6	16.24	0.01394284	27.766

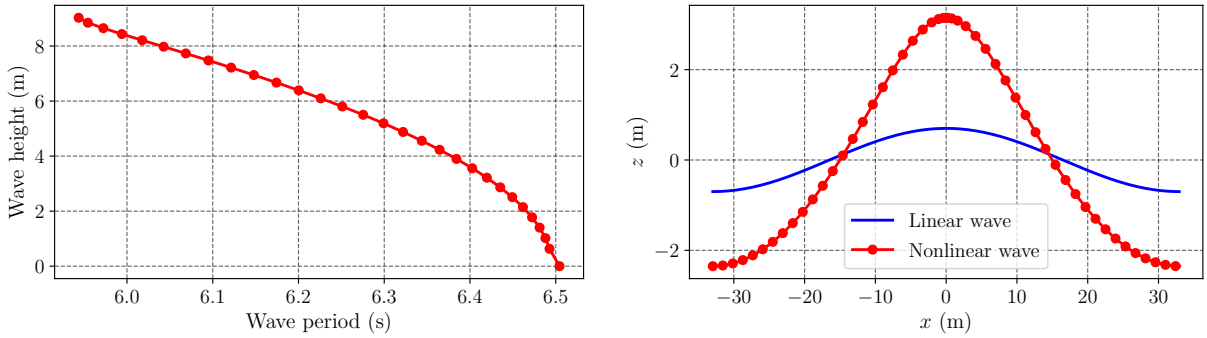

(a) (b)

Figure 2.17: Bifurcation diagram T = 6.5 s and wave amplitude.

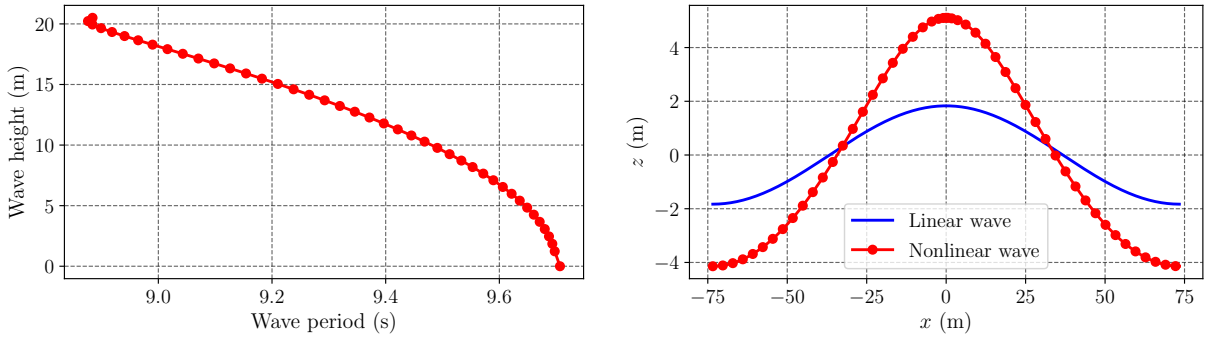

(a) (b)

Figure 2.18: Bifurcation diagram T = 9.7 s and wave amplitude.

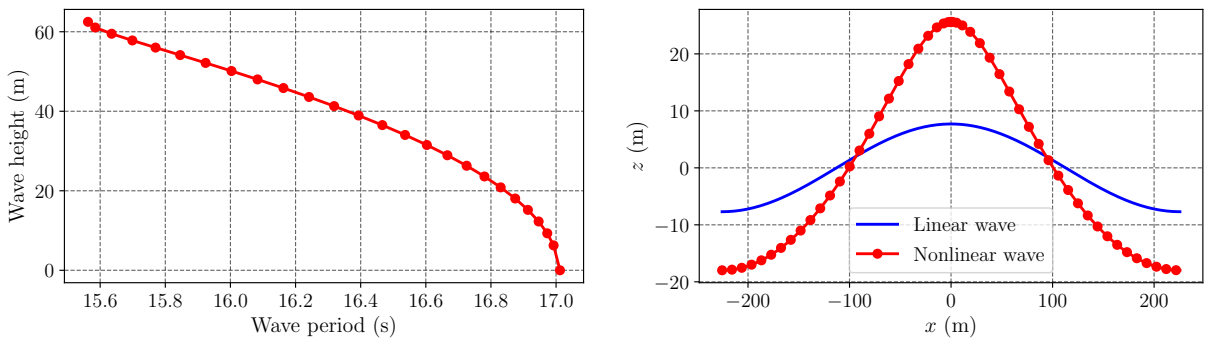

(a) (b)

Figure 2.19: Bifurcation diagram T = 17.0 s and wave amplitude.

The wave height-wave period diagram of three cases are described in Fig.2.17 through Fig.2.19. In these figures, the initial wave periods are T = 6.5 s, 9.7 s, and 17.0 s

which are equal to the linear waves periods. Subsequent solution (fifteenth with a step size of each bifurcation diagram) is chosen for the study in Fig.2.17(b), Fig.2.18(b), and Fig.2.19(b). The fifteenth solution of the large-amplitude wave are intermediate points along the bifurcation curves. The large-amplitude waves at these points possess a significantly higher wave amplitude than the initial linear waves. Figures also express that the wave heights are sensitive to wave periods. For instance, the wave height can approach 60 m as the wave period is 15.6 s, just 1.4 s from $T = 17.0$ s in Fig.2.19(a). In addition, the wave velocity and dynamic pressure are also larger than that from the linear waves, as seen in Fig.2.20 to Fig.2.22.

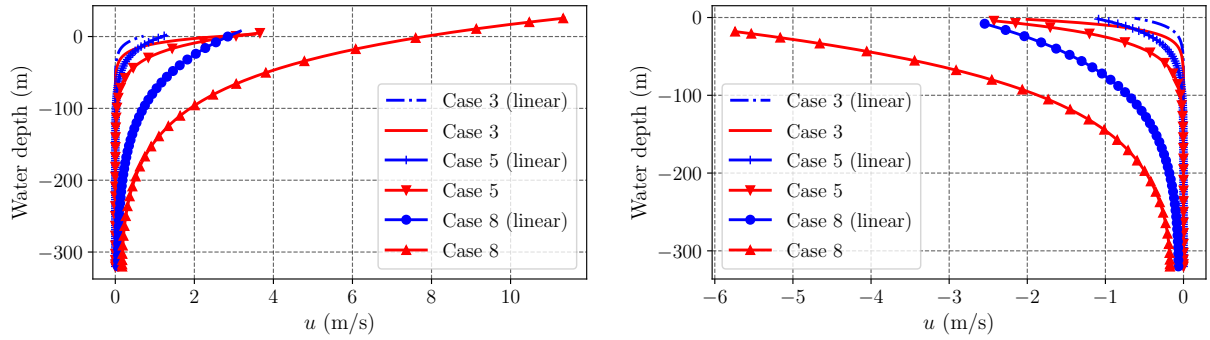

Figure 2.20: Comparison of the horizontal velocity for: (left) under the crest; (right) under the trough.

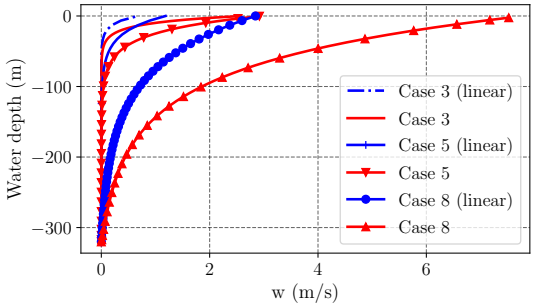

Figure 2.21: Comparison of the vertical velocity profiles.

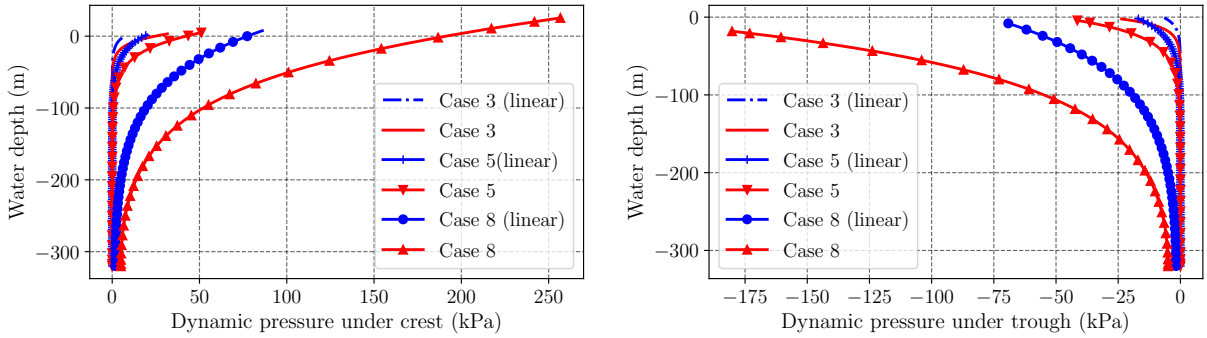

Figure 2.22: Comparison of the dynamic pressure for: (left) under the crest; (right) under the trough.

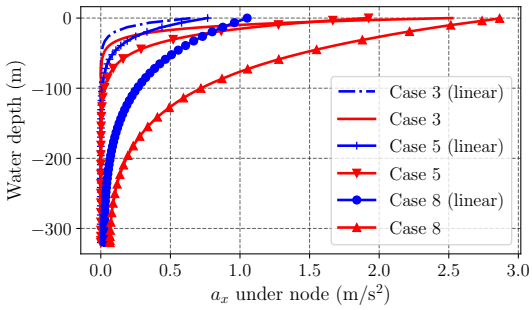

Figure 2.23: Comparison of the horizontal acceleration profiles.

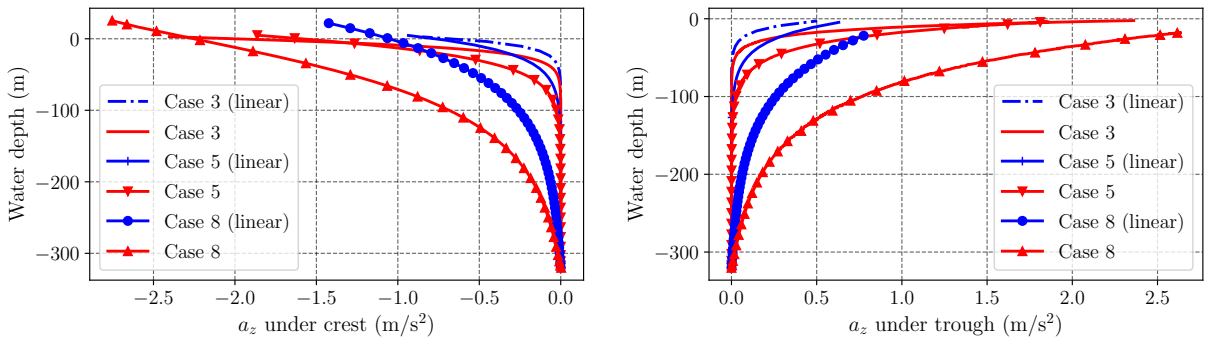

Figure 2.24: Comparison of the vertical acceleration for: (left) under the crest; (right) under the trough.

Fig.2.23 and Fig.2.24 summarise the wave accelerations for the considered cases. Both horizontal and vertical acceleration for the large-amplitude waves are considerably larger than that of the linear waves. In addition, the accelerations under the wave crest and the wave trough are not similar. This might be due to the naturally antisymmetry profile about the mean water level of the large-amplitude waves.

The large-amplitude wave results are compared with the linear waves kinematics in this section. The results from a large-amplitude wave is sensitive to the wave period; for instance, a slight change in the wave period results in a significant variation of the wave amplitude. In addition, the large-amplitude waves kinematics are substantially larger than that obtained from the linear waves profiles. We will apply the large amplitude waves in the following section to investigate the impact of the non-linear waves on the floating offshore wind turbines in the deep-water region.

2.4 Spar-type floating offshore wind turbine model

This thesis considers a numerical model of spar-type floating offshore wind turbine (SFOWT) for studying the large-amplitude waves effects. We only consider regular waves in this study. Detail model of the floating wind turbine is presented in this section. The theoretical model described in this section will be consequently used to determine the dynamic response of the wind turbine. The model considers the blades displacements and the coupled nacelle/tower motions. Since, in-plane or edge-wise motion have been developed very little or no damping at all, these will be primarily considered in the model.

In recent years, many wind turbine dynamics analysis codes have been developed, and they follow three main approaches: multi-body dynamics, finite element method, and the energy-based approach. The use of energy-based approach leads to reduced order model and is low in computational cost. This approach has the ability to accurately model the dynamics of the system with a few degrees of freedom. The approach however, requires considerable algebraic manipulation to derive the equation of motion. The calculation of the huge bending deflection of blades parked in high wind speeds is other shortcomings of the modal approach [232]. The use of the finite element method is likely to be more reliable for non-linear calculations.

The turbine rotor tilt angle is assumed zero for simplicity. The FOWT components are the tower, the nacelle, the blades, and the spar platform. The tower and the blades are flexible components. Model analysis is usually used to study the dynamics of the flexible structure. The tower side-to-side displacement is modelled. The blade first mode in edge-wise direction is used. The platform is assumed to be rigid with displacements in three axes. The degree-of-freedoms are the platform motions, tower top displacements, nacelle displacements, and the elastic deformation of the three blades.

- FOWT platform: The floating platform with mass M_p and inertia matrix $\mathbf{I}_p = diag(I_{px}, I_{py}, I_{pz})$. This platform has been proposed to support the NREL 5 MW baseline wind turbine [87].

- Nacelle and rotor: the nacelle with inertia matrix $\mathbf{I}_{nac} = diag(I_{nacx}, I_{nacy}, I_{nacz})$ and mass M_{nac}. The rotor is considered a rigid disc spinning around its axis with angular velocity $\Omega(t)$. The rotor mass is M_r and inertia matrix $\mathbf{I}_r = diag(I_{rx}, I_{ry}, I_{rz})$ with $I_{ry} = I_{rz}$.

- Tower: the flexible tower with mass m_t and the tower height h_t. The tower supports nacelle, rotor and blades.

- Blades: the three flexible blades with distributed mass μ_b and the blade length R.

A mooring system comprised of three catenary cables anchors the platform to the bottom bed. This thesis proposes a coupled numerical model simulating the dynamics of edgewise vibrations of S-FOWTs. The model considers the aerodynamic properties of the blade, variable mass and stiffness per unit length of the spar, the mooring stiffness and the mooring force, gravity, hydrostatic restoring moment, buoyancy; and the interactions among the blades, nacelle, tower, spar and mooring system. Details parameters of the SFOWT are listed in the following sections.

2.4.1 Numerical model of SFOWT

Due to its computational ease, Euler-Lagrangian energy based methods will be used in this thesis. This method requires modal information and theses are generally obtained for finite-element calculations. Hence, this method is accurate enough too. Also, the method has the advantage that any arbitrary number of modes could be considered to achieve a desired accuracy. The SFOWT structure and the moorings are shown in Fig.2.25. The global coordinate system (X, Y, Z) is at the free surface with $Z-$coordinate pointing upward.

The blade vibration is limited to the first main mode for the purpose of simplification since the edgewise vibrations of on-land wind turbines are shown to be lightly damped leading to violent vibrations. Staino showed that there is a very low or even negative damping in the first edgewise mode under certain circumstances [233]. Therefore, the edgewise vibrations are chosen in this study to highlight the impact of nonlinear waves.

Table.2.4 and Table.2.5 detail the general properties of the FOWT structure and the mooring system, respectively. The SFOWTs comprises of the spar floater, mooring system, wind turbine, and the tower similar to the OC3 S-FOWT [10]. The wind turbine is the 5-MW baseline wind turbine [7, 10]. The rotor radius is $R = 61.5m$. The cut-in and rated rotor speeds are 6.9 rpm and 12.1 rpm, respectively. The mean wind speed is 12 m/s, with the turbulence intensity assumed to be 15%. The mass of each blade is 17.74×10^3 kg. The mass of hub, nacelle, and tower are 56.78×10^3 kg, 240×10^3 kg, and 249.718×10^3 kg, respectively. The numerical simulation duration

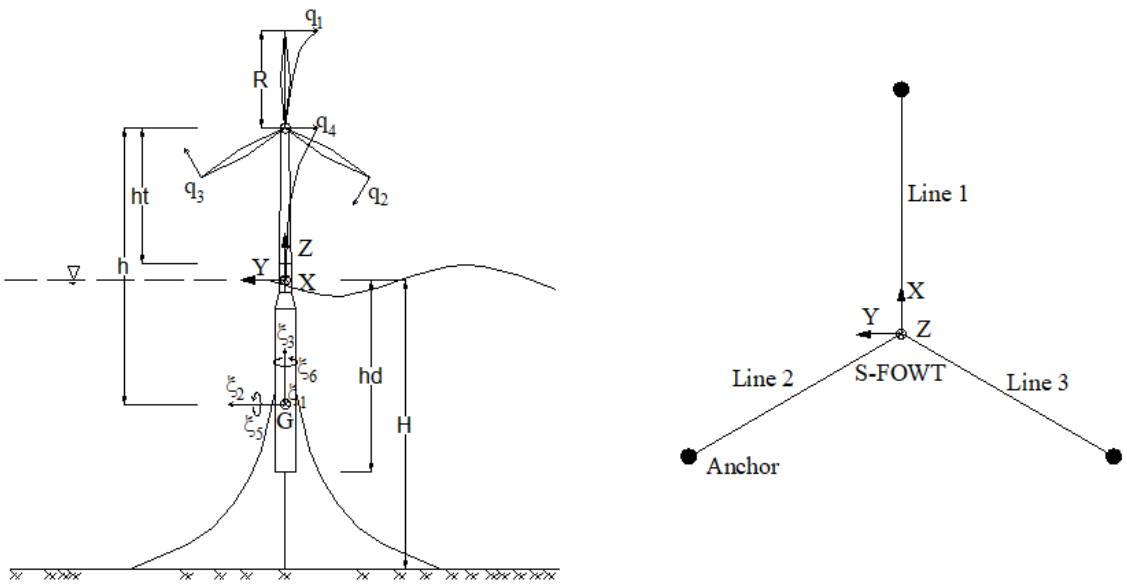

Figure 2.25: SFOWTs model and the mooring layout.

and the time step interval are chosen as 800 s and 0.02 s, respectively.

The in-plane elastic deformation of the blades and the in-plane deflection of the tower are in $yz-$plane. The nacelle and rotor are lumped as a mass on top of the tower. The axial deformation of the spar and the tower are neglected.

The generalized displacement of the three blades are $q_1(t)$, $q_2(t)$, and $q_3(t)$. The tower vibrates side-to-side with the generalized horizontal in-plane displacement at the top denoted by q_4. The vertical displacement of the tower is denoted by q_5. Both tower and blades are modelled using the Rayleigh-Ritz method. The vibration of the nacelle in the rotor plane, which is assumed to be the same as the in-plane vibration of the tower, is denoted by $q_4(t)$. The spar is a rigid body with 6 degree of freedom, i.e., surge, sway, heave, roll, pitch, and yaw are denoted by $(\xi_1(t), \xi_2(t), \xi_3(t), \xi_4(t), \xi_5(t), \xi_6(t))$ with a centre of gravity (G). The rotations of the spar are infinitesimal [9] and the tower axial deformation is neglected, so that $q_5 \approx \xi_3$. Therefore, the vertical nacelle displacement is also denoted by ξ_3. The generalized displacement vector of the system is expressed as

$$\mathbf{q}(t) = [q_1 \quad q_2 \quad q_3 \quad q_4 \quad \xi_1 \quad \xi_2 \quad \xi_3 \quad \xi_4 \quad \xi_5 \quad \xi_6]^T. \tag{2.77}$$

in which the superscript T is the the vector transpose operator. The Euler-Lagrange equation describing the motion of the SFOWT is given as

$$\frac{d}{dt}\left(\frac{\partial \mathcal{T}}{\partial \dot{\mathbf{q}}}\right) - \frac{\partial \mathcal{T}}{\partial \mathbf{q}} + \frac{\partial \mathcal{V}}{\partial \mathbf{q}} = \mathbf{f}(t), \tag{2.78}$$

in which $\mathbf{f}(t)$ is the external force vector that excites the floating offshore wind turbine. $\mathcal{T}$ and $\mathcal{V}$ are the total kinematic and potential energy of the SFOWT.

Table 2.4: NREL 5-MW wind turbine and OC3-Hywind sparbuoy properties.

Parameter	Symbol	Unit	Value
Nacelle mass and rotor mass	M_n	kg	350000
Tower mass	M_t	kg	249718
Spar draft	h_d	m	120
Spar diameter above taper	$d_{s,0}$	m	6.5
Spar diameter below taper	$d_{s,1}$	m	9.4
Gravity center location	z_G	m	-89.9155
Spar mass	M_s	kg	7.46633E6
Spar inertia about G	I_s	$kg \cdot m^2$	4.22923E9, 4.22923E9, 1.6423E8
Added mass coefficient	$C_{s,a}$	-	0.969954
Spar drag coefficient	$C_{s,d}$	-	0.6
Water density	ρ	kg/m^3	1025
Water depth	d	m	320

Table 2.5: Mooring system parameters.

Parameter	Symbol	Unit	Value
Angles between cables and x-axis	-	rad	$\left[0 \frac{2}{3}\pi \frac{4}{3}\pi\right]$
Fairlead depth below SWL	-	m	70
Fairlead radius	-	m	5.2
Anchor depth below SWL	-	m	320
Anchor radius	-	m	853.87
Unstretched length	L_0	m	902.2
Diameter	d_c	m	0.09
Mass per unit length	m_c	kg/m	77.7066
Elastic stiffness	EA	N	3.84243E8
Wet weight per unit length	w_0	N/m	698.094
Initial cable depth and radius	h_c, l_c	m	250,848.67
Structural damping coefficient	β_s	s/m	0.0001
Normalized seabed stiffness	k_{sb}	-	1.0
Added mass coefficient	C_{an}	-	1.0
Drag coefficient	C_{dt}, C_{dn}, C_{db}	-	0, 1.6, 1.6

2.4.2 Tower and nacelle

The tower origin is located at the bottom of the tower. The tower height is h_t and the distributed mass per unit length is $\mu_t(z_t)$. The tower motion is assumed in the first mode shape $\phi_t(z_t)$ with z_t as the tower axis pointing upward. The lateral displacement of the tower is $\phi_t(z_t)q_4(t)$. The tower velocities are

$$u_t(z_t, t) \approx \dot{\xi_1} + (h - h_t + z_t)\dot{\xi_5}, \tag{2.79a}$$

$$v_t(z_t, t) \approx \phi_t(z_t)\dot{q_4} + \dot{\xi_2} - (h - h_t + z_t)\dot{\xi_4}, \tag{2.79b}$$

$$w_t(z_t, t) \approx \dot{\xi_3}, \tag{2.79c}$$

where, the overdot represents the time derivative. The approximations of the displacement at the top of the tower in y- and z-direction are

$$\tilde{q_4} = q_4\phi_t(h_t) + \xi_2 - hsin\xi_4 \approx q_4\phi_t(h_t) + \xi_2 - h\xi_4, \tag{2.80a}$$

$$q_5 = \xi_3 - h(1 - cos\xi_4) \approx \xi_3, \tag{2.80b}$$

where, h is the distance between the hub center and the spar center of gravity G. It is worth noting that the mode shape function ϕ_t is normalised $\phi_t(h_t) = 1$. Hence, it is omitted.

2.4.3 Edgewise model

The blade is considered as a continuous beam of variable mass, $\mu_b(r)$, and variable bending stiffness. The notation r denotes the blade coordinate along the blade axial direction. Each blade is modelled as a Bernoulli-Euler cantilever beam of length R. The blades are attached at the root representing the nacelle of the turbine allowing for the inclusion of blade-tower interaction. A schematic model is shown in Fig.2.26.

The edgewise vibration of the blade i is modelled by a degree of freedom $q_i(i = 1, 2, 3)$. The related mode shape $\phi_b(r)$ has been normalized such that q_i represents the edgewise tip displacement of the i^{th} blade. The displacement at any point r along a blade is given in terms of the fundamental mode shape and the generalized coordinate, such that

$$u_i(r, t) = \phi_b(r)q_i(t) \tag{2.81}$$

Assuming the blade speed rotation is a constant Ω_b (rad/s), the azimuthal angle $\Psi_i(t)$ of blade $i(i = 1, 2, 3)$ at given time t is

$$\Psi_i(t) = \Omega_b t + (i - 1)\frac{2\pi}{3}. \tag{2.82}$$

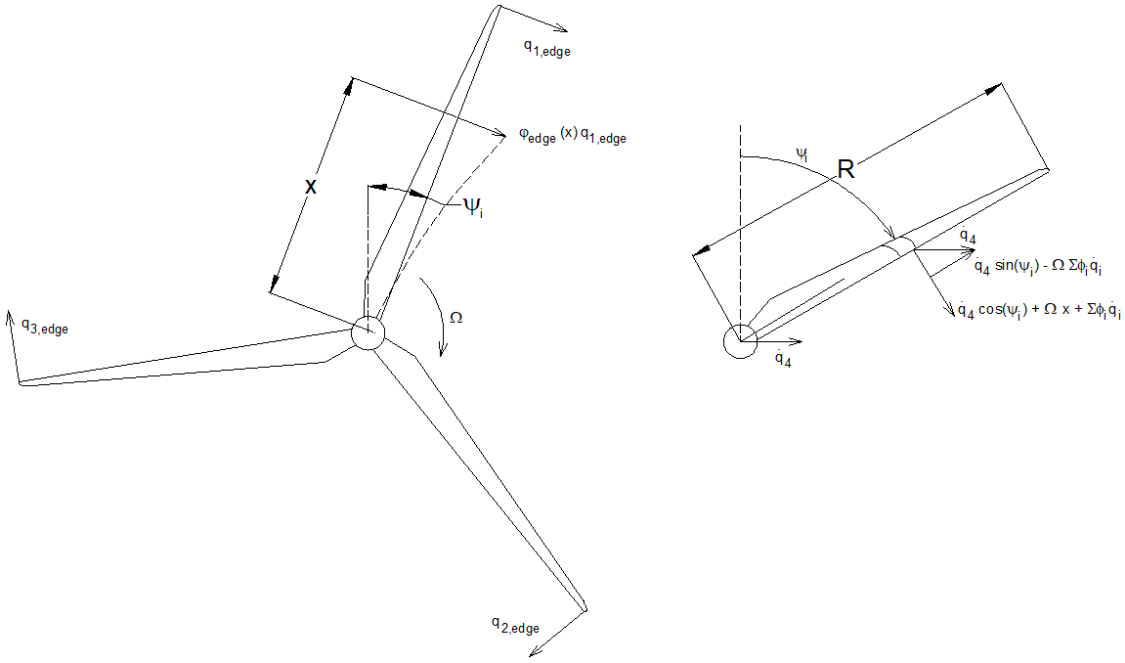

Figure 2.26: Edgewise wind turbine model.

The absolute velocities along the blade longitudinal and lateral axis are given by Dinh [28] as

$$v_{bi}(r,t) = -\dot{\tilde{q}}_4 sin\Psi_i + \dot{\xi}_3 cos\Psi_i - \Omega_b \phi_b(r) q_i, \tag{2.83a}$$

$$w_{bi}(r,t) = -\dot{\tilde{q}}_4 cos\Psi_i - \dot{\xi}_3 sin\Psi_i + \phi_b(r)\dot{q}_i + \Omega_b r, \tag{2.83b}$$

with the blade velocity in x-direction is computed by $u_{bi}(t) = \dot{\xi}_1 + h\dot{\xi}_5$. For more detail edge-wise flap-wise coupled model with variable rotational speed see [234]. Also, see [235] for the effect of pitch control.

2.4.4 Euler-Lagrangian formulation

The Euler-Lagrangian approach is used to derive the equations of motion. The formulation is helpful to formulate any coupling between the degree of freedoms. Although Arrigan [236] proved that the coupling effect between the blades and nacelle/tower is significantly weaker in the edgewise than in the flap-wise case, nevertheless, the coupling in the edgewise case is applied herein. The main focus of our work is the analyses of the hydrodynamic effects on the SFOWT responses.

The equations of motion of the system can be derived from the kinetic and potential energy and by substitution in the Euler-Lagrange equation. The specified energies automatically include the dynamic coupling in the system.

The total kinetic energy $\mathcal{T}$ of the spar is given by

$$\begin{aligned}\mathcal{T} = &\frac{1}{2}\sum_{i=1}^{3}\int_0^R \mu_b(r)[u_{bi}^2(t) + v_{bi}^2(r,t) + w_{bi}^2(r,t)]dr \\ &+ \frac{1}{2}\int_0^{h_t} \mu_t(z_t)[u_t^2(z_t,t) + v_t^2(z_t,t) + w_t^2(z_t,t)]dz_t \\ &+ \frac{1}{2}M_n(\dot{\tilde{q}}_4^2 + \dot{\xi}_3^{\,2} + \dot{\xi}_1 + h\dot{\xi}_5) + \frac{1}{2}M_s(\dot{\xi}_1^{\,2} + \dot{\xi}_2^{\,2} + \dot{\xi}_3^{\,2}) + \frac{1}{2}(I_{s,1}\dot{\xi}_4^{\,2} + I_{s,2}\dot{\xi}_5^{\,2} + I_{s,3}\dot{\xi}_6^{\,2}),\end{aligned} \tag{2.84}$$

where M_n is the nacelle mass and rotor mass, M_s is spar mass, and $I_{s,1}$, $I_{s,2}$, and $I_{s,3}$ are moment of inertia about the spar gravity centre in x, y, and z directions.

The total potential energy of the spar SFOWT takes the form

$$\mathcal{V} = \frac{1}{2}\sum_{i=1}^{3}(k_{b,e} + k_{bi,g} + k_{b,\Omega})q_i^2 + \frac{1}{2}k_{t,e}q_4^2 \tag{2.85}$$

where $k_{b,e} = \omega_b^2 M_{b,e}$ and $k_{t,e} = \omega_t^2 M_{t,e}$ are modal stiffness of the blade and the tower, respectively. The terms ω_b and ω_t are the natural angular frequencies of the blade and the tower, respectively. The blade and tower modal masses are $M_{b,e} = \int_0^R \mu_b(r)\phi_b^2 dr$ and $M_{t,e} = \int_0^{h_t} \mu_t \phi_t(z_t)dz_t$. The blade stiffness $k_{bi,g}(i = 1, 2, 3)$ affected by gravity is expressed as

$$k_{bi,g} = -gcos\Psi_i \int_0^R \left[\int_r^R \mu_b(\tau)d\tau\right]\left(\frac{d\phi_b}{dr}\right)^2 dr. \tag{2.86}$$

The centrifugal stiffening effect on the blade, denoted by $k_{b,c}$, is given as

$$k_{b,c} = \Omega^2 \int_0^R \left[\int_r^R \mu_b(\tau)\tau d\tau\right]\left(\frac{d\phi_b}{dr}\right)^2 dr \tag{2.87}$$

Substituting the external forces including the wind load including the rotationally sampled turbulence $\mathbf{f}_w$, gravitational load $\mathbf{f}_g$, hydrostatic load $\mathbf{f}_b$, hydrodynamic load $\mathbf{f}_h$, and mooring fair-lead tensions $\mathbf{f}_m$ into the Euler-Lagrange equation, we obtain the equation of motion

$$\mathbf{M}\ddot{\mathbf{q}} + \mathbf{C}\dot{\mathbf{q}} + \mathbf{K}\mathbf{q} = \mathbf{f}_w + \mathbf{f}_g + \mathbf{f}_b + \mathbf{f}_h + \mathbf{f}_m. \tag{2.88}$$

where, $\mathbf{M}, \mathbf{C}$, and $\mathbf{K}$ are the mass, damping, and stiffness matrices of the system, respectively. The stiffness of the system comprises of the hydrostatic stiffness and the mooring stiffness, $\mathbf{K} = (\mathbf{K}_h + \mathbf{K}_r)$ (detailed in appendix A1.1.5.). In order to derive the coefficient matrices ($\mathbf{M}, \mathbf{C}$, $\mathbf{K}$), the energy of the system ($\mathcal{T}$, $\mathcal{V}$), and description of the external loads ($\mathbf{f}(t)$), readers refer to previous studies [28, 30, 32, 233, 237, 238].

2.4.5 SFOWT loads

Numerical simulations have been performed to illustrate the impact of the large-amplitude waves. The numerical model of the SFOWT described in the previous section is implemented in MATLAB [239]. The ten-degree-of-freedom SFOWTs used in this study is coupled with the non-linear mooring model. The coupled model considers the aerodynamic properties of the blades, gravity, hydrostatic and hydrodynamic forces, and the interactions among the blades, nacelle, tower, and the floating foundation.

The wind flows toward the same direction as the rotor axis, as shown in Fig.2.27. The wind load along the blade length is calculated by using the BEM method [47, 233, 237]. The hydrostatic load is determined by Faltinsen [37], and the hydrodynamic forces per unit length are partially determined on each spar's segment by the Morison formula [240] combined with a pressure integration method. By that, the heave excitation forces and heave added mass are taken into account [65]. The drag forces and moments on each spar segment are computed using similar formulations as in previous studies by [30] and [28, 32, 237, 238, 241]. The structural loads include the mooring load at fair-lead positions. The mooring system herein consists of three single cables that are assumed to be flexible and inextensible. Each cable is modelled by the method introduced by Tjavaras [30, 242, 243, 244]. The Openmoor code [30, 245] developed by Chen and Basu estimates the spar platform's fairlead forces. Although the impact of the current on the spar response should not be neglected [31], but at first we donot consider the current effect as we will probably show the effects of the non-linear waves. Openmoor was validated with the experimentally validated MoorDyn [246] code. Chen and Basu [30] presented the detail of this work, where the coupled mooring model considering wave and current effects were studied and validated with various mooring models.

Generalized aerodynamic loads on blades

The edgewise vibration of the i^{th} blade is modelled by $q_i(t)(i = 1, 2, 3)$. The related in-plane mode shapes, $\phi_b(i = 1, 2, 3)$ have been normalised at the tip so that $q_i(t)$ represents the in-plane tip displacement. The displacement at any point x along a blade is given in terms of the fundamental mode shape and generalised coordinate such that

$$u_i(x, t) = \phi_b(x) q_i(t). \tag{2.89a}$$

In Fig.2.28, the lift and drag forces per unit length of the blade, p_L and p_D, are calculated

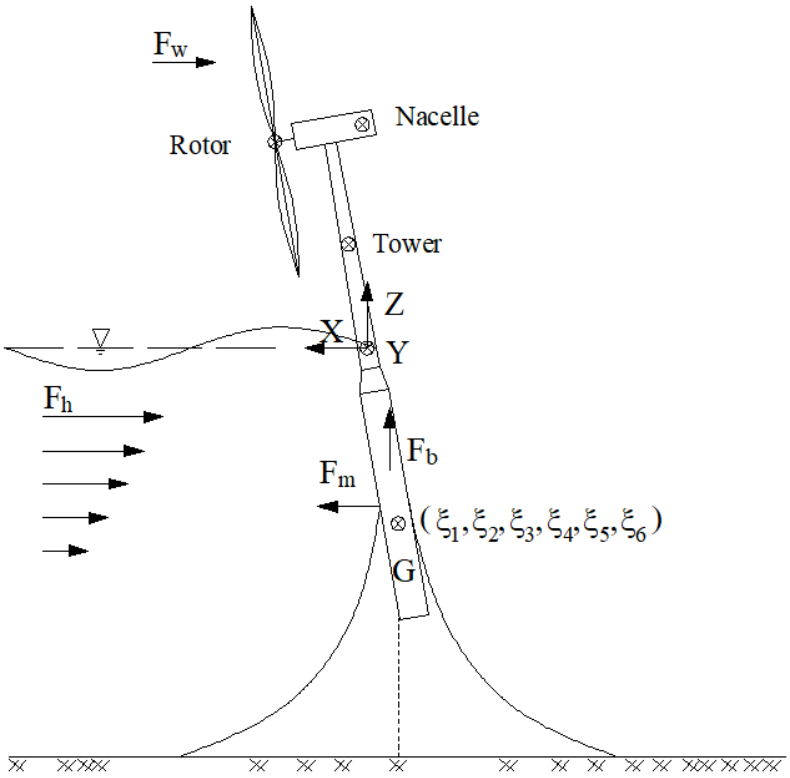

Figure 2.27: Loads on SFOWT.

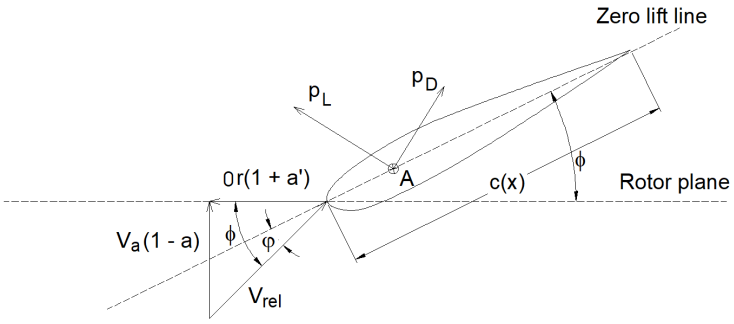

Figure 2.28: Blade cross-section.

using the BEM theory, respectively [47]. They are calculated as

$$p_L = \frac{1}{2}\rho V_{rel}^2(x,t)c(x)C_l(\phi) \tag{2.90a}$$

$$p_D = \frac{1}{2}\rho V_{rel}^2(x,t)c(x)C_d(\phi), \tag{2.90b}$$

where, ρ_a is the density of the air, $c(x)$ is the chord length, and $C_l(\phi)$, $C_d(\phi)$ are the drag and the lift coefficients, respectively depending on the angle of attack.

The normal and tangential load coefficients $C_N(\phi)$, $C_T(\phi)$ are computed using the lift

and drag coefficient from the air-foil data table.

$$C_N(\phi) = C_l(\phi)cos(\Phi) + C_d(\phi)sin(\Phi) \tag{2.91a}$$
$$C_T(\phi) = C_l(\phi)sin(\Phi) + C_d(\phi)cos(\Phi), \tag{2.91b}$$

The aerodynamic loads normal and tangential to the rotor plane (corresponding to the aerodynamic loads in the out-of-plane and in-plane direction, respectively) are given by

$$p_N = \frac{1}{2}\rho V_{rel}^2(x,t)c(x)C_N(\phi) \tag{2.92a}$$
$$p_T = \frac{1}{2}\rho V_{rel}^2(x,t)c(x)C_T(\phi), \tag{2.92b}$$

The principle of virtual work is used to determine the generalized aerodynamic loads on the system. The virtual work done is given by

$$\delta w = \sum_{i=1}^{3}(P_i\delta q_i - P_{nac4}\delta q_4 - P_{nac5}\delta q_5) = \sum_{i=1}^{3}(P_i\delta q_i - P_{nac4}\delta q_4 - P_{nac5}\delta \xi_3) \tag{2.93}$$

where P_i is calculated for the i^{th} blade by integrating the aerodynamic loads along the blade length with corresponding mode shape, as

$$P_i = \int_0^R p_{T,i}(r,t)\phi_b(r)dr. \tag{2.94}$$

The in-plane aerodynamic load on the nacelle, P_{nac4}, P_{nac5}, is given by

$$P_{nac4} = \sum_{1}^{3}\int_0^R p_{T,i}(r,t)drcos\Psi_i \tag{2.95a}$$
$$P_{nac5} = \sum_{1}^{3}\int_0^R p_{T,i}(r,t)drsin\Psi_i, \tag{2.95b}$$

Finally, the generalized aerodynamic load vector is obtained on the system as follows. The generalized aerodynamic load vector obtained is denoted as $\mathbf{f}_w = f_{w,j}$, with non-zero

components given as

$$f_{w,j} = \frac{\delta w}{\delta q_j} = P_j = \int_0^R p_{T,j}(r,t)\phi_b(r)dr, j = 1,2,3 \tag{2.96a}$$

$$f_{w,4} = -\frac{\delta w}{\delta q_4} = P_{nac4} = \sum_{i=1}^{3}\int_0^R p_{T,i}(r,t)drcos\Psi_i \tag{2.96b}$$

$$f_{w,5} = \sum_{i=1}^{3}\int_0^R p_{N,i}(r,t)dr, j = 1,2,3 \tag{2.96c}$$

$$f_{w,6} = f_{w,4} \tag{2.96d}$$

$$f_{w,7} = -\frac{\delta w}{\delta \xi_3} = P_{nac5} = \sum_{i=1}^{3}\int_0^R p_{T,i}(r,t)drsin\Psi_i \tag{2.96e}$$

$$f_{w,8} = -hf_{w,6} \tag{2.96f}$$

$$f_{w,9} = hf_{w,5} \tag{2.96g}$$

where, j is the generalized displacement index.

Generalized gravity force

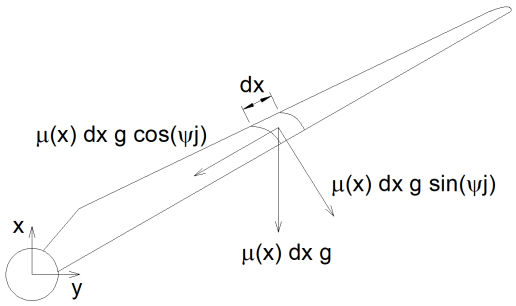

Figure 2.29: Blade gravity force.

The gravity load acting on the blade is illustrated in Fig.2.29 Resolving the gravity force leads to two forces, the normal component

$$dG_N = \mu(x)dxgsin\Psi_i, \tag{2.97}$$

and the other aligns along the length of the blade and is given by

$$dG_A = \mu(x)xgcos\Psi_i \tag{2.98}$$

where $\mu(x)$ is the mass per unit length of the blade and g is the acceleration due to gravity, $g = 9.81m/s^2$.

The principle of virtual work is used to determine the gravity load in the blades. The

virtual work done by the gravity force, δw_g, is given by

$$\begin{aligned}\delta w_g &= \sum_{j=1}^{3}\left[\int_0^R \mu_b(r) g sin(\Psi_j(t)) dr\right]\delta q_i(r,t)\phi_b(r) \\ &- \sum_{j=1}^{3}\int_0^R \mu_b(r) g dr \delta q5 - M_n g \delta q5 - M_s g \delta \xi_3 + M_t g \delta q5\end{aligned} \tag{2.99a}$$

$$\begin{aligned}&= \sum_{j=1}^{3}\left[\int_0^R \mu_b(r) g sin(\Psi_j(t)) dr\right]\delta q_i(r,t)\phi_b(r) \\ &- \sum_{j=1}^{3}\int_0^R \mu_b(r) g dr \delta \xi_3 - M_n g \delta \xi_3 - M_s g \delta \xi_3 - M_t g \delta \xi_3,\end{aligned} \tag{2.99b}$$

with,

$$f_{g,j} = \frac{\delta w_g}{\delta q_j} = g\int_0^R \mu_b(r)\phi_b(r) dr sin\Psi_j, j = 1,2,3 \tag{2.100a}$$

$$f_{g,7} = \frac{\delta w_g}{\delta \xi_3} = -g(M_n + M_s + M_t + 3M_b), \tag{2.100b}$$

$$f_{g,9} = M_{nac} g l_m(1) + M_{rotor} g l_r(1), \tag{2.100c}$$

Hydrostatic and hydrodynamic effect on the spar

The buoyancy force forms the hydrostatic effect on spar and can be written as

$$f_{b,7} = \rho_w g V_s, \tag{2.101a}$$

where V_s is the fluid volume determined by the diameter of the top of the taper.

The hydrodynamic forces per unit length on the spar in the horizontal directions are determined using the Morison's formula [240]. The moments due to these hydrodynamic force are calculated accordingly. They are given as

$$\begin{aligned}df_{h,5}(z) &= -C_{s,a}\frac{\rho\pi}{4}d_s^2(z)u_s(z)dz + (1+C_{s,a})\frac{\rho\pi}{4}d_s^2(z)\dot{u}_f(z)dz \\ &+ \frac{1}{2}C_{s,d}\rho d_s(z)u_{s,f}(z)[u_{s,f}^2(z) + v_{s,f}^2(z)]^{-1/2}dz\end{aligned} \tag{2.102a}$$

$$\begin{aligned}df_{h,6}(z) &= -C_{s,a}\frac{\rho\pi}{4}d_s^2(z)v_s(z)dz + (1+C_{s,a})\frac{\rho\pi}{4}d_s^2(z)\dot{v}_f(z)dz \\ &+ \frac{1}{2}C_{s,d}\rho d_s(z)v_{s,f}(z)[u_{s,f}^2(z) + v_{s,f}^2(z)]^{-1/2}dz\end{aligned} \tag{2.102b}$$

$$df_{h,8}(z) = -(z - z_G)df_{h,6}(z), \tag{2.102c}$$

$$df_{h,9}(z) = -(z - z_G)df_{h,5}(z), \tag{2.102d}$$

To be more specific, the inertia forces and moments are computed by the following equations as

$$df_{i,5}(z) = (1 + C_{s,a})\frac{\rho\pi}{4}d_s^2(z)\dot{u}_f(z)dz \tag{2.103a}$$

$$df_{i,6}(z) = (1 + C_{s,a})\frac{\rho\pi}{4}d_s^2(z)\dot{v}_f(z)dz \tag{2.103b}$$

$$df_{i,7}(z) = p_d\frac{\pi}{4}d_s^2(z = bottom) - p_d(mean)\frac{\pi}{4}(d_s^2(bottom) - d_s^2(top)) \tag{2.103c}$$

$$df_{i,8}(z) = -(z - z_G)df_{h,6}(z), \tag{2.103d}$$

$$df_{i,9}(z) = (z - z_G)df_{h,5}(z), \tag{2.103e}$$

and the drag forces and moments are defined by

$$df_{d,5}(z) = \frac{1}{2}C_{s,d}\rho d_s(z)u_{s,f}(z)[u_{s,f}^2(z) + v_{s,f}^2(z)]^{-1/2}dz \tag{2.104a}$$

$$df_{d,6}(z) = \frac{1}{2}C_{s,d}\rho d_s(z)v_{s,f}(z)[u_{s,f}^2(z) + v_{s,f}^2(z)]^{-1/2}dz \tag{2.104b}$$

$$df_{d,8}(z) = -(z - z_G)df_{d,6}(z), \tag{2.104c}$$

$$df_{d,9}(z) = (z - z_G)df_{d,5}(z). \tag{2.104d}$$

where, $C_{s,a}$, $C_{s,d}$ are the added mass coefficient and drag coefficient of the spar, respectively. The terms $u_s(z)$, $v_s(z)$ are the spar horizontal velocity component in $xy-$plane, $u_f(z)$, $v_f(z)$ are the fluid velocity components in x, y directions. The relative horizontal velocity of the spar and the fluid flow are $u_{s,f} = u_f - u_s$ and $v_{s,f} = v_f - v_s$, respectively.

The spar velocity at a particular depth can be computed from the velocity of the spar at the reference point. The spar is divided into segments using the strip theory, and the above expressions are used to obtain the hydrodynamic forces on each segment. The total forces are then summed up over the spar draft.

The spar added mass and damping effect in the vertical direction due to the heave motions, are neglected. The hydrodynamic force, the Froude-Kriloff pressure force, for spar heave motion $f_{h,7}$ is due to the wave excitation that is integrated using the dynamic pressure on spar [37]. The dynamic pressure is calculated using the wave theory and then integrated over the bottom and the conical area of the spar.

In the above equations, the added mass is considered separately in the added mass matrix of the spar. The two force components are the drag force and the inertia force, and they are calculated and added into the generalized force vector.

2.5 Mooring forces

The temporal mooring forces are coupled into the generalized force vector through three fairleads positions. The mooring forces herein are computed using the validated open-source OpenMoor code developed by Chen and Basu [30, 245].

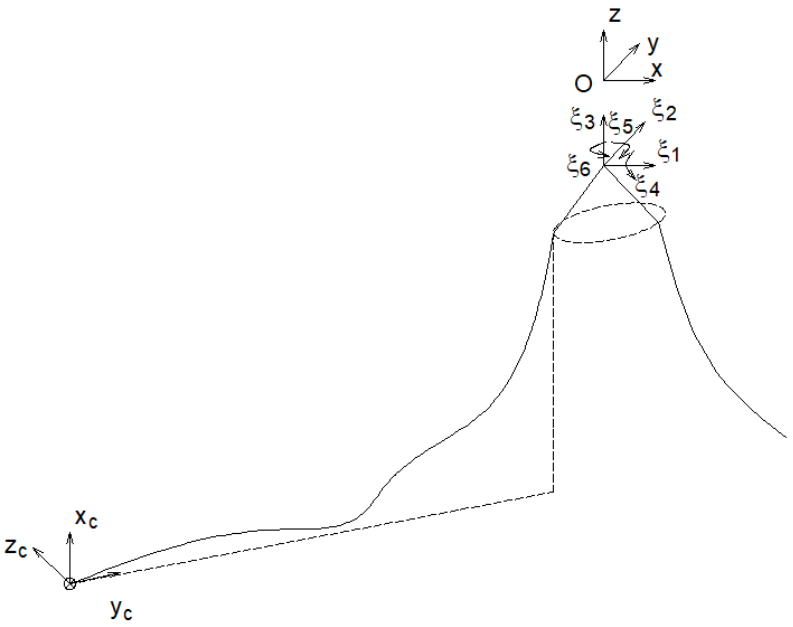

Figure 2.30: Mooring coordinate system.

A typical mooring system is described in Fig.2.30. The cables are attached to the floater at the fairleads. The floater and the mooring lines are subject to the wave and current loads and the superstructure loads. The floater has six degrees of freedom (6 dofs) $(\xi_1, \xi_2, \xi_3, \xi_4, \xi_5, \xi_6)$ at the reference point (G). Cables properties are identical. The environmental loads induce platform motions and thus generate static offset of the platform. The static offset leads to changes in the fairlead position; thus, the spar and the cables must be analysed simultaneously. The static and dynamic responses of the cable are two-point boundary problems whose boundary conditions at the fairleads of the cables are estimated with the platform motion.

2.5.1 Cable model

Tjavaras presented the cable model for solving the two-point boundary-value problem [242, 243, 244]. It assumed a uniform circular cross-section cable with diameter d, mass per unit length m, bending stiffness EI, and torsion stiffness GJ. A fixed coordinate is defined as (o_c, x_c, y_c, z_c) at the anchor position with x_c pointing upward, y_c and z_c in the plane are defined by the anchor and initial fairlead position. The vertical and horizontal distances between the anchor and initial fairlead position are h_c and l_c, respectively.

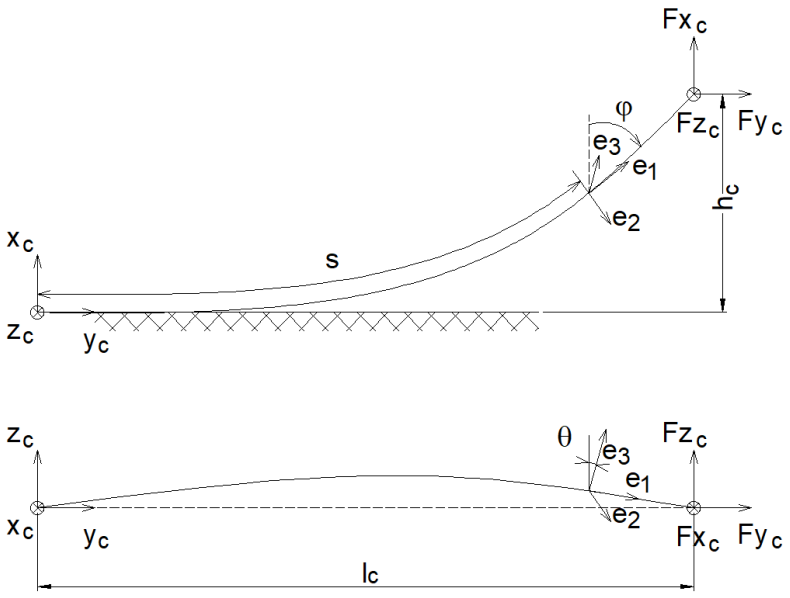

Figure 2.31: Cable motion description and the coordinate systems: (a) vertical plane; (b) horizontal plane.

The local Lagrangian reference coordinate is attached to unstretched cable at an arc length of s with the local tangential (e_1), normal (e_2), and binormal directions (e_3). The cable position in the Cartesian coordinate can be estimated using s, ϕ, φ and cable strain ϵ. The Poison ratio equals 0.5 in the following sections.

2.5.2 Governing equations

The system of equations describing the three dimensional motion of a cable are given by [125]

$$\frac{\partial \varepsilon}{\partial s} - \frac{m}{f'(\varepsilon)}\frac{\partial u}{\partial t} + \frac{m}{f'(\varepsilon)} v cos\theta \frac{\partial \varphi}{\partial t} - \frac{m}{f'(\varepsilon)} w \frac{\partial \theta}{\partial t} + \beta \frac{\partial \varepsilon}{\partial t} + \frac{S_b \kappa_2}{f'(\varepsilon)} - \frac{S_n \kappa_3}{f'(\varepsilon)} - \frac{w_0}{f'(\varepsilon)} cos\varphi cos\theta + \frac{F_{dt}}{f'(\varepsilon)} = 0 \tag{2.105a}$$

$$\frac{\partial S_n}{\partial s} - (m + m_{an})\frac{\partial v}{\partial t} - m(ucos\theta + wsin\theta)\frac{\partial \varphi}{\partial t} - C_m \rho \frac{\pi d^2}{4}(U_c cos\varphi + V_c sin\varphi)\frac{\partial \varphi}{\partial t} + f(\varepsilon)\kappa_3 + S_b \kappa_3 tan\theta + w_0 sin\varphi + F_{dn} = 0 \tag{2.105b}$$

$$\frac{\partial S_b}{\partial s} - (m + m_{an})\frac{\partial w}{\partial t} + mvsin\theta \frac{\partial \varphi}{\partial t} - C_m \rho \frac{\pi d^2}{4}(U_c sin\varphi sin\theta - V_c cos\varphi sin\theta)\frac{\partial \varphi}{\partial t} + mu\frac{\partial \theta}{\partial t} + C_m \rho \frac{\pi d^2}{4}(U_c cos\varphi cos\theta + V_c sin\varphi cos\theta - W_c sin\theta)\frac{\partial \theta}{\partial t} - S_n \kappa_3 tan\theta - f(\varepsilon)\kappa_2 - w_0 cos\varphi sin\theta + F_{db} = 0 \tag{2.105c}$$

$$EI\frac{\partial \kappa_2}{\partial s} + (EI - GJ)\kappa_3^2 tan\theta - S_b(1 + \varepsilon)^3 = 0 \tag{2.105d}$$

$$EI\frac{\partial \kappa_3}{\partial s} + (GJ - EI)\kappa_3 \kappa_2 tan\theta + S_n(1 + \varepsilon)^3 = 0 \tag{2.105e}$$

$$\frac{\partial u}{\partial s} - \frac{\partial \varepsilon}{\partial t} + \kappa_2 w - \kappa_3 v = 0 \tag{2.105f}$$

$$\frac{\partial v}{\partial s} - (1 + \varepsilon)cos\theta \frac{\partial \varphi}{\partial t} + \kappa_3(u + wtan\theta) = 0 \tag{2.105g}$$

$$\frac{\partial w}{\partial s} + (1 + \varepsilon)\frac{\partial \theta}{\partial t} - \kappa_3 vtan\theta - \kappa_2 u = 0 \tag{2.105h}$$

$$\frac{\partial \varphi}{\partial s} - \frac{\kappa_3}{cos\theta} = 0 \tag{2.105i}$$

$$\frac{\partial \theta}{\partial s} - \kappa_2 = 0, \tag{2.105j}$$

where Eq.2.105(a,b,c) represent the balance of the forces in the local reference frame; Eq.2.105(d,e) govern the balance of the moments without external moments; Eq.2.105 (f,g,h) describe the compatibility relations; and Eq.2.105(i,j) define the material curvatures. In Eq.2.105(a,b,c), w_0 is the wet cable weight per unit length; $f(\varepsilon)$ is tension function of ε such that $f'(\varepsilon)$ is its derivative with respect to ε. The added mass m_{an} in the normal direction are computed by $m_{an} = C_{an}\rho\frac{\pi d^2}{4}$ with C_{an} is the added mass coefficient. The Froude-Krylov force is taken into account by using the inertia coefficient $C_m = 1 + C_{an}$. S_n, S_b, u, v, and w are the in-plane shear force, out-of-plane shear force, tangential velocity, normal velocity, and binormal velocity, respectively. The terms κ_3 and κ_2 are in-plane and out-of-plane material curvatures, respectively. The proportional structural damping [157] is given by $F_{sd} = \beta f'(\varepsilon)\frac{\partial\varepsilon}{\partial t}$ where $\beta(s/m)$ is a damping coefficient. The current velocity in the cable reference frame along the x_c, y_c, z_c direction are U_c, V_c, and W_c, respectively. The relative cable velocity in the local Lagrangian coordiante system are u_r, v_r, and w_r which are expressed as

$$u_r = u - U_c cos\varphi cos\theta - V_c sin\varphi cos\theta + W_c sin\theta \tag{2.106a}$$

$$v_r = v + U_c sin\varphi - V_c cos\varphi \tag{2.106b}$$

$$w_r = w - U_c cos\varphi sin\theta - V_c sin\varphi sin\theta - W_c cos\theta. \tag{2.106c}$$

Morison's equations are used to estimate the hydrodynamic drag forces in the tangential, normal and binormal directions as

$$F_{dt} = -\frac{1}{2}\rho d\pi C_{dt} u_r |u_r| \sqrt{1+\varepsilon} \tag{2.107a}$$

$$F_{dn} = -\frac{1}{2}\rho d C_{dn} v_r \sqrt{v_r^2 + w_r^2}\sqrt{1+\varepsilon} \tag{2.107b}$$

$$F_{db} = -\frac{1}{2}\rho d C_{db} w_r \sqrt{v_r^2 + w_r^2}\sqrt{1+\varepsilon}. \tag{2.107c}$$

in which, C_{dt}, C_{dn}, and C_{db} are the drag coefficients in the three local coordinates.

2.5.3 Finite difference solver

There are ten unknowns in Eq.2.105,i.e. $\varepsilon, S_n, S_b, u, v, w, \varphi, \theta, \kappa_2, \kappa_3$. The system of equations are then discretized by applying Keller Box finite difference method and solved with the associated boundary conditions, using relaxation method [247]. The solver has been applied by Chen and Basu [245] and hereby the lib file are then call by Matlab [239] as a $C++$ function.

2.5.4 Boundary conditions

The boundary conditions include the bottom boundary condition at the anchor and the top boundary at the fairleads. At the seabed, the floor is assumed as an elastic foundation, and the fiction is neglected. In addition, the seabed force is always considered in the vertical direction. The seabed reduces of the wet weight of the cable as

$$w_e(s_j) = w_0 + \bar{k}_{sb} x_c(s_j) \tag{2.108}$$

in which $\bar{k}_{sb}$ is the seabed stiffness, and s_j is the cable coordinate of node j. For static problem, $w_0 \geq w_e \geq 0$. Since the choice of k_{sb} has negligible influence on the cable solution, the stiffness is chosen to completely balance the cable wet weight with the seabed, $k_{sb} = w_0/d$ at the sea bottom [248]. More details are in [242, 244].

For dynamic analysis, the catenary solution can be used to initialize the problem. The angle φ can be computed from the catenary profile assuming that $\theta = \kappa_2 = S_b = 0$, then κ_3 and S_n are computed from Eq.2.105(i-e). The zero curvature at the anchor and the fairlead are the typical boundary conditions as following

$$\begin{aligned} u^{(1)} = 0, v^{(1)} = 0, w^{(1)} = 0, \kappa_2^{(1)} = 0, \kappa_3^{(1)} = 0 \\ \kappa_2^{(N)} = 0, \kappa_3^{(N)} = 0 \end{aligned} \tag{2.109}$$

where the superscript (1) is the anchor node and (N) is the fairlead node.

For static analysis, the temporal terms in Eq.2.105 are absent. The cable velocity is zero. If the fairlead positions are used as boundary conditions, the fairlead positions are computed using the fairlead tension using a shooting procedure [249]. If the fairlead force are used as boundary conditions, the tension force components in the local (x_c, y_c, z_c) coordinate system are

$$F_{x_c} = [f(\varepsilon) cos\varphi cos\theta - S_n sin\varphi + S_b cos\varphi sin\theta]^{(N)} \tag{2.110a}$$

$$F_{y_c} = [f(\varepsilon) sin\varphi cos\theta + S_n cos\varphi + S_b sin\varphi sin\theta]^{(N)} \tag{2.110b}$$

$$F_{z_c} = [-f(\varepsilon) sin\theta + S_b cos\theta]^{(N)}. \tag{2.110c}$$

In the dynamic analysis, Eq.2.105 can be solved with ten boundary conditions including the zero curvature boundary conditions in Eq.2.109 and the fairlead velocity (U_t, V_t, W_t)

resulting from the spar motion

$$U_t = (u\cos\varphi\cos\theta - v\sin\varphi + w\cos\varphi\sin\theta)^{(N)} \tag{2.111a}$$

$$V_t = (u\sin\varphi\cos\theta + v\cos\varphi + w\sin\varphi\sin\theta)^{(N)} \tag{2.111b}$$

$$W_t = (-u\sin\theta + w\cos\theta)^{(N)}. \tag{2.111c}$$

Therefore, the cable states are obtained. The fairlead tension in cable reference frame are then computed using Eq.2.110.

2.5.5 Implementation

The code for the coupled model is available on GitHub and is called OpenMOOR. It is a Trinity College licensed code developed by Chen *et al.* [30] dynamic mooring analysis is carried out with the following steps.

i. Exact current fairlead positions and velocity in spar local coordinate.

ii. Compute the fairlead displacement and velocity for each cable in the cable coordinate system.

iii. Solve the cable state for given displacement and velocity for each cable and compute the fairlead force in the cable coordinate.

iv. Transfer the fairlead forces to the platform coordinate system and compute the corresponding moment at the spar's reference point.

v. Sum up the fairlead forces and moments over the cable to assemble the mooring load associated with the platform's translational and rotational motion.

The fairlead forces and moment on each cable are provided as

$$\begin{bmatrix} f_{x1} & f_{x2} & f_{x3} \\ f_{y1} & f_{y2} & f_{y3} \\ f_{z1} & f_{z2} & f_{z3} \\ m_{11} & m_{21} & m_{31} \\ m_{12} & m_{22} & m_{32} \\ m_{13} & m_{23} & m_{33} \end{bmatrix} \tag{2.112}$$

The total fairlead forces and moment on spar is given by summing up all force and

moment components in the same row

$$\begin{bmatrix} f_{m,1} \\ f_{m,2} \\ f_{m,3} \\ f_{m,4} \\ f_{m,5} \\ f_{m,6} \end{bmatrix} \tag{2.113}$$

where $f_{m,i}(i = 1, 2, 3)$ are the translation force and $f_{m_i}(i = 4, 5, 6)$ are the rotational moment at the reference point of the spar (G).

2.6 Interpolation scheme for waves kinematics

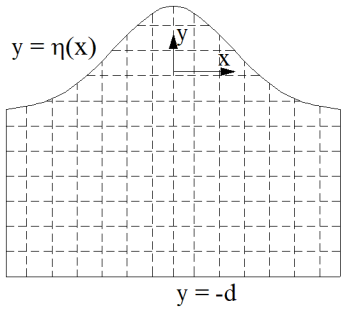

Figure 2.32: Discretised domain within one wavelength

The flow kinematics are obtained at grid nodes using the finite difference scheme. The numerical solutions are provided within one wavelength. The length of the fluid field is determined by the wave speed and the duration of the simulation.

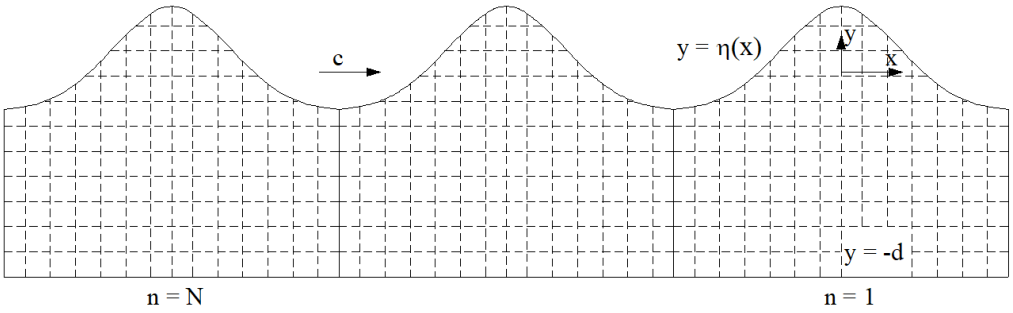

Figure 2.33: Flow domain generated from one wave length.

Then, the spacial and temporal coordinate of the spar segments at each time step is used as interpolation points to obtain the wave kinematic at spar segment positions following Sec.2.2.6.

2.7 Impact of non-linear large-amplitude waves on SFOWT responses

No existing research currently applies large-amplitude waves to study wave-structure interaction and LAW wave-current interaction. Therefore, the large amplitude waves are used in this thesis to explore the large amplitude wave effect on floating offshore wind turbines. The wave effect is considered with the uniform current modifying the Euler equations and other relations appropriately to investigate the impact of wave-current on a floating structure. The sea-states from [10] are used to choose the wave parameters in this thesis. The sea-state includes eight wave heights and corresponding wave periods. The linear waves are selected based on sea-state three, five, and eight, respectively.

The results of time-domain dynamic simulations are presented and discussed for the system that encounters both linear waves and large-amplitude waves. We focus on the comparison of structural response predictions from two wave theories.

2.7.1 SFOWT response to waves of slightly wave period

The large amplitude wave solutions are a set of waves of similar wavelength, but wave period and wave height varies on the bifurcation diagram. As the wave height increases the wave period decreases until the wave of "greatest height" is reached. The waves used for investigation in this section are the intermediate points on the bifurcation diagram, given in Table 2.1.

The non-linear waves can have significantly different wave height and fluid kinematics than the corresponding linear waves with the same wavelength. These findings raise intriguing questions regarding the impact the non-linear waves may have on the response of SFOWT. Therefore, the response of the SFOWT to the non-linear and linear waves (in cases 1-4) are computed and presented in Fig.2.35 to Fig.2.40.

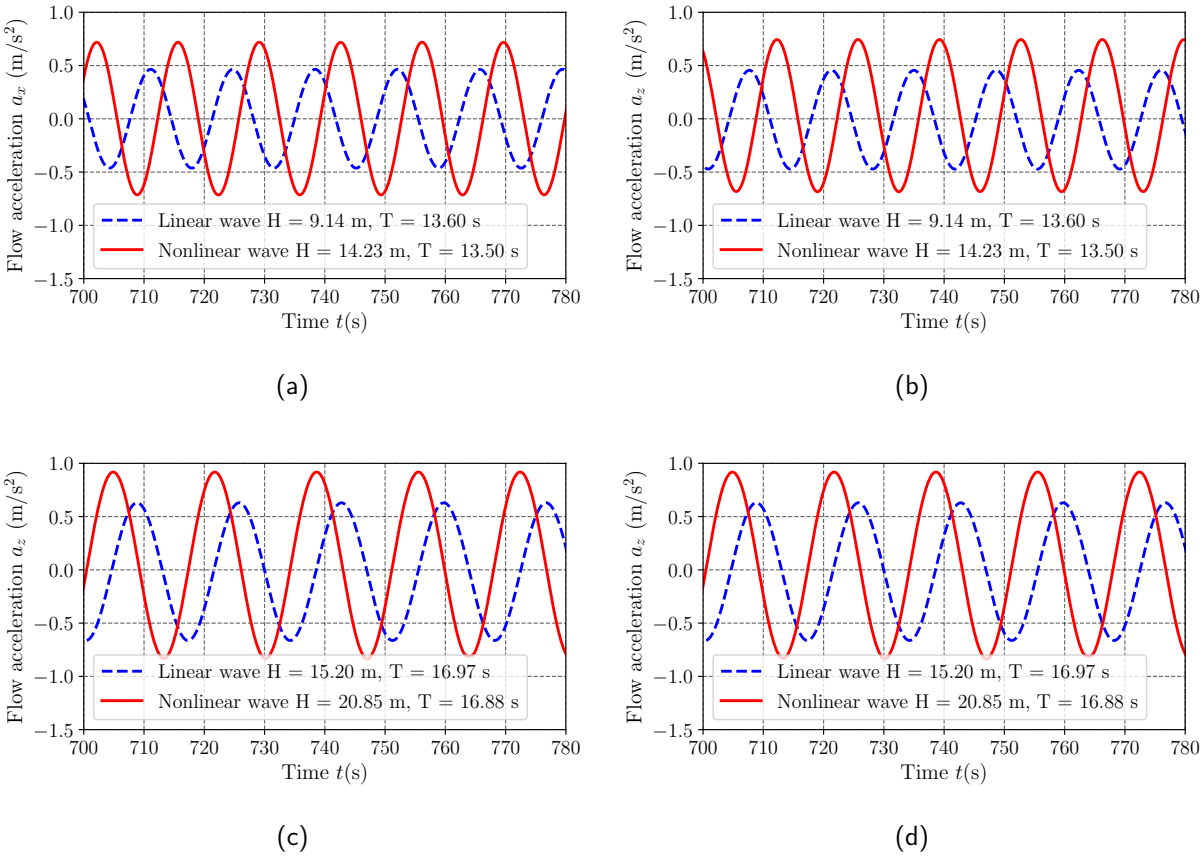

Figure 2.34: Flow acceleration time history of 4^{th} segment: (a,b) Case 2; (c,d) Case 4.

The acceleration time history of the fluid at a point, which is completely submerged within the water but near the free surface, is presented in Fig.2.34. The spar cylinder is divided into 30 segments, each segment had a length of 4m. Therefore, the 4th segment initially located at −14m under the free surface. Similarly, the 5th segment is initially at −18m. The spar is moving with the flow; hence the fluid acceleration at a point located on the spar is interpolated from the fluid accelerations following the scheme described in Section 2. Fig.2.34 shows the apparent difference in results from the two wave theories. Horizontal and vertical accelerations obtained from the waves generated from the linear and non-linear theories are considerably different. We draw similar conclusions for flow velocities and hydrodynamic pressure for a point located on the spar.

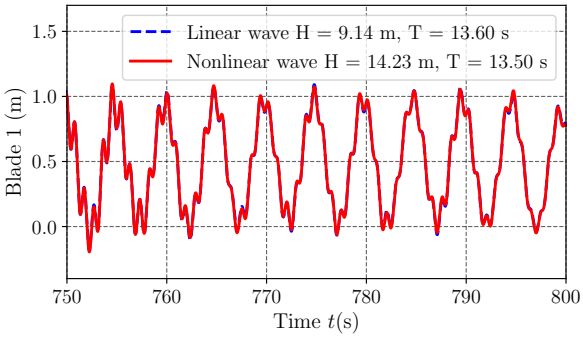

(a)

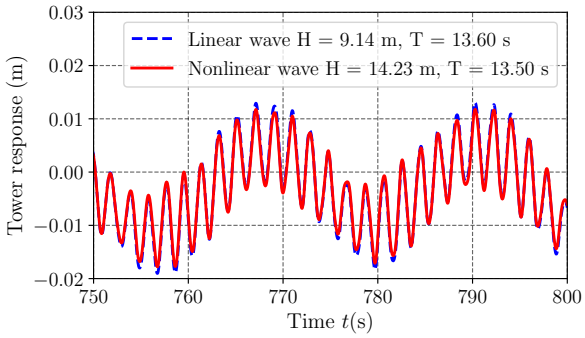

(b)

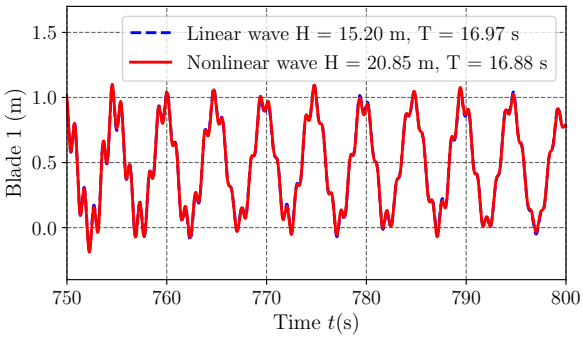

(c)

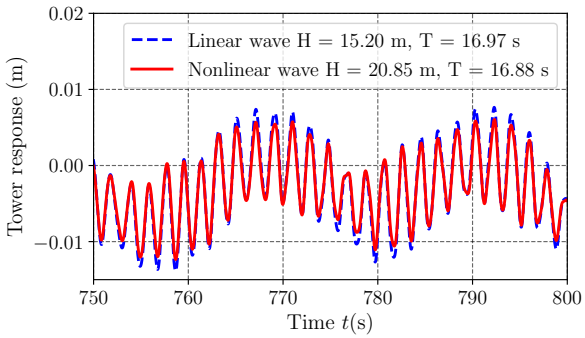

(d)

Figure 2.35: Blade and tower response: (a,b) Case 2; (c,d) Case 4.

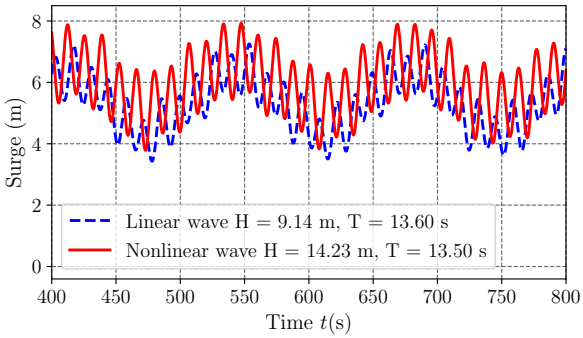

(a)

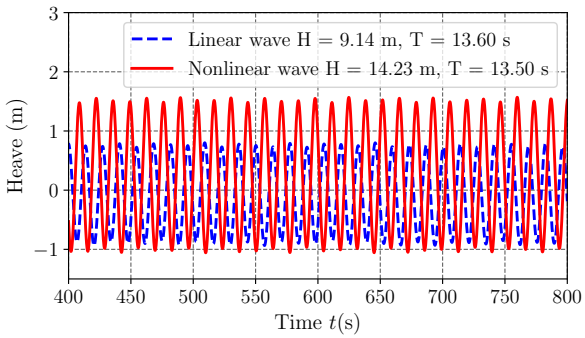

(b)

Figure 2.36: Spar FOWT responses (surge and heave) case 2.

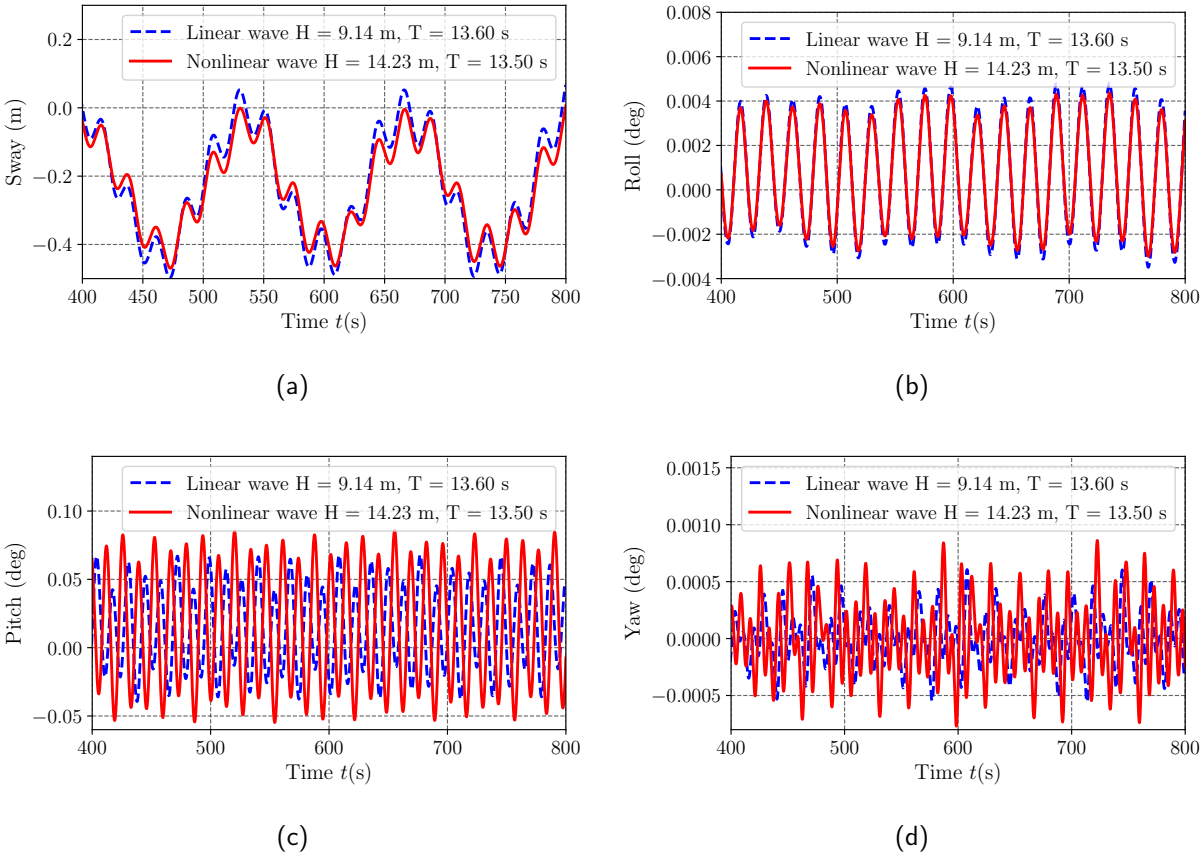

Figure 2.37: Spar FOWT responses (sway, roll, pitch, and yaw) case 2.

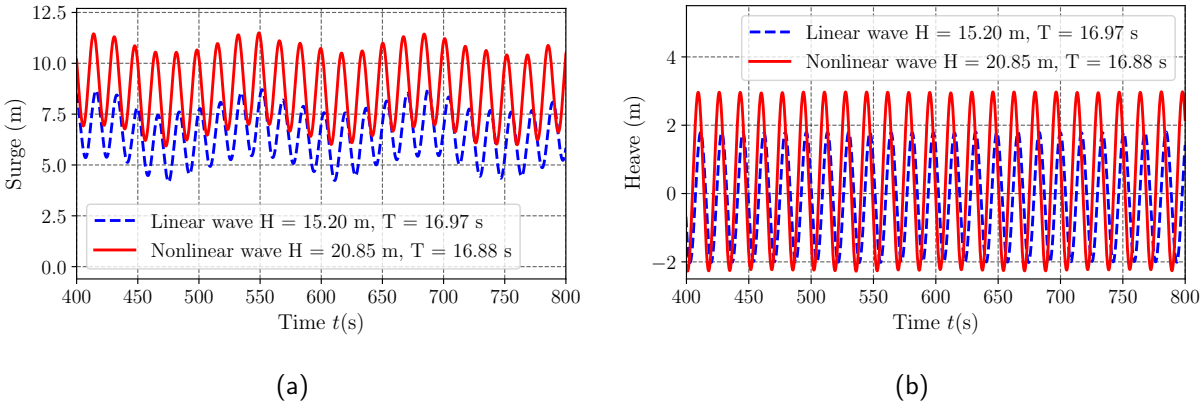

Figure 2.38: Spar FOWT responses (surge and heave) case 4.

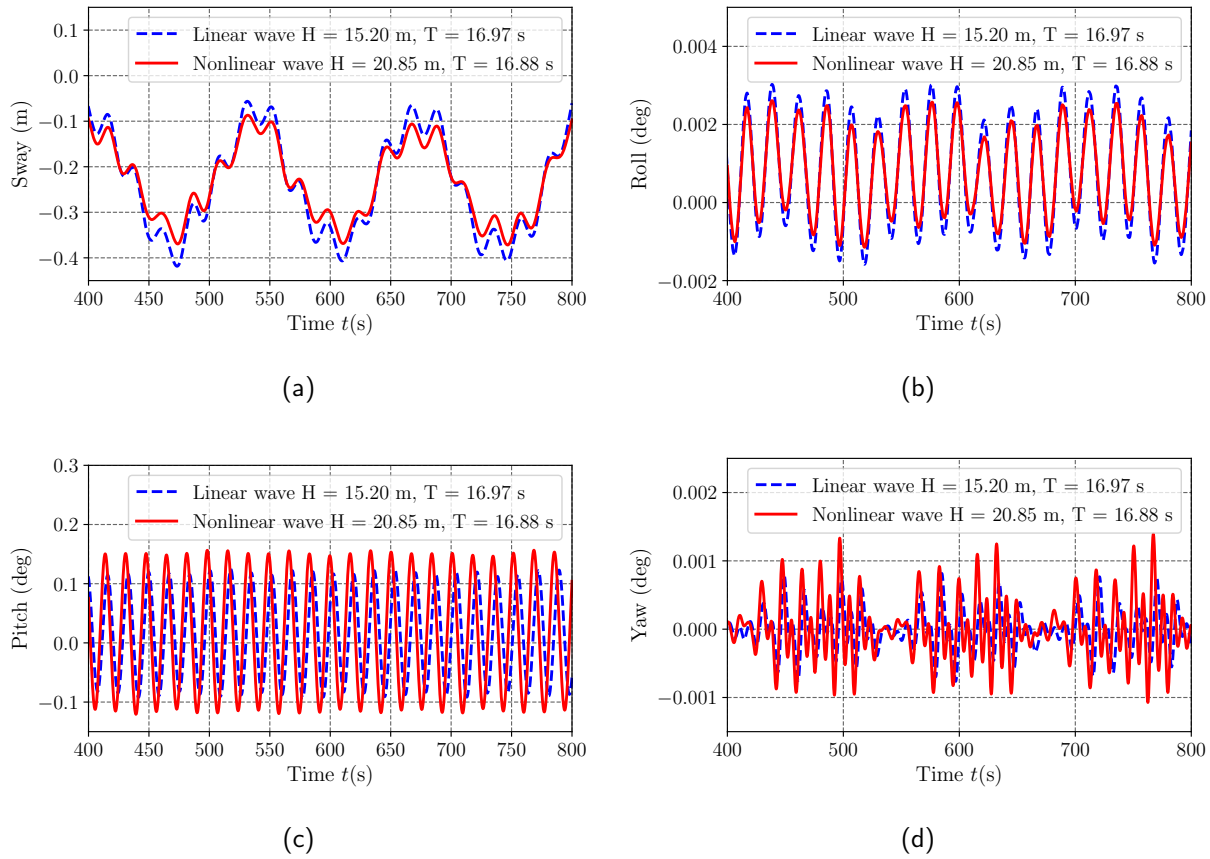

Figure 2.39: Spar FOWT responses (sway, roll, pitch, and yaw) case 4.

Fig.2.35 to Fig.2.40 compare the response of the spar. Fig.2.35 reveals that the waves have negligible impact on the relative blade and tower responses. The surge and heave motions shown in Fig.2.36 and Fig.2.38 are impacted dramatically by to the non-linear waves. The surge response to non-linear waves for both the sea-states are much larger than the response of the SFOWTs to linear waves. Besides, it can be seen that the wave kinematics of the large-amplitude non-linear waves are different compared to the linear waves. This causes the equilibrium point to be different from zero (Fig.2.36(b)) and case 4 (Fig.2.38(b)). While the mean value of the heave motions of the spar is above the MWL due to the effect of non-linear wave kinematics, when subjected to the non-linear waves, the corresponding mean value is under the MWL for linear waves. These results may be due to the fluid kinematics contributing to the floater's motion and asymmetrical water surface about the MWL with the higher wave crest (shown in Fig.2.11). Thus, the surrounding fluid in a non-linear wave tends to push the spar up more than it would for a linear wave.

A comparison of the results also reveals an increase in the pitch and yaw motion of the SFOWTs, whose maximum amplitudes are slightly larger than that obtained from linear waves (shown in Fig.2.37(c,d) and Fig.2.39(c,d)). In contrast, Fig.2.37(a,b) and

Fig.2.39(a,b) present sway and roll responses, where only small amounts of difference were observed between the results obtained from non-linear and linear waves. The responses in non-linear cases are less than that obtained for the linear waves. The close enough results might result from the fact that the above motions are mainly wind-dominated while the waves control the heave motion.

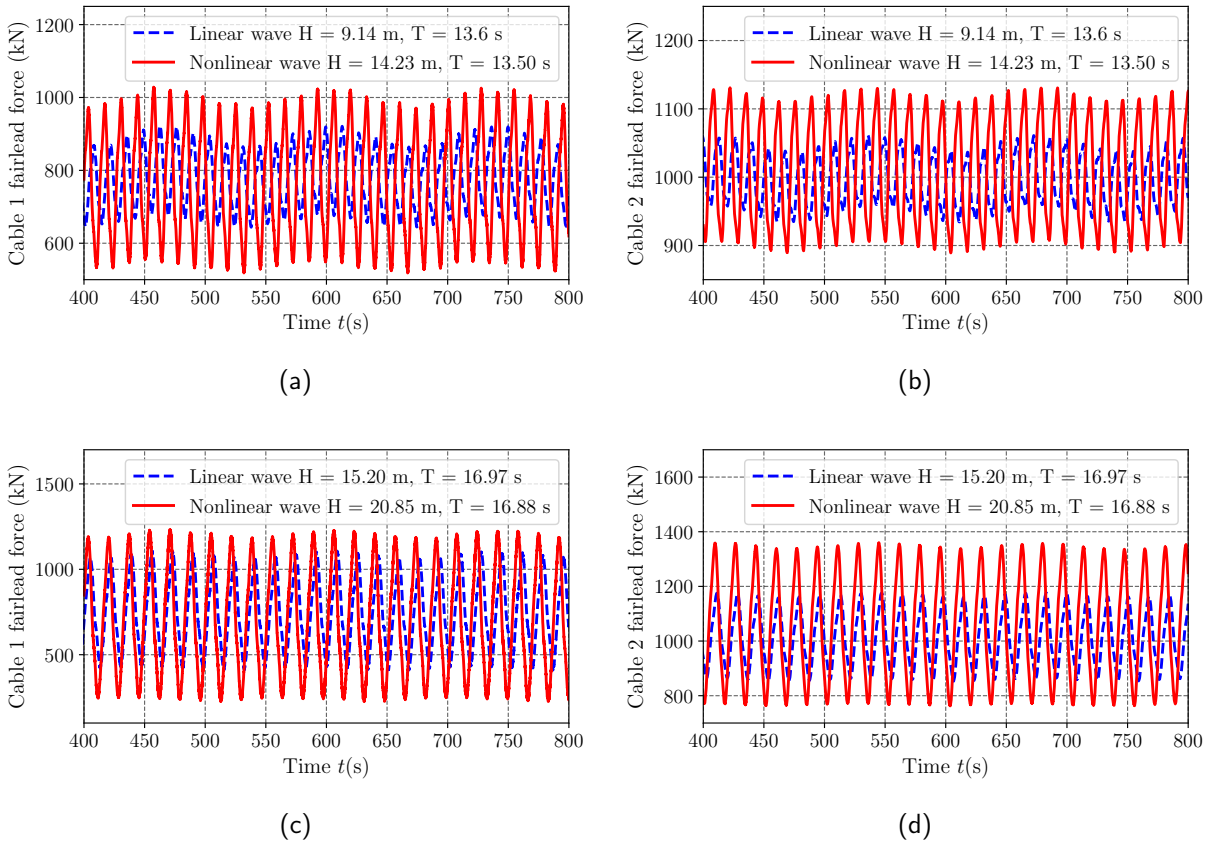

Figure 2.40: Cable fairlead forces: (a,b) Case 2; (c,d) Case 4.

Since the motion of the spar directly influences the mooring line tension, the comparison of fairlead forces of the mooring system is of interest. In addition, the mooring lines are responsible for the overall stability of the SFOWTs and for keeping it at a stationary location. Among the three cables, the first and the second cables are selected to study the effect of the non-linear and linear waves. The first mooring cable is in line with the incoming wave and wind direction, while the second is inclined towards the positive $y-$direction, as shown in Fig.2.27. The fairlead forces of cable three are equal to that of cable two due to the symmetrical layout of the mooring system; therefore, they are not shown. Fig.2.40 shows the time history of the fairlead forces of cable one and cable two. These forces are critical in affecting the spar motion. In general, the fairlead force from cable one is considerably lower than that from cable two regardless of the water wave model, linear or non-linear. However, the fairlead forces rise sharply in each case as the SFOWT encounters non-linear waves in both cables. In addition, Fig.2.40(b,d)

shows that the mean fairlead forces of cable two are slightly higher for the case of non-linear waves than those for the corresponding linear waves.

Surge and heave responses of the spar and cable fairlead forces are significantly impacted when the SFOWT is subjected to non-linear large-amplitude waves. Pitch and yaw motions are affected, too but to a smaller extent. The findings in this thesis have significant implications. Based on the linear wave parameters, one can initially design a model to avoid the natural frequencies of the SFOWT structures. At the same time, it requires thoughtful consideration as the SFOWT is subjected to non-linear waves. The results highlight that a more cautious approach is needed for choosing the wave height and corresponding wave period. Note that this has not been discussed so far in the literature.

2.7.2 SFOWT response to different non-linear waves on the bifurcation diagram

The previous section shows a slight change in the wave period, leading to a significant difference in the wave amplitude and thus the wave kinematics. However, this is not the only scenario to be considered for the non-linear waves. Depending on the given wave period and the water depth, the numerical model can provide a set of waves having a similar wavelength but various wave amplitudes. In this section, the numerical model generates a set of waves in Fig.2.4. Compared to the given sea state, the numerical bifurcation can generate a significant wave amplitude that dramatically impacts the SFOWT structure. Note that being on the curve this wave is physically realizable. The following parts describe the large amplitude wave impact compared to the base sea state given in [10].

Table.2.6 shows the large-amplitude wave properties and the linear counterpart. It is clearly seen that the wave height generated by the large amplitude non-linear wave theory are much larger than that of the linear waves. Therefore, the following studies are conducted to investigate the influence of the large amplitude waves on the response of the SFOWT structure.

Table 2.6: Sea state definitions.

Sea state	Linear wave height (m)	Linear wave period (s)	Large amplitude wave height (m)	Non-linear wave period (s)	Wavenumber (κ)	Wave speed
3	1.40	6.5	5.50	6.27	0.095282	10.5081
5	3.66	9.7	9.25	9.51	0.042785	15.4382
8	15.24	17.0	43.6	16.24	0.01394284	27.766

On the bifurcation diagram, a small change in the period leads to a significant difference in the wave amplitude. The wave kinematics were investigated in the previous section showing that the linear waves possess smaller wave kinematics near the free surface than its non-linear counterpart. Due to these changes near the free surface where the SFOWT platform is located, the non-linear waves are expected to affect the SFOWT more considerably than the linear waves.

Fig.2.41 and 2.42 reveal the flow velocity and acceleration history of a spar segment near the free surface. The spar's position accelerates in time, and thus its velocity and also acceleration that are interpolated from the fluid domain vary accordingly. In all cases, the interpolated results from non-linear waves are larger than that from the linear waves. The peak values from non-linear waves are generally double that obtained from the linear results, while the excitation load period remains unchanged from the small wave to larger waves. The results have identical trend for all three cases so that the SFOWT responses consequently are affected significantly.

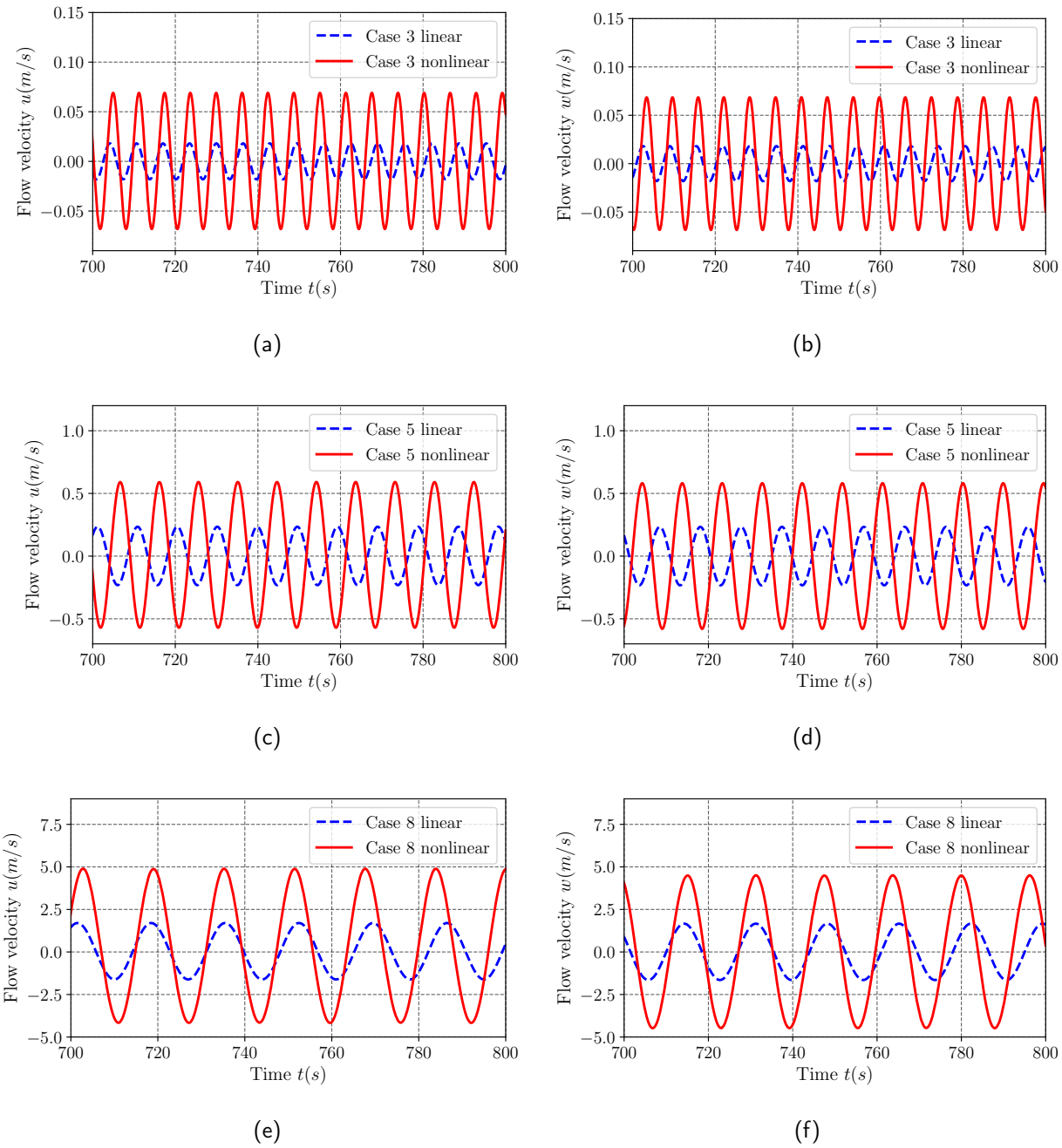

Figure 2.41: Flow velocity time history of 5^{th} segment: (a,b) Case 3; (c,d) Case 5; (e,f) Case 8.

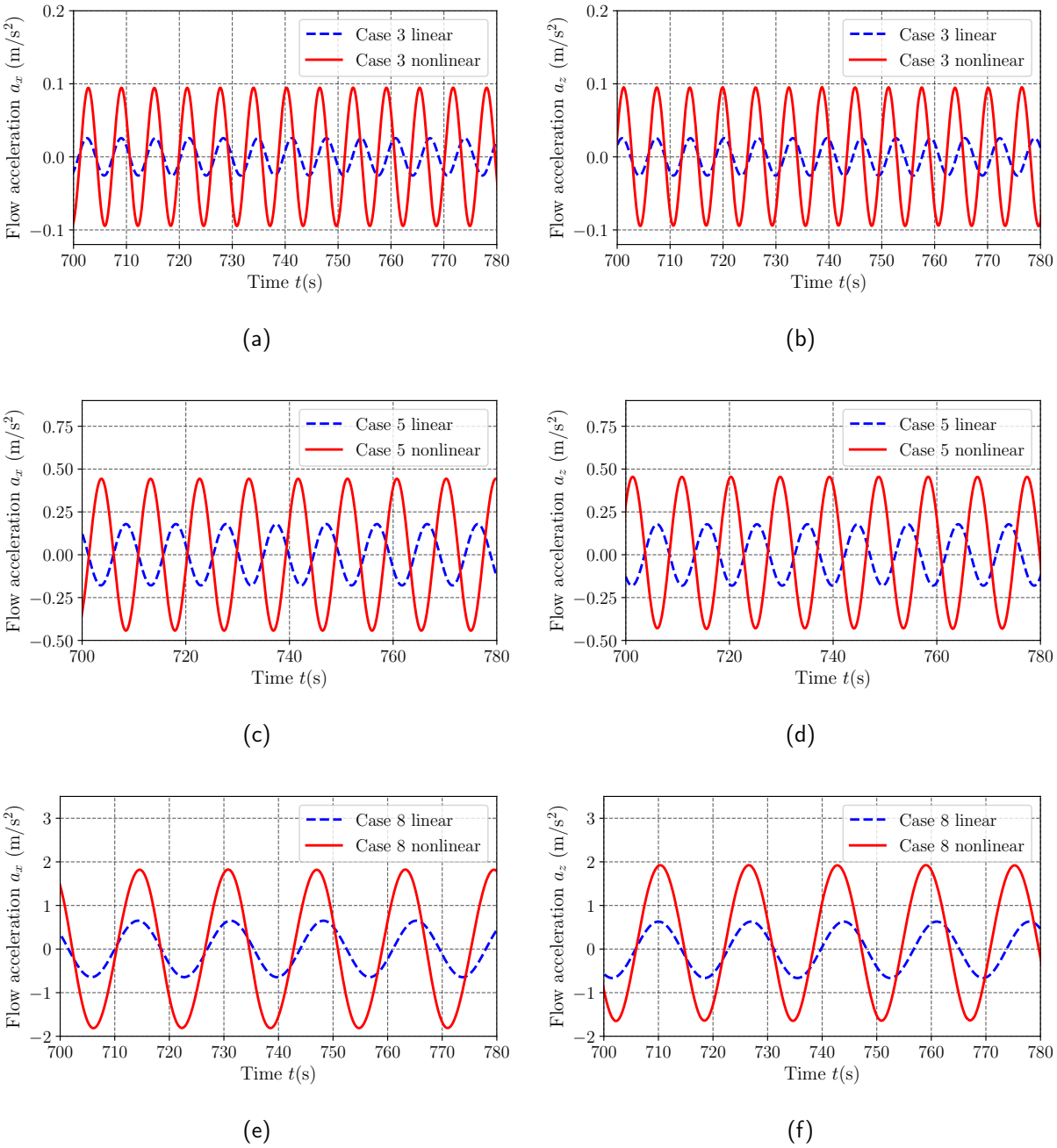

Figure 2.42: Flow acceleration time history of 4^{th} segment: (a,b) Case 3; (c,d) Case 5; (e,f) Case 8.

In general, the use of wave theory doesn't have any impact on the relative blades responses, even with the significant wave height, shown in Fig.2.43, Fig.2.45, and Fig.2.47. However, the absolute response are indeed affected. The wave models also strongly influence the other responses, especially in the horizontal and vertical direction, i.e. surge and heave motion. The other SFOWT motions respond in various ways to the wave models. Firstly, the tower illustrates an interesting phenomenon. With increasing wave amplitude, the relative tower response shows a decreasing trend. Fig.2.43(d),

Fig.2.45(d), and Fig.2.47(d) are the tower responses in three cases. It is noteworthy that the reduction is small; however, the accumulated displacement on the top of the tower will receive tremendous benefit from that reduction in terms of base moment. However, again the absolute response if of concern due to the platform motion.

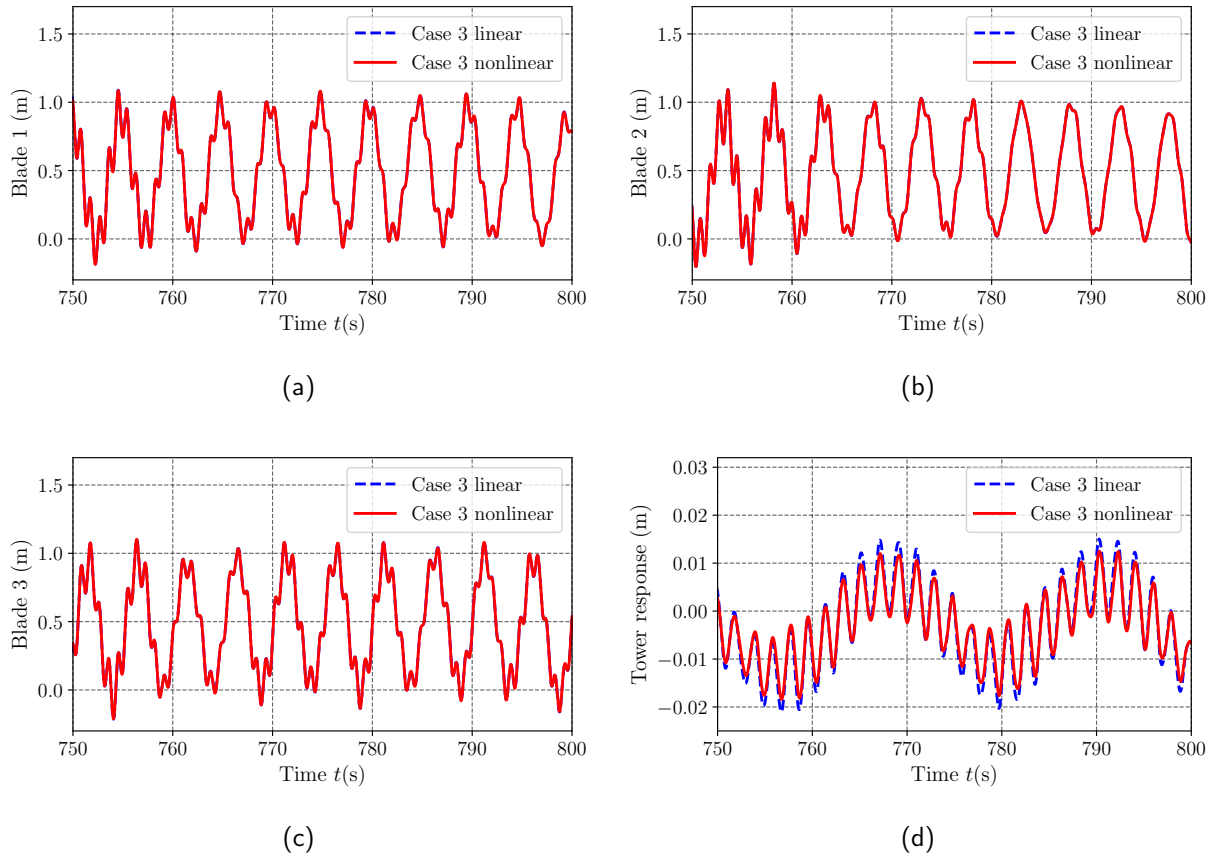

Figure 2.43: SFOWT blade and tower responses in case 3.

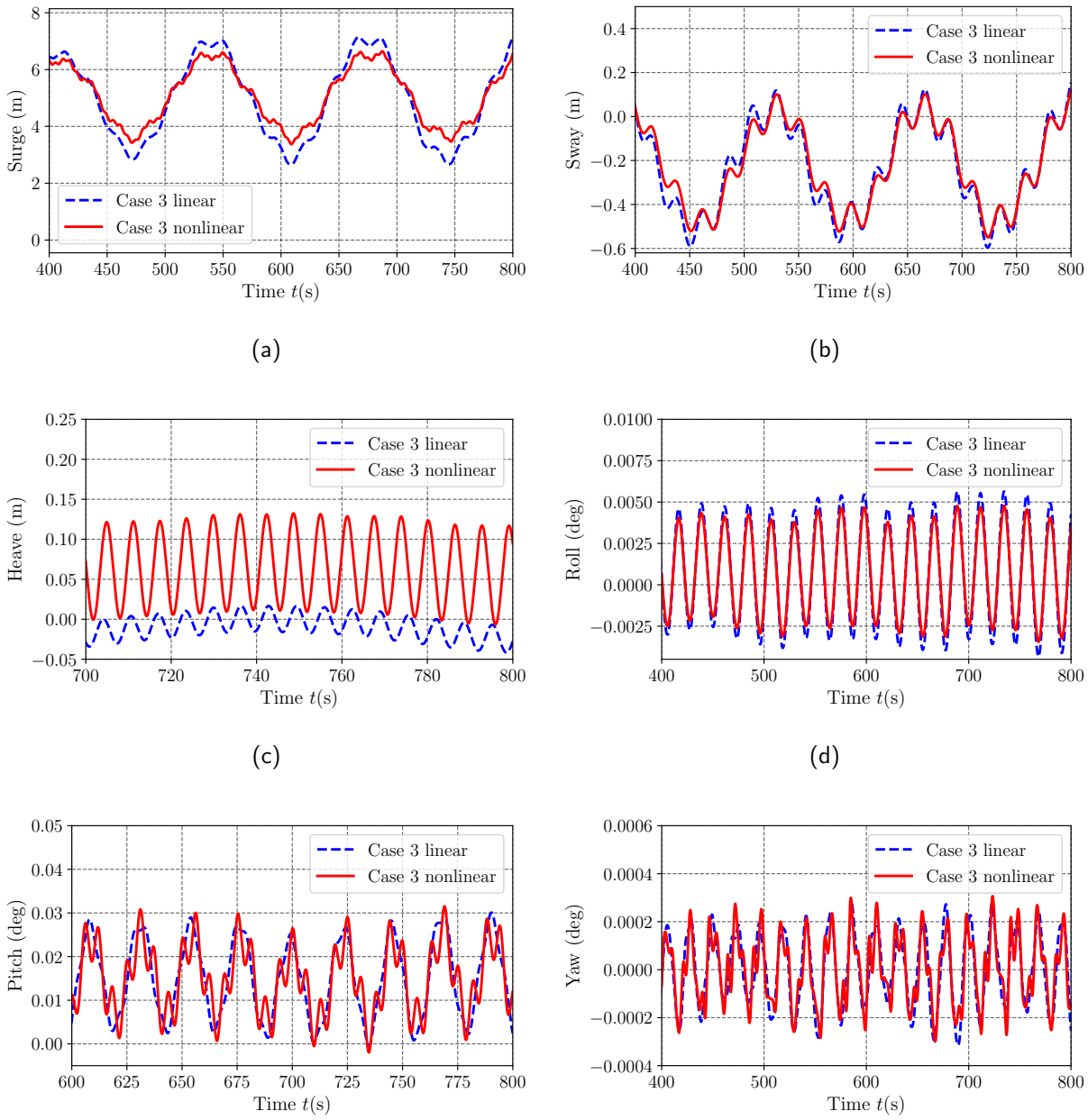

Figure 2.44: SFOWT spar responses in case 3.

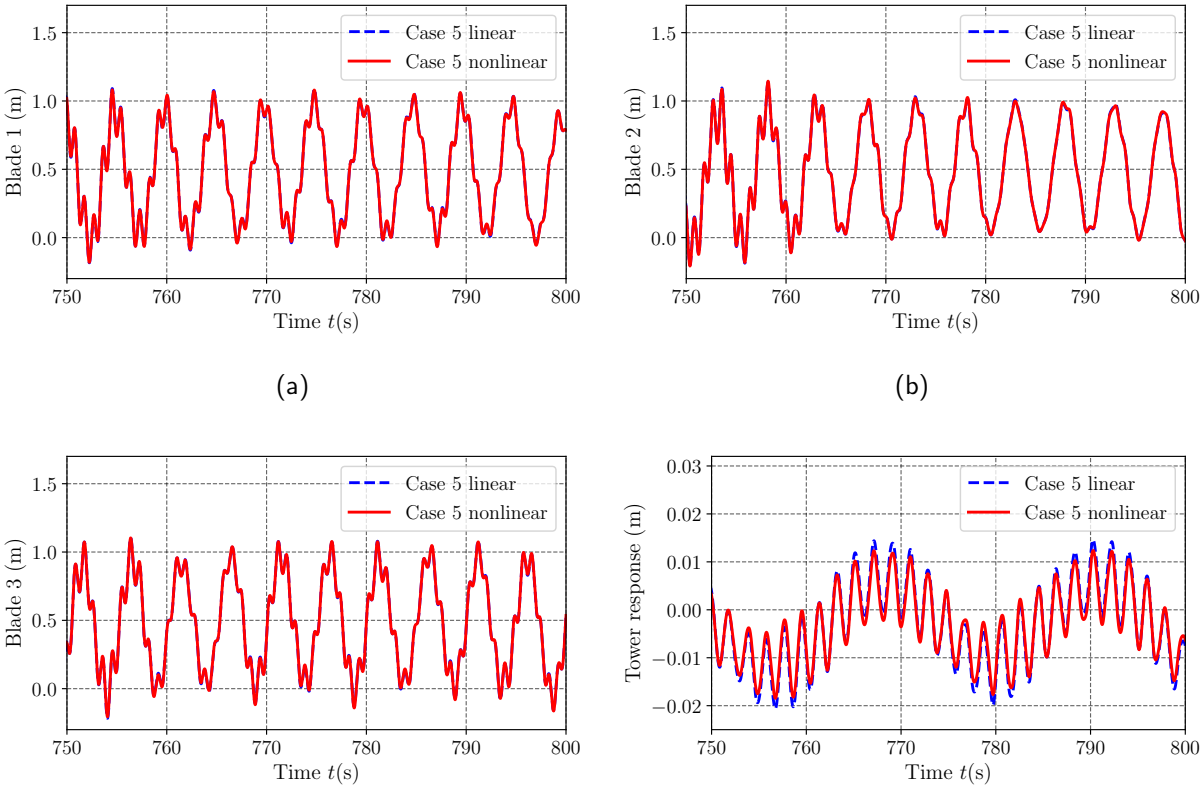

Figure 2.45: SFOWT blade and tower responses in case 5.

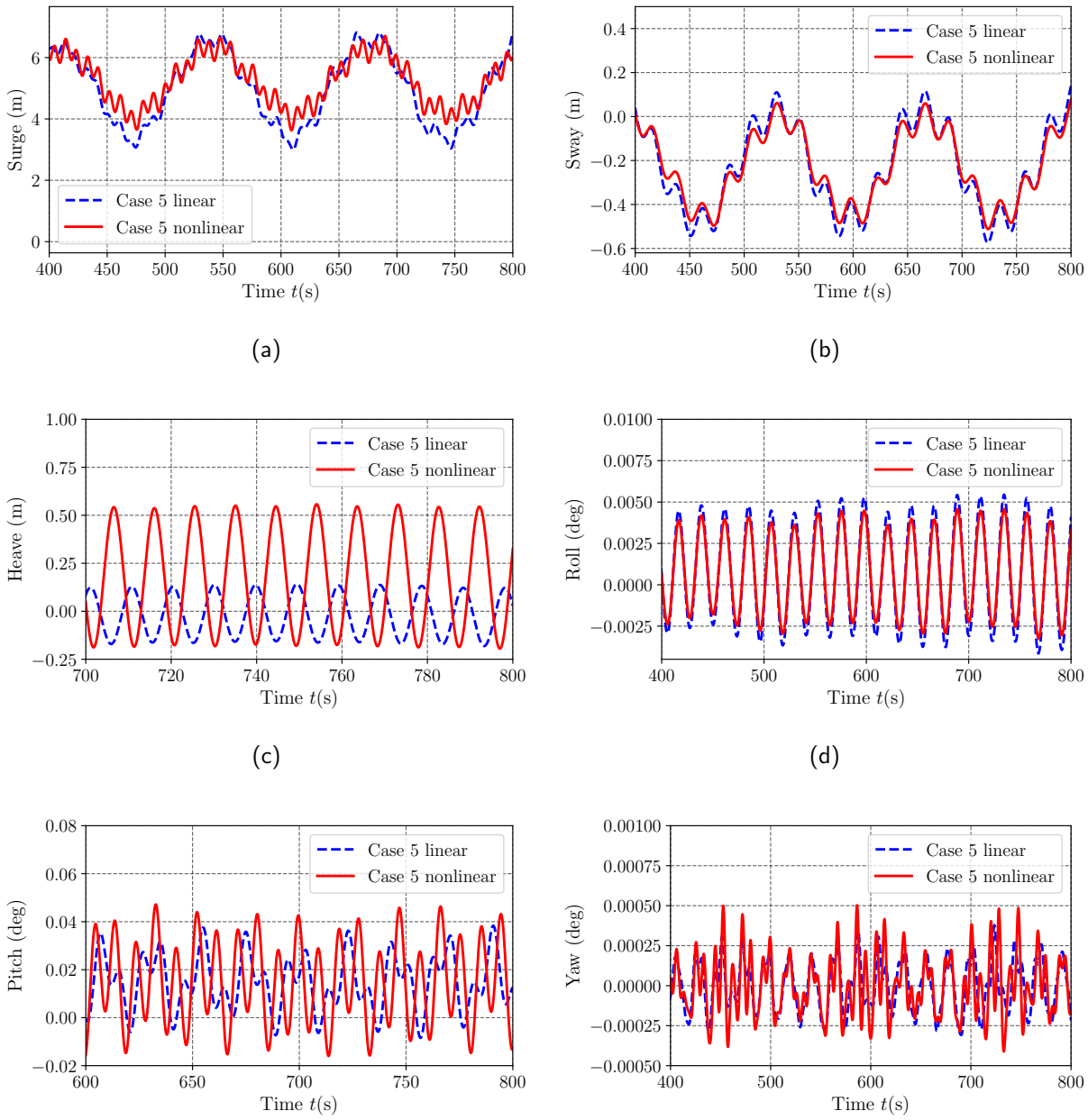

Figure 2.46: SFOWT spar responses in case 5.

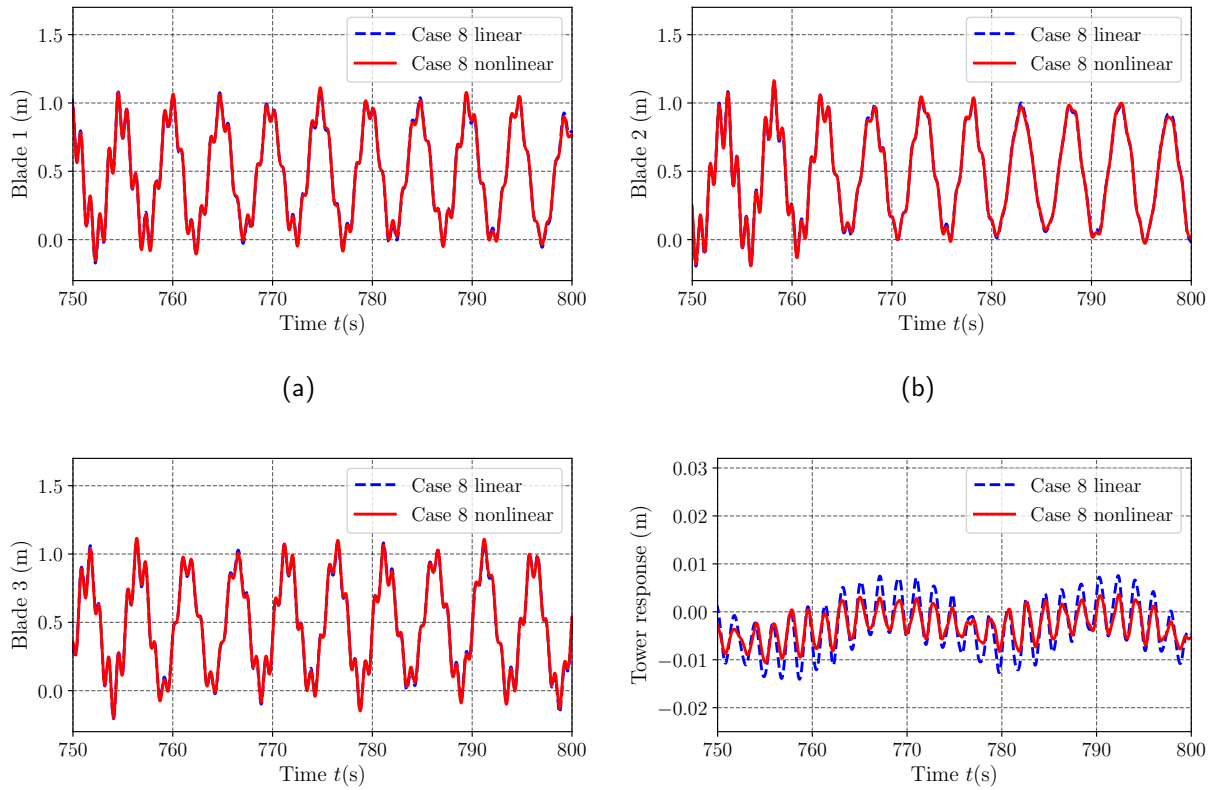

Figure 2.47: SFOWT blades and tower responses in case 8.

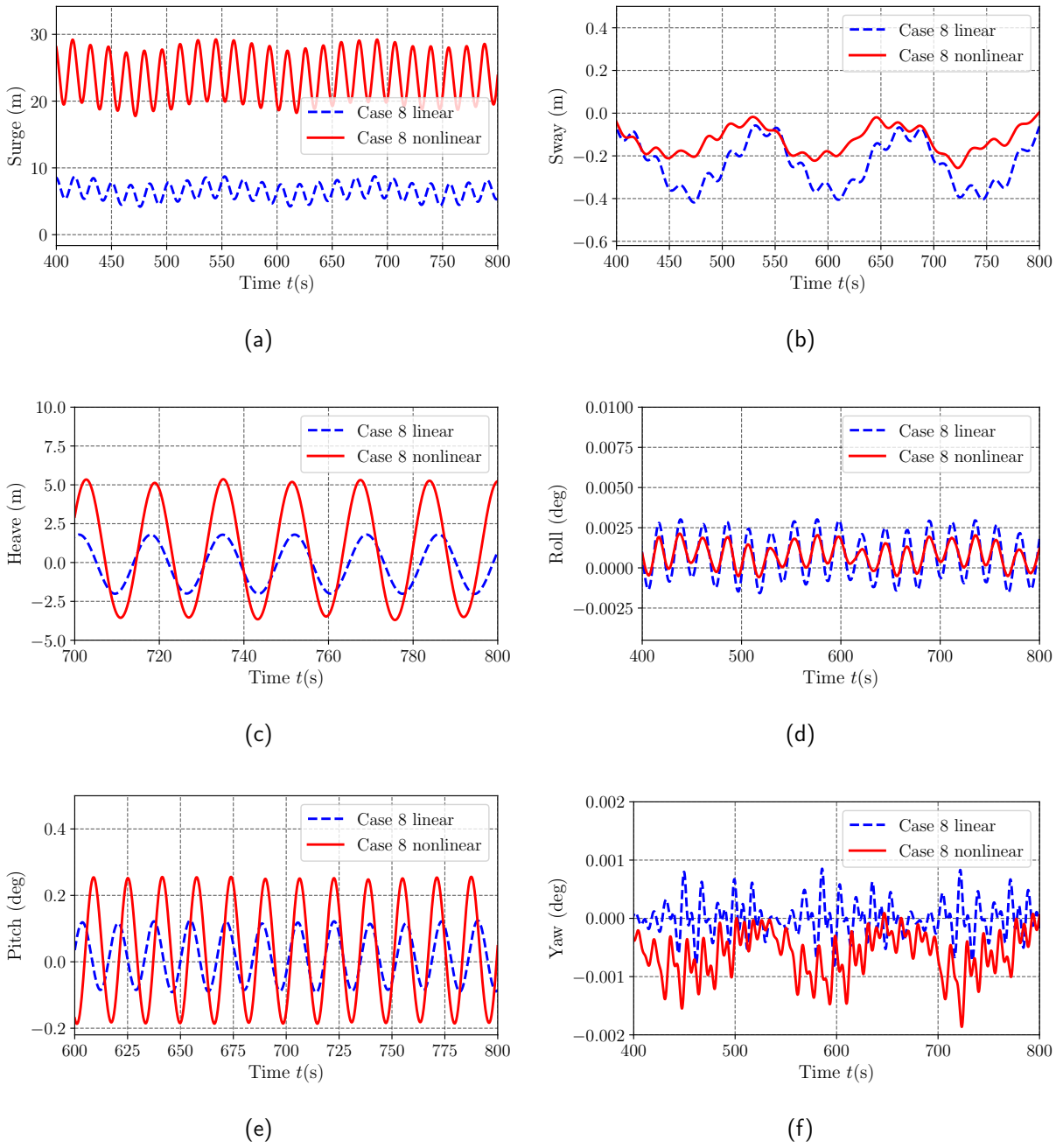

Figure 2.48: SFOWT spar responses in case 8.

Turning our attention now to the surge motion, the SFOWT response depends particularly on the wave amplitude, shown in Fig.2.44(a), Fig.2.46(a), and Fig.2.48(a). In case three and five, the SFOWT surge amplitude is generally smaller than in case eight. In addition, the SFOWT surge response is dominated by the structure period in the first two cases while the wave period influences the surge motion as the wave is more extreme, i.e. case eight in this study. Moreover, both the mean value and the amplitude of surge motion of case eight are considerably larger than that from the linear wave results. The findings illustrate the impact of the large-amplitude waves in terms of the

extreme waves and describe the damping effect of the wave if the wave amplitude is small or moderate.

Fig.2.44(c), Fig.2.46(c), and Fig.2.48(c) highlight the significance of the SFOWT vertical displacement. The vertical displacement captures the difference between the two wave theories from the small to extreme waves. The large amplitude wave affects the motion of the spar strongly, notwithstanding the wave amplitude. For instance, the large-amplitude waves in case three impacts the mean value and the amplitude of the heave motion; the motion is larger than that from the linear wave. Similar trends are observed in cases five and eight, where the large-amplitude wave creates a larger heave motion.

Other responses, such as pitch and yaw, also receive the large-amplitude wave impact but are less noticed than the surge and heave motions, except for case eight. A possible reason is that these responses being out of the incoming wave plane. On the other hand, the pitch motion in case eight is notably affected by a large-amplitude wave, shown in Fig.2.48(e). Similarly, the yaw motion in small and moderate waves increases by a small amount as the SFOWT reacts to the large-amplitude waves. In terms of the extreme large-amplitude wave, the non-linear wave generates a considerable negative yaw displacement. Still, the absolute value of the amplitude is almost double response to the linear wave.

Another point to note is the damping effect of the large amplitude wave in roll and sway responses, seen in Fig.2.44(b,d), Fig.2.46(b,d), and Fig.2.48(b,d). Compared to the roll motion due to the linear waves, that due to the non-linear waves are generally smaller in all cases, particularly in case eight, whose roll amplitude is half of the roll amplitude due to the linear waves.

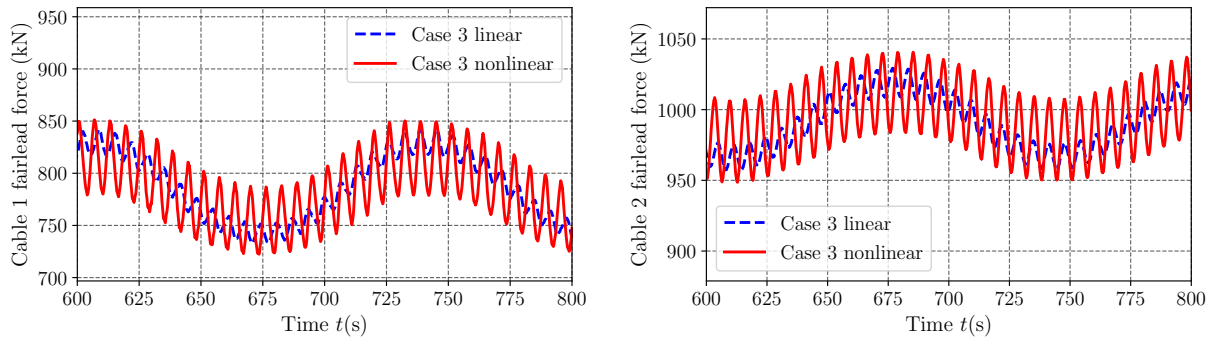

(a) (b)

Figure 2.49: Cables fairlead force in case 3.

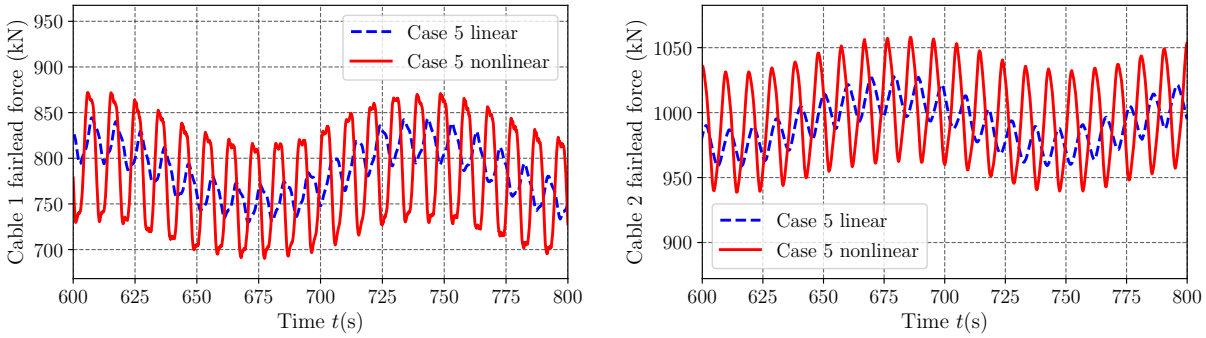

(a) (b)

Figure 2.50: Cables fairlead force in case 5.

Cable forces in case 3 and case 5 are illustrated in Fig.2.49 and Fig.2.50. In both cases, the impacts of large-amplitude waves are obvious when the cable forces due to large-amplitude waves are larger than the forces due to linear waves in both cable one and cable two. However, an interesting phenomenon is found in cable forces of case 8 where the cable one's force due to linear wave is larger than that of the large-amplitude wave. This is actually due to the fact that the spar is pushed further downstream (see Fig.2.48(a)). Consequently, cable one has less tension since the spar is dragged closer to the anchor of cable 1. Moreover, cable two's fairlead force increases significantly as the large-amplitude is used—the mean value of the fairlead force of cable two increases from 1000 kN to 1400 kN. Due to the spar's surge increase, the fairlead force of cable two and cable three are significantly impacted.

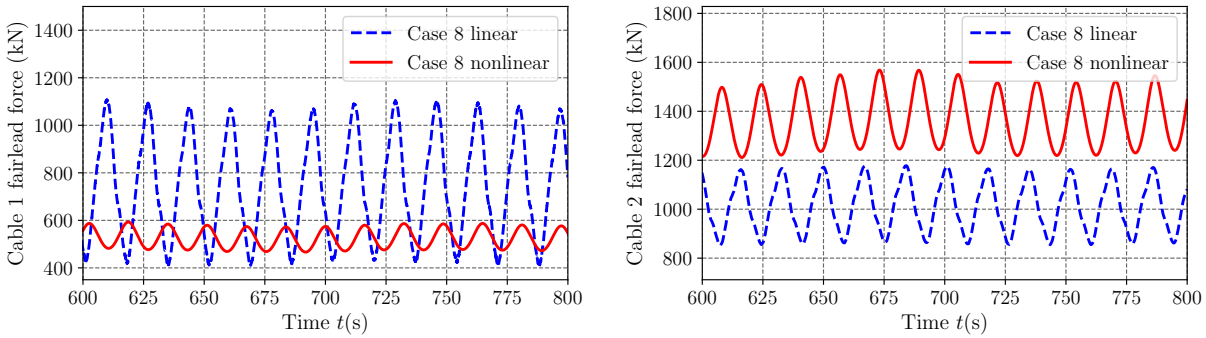

(a) (b)

Figure 2.51: Cables fairlead force in case 8.

3 Large amplitude waves-uniform current effect on FOWTs

3.1 Introduction

Chapter 2 focused on deriving the coupled FOWT model and proposed a formulation for computing the dynamic responses of FOWT under large-amplitude non-linear waves. This chapter aims to investigate the impact of large-amplitude wave-uniform current on the FOWT. The coupled FOWT model derived in Chapter 2 is used for this purpose. In order to do this, flow kinematics are first computed with wave-current interaction. Different current directions (favourable and adverse) with the same current strength are implemented and examined here.

3.2 Linear wave-current interaction

Interactions of regular linear wave and current are analytically modelled by Thomas [140] and numerically studied by Silva [163]. As a small amplitude wave propagates over an existing current, the resulting horizontal velocity field is represented by summarizing the wave field and the current strength as

$$u_T(x,z,t) = U(z) + u(z)cos(\kappa x - \omega t), \tag{3.1}$$

while the vertical velocity and the total pressure are represented by the wave components

$$w_T(x,z,t) = w(z)sin(\kappa x - \omega t), \tag{3.2}$$

$$p_T(x,z,t) = -\rho g z + p(z)cos(\kappa x - \omega t), \tag{3.3}$$

where, ρ is the density of seawater, g is the gravitational acceleration. κ and ω are the wave number and the angular frequency, respectively. Here, the angular frequency is different from the angular frequency of the linear wave only, which considers the current effect.

The free surface elevation of the linear wave theory is written as

$$\eta(x,t) = Acos(\kappa x - \omega t) \tag{3.4}$$

where A is the wave amplitude.

Using Rayleigh equation of classical inviscid stability theory [140], the vertical velocity, $w(z)$, is governed by

$$\frac{d^2w}{dz^2} - \left(\kappa^2 - \frac{\kappa}{\omega - \kappa U}\frac{d^2U}{dz^2}\right) w = 0 \tag{3.5}$$

from $-h_W < z < 0$. The boundary conditions are given by

$$w(z) = 0 \text{ on } z = -h_w, \tag{3.6}$$

$$\begin{cases} (\omega - \kappa U)^2 \frac{dw}{dz} + \kappa(\omega - \kappa U) w \frac{dU}{dz} - g\kappa^2 w = 0, \\ w(z) = A(\omega - \kappa U) \end{cases} \quad \text{on } z = 0. \tag{3.7}$$

The horizontal component is withdrawn from the solution of the vertical component [140] from

$$u(z) = \frac{1}{\kappa}\frac{dw}{dz}. \tag{3.8}$$

The system of equation (3.5, 3.6, 3.7) is solved with the assumption that $d^2U(z)/dz^2 = 0$. From [163], the solutions are

$$u_T(x,z,t) = U(z) + A(\omega - \kappa U_0)\frac{cosh[\kappa(z+h_w)]}{sinh(\kappa h_w)} cos(\kappa x - \omega t), \tag{3.9}$$

$$w_T(x,z,t) = A(\omega - \kappa U_0)\frac{sinh[\kappa(z+h_w)]}{sinh(\kappa h_w)} sin(\kappa x - \omega t), \tag{3.10}$$

$$p_T(x,z,t) = -\rho g z + \frac{\rho A(\omega - \kappa U_0)}{\kappa sinh(\kappa h_w)}\left([\omega - \kappa U(z)]cosh[\kappa(z+h_w)] + \frac{dU(z)}{dz} sinh[\kappa(z+h_w)]\right) cos(\kappa x - \omega t), \tag{3.11}$$

where, U_0 is the current velocity at $z = 0$. The modified dispersion relation because of the current effect is

$$(\omega - \kappa U_0)^2 = \left(g\kappa - (\omega - \kappa U_0)\frac{dU(z)}{dz}\right) tanh(\kappa h_w), \tag{3.12}$$

It is worth to note that the modified dispersion relation can be used for both uniform

and shear currents. As the uniform current is in use, the dispersion is simplified as

$$(\omega - \kappa U)^2 = g\kappa tanh(\kappa h_w) \tag{3.13}$$

with $U = U_0$ denoting the constant current strength. As the current varies along the water depth, the general solution can be found in [140].

3.3 Non-linear wave-current interaction

In the preceding section, the current effects on the linear waves are discussed, the flow kinematics are determined using the modified dispersion relation. As the non-linear wave is used, the wave profile is non-linear, and the flow kinematics are also changed accordingly. Hence, the formulations used for the linear waves are not applicable for the non-linear waves.

A recent study of Basu [121, 124] on the existence of two-dimensional irrotational large-amplitude waves with uniform current investigated three possible relations between strength of the current (k) and the velocity of the propagating waves (c). The average current strength k could be larger, equal, or smaller than c. For each possibility, the structures of the flow, the pressure fields, and surface profile of the free boundary were investigated [175].

3.3.1 Governing equations

A smooth solution to Euler governing equations is sought for the free surface η, the flow field (u, w), and the pressure P have period L in X variable; η depends on $X - cT$ while P depends on $X - cT$ and Z in which a period $L > 0$, a wave speed c, and a current strength K. There are several assumptions that u and w have one crest and one trough in period L; η is strictly monotonic between crests and troughs; η, u, and P are symmetric about crest line; w is asymmetric about the crest line. All functions are smooth, the free surface has to be a graph and a profile must be symmetric [124].

The governing equations in moving frame $x = X - cT, z = Z$ are given as follows

$$(u-c)u_x + wu_z = -\frac{1}{\rho}P_x, \qquad \text{for} \quad -d \le z \le \eta(x), \tag{3.14a}$$

$$(u-c)w_x + ww_z = -\frac{1}{\rho}P_z - g, \qquad \text{for} \quad -d \le z \le \eta(x), \tag{3.14b}$$

$$u_x + w_z = 0, \qquad \text{for} \quad -d \le z \le \eta(x), \tag{3.14c}$$

$$u_z = w_x, \qquad \text{for} \quad -d \le z \le \eta(x), \tag{3.14d}$$

$$w = 0, \qquad \text{on} \qquad Z = -d, \tag{3.14e}$$

$$w = (u-c)\eta_x, \qquad \text{on} \qquad z = \eta(x), \tag{3.14f}$$

$$P = P_{atm}, \qquad \text{on} \qquad z = \eta(x), \tag{3.14g}$$

There are flow invariants in setting of the governing equations explained as follows

- Mass flux is invariant with x

$$M = \rho \int_{-d}^{\eta(x)} [u(x,z) - c]dz. \tag{3.15}$$

- The energy is constant throughout the fluid (Bernoulli's law)

$$\varepsilon = \rho\frac{(u-c)^2 + w^2}{2} + P + \rho g(z+d). \tag{3.16}$$

- The flow force per unit width is invariant with x as

$$S = \rho \int_{-d}^{\eta(x)} [u(x,z) - c]^2 dz + \int_{-d}^{\eta(x)} [P(x,z) - P_{atm}]dz. \tag{3.17}$$

A stream function $\Psi(x,z)$ used to reduce the number of variables is defined as

$$\Psi_x = -w, \qquad \Psi_z = u - c. \tag{3.18}$$

One obtains the transformed equations as follows

$$\Psi_{xx} + \Psi_{zz} = 0, \qquad \text{for} \quad -d \le z \le \eta(x), \tag{3.19a}$$

$$\Psi = 0, \qquad \text{on} \qquad z = \eta(x), \tag{3.19b}$$

$$\Psi = -M/\rho, \qquad \text{on} \qquad Z = -d, \tag{3.19c}$$

$$\Psi_{xx}^2 + \Psi_{zz}^2 + 2g(z+d) = 2gH, \qquad \text{on} \qquad z = \eta(x), \tag{3.19d}$$

where, H is a physical constant called head. $\eta(x)$ and $\Psi(x,z)$ which are both L-periodic

and symmetric in the x-variable are the two functions to be determined.

The pressure can be estimated from

$$P = P_{atm} + \rho g H - \rho g(z+d) - \rho \frac{\Psi_x^2 + \Psi_z^2}{2}. \tag{3.20}$$

The strength of the uniform current can be recovered by $u(x,-d)$ as follows

$$k = \frac{1}{L}\int_0^L u(x,-d)dx, \tag{3.21}$$

which is invariant with z [124]. The current speed can also recovered using the stream function

$$k = c + \frac{1}{L}\int_0^L \Psi(x,-d)dx. \tag{3.22}$$

3.3.2 Relations of the wave speed and the underlying current strength

Three cases arise depending on the relative speed of the surface waves and the average strength (speed) of the underlying current as:

- $k > c$: a qualitative study of the flow velocity, pressure, and free surface profile was investigated by Basu [121]. The flow field is different from the flow field with no underlying current [122, 250]. However, the pressure field is not affected by the underlying current. Moreover, Basu [124] proved the existence of the large-amplitude water waves propagating on the surface of an irrotational flow with underlying uniform current.

- $k = c$: denoting $k - c = \bar{c}$, we have

$$\bar{c} = \frac{1}{L}\int_0^L \Psi_z(x,-d)dx. \tag{3.23}$$

We have Ψ harmonic thus Ψ_z is harmonic and $\Psi_z = 0$ on some point on the flat bed $z = -d$ [175].

The mass flux relating to the uniform current of constant speed c [175]

$$M = \rho \int_{-d}^{\eta(x)} \Psi_z(x,z)dz \tag{3.24}$$

With all M, $(M > 0, M < 0, M = 0)$, $\Psi_z \equiv 0$ throughout Ω [121]. It leads to $u = c$ and $w = 0$. A uniform current with the same wave speed equal to the current speed

has eliminated any hydrodynamic structure [175]. The maximum pressure is at the bed $z = -d$ and the minimum at the surface $z = \eta(x)$.

- $k < c$: since $k - c = \bar{c} < 0$, we have

$$0 = \bar{c} + \frac{1}{L}\int_0^L \Psi_z(x, -d)dx. \tag{3.25}$$

This is a flow with wave speed $\bar{c}$ without current $k = 0$ [121]. This is similar to the Stokes wave flow without current. With the change of variable $\Psi_x = -w, \Psi_z = u - \bar{c}$, the strength of the current becomes Eq.3.21 as follows

$$k = \int_0^L u(x, -d)dx = 0. \tag{3.26}$$

The current strength is zero meaning that the waves enter a still water region [2]. The fluid properties proved in case of $k = c$ still hold in this case. The results for the case without current is previously studied in [2, 92].

In this thesis, the current velocity is chosen to be smaller than the propagating speed of the surface waves ($k < c$) [121, 124]. The flow kinematics, which describe the large-amplitude waves and the uniform current interaction, are determined straightforwardly as follows

$$u_T(x, z, t) = u_{non}(x, z, t) + U(z) \tag{3.27}$$

$$w_T(x, z, t) = w_{non}(x, z, t) \tag{3.28}$$

$$p_T(x, z, t) = p_{non}(x, z, t) \tag{3.29}$$

$$\dot{u}_T(x, z, t) = \dot{u}_{non}(x, z, t) \tag{3.30}$$

$$\dot{w}_T(x, z, t) = \dot{w}_{non}(x, z, t) \tag{3.31}$$

where, $U(z)$ is the current strength distributed along the depth of the water. The subscript $_{non}$ refers to the non-linear waves, i.e. u_{non} is the horizontal velocity component of the flow under the non-linear waves. In the following section, the non-linear waves-current interaction is presented by the flow kinematics shown in the Eq.3.27 to Eq.3.31.

Fig.3.1 and Fig.3.2 reveal the velocity profiles of the large-amplitude wave-uniform current flow. Due to the effect of the current, the velocity increase as the wave follows the current and vice versa. Nevertheless, the current does not have influence on the vertical velocity since the current is uniformly distributed in this study. Therefore, there is no change in the vertical velocity of the flow.

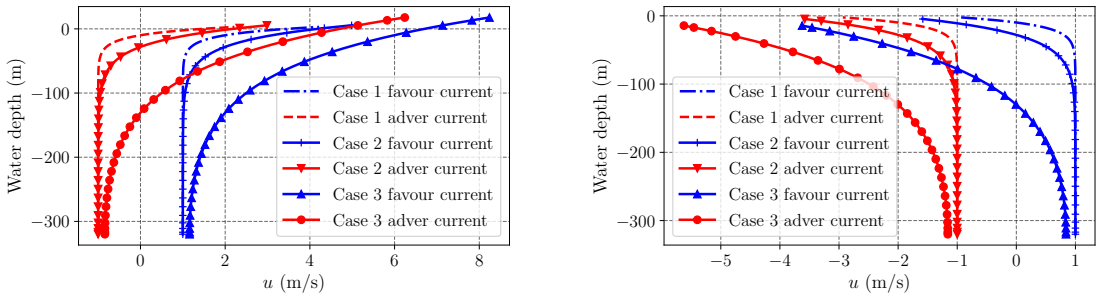

(a) (b)

Figure 3.1: Horizontal velocity under wave crest (a) and under wave trough (b).

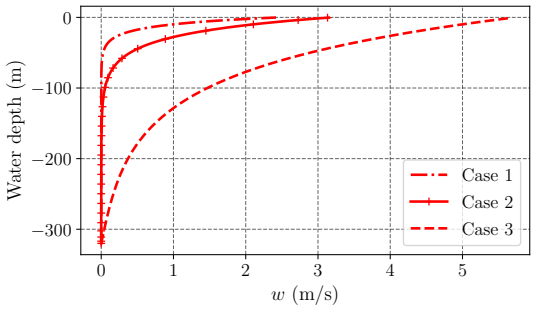

Figure 3.2: Vertical velocity under node.

3.4 Numerical model setup

Since the waves coming in the y-direction are expected to induce large edge-wise motions of the blades, they are of particular interest. It is practically feasible to have waves and winds acting in perpendicular directions as they have different propagation speed and hence different arrival times [251]. However, we only consider the current in the same direction with propagating waves herein to highlight the impact of non-linear large-amplitude wave-current interactions on the FOWT. The chosen current strength based on the paper of Azcona [157] is 1.0 m/s. Table 3.1 illustrates the wave and current properties used in the following non-linear model.

Table 3.1: Wave and current properties.

Case	Wave height (m)	Wave period (s)	Wave number (κ)	Wave speed (m/s)	U (m/s)	Direction
1a	5.32	6.5	0.089	10.76	1.0	Favourable
1b	5.32	6.5	0.089	10.76	1.0	Adverse
1c	5.32	6.5	0.089	10.76	0.0	
2a	10.17	9.7	0.041	15.82	1.0	Favourable
2b	10.17	9.7	0.041	15.82	1.0	Adverse
2c	10.17	9.7	0.041	15.82	0.0	
3a	32.06	17.0	0.013	27.76	1.0	Favourable
3b	32.06	17.0	0.013	27.76	1.0	Adverse
3c	32.06	17.0	0.013	27.76	0.0	

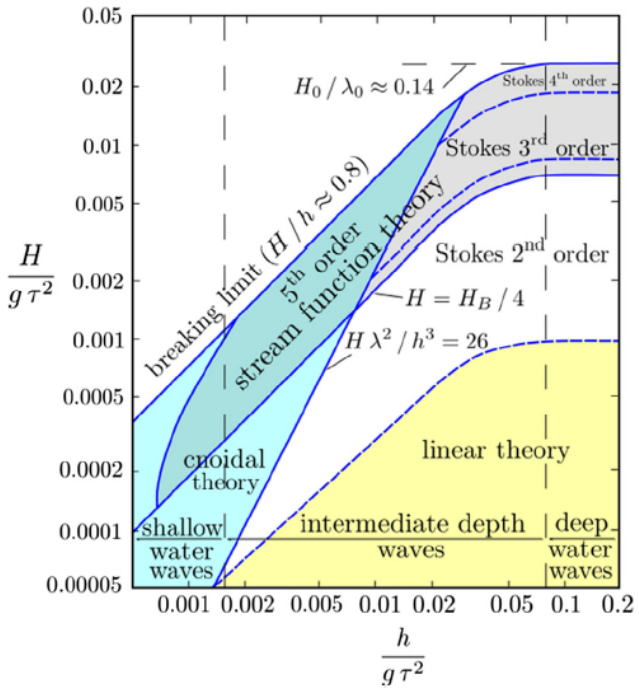

Figure 3.3: Applicability of wave theory [3].

Fig.3.3 shows wave theory applicability [3] illustrating linear wave theory limitation at $H/g\tau^2 = 0.001$ (τ is the wave period in [3]). Therefore, the corresponding linear wave height of the non-linear wave period 6.5 s, 9.7 s, and 17.0 s in Table.3.1 are 0.4145 m, 0.9230 m, and 2.8351 m, respectively. The marked differences of the wave height between the large-amplitude wave theory and the linear wave theory might contribute significantly to the wave-current-structure interaction. Since linear wave theory cannot generate waves of the same wave height as compared to the large-amplitude waves

(shown in Table.3.1), the linear wave-current impact on FOWT will not be investigated and the large-amplitude wave-current impacts on FOWT will be discussed in the following sections. However, for the purpose of comparison we consider a case where the results from the two theories are computed with moderately high wave as the linear and non-linear theories are expected to produce similar results for this case. Reader might refer [31] for investigation of linear waves-current impacts on FOWT.

3.5 Dynamic responses of FOWT

The analysis method proposed in this thesis may give some insight about the relationship between uniform distributed current and the large-amplitude waves. As shown in Table 3.1, both the case of current in favourable and in adverse directions with respect to the wave direction is considered. In this study, we only consider the wave propagating in the x-direction so that the currents are in line with the incoming waves and cable one.

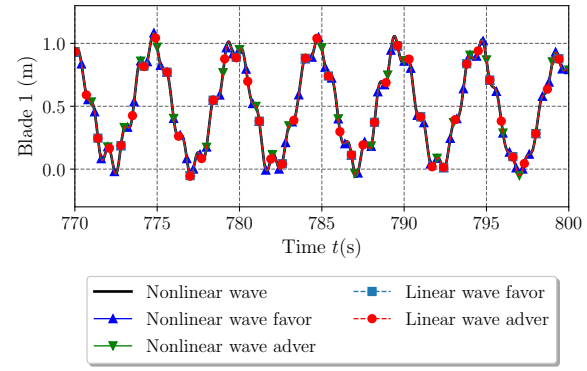

(a) Case 1a, 1b, 1c

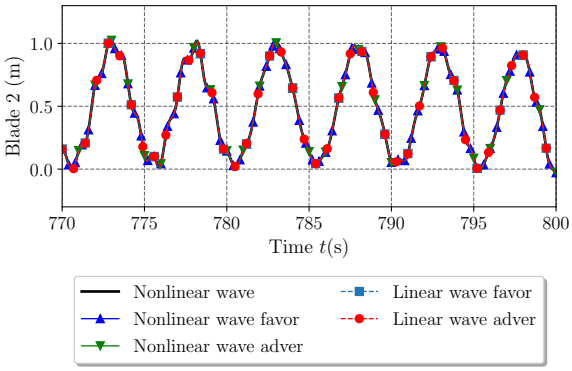

(b) Case 1a, 1b, 1c

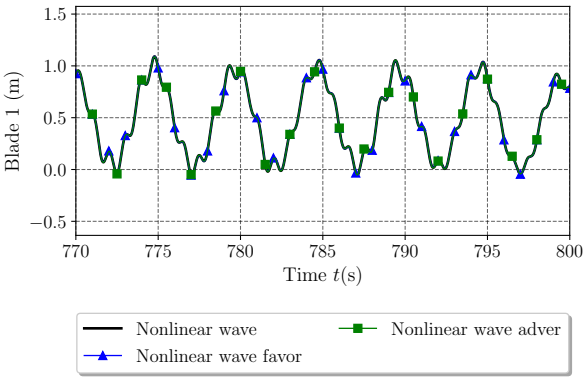

(c) Case 2a, 2b, 2c

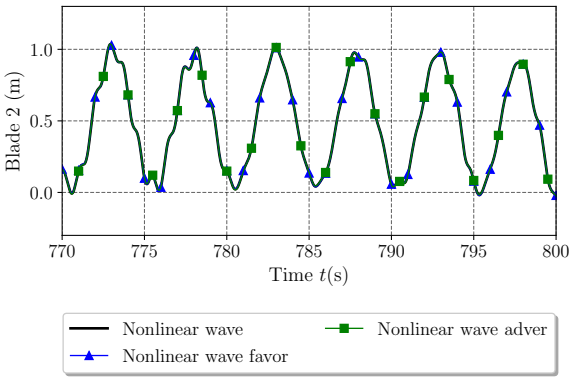

(d) Case 2a, 2b, 2c

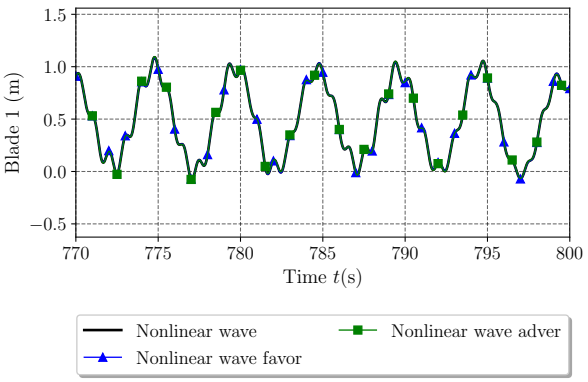

(e) Case 3a, 3b, 3c

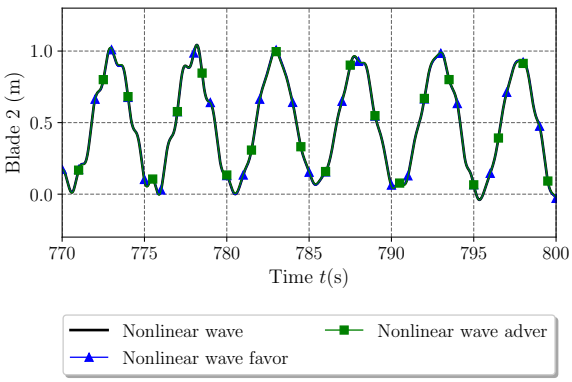

(f) Case 3a, 3b, 3c

Figure 3.4: Blade one (left) and blade two (right) displacement in nine cases.

The existence of current in the fluid flow generally has the hydrodynamic effect that drives the motion of the spar and submerged components of the FOWTs. In this study, the current's direction is in *xz*-plane as the incoming wind direction; and, the current generates a limited effect on the wind turbine blades as the excitation is filtered out and

not exciting the blades and also limited effect on the sway motion whose directions are out of the plane. The edge-wise blades responses are illustrated in Fig.3.4 and Fig.3.5. It is clearly seen that the current has a negligible effect on the blade responses regardless of the wave theories.

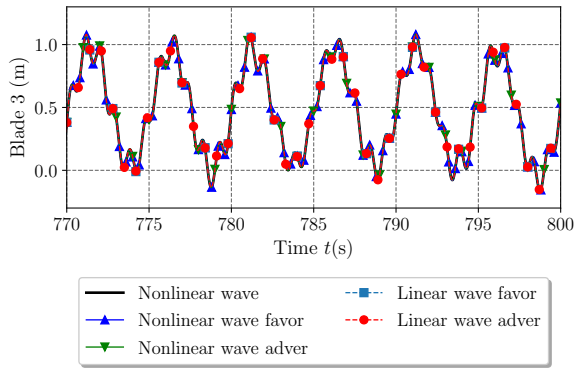

(a) Case 1a, 1b, 1c

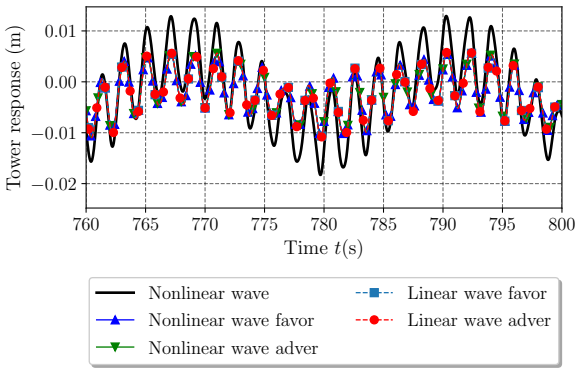

(b) Case 1a, 1b, 1c

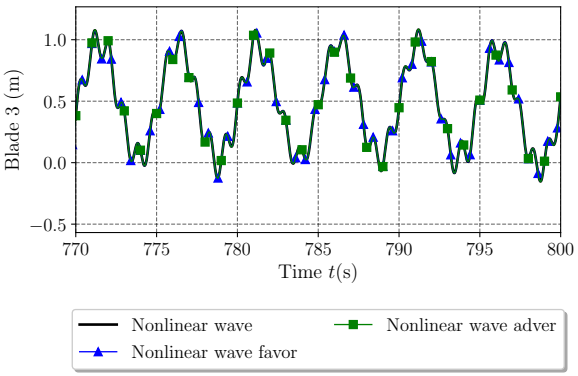

(c) Case 2a, 2b, 2c

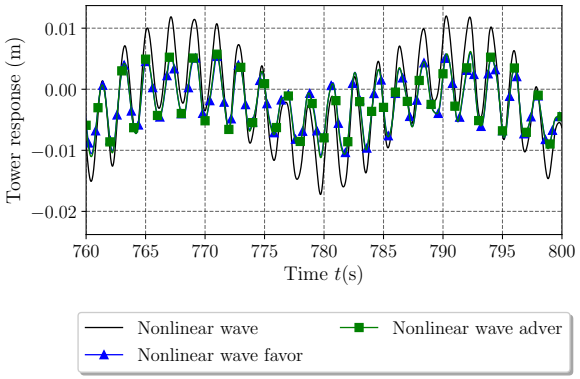

(d) Case 2a, 2b, 2c

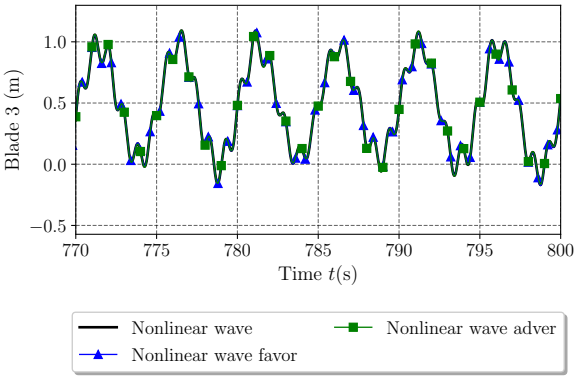

(e) Case 3a, 3b, 3c

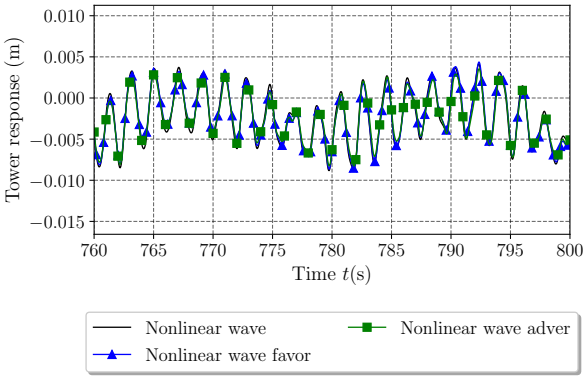

(f) Case 3a, 3b, 3c

Figure 3.5: Blade three (left) and tower response (right) displacement in nine cases.

Fig.3.5(b,d,f) presents the comparison of the tower side-to-side displacement for the nine cases. Due to the combined effect of wave and underlying current, in case 1(a,b) and case 2(a,b), the tower responses are identical regardless the direction of the current. In addition, the FOWT responses are seem to be strongly damped by the existence of the current. The reduction of the amplitude of these motions might result from the non-linear drag effects on the mooring and the spar by surrounding fluid. In contrast, the current has negligible impact on FOWT's responses in case 3(a,b), where the waves possess extreme amplitudes and thus dominate the tower responses, as seen in Fig.3.5(f).

When the current is present, the equilibrium position of the platform alters, moving downstream or upstream with respect to the incoming wave. This leads to unbalanced forces onto the platform at the beginning of the simulations. Then, the transient response dampens out entirely as the structure reaches a horizontal equilibrium position. As such, the current affects the static responses and the dynamic responses of the floating body. The current impacts the fairlead force, mooring positions, spar responses, and particularly the surge motion and FOWT's equilibrium position. Because the mooring has a more negligible effect on drag, the platform position is strongly dependent on the current, In addition, the platform's position is crucial for wind farm layout; hence the impact of current is vital.

Fig.3.6(a,c,e) reveals that the current has a major impact on the floater's surge motion in all cases. When the current exists, it affects the equilibrium position of the surge motion of the spar, while it has a negligible impact on the amplitude of the motion. In Fig.3.6(a,c,e), waves with favourable current induce more significant horizontal displacement of spar than the waves with no current. In contrast, the adverse current encounters incoming waves and thus reduces the horizontal displacement of the spar. The most likely cause of the above changes is from the effect of the current on the flow kinematics, especially the horizontal velocity components, that drives the hydrodynamics of the system.

Fig.3.7(a,c,e) shows the evidence of the effect of large amplitude waves and the combination of large-amplitude waves with the current on the FOWT's vertical responses. The wave only cases and waves with adverse current cases generate similar heave response. In contrast, with favourable current, FOWT's heave response is higher due to the effect of the large-amplitude waves. In such cases, the large-amplitude waves' effect is pronounced in comparison with the linear waves. Although the current effect is less noticed as the wave amplitude becomes more severe in cases two and three, the amplitude of the motion is significantly larger than smaller waves, about 1,5 m to 2 m depending on the wave amplitudes. This exciting phenomenon might have resulted from the modification of the free surface by the large-amplitude waves surrounding the spar. Fig.3.7(b,d,f) presents the spar's roll motion for three cases. In small and moderate sea

states, the direction of current has negligible effect on the spar's roll motion, seen in Fig.3.7(b,d), while the current dampens the FOWT responses heavily compared to the cases with wave only. However, the current effect disappears in extreme wave condition where the wave motion dominates spar's roll displacement, shown in Fig.3.7(f).

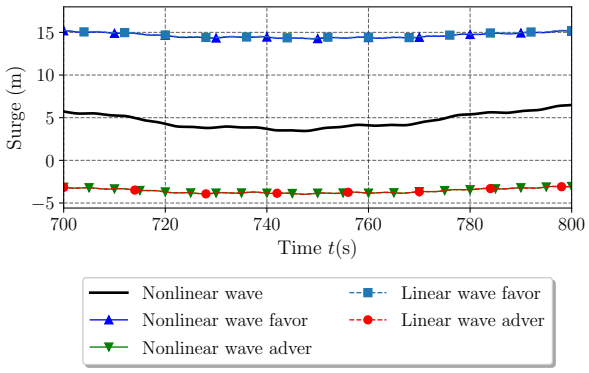

(a) Case 1a, 1b, 1c

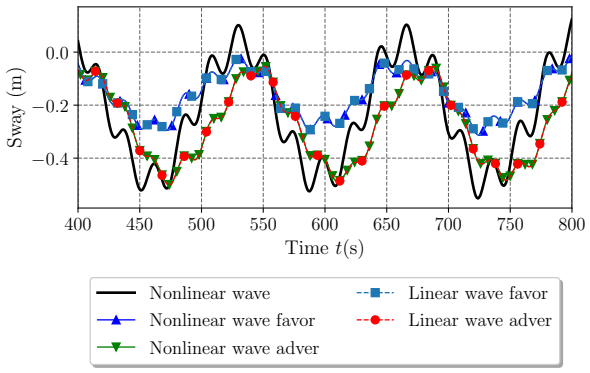

(b) Case 1a, 1b, 1c

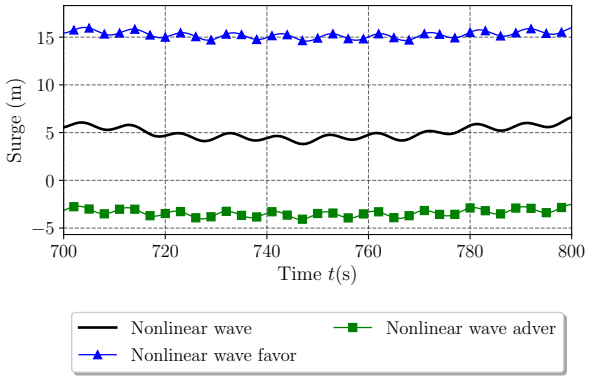

(c) Case 2a, 2b, 2c

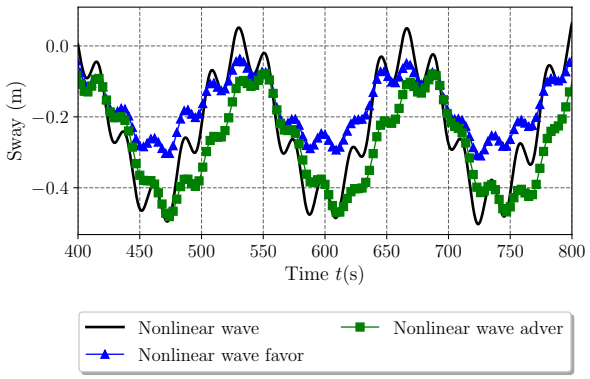

(d) Case 2a, 2b, 2c

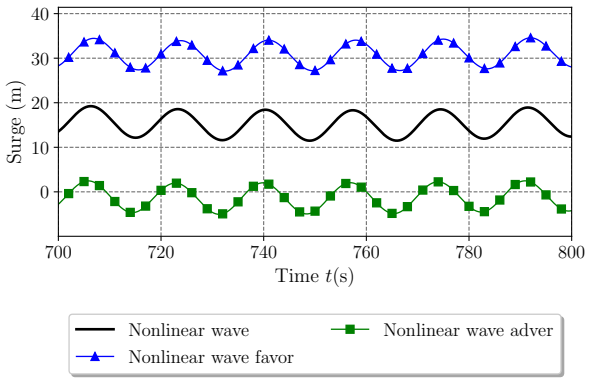

(e) Case 3a, 3b, 3c

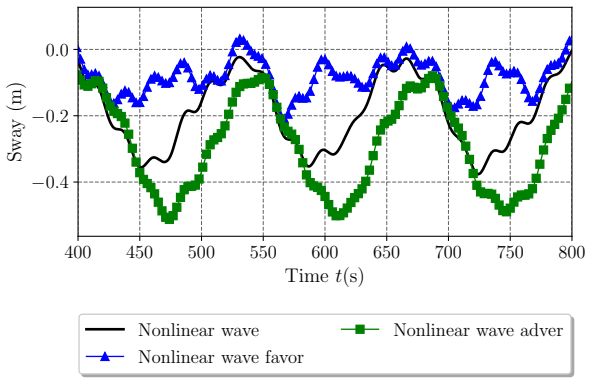

(f) Case 3a, 3b, 3c

Figure 3.6: Spar surge (left) and sway (right) response in three cases.

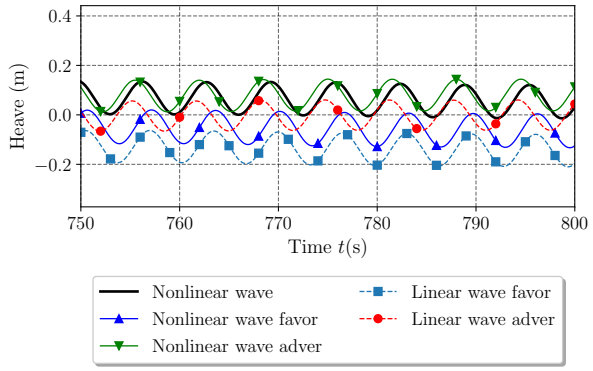

(a) Case 1a, 1b, 1c

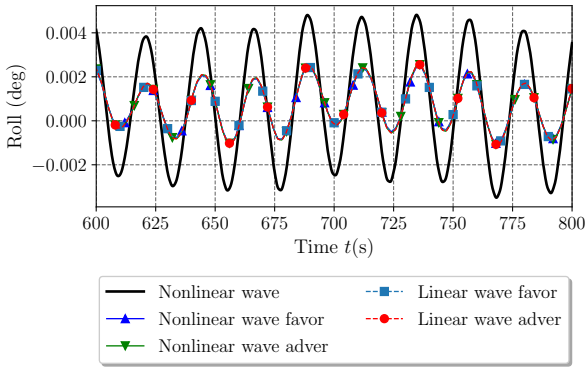

(b) Case 1a, 1b, 1c

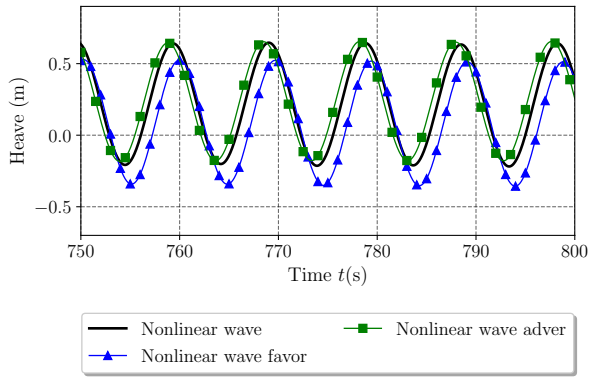

(c) Case 2a, 2b, 2c

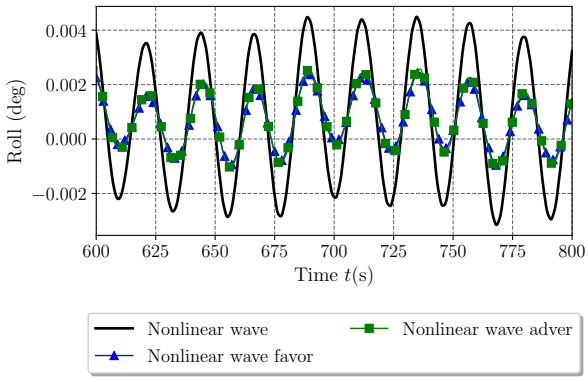

(d) Case 2a, 2b, 2c

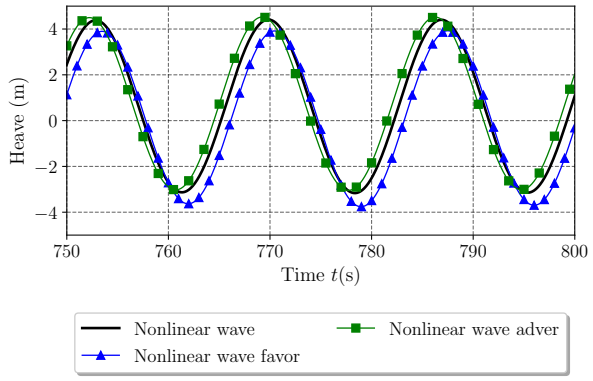

(e) Case 3a, 3b, 3c

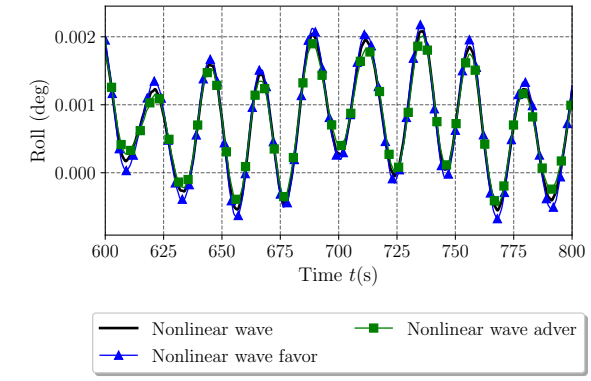

(f) Case 3a, 3b, 3c

Figure 3.7: Spar heave (left) and roll (right) response in three cases.

The pitch and yaw motion of the FOWTs are almost identical in all the nine cases, seen in Fig.3.8.

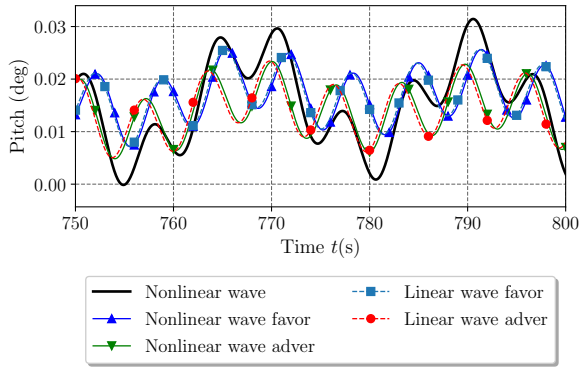

(a) Case 1a, 1b, 1c

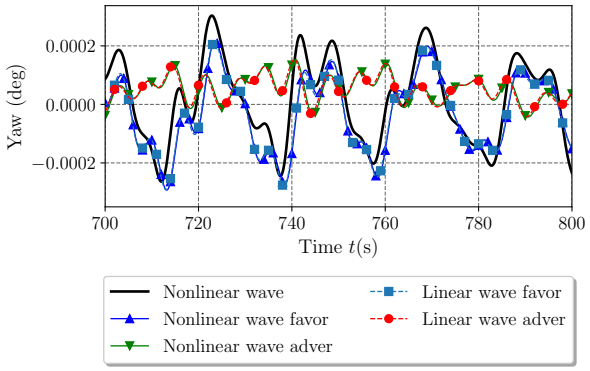

(b) Case 1a, 1b, 1c

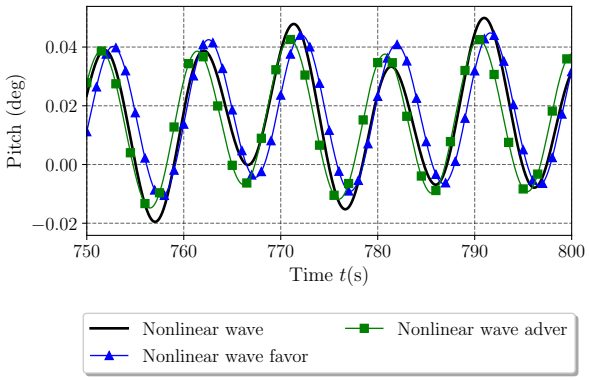

(c) Case 2a, 2b, 2c

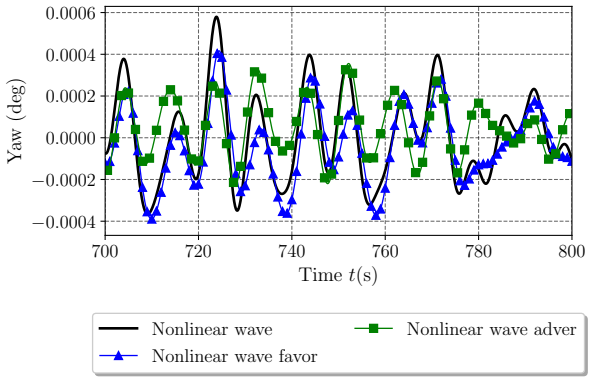

(d) Case 2a, 2b, 2c

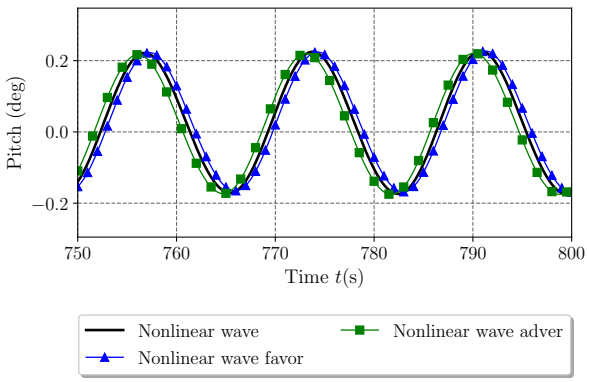

(e) Case 3a, 3b, 3c

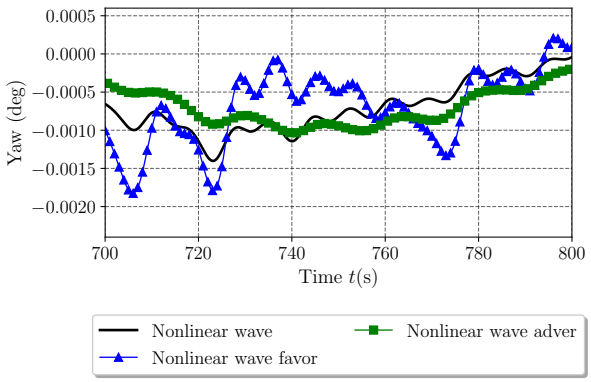

(f) Case 3a, 3b, 3c

Figure 3.8: Spar pitch (left) and yaw (right) response in nine cases.

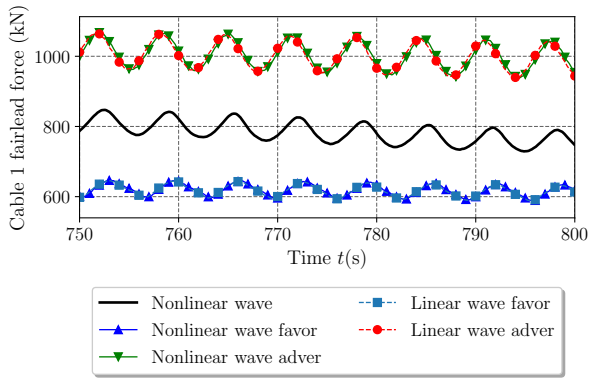

(a) Case 1a, 1b, 1c

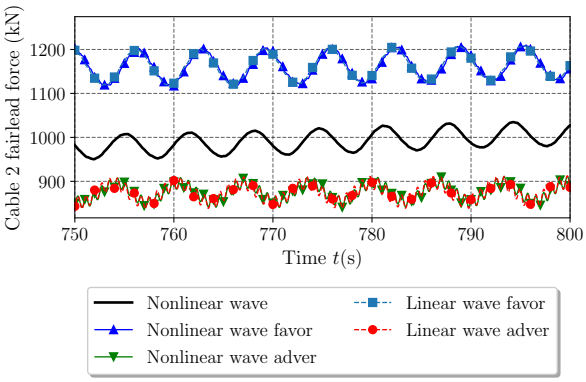

(b) Case 1a, 1b, 1c

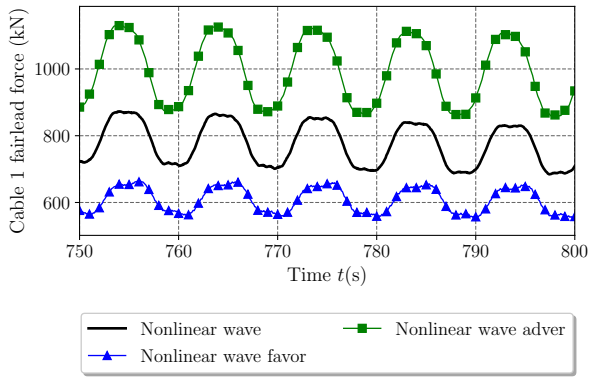

(c) Case 2a, 2b, 2c

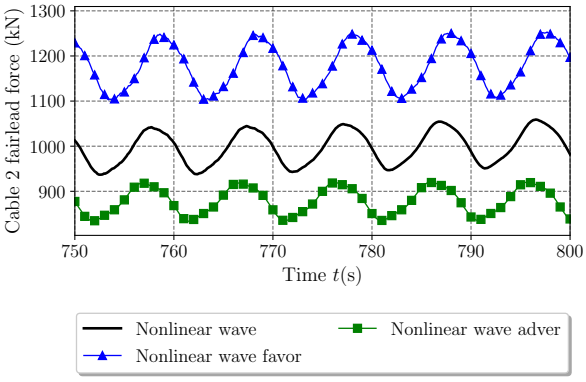

(d) Case 2a, 2b, 2c

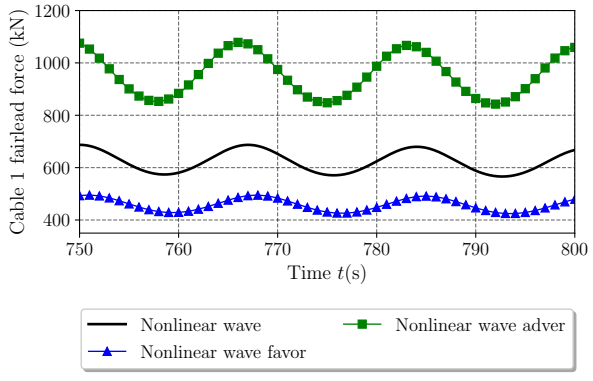

(e) Case 3a, 3b, 3c

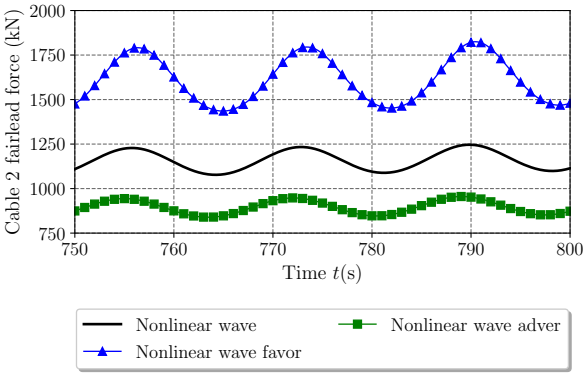

(f) Case 3a, 3b, 3c

Figure 3.9: Cable fairlead force in cable 1 (left) and cable 2 (right) in nine cases.

The cable fairlead forces are shown in Fig.3.9 to investigate the effect of large-amplitude waves further and the additional influence induced by the current. Recall that cable one is in line with $x-$direction where the current is approaching the floater, and cable two and cable three are 120° apart from cable one upstream. Even though the period response

of the FOWT remains unchanged, there is a significant increase in the amplitude of the cable forces. The fairlead force of cable one is generally smaller than that of cable two and cable three. The presence of current in the flow generates larger cable forces than the case with wave only. It is also clearly seen that the large-amplitude waves and the current create higher fairlead forces compared with the linear waves and the current depending on the positions of the cable and the current direction.

In Fig.3.9, results show that the waves and the adverse current generate a more significant fairlead force on cable one than the waves with a favourable current in all cases. Due to the action of the current, the large-amplitude waves and interaction with the underlying current creates a significant impact on the cable forces, for instance the cable forces can increase by an amount of above 500 kN depending on the cases as seen in Fig.3.9. While the figures illustrate an increase in cable fairlead force due to effect of large-amplitude waves with adverse current, the large-amplitude waves and the favourable current create less cable fairlead forces. One possible reason for such results can be from the horizontal displacement of the FOWTs platform. The adverse current reduces the horizontal displacement of the spar, Fig.3.6(a,c,e); thus, cable has more tension, and cable force increases. The favourable current, in turn, pushes the spar downstream so that the FOWTs is close to the cable one's anchor leading to the reduction of the cable length and thus the cable force.

We turn our attention now to cable two whose fairlead force shows an opposite behaviour to cable one's force, see Fig.3.9(b,d,f). As the current is in the same direction as the incoming waves, cable forces are more significant than the cases with only waves, which illustrates that the current is a significant contributor to the increase of the cable fairlead force. In contrast, the adverse current encounters the surface waves and reduces the spar's horizontal displacement, reducing the cable fairlead forces. Through such analysis, when using combined current and large-amplitude waves for dynamic study of FOWTs, we can infer how the current has a significant impact on the horizontal response of the FOWT system and the mooring cables to ensure the accuracy of the analysis results.

4 Impact of solitary waves on FOWTs

4.1 Introduction

In the previous chapters the wind turbine has been assumed to be subjected to large-amplitude waves and wave-current interactions. The effect of solitary waves are usually investigated in near shore regions where their amplitudes increase dramatically due to its interaction with seabed. In deep water regions, solitary waves are usually neglected in the FOWT studies due to its small amplitude far shore. Nevertheless, solitary waves contain large energy and they are considered as the hump of water having considerable propagating speed compared to the surface waves. Large-amplitude solitary waves do exist for offshore and can propagate over long distances without dissipating. Therefore, the impulsive effects of solitary waves on the response of the wind turbine and on the mooring cables are investigated in this chapter.

4.2 Solitary waves kinematics using Finite Element Method

The analytical solutions of steady solitary waves have been provided in works of literature. Nevertheless, these analytical solutions donot account for the solitary wave-structure interaction and the modification of the free surface, waves kinematics due to the presence of the structure in the flow field. We aim to develop an approach that computes wave kinematics with an arbitrary given free surface profile. Therefore, we can investigate the impact of the wave-structure interaction on a structure.

This chapter uses our developed approach to analyse the fluid kinematics under a permanent solitary wave. First, the results are compared with the analytical solutions provided by the re-normalisation method [252] for validation. The numerical results are then applied to study the impact of permanent solitary waves on the FOWT.

4.2.1 Governing equations of permanent solitary waves

A cross-section of the two-dimensional flow in the direction of propagation of the wave is considered [228]. The Cartesian coordinates (X, Z) have the horizontal $X-$axis pointing in the wave's propagation direction, while the $Z-$axis points vertically upwards. The water depth as the flow is at rest by $d > 0$, so as the flatbed is given by $Z = -d$. The free surface is given by $Z = \eta(X - ct)$, where $c > 0$ denotes the constant speed of the travelling wave. The velocity field of the flow is denoted by $U(X - ct, Z) := (u(X - ct, Z), w(X - ct, Z))$. As such, we study a permanent wave with profile η, moving at constant speed c.

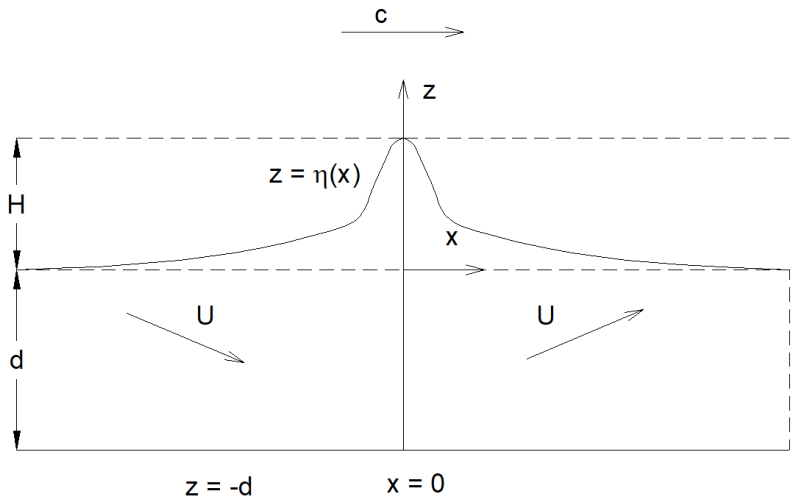

Figure 4.1: A permanent solitary wave propagating with constant speed c with velocity field denoted $U = (u, w)$.

The fluid is assumed to be homogeneous with constant density $\rho = 1$, the mass conservation states

$$u_X + w_Z = 0. \tag{4.1}$$

The water is assumed the inviscid fluid, the laminar viscosity and turbulence mixing are neglected, hence the Euler's equations are

$$\begin{cases} (u - c)u_X + wu_Z = -P_X \\ (u - c)w_X + ww_Z = -P_Z - g \end{cases} \tag{4.2}$$

in which $P(X - ct, Z)$ is the hydrodynamic pressure and g is the gravitational constant of acceleration.

At the free surface, two boundary conditions are applied

$$w = (u - c)\eta_X \text{ on } Z = \eta(X - ct), \tag{4.3}$$

$$P = P_{atm} \text{ on } Z = \eta(X - ct), \tag{4.4}$$

where P_{atm} is the constant atmospheric pressure. The kinematic boundary condition Eq.4.3 describes the motion of the surface particles that are always on the free surface. In addition, the dynamic boundary condition Eq.4.4 describes the impermeable surface between fluid and air domain, neglecting surface tension [253]. Since the flatbed is impermeable, one gets

$$w = 0 \text{ on } Z = -d. \tag{4.5}$$

The flow is assumed irrotational describing how the wave enters the still water region [253],

$$u_Z = w_X. \tag{4.6}$$

The governing equations for irrotational travelling waves are

$$\begin{cases} u_X + w_Z = 0 \\ (u - c)u_X + wu_Z = -P_X \\ (u - c)w_X + ww_Z = -P_Z - g \\ w = (u - c)\eta_X \text{ on } Z = \eta(X - ct), \\ P = P_{atm} \text{ on } Z = \eta(X - ct), \\ w = 0 \text{ on } Z = -d, \\ u_Z = w_X. \end{cases} \tag{4.7}$$

To select a solution for solitary waves, the flow is at rest at the far upstream and downstream; the free surface approaches $d > 0$ above the flatbed [254].

The parameters c and d are chosen following the relation

$$c > \sqrt{gd} \tag{4.8}$$

to ensure the existence of non-trivial solutions. The solitary waves possess a symmetrical profile about a single crest, with a strictly monotone profile on either side of this crest [255]. Moreover, the wave speed, c, is larger than the horizontal velocity, u, for smooth solitary wave [82]

$$u(X, Z) < c \text{ throughout the closed fluid domain,} \tag{4.9}$$

and the maximum slope of the free surface is 45° degrees [256, 257],

$$\eta_X^2(X) < 1 \text{ for all } X \in \mathcal{R}. \tag{4.10}$$

The inequality in Eq.4.10 expresses the motion of the solitary wave that is faster than the water particles [228].

4.2.2 Solitary waves kinematics

As the waves approach FOWTs, the stable free surface in Fig.4.1 is modified due to the wave-structure interaction. This leads to the modification of the entire wave kinematics which must be recomputed since the modified free surface has a new slope compared to the permanent shape shown in Fig.4.1.

On the free surface, the kinematic boundary condition gives the new vertical velocity component as follows

$$w = (u - c)\eta_X \tag{4.11}$$

where η_X is the slope of the free surface in x-direction resulting from the interaction of the wave and the structure. Note that the new slope is totally different from the slope of the free surface of the permanent solitary waves solution. In addition, we have the Bernoulli's equations

$$|\nabla\psi(x, \eta(x))|^2 + 2g\eta(x) = c^2, x \in \mathcal{R} \tag{4.12}$$

The stream function, ψ, is given as

$$\psi_x = -w; \quad \psi_z = u - c, \quad \psi(0, \eta(0)) = 0 \tag{4.13}$$

From Eq.4.11, Eq.4.12, and Eq.4.13 we can estimate the vertical velocity using the free surface profile ($\eta(x)$), the wave speed (c) as

$$\begin{aligned} |\nabla\psi(x, \eta(x))|^2 + 2g\eta(x) &= c^2 \\ (u - c)^2 + w^2 + 2g\eta(x) &= c^2 \\ w^2\left(1 + \frac{1}{\eta_X^2}\right) + 2g\eta(x) &= c^2 \\ w^2 &= \frac{c^2 - 2g\eta(x)}{1 + \frac{1}{\eta_X^2}} \\ w &= \sqrt{\frac{c^2 - 2g\eta(x)}{1 + \frac{1}{\eta_X^2}}} \end{aligned} \tag{4.14}$$

Hence, a new boundary value problem is shown in Fig.4.2

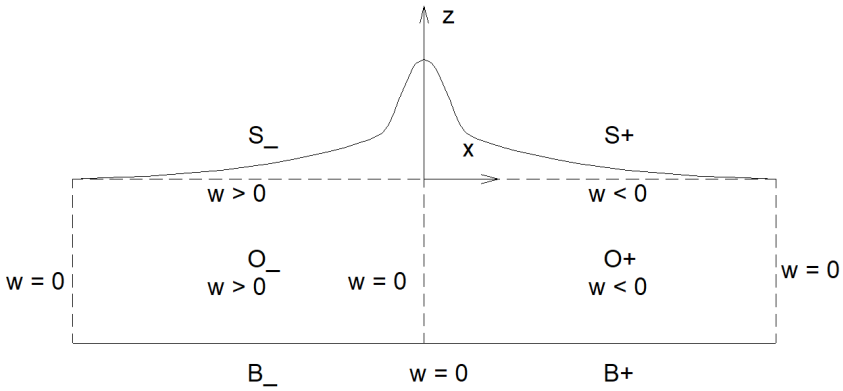

Figure 4.2: An arbitrary solitary wave propagating with constant speed c with velocity field denoted $U = (u, w)$.

with $c = \sqrt{gd}$, and $\eta(x)$ is exacted from the wave-structure interaction. It is worth noting that all the length parameters are scaled by water depth d, all related fluid parameters are calculated with the assumption that $g = d = \rho = 1$, where ρ is the fluid density, g is the gravitational acceleration, and d is the constant water depth. It means that all the lengths are scaled by d, acceleration by g, wave speed by $\sqrt{gd}$, and pressure by ρgd.

The fluid domain has a symmetry vertical velocity profile so that we only solve for a half of the domain. Fig.4.3 illustrates the boundary values problem of a half wave length with the modified wave height due to wave-structure interaction. The vertical velocity of bottom and two sides boundaries are zero, while that of the surface boundary is computed using Eq.4.14.

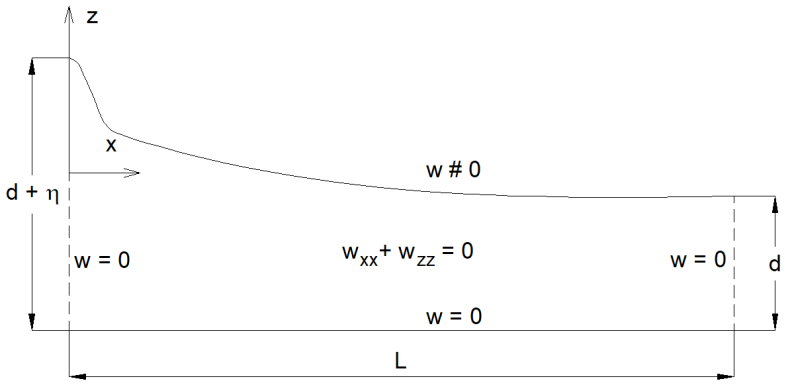

Figure 4.3: The boundary value problem.

Solving the Laplace equation of the vertical velocity, $w_{xx} + w_{zz} = 0$, one obtains the vertical velocity profile for the whole fluid domain under modified solitary wave. The boundary value problem is solved using the Finite Element Method (FEM) provided in Partial Differential Equation Toolbox in Matlab [239]. The Matlab code is provided in Appendix.A1.2.

4.2.3 Recovering the wave kinematics

Eq.4.7 is then used to compute the horizontal velocity and the pressure distribution in the fluid domain. The acceleration is computed by using the Euler equation with the assumption that the flow is steady; the temporal terms are neglected. Thus the following equations are used to estimate the fluid accelerations

$$\begin{aligned} a_x &= (u-c)u_x + wu_z \\ a_z &= (u-c)w_x + ww_z \end{aligned} \tag{4.15}$$

The total pressure, P, and the dynamic pressure, P_d, are computed respectively by using Bernoulli's equations

$$P = \frac{c^2}{2} + P_0 - \frac{(u-c)^2 + w^2}{2} - gz, \tag{4.16}$$

where P_0 is the pressure at free surface. The hydrodynamic pressure is calculated using the following formula

$$P_d = \frac{c^2}{2} + P_0 - \frac{(u-c)^2 + w^2}{2}. \tag{4.17}$$

The fluid kinematics are now completed with $(u, w), (a_x, a_z), P$, and P_d.

4.3 Solitary wave solution using re-normalization formula

Since short waves [254] are incapable of describing long waves such as solitary waves [252], the shallow-water or long-wave theory are alternative methodologies in which solitary waves are a limiting case. The long-wave theory, in turn, can not be used to derive solutions for the Stokes waves because of two different domains of applicability. Clamond [252] presented a renormalization formula, an exact general analytical formula, to construct the velocity fields from the velocity potential at the bottom of the bed. The renormalization formula was then applied to the KdV solution to prove the applicability of long-wave theory to deep water.

In this thesis, the FOWT is located in a deep-sea region where the short-wave theory is not applicable to replicate the solitary wave. We use the re-normalization formula of Clamond as a validation method for the approach of solution proposed in this thesis and the code developed. The derivation of the exact general analytical formula is given in [252, 258, 259]. In this section, we develop analytical model recalling the paper of Clamond [252] for the sake of completeness.

The KdV equation [260] presented as the stationary solution of the first-order shallow water theory is:

$$\hat{u}_t + C_0\hat{u}_x + \frac{3}{2}\hat{u}\hat{u}_x + \frac{1}{6}C_0h^2\hat{u}_{xxx} = 0, \tag{4.18}$$

where $C_0^2 = gh$. $\hat{u} = \hat{\varphi}_x \approx C_0\eta/h$ describes the relation of the horizontal velocity with the free surface η. The stationary solution of the KdV equation depends on the variable $\theta = x - Ct + \delta$, where C is the phase velocity and δ is a constant phase shift.

Application to linear very long waves.

The stationary solution of the linearized KdV equation is given by the potential at the bottom

$$\hat{\varphi} = Asin(\kappa\theta), \qquad \eta = acos(\kappa\theta), \tag{4.19}$$

where $\kappa = 2\pi/L$, $C/C_0 = 1 - (\kappa h)^2/6$, $A = aC_0/kh$. L and a are the wavelength and the wave amplitude, respectively. In contrast to strongly dispersive Airy's short-wave solution, the linear approximation in Eq.4.19 is weakly dispersive. In addition, the above stationary solution is unable to exactly satisfy the Laplace equation. Hence the solution can be improved by providing the renormalization formula using the general solution of Laplace equation at the bottom to satisfy the Laplace equation identically as

$$\varphi(x, z, t) = \frac{1}{2}\hat{\varphi}(x + iz, t) + \frac{1}{2}\hat{\varphi}(x - iz, t), \tag{4.20}$$

where $\hat{\varphi}(x, t) \equiv \varphi(x, 0, t)$ is the potential at the impermeable bottom, and $i^2 = -1$. This general solution is a special form of dÁlembert's solution [252]. The renormalized formula for the stationary solution becomes

$$\begin{aligned}\varphi(\theta, z) &= \frac{1}{2}\hat{\varphi}(x + iz, t) + \frac{1}{2}\hat{\varphi}(x - iz, t) \\ &= \frac{1}{2}Asin[\kappa(\varphi + iz)] + \frac{1}{2}Asin[\kappa(\varphi - iz)] \\ &= Asin(\kappa\varphi)cosh(\kappa z).\end{aligned} \tag{4.21}$$

This is the Airy solution of short waves.

Application to cnoidal waves.

The stationary solution to the KdV equation is given by Jacobi's elliptic functions and the elliptic integrals [261] with

$$\hat{\varphi} = \frac{A}{\kappa}Z(\kappa\theta|m), \qquad \hat{u} = A[dn^2(\kappa\theta|m) - E/K], \qquad \eta = a\frac{dn^2(\kappa\theta|m) - E/K}{1 - E/K}, \tag{4.22}$$

where dn is the elliptic function, Z is the zeta-function which is also a Jacobi elliptic function. K and E are the elliptic integrals of the first and second kind of parameter m.

κ and a are a kind of wavenumber and the wave amplitude, respectively. A is a related parameter of the maximum speed. Given relations state

$$\frac{a}{h}\frac{C_0}{A} = 1 - \frac{E}{K}, \qquad \kappa^2 h^2 = \frac{3}{4}\frac{A}{C_0}, \qquad \frac{C}{C_0} = 1 + \frac{a}{2h}\frac{2 - m - 3E/K}{1 - E/K}, \qquad \kappa L = 2K, \tag{4.23}$$

in which L is the wavelength. m can be considered as an Ursell parameter [262]. Total wave elevation H from the trough to the crest elevation is computed using the wave amplitude $H = ma/(1 - E/K)$. The stationary solution is weakly non-linear and weakly dispersive for $m \ll 1$. The solution is renormalized using the renormalization formula, Eq.4.20, and one obtains [261]

$$\begin{aligned} \varphi &= \frac{A}{2\kappa} Z[\kappa(\theta + iz)|m] + \frac{A}{2\kappa} Z[\kappa(\theta - iz)|m] \\ &= \frac{A}{\kappa}\left[Z(\kappa\theta|m) + \frac{m \quad sn(\kappa\theta|m)cn(\kappa\theta|m)dn(\kappa\theta|m)sn^2(\kappa z|m_1)}{cn^2(\kappa z|m_1) + m \quad sn^2(\kappa\theta|m)sn^2(\kappa z|m_1)} \right] \end{aligned} \tag{4.24}$$

where $m_1 = 1 - m$. The stream function and the velocity components are

$$\psi = \frac{A}{\kappa}\left(\frac{d^2 s_1 c_1 d_1}{c_1^2 + m s^2 s_1^2} - z_1 - \frac{\pi\kappa z}{2KK'} \right), \tag{4.25}$$

$$u = A\left(\frac{d^2 c_1^2 d_1^2 - m^2 s^2 c^2 s_1^2}{(c_1^2 + m s^2 s_1^2)^2} \frac{E}{K} \right), \tag{4.26}$$

$$w = 2mA\left(\frac{scds_1 c_1 d_1}{(c_1^2 + m s^2 s_1^2)^2} \right), \tag{4.27}$$

with $K' = K(m_1)$ and

$$\begin{bmatrix} s \\ c \\ d \\ z \end{bmatrix} = \begin{bmatrix} sn \\ cn \\ dn \\ Z \end{bmatrix} (\kappa\theta|m), \qquad \begin{bmatrix} s_1 \\ c_1 \\ d_1 \\ z_1 \end{bmatrix} = \begin{bmatrix} sn \\ cn \\ dn \\ Z \end{bmatrix} (\kappa z|m_1). \tag{4.28}$$

The renormalized KdV potential in Eq.4.24 is periodic for $m \neq 1$ and it is expanded using the Fourier series as

$$\varphi = \frac{\pi A}{\kappa K} \sum_{n=1}^{\infty} cosech\left(\frac{n\pi K'}{K} \right) sin\left(\frac{n\pi\kappa\theta}{K} \right) cosh\left(\frac{n\pi\kappa z}{K} \right) \tag{4.29}$$

at the bottom [261] by applying the re-normalization. As $m = 1$ in terms of the solitary waves, the potential is given by

$$\varphi = \frac{A}{\kappa} \frac{tanh(\kappa\theta)}{1 - sech^2(\kappa\theta) sin^2(\kappa z)}, \tag{4.30}$$

which is the exact solution of the Laplace equation.

Evaluation of the free surface elevation

Due to normalization, φ is not constant along the vertical axis so that the potential value at surface is modified. Consequently, η must be recalculated leading to the fact that the equation at the free surface have to be resolved using Bernoulli's equation for steady and unsteady flows. On the other hand, the free surface η is derived from the flow conservation law, thus

$$\eta_t + \tilde{\psi}_x = 0, \tag{4.31}$$

where $\tilde{\psi} \equiv \psi(x, h+\eta, t)$ is the stream function at the surface. For a progressive wave, the η is integrated

$$\eta = C^{-1}\tilde{\psi} - \alpha, \tag{4.32}$$

where α is an integration constant. An explicit approximation of η by using an expansion of $\tilde{\psi}$ truncated at the quadratic term [252] is

$$\eta \simeq C^{-1}[\psi(\theta, h) + \eta u(\theta, h)] - \alpha. \tag{4.33}$$

Therefore, the free surface is obtained by

$$\eta \simeq \frac{\psi(\theta, h) - \alpha C}{C - u(\theta, h)}. \tag{4.34}$$

Due to the re-normalization, the relations among parameters have to be re-derived, however the wavelength remains unchanged, as $L = 2K/\kappa$.

Mean water level and the wave amplitude.

Due to the re-normalization, the wave amplitude and the mean water level require recalculation. Considering η is the surface elevation from the mean depth h and the solution is given in the frame without mean velocity at the bottom depth. The conditions

$$\langle \hat{u} \rangle = 0, \qquad \langle \eta \rangle = 0, \tag{4.35}$$

are given where the Eulerian average operator $\langle\rangle$ is defined with

$$\langle \bullet \rangle = \frac{1}{L} \int_{-L/2}^{+L/2} \bullet d\theta. \tag{4.36}$$

The parameter α is found as the condition $\langle \eta \rangle = 0$, hence

$$\alpha = \frac{1}{C} \langle \frac{\psi(\theta, h)}{C - u(\theta, h)} \rangle / \langle \frac{1}{C - u(\theta, h)} \rangle. \tag{4.37}$$

Applying $\langle\eta\rangle = 0$ to the Bernoulli's equation, β is obtained as

$$\beta = \frac{1}{2}\langle\tilde{u}^2 + \tilde{w}^2\rangle - C\langle\tilde{u}\rangle, \tag{4.38}$$

in which $(\tilde{u}, \tilde{w})$ are the velocity at the free surface.

The wave amplitude and the maximum wave speed.

The wave amplitude is the maximum elevation from the mean water level h with

$$a = \frac{\psi(0,h) - \alpha C}{C - u(0,h)}, \tag{4.39}$$

and

$$\psi(0,h) = \frac{A}{\kappa}\left[\frac{sn(\kappa h|m_1)dn(\kappa h|m_1)}{cn(\kappa h|m_1)} - Z(\kappa h|m_1) - \frac{\pi\kappa h}{2KK'}\right],$$
$$u(0,h) = A\left[\frac{dn^2(\kappa h|m_1)}{cn^2(\kappa h|m_1)} - \frac{E}{K}\right].$$

Simplification solution for a solitary wave.

The re-normalization formulations for a solitary wave is simplified as follows

$$\phi = \frac{A}{\kappa}\frac{tanh(\kappa\theta)}{1 - sech^2(\kappa\theta)sin^2(\kappa z)}, \tag{4.40}$$

$$\psi = \frac{A}{2\kappa}\frac{sech^2(\kappa\theta)sin(2\kappa z)}{1 - sech^2(\kappa\theta)sin^2(\kappa z)} \tag{4.41}$$

$$u = A\frac{sech^2(\kappa\theta)cos(2\kappa z) + sech^4(\kappa\theta)sin^2(\kappa z)}{[1 - sech^2(\kappa\theta)sin^2(\kappa z)]^2} \tag{4.42}$$

$$w = A\frac{tanh(\kappa\theta)sech^2(\kappa\theta)sin(2\kappa z)}{[1 - sech^2(\kappa\theta)sin^2(\kappa z)]^2}. \tag{4.43}$$

The parameters are related by

$$m = 1, \quad L = \infty, \quad \alpha = 0, \beta = 0, \quad b = 0,$$
$$a = \frac{A}{\kappa}\frac{tan(\kappa h)}{C - Asec^2(\kappa h)}, \quad C - (C^2 - 2ga)^{1/2} = Asec^2[\kappa(h+a)],$$

and the dispersion relation is given as

$$C - (C^2 + 2\beta + 2gb)^{1/2} = \tilde{u}(L/2) = A\left(\frac{m_1 cn^2[\kappa(h-b)|m_1]}{dn^2[\kappa(h-b)|m_1]} - \frac{E}{K}\right) \tag{4.44}$$

where b is the trough height which is the minimum of the surface elevation from the

mean level given as

$$b = \frac{\psi(L/2, h) - \alpha C}{u(L/2, h) - C}, \tag{4.45}$$

with

$$\psi(L/2, h) = \frac{A}{\kappa}\left[\frac{m_1 sn(\kappa h|m_1) cn(\kappa h|m_1)}{dn(\kappa h|m_1)} - Z(\kappa h|m_1) - \frac{\pi \kappa h}{2KK'}\right],$$
$$u(L/2, h) = A\left[\frac{m_1 cn^2(\kappa h|m_1)}{dn^2(\kappa h|m_1)} - \frac{E}{K}\right].$$

The dispersion relation in the limiting case where $m_1 \to 1$ is

$$\frac{C^2}{gh} = \frac{tan(2\kappa h)}{2\kappa h}. \tag{4.46}$$

The permanent solitary waves solutions presented in this section will be used for computation of small amplitude solitary waves and their impact on the dynamic responses of FOWT in the following sections.

4.4 Validation of numerical results

In this section, our approach is validated with analytical results provided theoretically by Clamond [259] distributed by Matlab community [263] for surface velocity profiles, horizontal and vertical velocity, fluid accelerations, and pressure profiles.

The method based on the conformal mapping technique [259] is Tanaka's method [264] which is coupled with the Newton method [265] requiring the computation of Jacobian matrix and the resolution of the linear system of equations (direct or iterative method) [263, 266]. A simple iterative scheme is more attractive and practicable with the main focus on evaluating the operator involved in the equation to be solved. Hence, classical Petviashvili iteration [267] is applied and freely downloaded from *Matlab Central* [263]. The combination of the Petviashvili scheme and the conformal mapping technique gives an efficient numerical scheme for computation of solitary waves of full Euler equations in the water of finite depth [263]. Several important integral characteristics such as mass, momentum, energy are derived from conformal mapping space for small-amplitude waves. In addition, the waves kinematics are also computed inside the bulk of the fluid domain. Needed pressure profiles, velocity profiles, and acceleration distributions are withdrawn under surface waves.

A solitary wave of $\eta/d = 0.021$ with a characteristic wavelength $L_c = 30m$ is investigated. The water depth, d, is 320m. The free surface and the fluid kinematics are computed analytically. Using the same free surface as the input parameter, our approach

computes the wave kinematics that then are compared with the analytical results for validation.

The free surface profile of the solitary wave of $\eta/d = 0.021$ is shown in the Fig.4.4 below. The computational domain and the discretised mesh are shown in Fig.4.5 for a characteristic wave length of L_c.

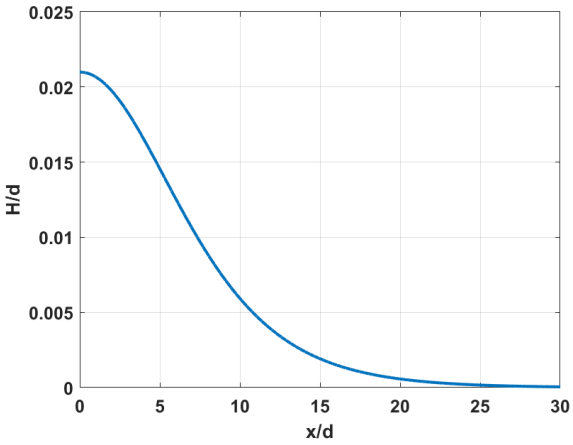

Figure 4.4: Solitary wave profile.

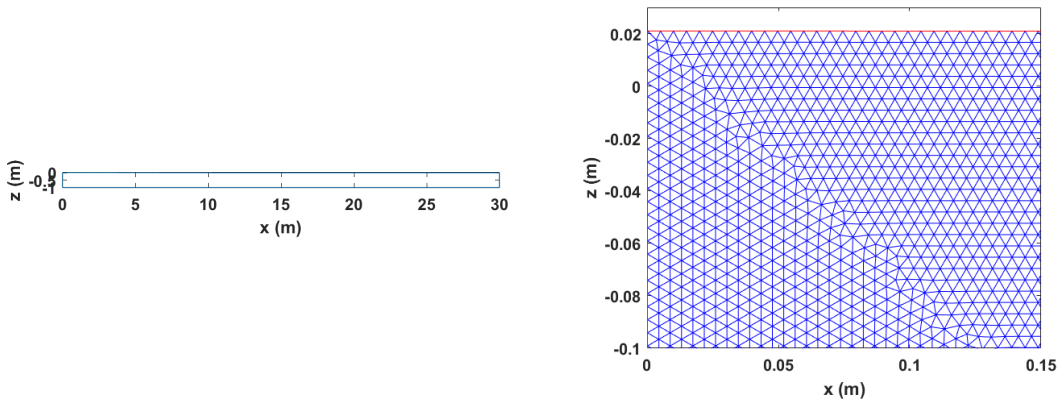

(a) Computational domain (b) Mesh grid

Figure 4.5: Computational domain with boundaries and the mesh.

The solutions are then compared with analytical results in the following Fig.4.6 to Fig.4.9. Fig.4.6 illustrate the flow velocity components at the free surface. The numerical results perfectly match the analytical solutions, which confirm the accuracy of our approach. Next, the velocity is interpolated from the grid's value to calculate the vertical velocity along the streamlines within the fluid.

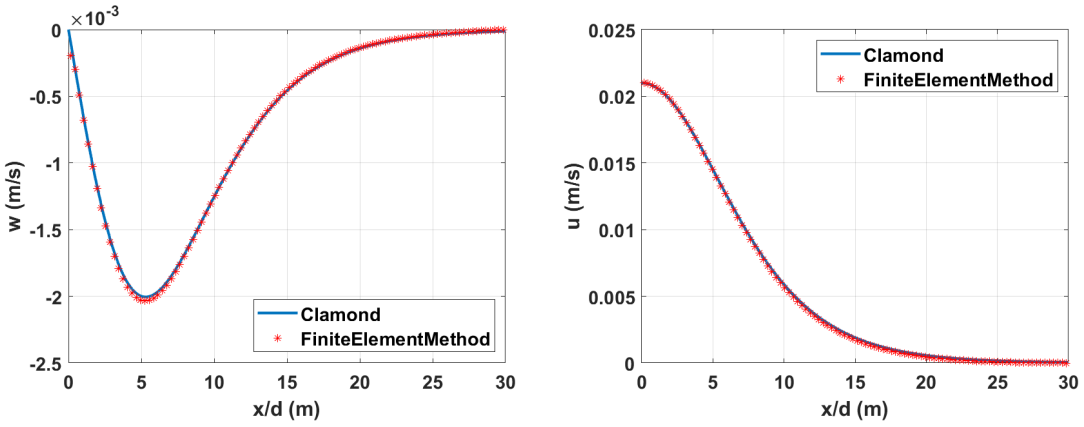

(a) (b)

Figure 4.6: Velocity components at the free surface.

Since we only know the horizontal velocity at the surface, the horizontal velocity in the deeper region is estimated using the linear approximation step in which a function value is estimated at the point using Taylor series expansion as

$$f(x) = f(x_0) + \frac{\partial f}{\partial x}(x - x_0), \tag{4.47}$$

hence, the value of the horizontal velocity at the streamline adjacent to the surface is computed by the horizontal velocity at the surface and the derivative of the horizontal velocity component in the corresponding axis. From the vorticity equation, we get

$$u_x = w_z \text{ or } u_z = w_x, \tag{4.48}$$

thus the horizontal velocity gradient is equal to the gradient of the vertical velocity in the perpendicular direction. Since we know the vertical velocity for the whole domain and the grid from the mesh, the horizontal velocity gradient is computed accordingly.

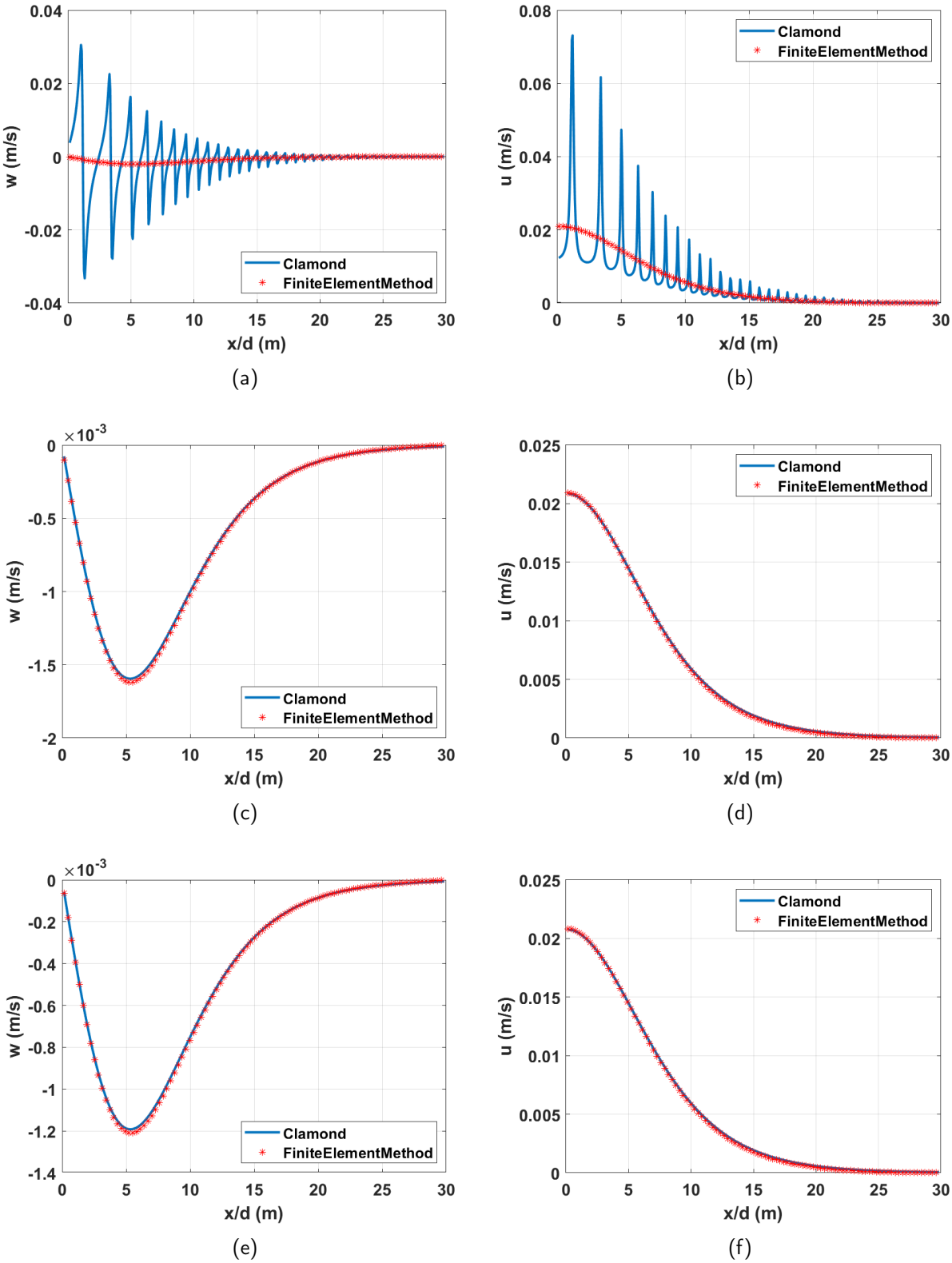

Figure 4.7: Velocity components at various streamline.

Acceleration profiles along streamlines

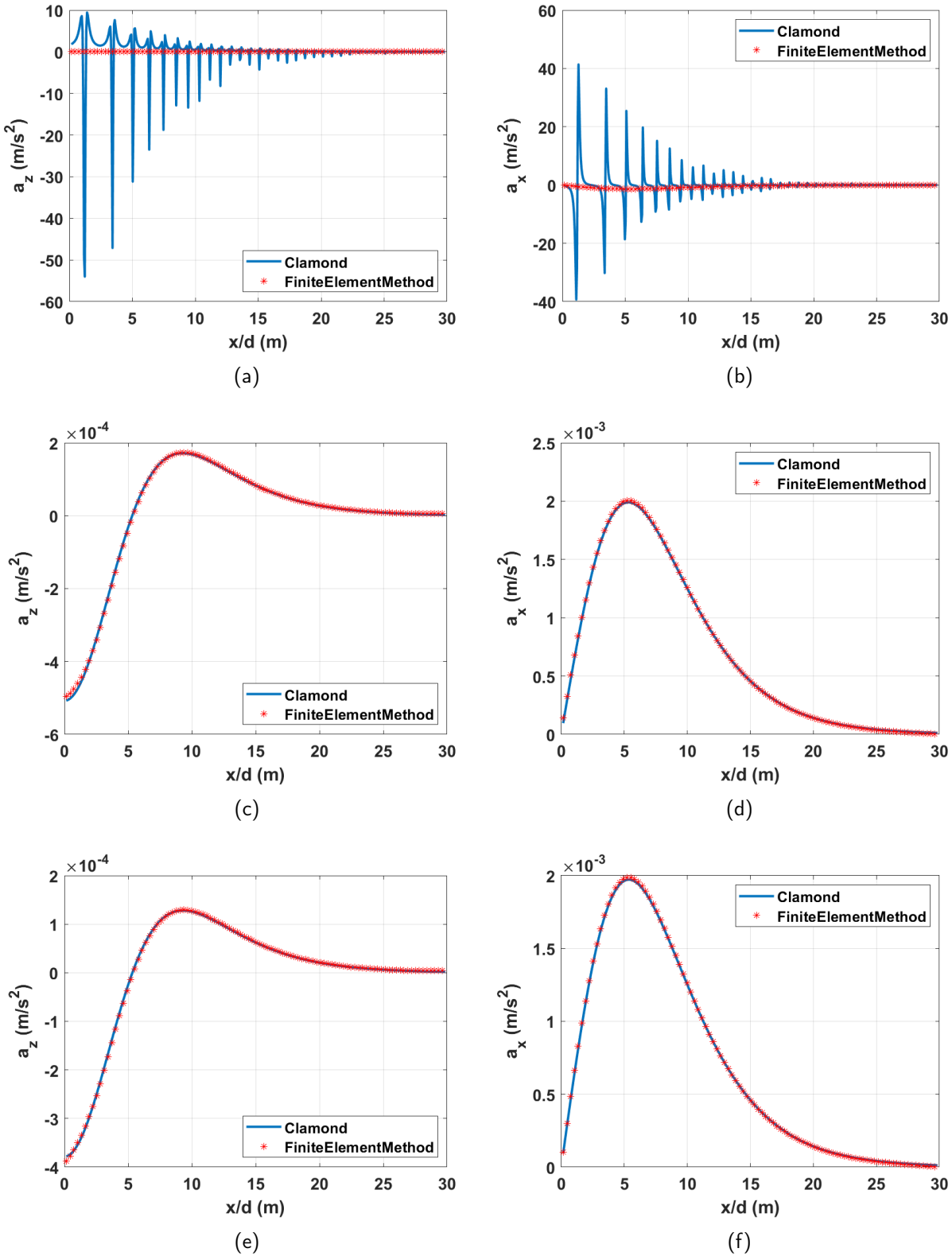

Figure 4.8: Acceleration profiles along streamlines.

Pressure profiles along streamlines

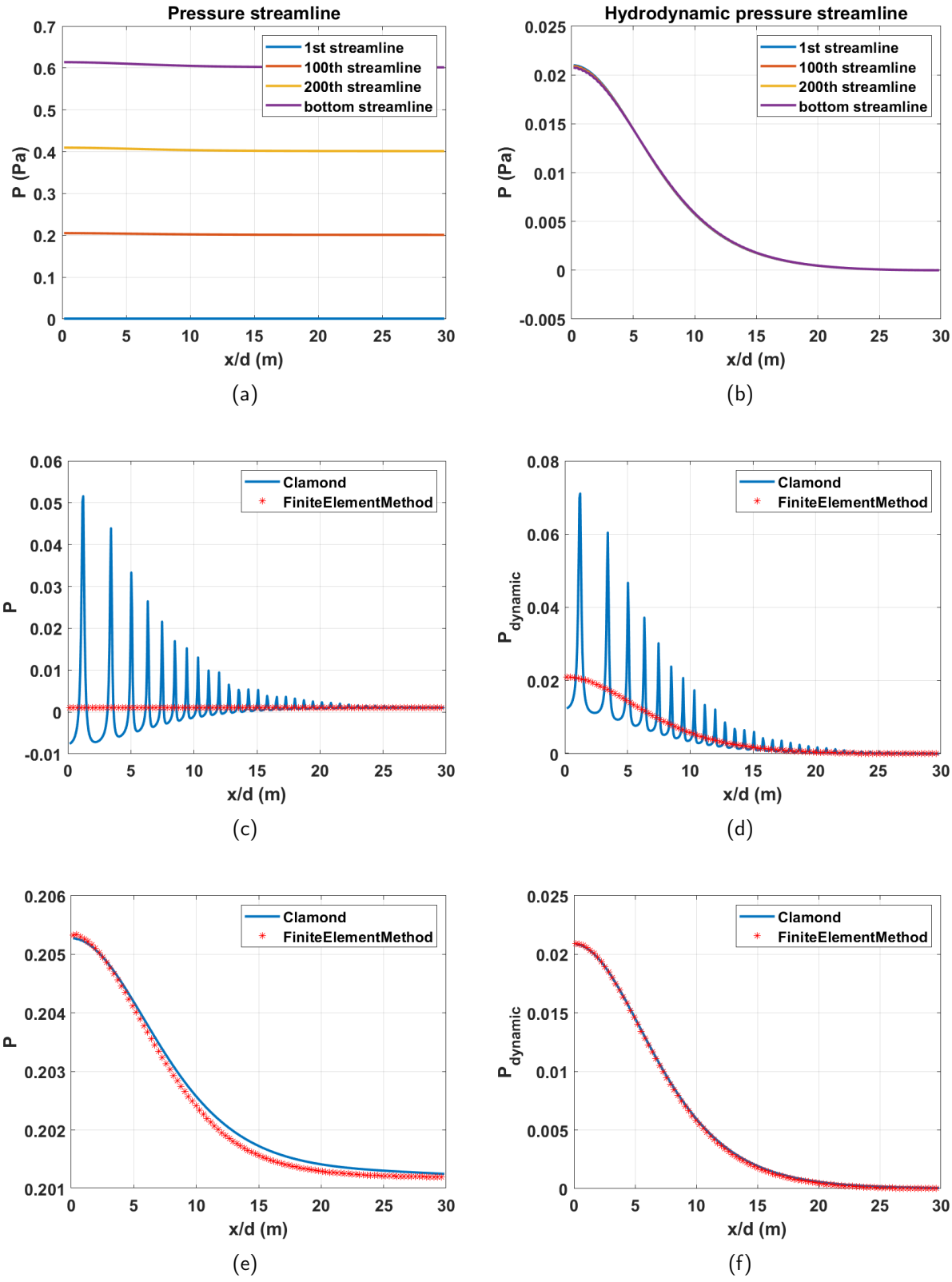

Figure 4.9: Pressure profiles.

The numerical error in Clamond's analytical results are founded near the free surface due to the fluctuation of the vertical velocity on the free surface boundary. The fluctuation

and noisy near surface wave kinematics has been confirmed by various researchers [263]. Our approach overcomes these issues; there is no error near the free surface as the analytical solutions.

The wave kinematics in one wave length

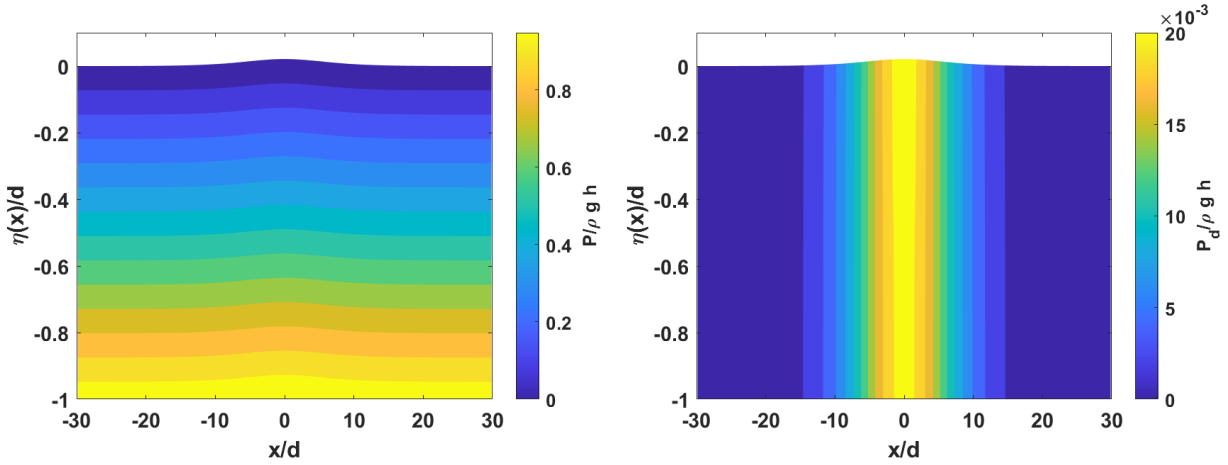

Figure 4.10: Isobars (left) and iso-dynamic pressure p+gy (right) under a solitary wave.

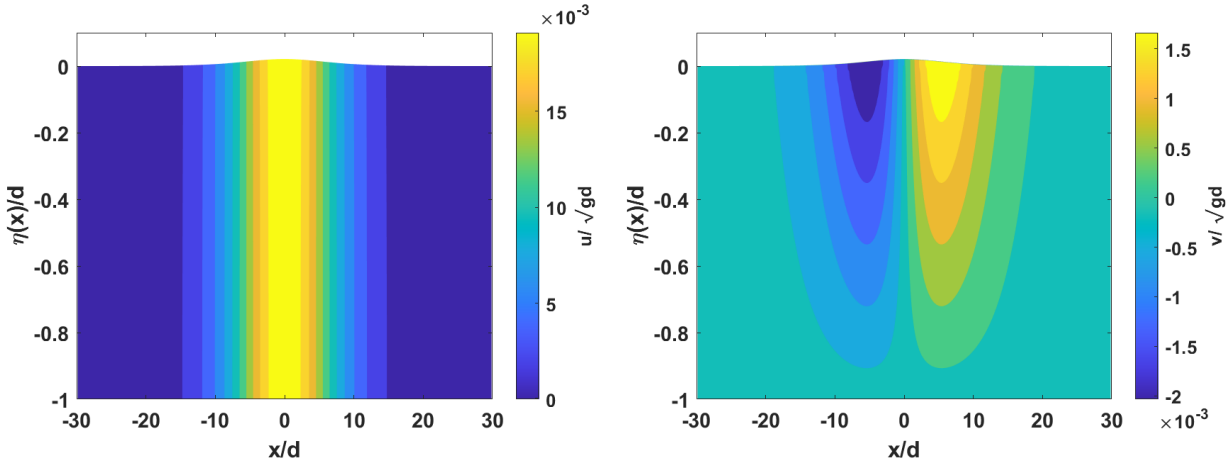

Figure 4.11: Iso-horizontal (left) and iso-vertical (right) velocities under a solitary wave. The iso-values are computed in the 'fixed' frame of reference where the fluid is at rest $x \to \pm\infty$.

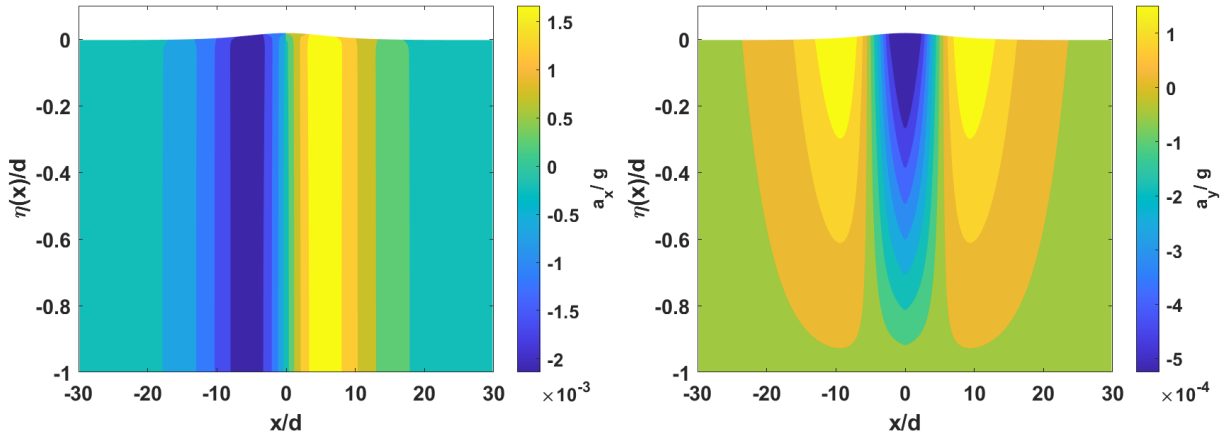

Figure 4.12: Iso-horizontal (left) and iso-vertical (right) accelerations under a solitary wave.

In this section, our approach is compared and validated with the analytical results. The results show a good agreement of the wave kinematics under a steady solitary waves free surface. In the following section, the solitary waves are applied to the FOWT model developed in Chapter 2 to investigate the impulsive effect of the solitary waves.

4.5 Numerical model

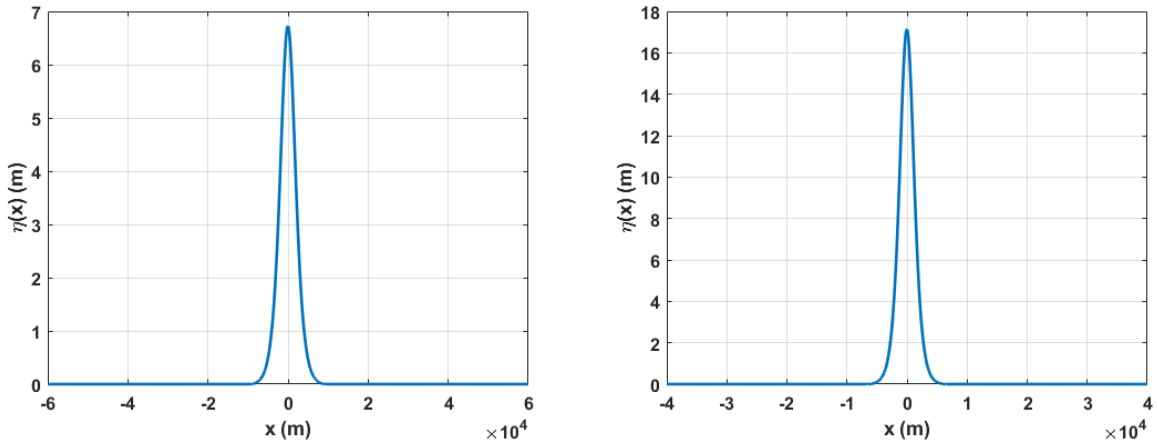

(a) (b)

Figure 4.13: Free surface profiles of two considered cases.

The numerical model presented in the previous chapters is reused herein to investigate the impact of the solitary waves on the dynamic response of the FOWT. There are two cases where the wave height ratio, H/d, equals 0.021 and 0.053, corresponding

to the realistic wave amplitudes 6.72 m and 16.96 m. The wave amplitudes represent the moderate and extreme wave height in OC3 report [10]. Solitary waves possess high wave speed and long wavelength. For instance, case H = 6.72 m has a wavelength of 10278 m, and case H = 16.96 m has a wavelength of 6513 m. In both cases, the wave speed is dependent on the depth of the water with $c = \sqrt{gd} = 56.0285$ m/s. Fig.4.13 describes the free surface profiles of two solitary waves used in this chapter.

4.6 Numerical results

The impact of the solitary waves on the FOWT dynamic responses are investigated in this section. The focus is on the impulsive effect of the solitary waves as they interact with the FOWT structure. During the propagation period, the solitary waves might have a considerable impact on the submerged components than the above water components due to the large amount of energy it carries.

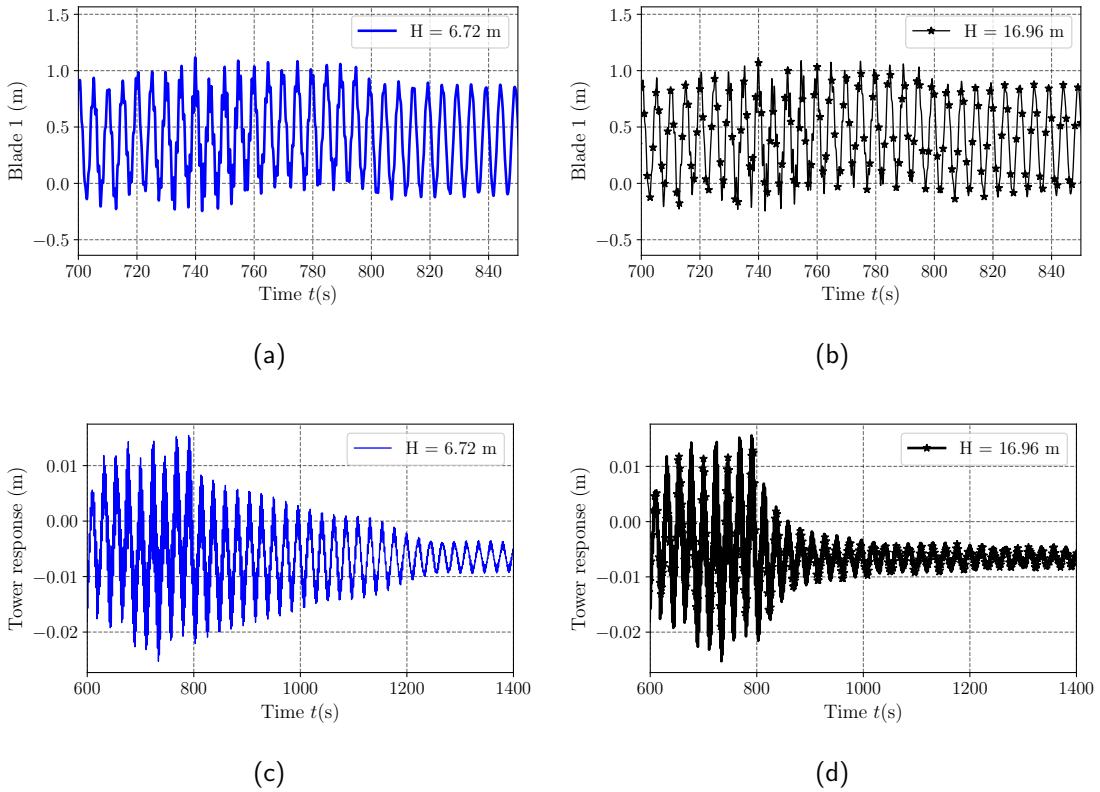

Figure 4.14: SFOWTs blade edge-wise and tower responses in solitary waves.

Turbine blades edge-wise responses and tower response are shown in Fig.4.14. Fig.4.14(a) reveal that the blade displacements are not influenced by the solitary waves of any arbitrary wave amplitudes.

For $H = 16.96$ m and $H = 6.72$ m, the estimated heave responses increase until solitary

wave approaches FOWT and then declining as solitary wave passes. The peak responses for $H = 6.72$ m and $H = 16.96$ m are about at $t = 1200$ s and $t = 800$ s, respectively.

As shown in Fig.4.15, the two most affected FOWT responses are the spar/platform response in the vertical and horizontal directions. The maximum vertical displacement for the case $H = 16.96$ m and $H = 6.72$ m are 16.2 m and 6.45 m, respectively. This shows a relation between the wave amplitude and the vertical response of the FOWT. In addition, the maximum surge motion for the case of $H = 16.96$ m is 34.56 m, while that for the case of $H = 6.72$ m is 13.73 m. Another point to note is that the heave responses reach their peak earlier than the surge. For instance, for $H = 16.96$ m, the heave response reaches its peak at $t = 835.92$ s, while surge peaks at $t = 858.22$ s.

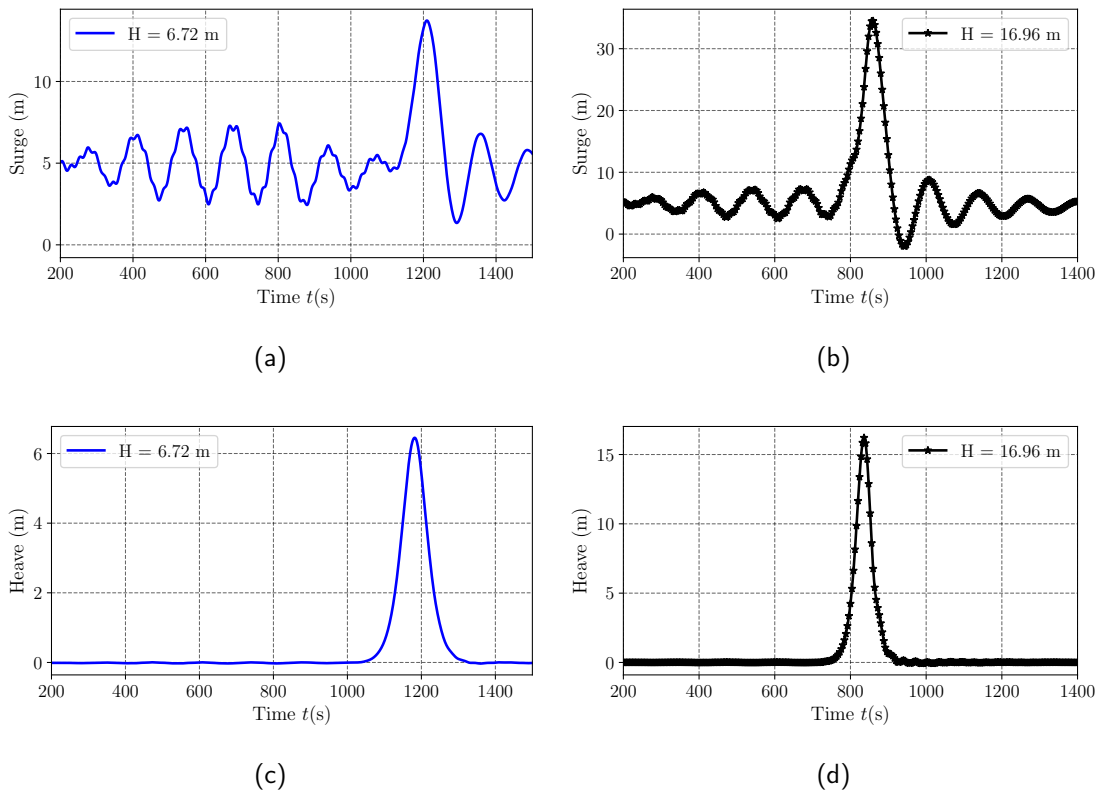

Figure 4.15: SFOWTs surge and heave responses.

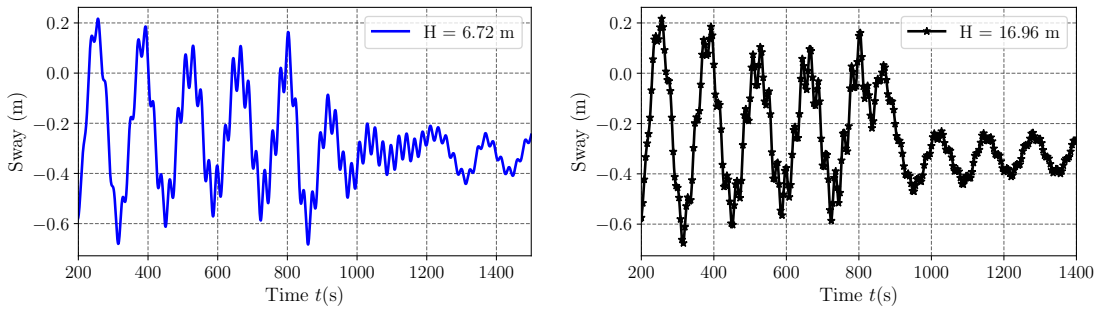

(a)

(b)

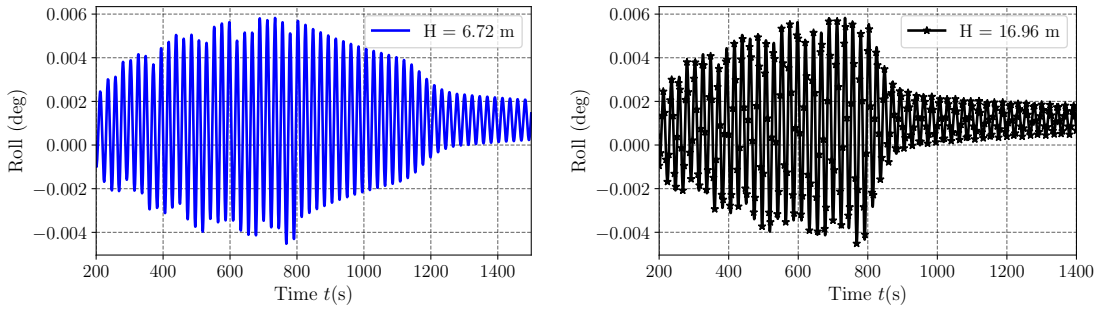

(c)

(d)

Figure 4.16: SFOWTs sway and roll responses.

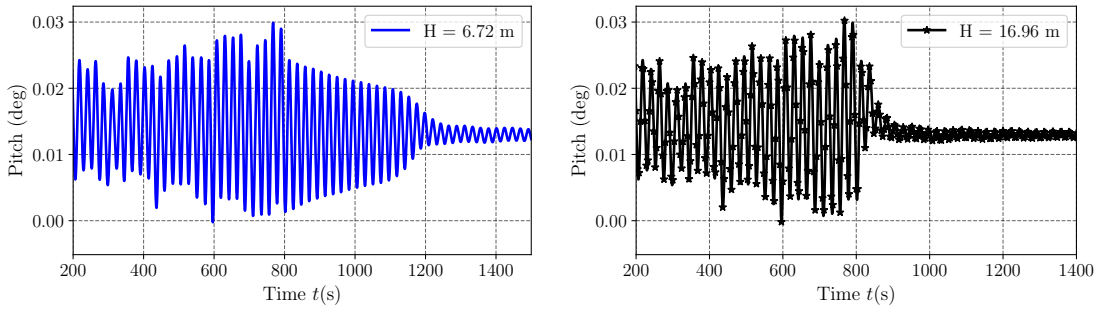

(a)

(b)

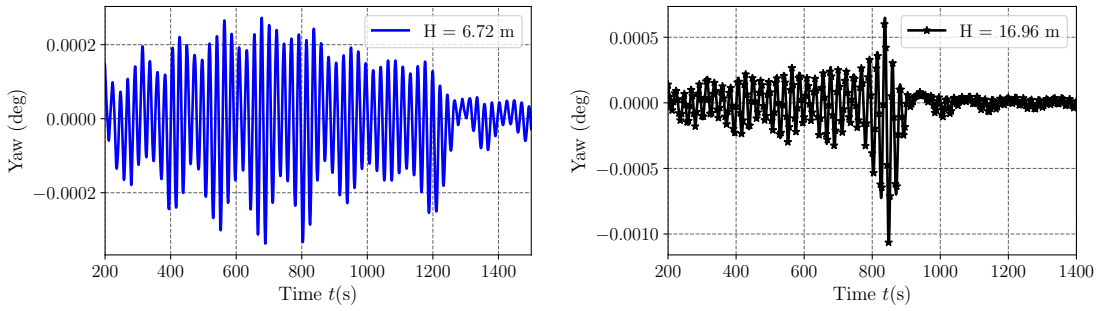

(c)

(d)

Figure 4.17: SFOWTs pitch and yaw responses.

Fig.4.16 and Fig.4.17 shows the remaining FOWT responses. Yaw response increase dramatically as the FOWT experiences the extreme solitary wave (H = 16.96 m), but it is not observed in the case of H = 6.72 m. In addition, as the wave crosses the structure, the yaw responses for both the cases are decline, as seen in Fig.4.17(d). Similarly, there is a significant reduction illustrated in other FOWT responses, i.e. sway, roll and pitch in Fig.4.16 and Fig.4.17(a,b) following passage of the solitary wave. This is due to the fact that the surface profile again recovers close to the still water profile.

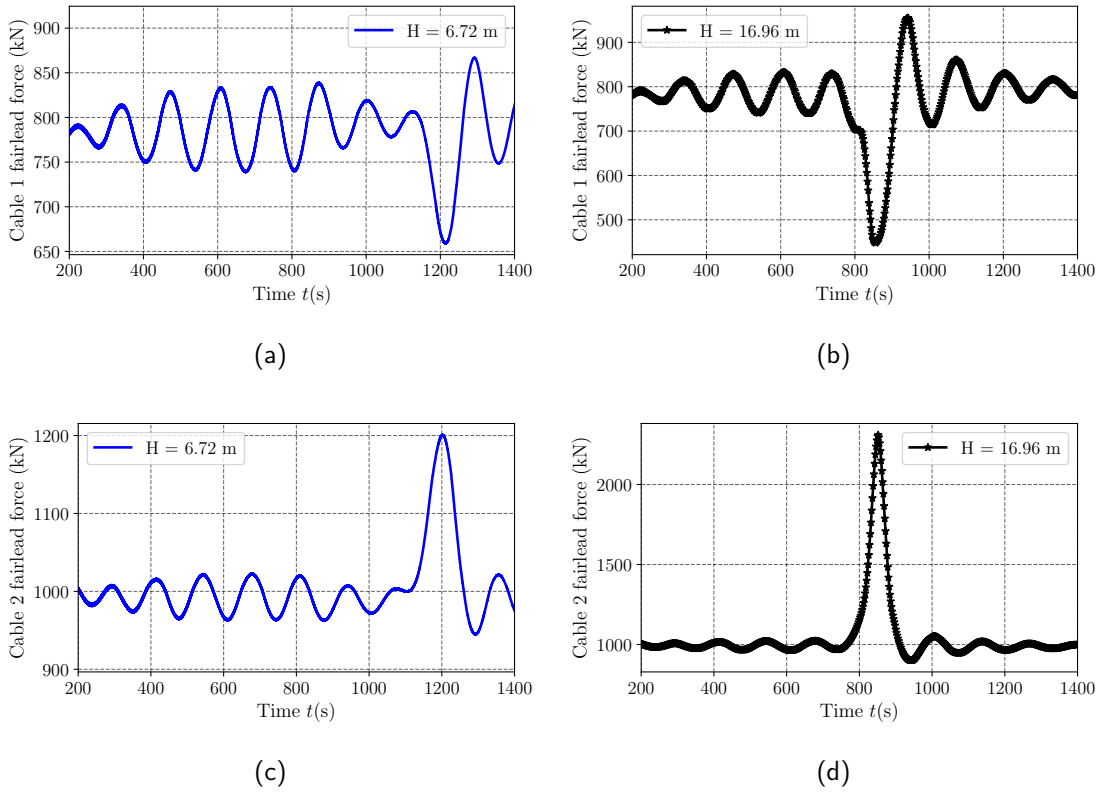

Figure 4.18: Cable fairlead forces in two cases.

The cable fairlead force of cable two and cable three are equal due to their symmetrical position. Therefore, only cable two fairlead force is presented in Fig.4.18(c,d). Fig.4.18(a,b) describes the cable one fairlead force, being generally smaller than the cable two fairlead force. For H = 16.96 m, the maximum fairlead force of cable two is about 2300 kN, nearly three times larger than that of cable one whose maximum fairlead force of 955 kN. In addition, the cable two fairlead force in case of H = 6.72 m is approximately 1200 kN, almost double that of cable one force with 850 kN. Compared to the cable forces of surface waves the solitary waves generate a significantly larger fairlead forces of cable two and cable three than the surface waves. For regular waves with H = 14.23 m and T = 13.50 s (Fig.2.41(a,b)), the cable one and cable two fairlead forces are about 1000 kN ad 1150 kN, respectively. While these forces are

about 850 kN and 1200 kN with solitary wave of $H = 6.72$ m, respectively. Even when the solitary waves' amplitude is slightly smaller than the surface waves, the larger cable forces show the dramatic impact of the solitary waves on the FOWT.

In this chapter, the solitary waves show a impulsive impact on the FOWT structure. Although their effect is in a short period, the FOWT responses however reach their maximum displacements in this period and thus the solitary waves affect the operation of the overall structure. Nevertheless, the hydrodynamic forces do not consider the impact of the solitary waves-structure interactions in this study. Therefore, the following chapters will investigate the changes in the water free surface due to solitary waves-structure interaction and consequently the flow kinematics to ensure a comprehensive investigation on the effects of the solitary waves.

5 Smoothed Particle Hydrodynamics

5.1 Introduction

The previous chapter has highlighted the importance of considering modified surface profiles with interaction of a solitary wave with the FOWT is to be analysed. However, analytical approach for this is non-existent. Hence, we need to take recourse to numerical approaches such as Smoothed Particle Hydrodynamics (SPH) which is able to tackle the interaction effects and solve for the surface profile tracking the surface particles based on a Lagrangian approach of fluid dynamics.

This chapter outlines the essential formulation of the Lagrangian based SPH methodology, starting from the integral approximation and the discretization formulation. The kernel function that is included in all approximation are discussed and some typical kernel function are given. Then the fundamental equations of the fluid governing equation, the different boundary conditions, and the time integration schemes are then introduced. The application of SPH in studying the wave generation, wave structure interaction, and the abilities of the method to model the large-amplitude waves are discussed in detail with numerical model and numerical results.

5.2 Fundamentals of SPH

SPH is a Lagrangian method. The Lagrangian is a function of generalized coordinates, their time derivatives, and time. In the following sections, the derivative of a spatial variable are determined. The properties of the particles can be calculated based on the particle's position, velocity, and density.

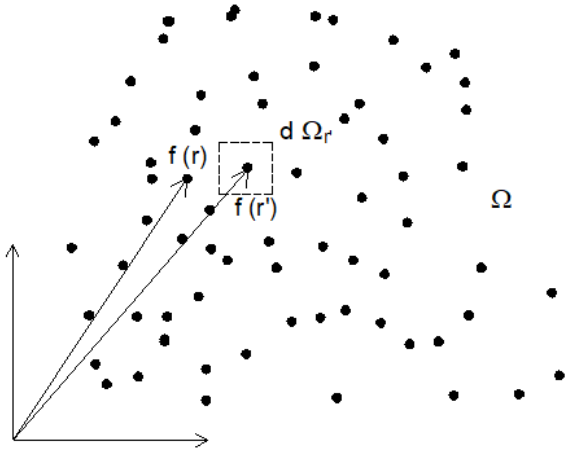

Figure 5.1: Particle position and its neighbours

5.2.1 Integral approximation

Function values

A local value of an arbitrary spatial function $f(\mathbf{r}_i)$ (see Fig.5.1) is reproduced by the integral identity

$$f(\mathbf{r}) = \int f(\mathbf{r}')\delta(\mathbf{r} - \mathbf{r}')d(\mathbf{r}') \tag{5.1}$$

with the surrounding value $f(\mathbf{r}')$ and the Dirac delta function δ in the surrounding volume Ω. The Dirac delta function is defined by

$$\delta(\mathbf{r} - \mathbf{r}') = \begin{cases} 1, & \text{if } \mathbf{r} = \mathbf{r}'; \\ 0, & \text{if } \mathbf{r} \# \mathbf{r}'; \end{cases} \tag{5.2}$$

The approximation includes two steps to represent Delta function by a smooth analytical kernel function W, and convert the integral into discrete summations.

We assume W mimics the delta function, so the kernel approximaton of a function at $\mathbf{r}$ is given by

$$f(\mathbf{r}) = \int_{\Omega} f(\mathbf{r}')W(\mathbf{r} - \mathbf{r}', h)d(\mathbf{r}'). \tag{5.3}$$

The kernel function is an even function, it has a bell shape and occupies a volumetric Ω which is proportional to the smoothing length h_s. In this study, the radius of the support domain of W is $1.5h_s$ (see in Fig.5.2).

Function gradient

The rate of change of a spatial function is estimated from their spatial derivatives. In SPH, the derivative of a function is approximated using information from function gradient at their neighbouring particles. The SPH approximation in Eq.5.3 can be used

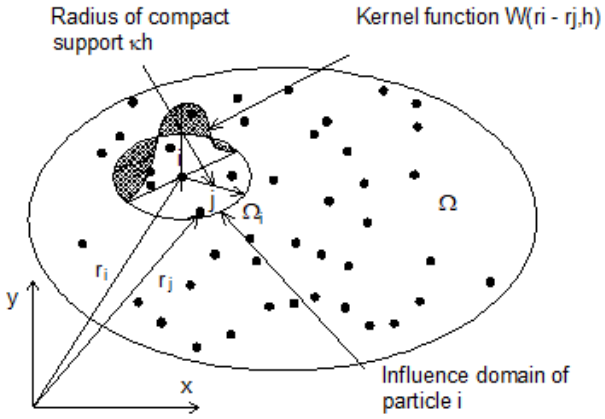

Figure 5.2: Particle approximation

to derive the function gradient

$$\langle \nabla f(\mathbf{r}) \rangle \approx \int_{\Omega} \left[\nabla_{r'} . f(\mathbf{r}') \right] W(\mathbf{r} - \mathbf{r}', h) d\mathbf{r}' \tag{5.4}$$

To obtain higher accuracy on the gradient of a quantity field, the interpolant are expressed by Gauss's theorem as

$$\begin{aligned} \int_{\Omega} \nabla_{r'} . \left[f(\mathbf{r}') W(\mathbf{r} - \mathbf{r}', h) \right] d\mathbf{r}' &= \int_{\Omega} f(\mathbf{r}') \left[\nabla_{r'} W(\mathbf{r} - \mathbf{r}', h) \right] d\mathbf{r}' + \left[\nabla_{r'} f(\mathbf{r}') \right] W(\mathbf{r} - \mathbf{r}', h) d\mathbf{r}' \\ &= \int_{\partial\Omega} f(\mathbf{r}') W(\mathbf{r} - \mathbf{r}', h) dS', \end{aligned} \tag{5.5}$$

The interpolant is achieved after rearranging

$$\langle \nabla f(\mathbf{r}) \rangle \approx \int_{\partial\Omega} f(\mathbf{r}') W(\mathbf{r} - \mathbf{r}', h) dS' - \int_{\Omega} f(\mathbf{r}') \left[\nabla_{r'} W(\mathbf{r} - \mathbf{r}', h) \right] d\mathbf{r}', \tag{5.6}$$

The first integral on the right hand side of Eq.5.6 can be converted using the divergence theorem into an integral over the surface S of the domain of the integration, Ω

$$\langle \nabla f(\mathbf{r}) \rangle \approx \int_{S} f(\mathbf{r}') W(\mathbf{r} - \mathbf{r}', h) . \vec{n} dS - \int_{\Omega} f(\mathbf{r}') \nabla_{r'} W(\mathbf{r} - \mathbf{r}', h) d\mathbf{r}' \tag{5.7}$$

where $\vec{n}$ is the unit vector normal to the surface S. The smoothing function W has compact support, thus the surface integral is zero as the support domain is entirely located inside the problem domain, as shown in Fig.5.3(a). Otherwise, the surface integral differs from zero when the support domain overlaps the problem domain, Fig.5.3(b), where the smoothing function is truncated by the problem boundaries. This leads to a modification required if the surface integration is assumed zero. For those points whose support domain is completely inside the problem domain, the function gradient

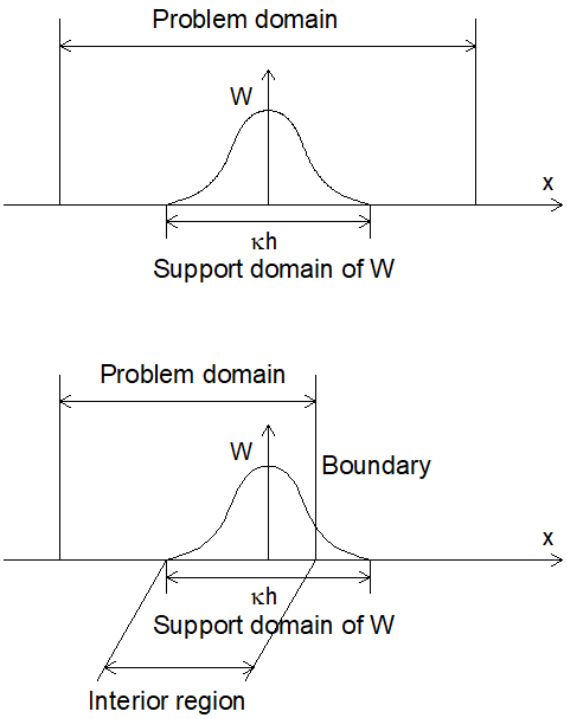

Figure 5.3: The support domain and the problem domain.

is simplified as follows

$$\langle \nabla f(\mathbf{r}) \rangle \approx -\int_{\Omega} f(\mathbf{r}') \nabla_{r'} W(\mathbf{r} - \mathbf{r}', h) d\mathbf{r}' \tag{5.8}$$

The function gradient now shifts from the function itself $f(\mathbf{r})$ to the gradient of the kernel function W. The shifting simplifies the whole computational procedure however the simplification impacts the accuracy and convergence near the rigid boundaries and free surfaces [268] which necessitates the improvement in the function gradient.

5.2.2 Discrete summation approximation

In SPH method, the domain has to be discretised into a finite number of particles that carry individual mass and occupy their own space. Particles' properties are achieved by the *particle approximation*, which is another key operation in the SPH method. The continuous integral representations concerning the SPH kernel approximation can be converted to discretised forms of summation over all the particles in the support domain as shown in Fig.5.4.

If the infinitesimal volume $d\mathbf{r}'$ in the above integration at the location of particle j is replaced by the finite volume of the particle V_j that is related to the mass of the particles m_j by

$$m_j = V_j \rho_j \tag{5.9}$$

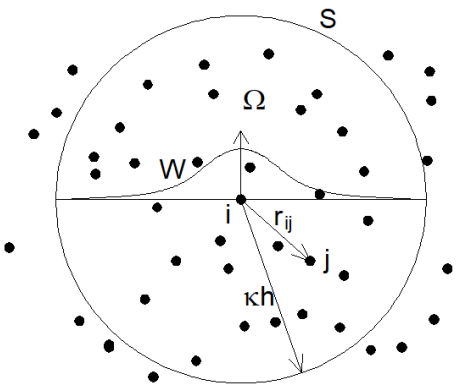

Figure 5.4: Particle approximation using particles within the support domain of the smoothing function W for particle i. The support domain is circular.

where ρ_j is the density of particle, $j(= 1, 2, 3, .., N)$ in which N is the number of particles within the support domain of particle i. The continuous SPH integral representation for $f(\mathbf{r})$ can be written in the following form of discretized *particle approximation*

$$f_i \approx \sum_{j=1}^{N} V_j f_j W_{ij}, \tag{5.10}$$

where $W_{ij} = W(\mathbf{r}-\mathbf{r_j}, h_s) = W(|\mathbf{r_i}-\mathbf{r_j}|, h_s)$. Equation states that the value of a function at particle i is approximated using the average of those values of the function at all the particles in the support domain of particle i weighted by the smoothing function. The particle approximation for the spatial derivative of the function is

$$\nabla f_i \approx -\sum_{j=1}^{N} V_j f_j \nabla_j W_{ij} = \sum_{j=1}^{N} V_j f_j \nabla_i W_{ij}, \tag{5.11}$$

$$\nabla^2 f_i \approx -\sum_{j=1}^{N} V_j f_j \nabla_j^2 W_{ij} = \sum_{j=1}^{N} V_j f_j \nabla_i^2 W_{ij}, \tag{5.12}$$

where

$$\nabla_i W_{ij} = \frac{\mathbf{r_i} - \mathbf{r_j}}{r_{ij}} \frac{\partial W_{ij}}{\partial r_{ij}} = \frac{\mathbf{r}_{ij}}{r_{ij}} \frac{\partial W_{ij}}{\partial r_{ij}}, \tag{5.13}$$

in which r_{ij} is the distance between particle i and j. It should be noted that $\nabla_i W_{ij}$ is taken with respect to particle i, so the negative sign is removed. The use of particle summation to approximate the integral is a key approximation that makes the SPH method simple without using a background mesh for numerical integration. In addition, the particle approximation introduces the *mass* and *density* of the particle into the equations. This can be conveniently applied to hydrodynamic problems in which the density is a key field variable. This is a major reason for the SPH method being particularly popular for dynamic fluid flow problems. However, the particle approximation is also related to some

numerical problems inherent in the SPH method, such as the particle inconsistency and the tensile instability.

5.2.3 Kernel functions

A kernel function replaces the Delta function in SPH approximation, thus it has to fulfil the requirements following Liu and Liu [269].

Unity The kernel function must obey the normalisation principle to ensure the consistent approximations of homogeneous fields as well as discrete space

$$\int_{\Omega} W(\mathbf{r} - \mathbf{r}', h_s) d(\mathbf{r}') = 1. \tag{5.14}$$

Compact support The condition transforms the approximation from the global operation to the local operation

$$W(\mathbf{r} - \mathbf{r}', h_s) = 0, \text{ if } |\mathbf{r} - \mathbf{r}'| > \kappa_s h_s. \tag{5.15}$$

Positive The kernel function must always be positive for all particles

$$W(\mathbf{r} - \mathbf{r}', h_s) \geq 0. \tag{5.16}$$

Decay The kernel function has to decrease monotonically with a growing distance from the focal particle to the neighbouring particles.

Delta function property W needs to be similar to the Delta-Dirac function

$$\lim_{h \to 0} W(\mathbf{r} - \mathbf{r}', h_s) = \delta(\mathbf{r} - \mathbf{r}') \tag{5.17}$$

with

$$\delta(\mathbf{r} - \mathbf{r}') = \begin{cases} 1, & \text{if } r = r'; \\ 0, & \text{if } r \# r'; \end{cases} \tag{5.18}$$

This condition is achieved if previous four above conditions are fulfilled.

Symmetric property The kernel function should be even to ensure the particles having equal distance from the focal particles have the similar influence.

$$W(\mathbf{r} - \mathbf{r}', h_s) = W(\mathbf{r}' - \mathbf{r}, h_s) \tag{5.19}$$

Smoothness The smooth and continuous kernel function and its derivatives reduce the

effect of particle disorder and the error in approximation of the integral interpolation.

Some kernel functions The primary difference among kernel functions is the order. The choice of the kernel function depends on the problem, the computational algorithm and thus influences the final results.

The Gaussian kernel is considered the best function in SPH by Monaghan [209]. The function states

$$W(R_s, h_s) = \alpha_d e^{-(2R_s)^2} \tag{5.20}$$

with the relative particle distance $R_s = \frac{r}{h_s}$, $r = |\mathbf{r}_i - \mathbf{r}_j|$. The normalisation parameter α_d is chosen from the dimension of the problem, such as $\alpha_d = \frac{2}{\pi^{1/2}h}$, $\alpha_d = \frac{4}{\pi h^2}$, $\alpha_d = \frac{8}{\pi^3 h^3}$ for 1D, 2D and 3D, respectively. In the above equation, the kernel length, h_s, is not $2h_s$. The Gaussian function is independent on the relative distance between particles, thus it ensures smooth and continuous higher derivatives. The function will be zero if $R_s \to \infty$ thus it violates the compact condition. In practice, the function approaches zero quickly thus the compact support condition can be achieved by truncating the kernel without impacting the numerical results.

An alternative kernel function is the Cubic spline kernel that was firstly introduced in [270]. The function reads

$$W(r, h_s) = \alpha_d \begin{cases} 1 - 6R_s^2 + 6R_s^3 & \text{if } 0 \geq R_s \geq 1/2; \\ 2(1 - R_s)^3 & \text{if } 1/2 < R_s \geq 1, \\ 0 & \text{if } R_s > 1 \end{cases} \tag{5.21}$$

with $\alpha_d = \frac{4}{3h_s}$, $\alpha_d = \frac{40}{7\pi h_s^3}$, $\alpha_d = \frac{8}{\pi h_s^3}$ in 1D, 2D and 3D, respectively. The Cubic spline and its first derivative comply with the above kernel function conditions. However, the second derivative becomes a linear step function that can be overcome using higher polynomials, i.e. Quadratic and Quintic spline kernel function.

The Quintic kernel function proposed by Wendland [271] states

$$W(R_s, h_s) = \alpha_d \left(1 - \frac{R_s}{2}\right)^4 (2R_s + 1) \qquad 0 \leq R_s \leq 2 \tag{5.22}$$

where α_d is equal to $7/4\pi h_s^2$ in 2D and $21/16\pi h_s^3$ in 3D. In the following parts, only kernel having influence domain of $2h_s$ ($R_s \leq 2$) is considered. Since the scope of this thesis is wave generation, further detail for kernel function can be found in the book by Liu and Liu [269].

5.2.4 SPH-approximation of the governing equations

The Lagrangian form of the continuity equation states

$$\frac{D\rho}{Dt} + \rho\nabla\mathbf{v} = s_m \tag{5.23}$$

where D/Dt represents the substantial derivative by time t, $\mathbf{v}$ is the velocity vector, ρ is the material density. The source term s_m is zero for source-free fields, thus the shortened continuity equation is given by

$$\frac{D\rho}{Dt} = -\rho\nabla\mathbf{v}. \tag{5.24}$$

The momentum equation that represents a relationship between the stress acting on a piece of the domain and its acceleration states

$$\frac{D\mathbf{v}}{Dt} = \frac{1}{\rho}\left[\nabla\sigma + \mathbf{f}\right] + s_v, \tag{5.25}$$

with

$$s_v = -\mathbf{v}s_m\frac{1}{\rho}. \tag{5.26}$$

The vector $\mathbf{f}$ is the external volumetric forces, i.e. gravity or external body forces. The surface stress tensor σ can be split into isotropic pressure portion by mean of the mean normal stresses and a deviatoric part:

$$\sigma = -p\delta + \tau, \tag{5.27}$$

with the pressure p, the unity tensor δ_s, and the traceless deviatoric stress tensor τ.

Continuity equation

There are two approaches to estimate the density of SPH particles. The first one is the summation of all neighbouring particles which are located within the kernel length. The second approach is SPH estimation of the continuity equation for flow.

Direct density evaluation A weighted sum over neighbouring particles

$$\rho_i = \sum_{j=1}^{N} m_j W_{ij} = \sum_{j=1}^{N} V_j \rho_j W_{ij}, \tag{5.28}$$

with $V_j = \frac{m_j}{\rho_j}$. This approach directly conserves the mass m_i is a constant as the number of neighbouring particles are the same. However, this approach is unable to

handle the large surface deformation or the particles near boundaries since the kernel area is truncated. Thus, the second approach is derived.

Continuity equation Applying the SPH operation to the continuity equation, we obtain

$$\frac{D\rho_i}{Dt} = -\rho_i \sum_{j=1}^{N} V_j \mathbf{v}_j \nabla_i W_{ij}. \tag{5.29}$$

However, the above equation only considers the neighbouring particles except the focal particle. Hence, this does not ensure symmetric particle interaction. To include a relative particle velocity, the identity

$$\nabla 1 = 0 \tag{5.30}$$

is used and its respective SPH approximation is

$$\nabla 1 = \sum_{j=1}^{N} V_j \nabla_i v_i W_{ij} = 0. \tag{5.31}$$

The above approximation is added to the right hand side of the Eq.5.29 leading to the symmetric formulation

$$\frac{D\rho_i}{Dt} = \rho_i \sum_{j=1}^{N} [V_j(\mathbf{v}_i - \mathbf{v}_j)] \nabla_i W_{ij}. \tag{5.32}$$

Alternatively, the following identity can be used

$$-\rho \nabla v = -[\nabla(\rho v) - v \nabla \rho] \tag{5.33}$$

in addition to the fundamental momentum equation that leads to the discrete form

$$\frac{D\rho_i}{Dt} = v_i \sum_{j=1}^{N} V_j \rho_j \nabla_i W_{ij} - \sum_{j=1}^{N} V_j v_j \rho_j \nabla_i W_{ij}, \tag{5.34}$$

hence, one gets

$$\frac{D\rho_i}{Dt} = \sum_{j=1}^{N} m_j (\mathbf{v}_i - \mathbf{v}_j) \nabla_i W_{ij}. \tag{5.35}$$

Equivalence of direct and continuity approaches

The two above approaches to approximate the density, which are direct summation and differential form, are formally equivalent [272]. At a time t, the presented approaches

have been written as

$$\rho_i(t) = \sum_j m_i W(r(t)), \tag{5.36}$$

$$\frac{D\rho_i(t)}{Dt} = \sum_j m_j(\mathbf{v}_i(t) - \mathbf{v}_j(t))\nabla_i W(r(t)) \tag{5.37}$$

Then, a constant smoothing length is assumed. Hence, the distance between particle r represents the time independent variable for the kernel function W. The first equations has the following differentiation with respect to time

$$\frac{D\rho_i(t)}{Dt} = \sum_j m_j \frac{d}{dt}[W(r(t))] = \sum_j m_j \frac{dr(t)}{dt}\frac{W(r(t))}{dr(t)}, \tag{5.38}$$

Introducing the two substitutions

$$\frac{dr(t)}{dt} = \frac{(x_i(t) - x_j(t))(v_i(t) - v_j(t))}{r(t)} \tag{5.39}$$

and

$$\nabla W(r(t)) = \frac{1}{r(t)}\frac{dW(r(t))}{dr(t)}(r_i(t) - r_j(t)) \tag{5.40}$$

and applying to

$$\frac{D\rho_i(t)}{Dt} = \sum_j m_j \frac{(r_i(t) - r_j(t))(v_i(t) - v_j(t))}{r(t)}\frac{\nabla_i W(r(t))r(t)}{(r_i(t) - r_j(t))} \tag{5.41}$$

leads to

$$\frac{D\rho_i(t)}{Dt} = \sum_j m_j(v_i(t) - v_j(t))\nabla_i W(r(t)), \tag{5.42}$$

which is equivalent to the direct summation equation. Thus, applying the two equations (Eq.5.39-5.40) will result in an equivalent theoretical solution is the initial condition

$$\rho_i(t) = \sum_j m_i W(r(t_0)), \tag{5.43}$$

is applied to the differential formulation.

However, it should be noted that the practical solution will be definitely slightly different because of numerical issues [208]. Moreover, the equivalency is achieved with a specific kernel function and it is only valid for the isotropic and homogenerous kernels.

Momentum equation

Applying SPH operations in the Eq.5.25 one obtains

$$\frac{Dv_i}{Dt} = -\frac{1}{\rho_i}\sum_j \left[m_j \frac{\sigma_j}{\rho_j}\right] \nabla_i W_{ij} + \frac{\mathbf{f}}{\rho_i}. \tag{5.44}$$

Considering the identity

$$\sum_{j=1}^{N} m_j \frac{\sigma_i}{\rho_i \rho_j} \nabla_i W_{ij} = \frac{\sigma_i}{\rho_i}\left(\sum_{j=1}^{N} \frac{m_j}{\rho_j} \nabla_i W_{ij}\right) = 0, \tag{5.45}$$

we get the symmetric formulation

$$\frac{Dv_i}{Dt} = \sum_j m_j \left[\frac{\sigma_i + \sigma_j}{\rho_i \rho_j}\right] \nabla_i W_{ij} + \frac{\mathbf{f}_i}{\rho_i}. \tag{5.46}$$

Another approximation of the momentum equation can be obtained if we use the following identity

$$\frac{1}{\rho}\nabla\sigma = \nabla\left(\frac{\sigma}{\rho}\right) + \frac{\sigma}{\rho^2}\nabla\rho. \tag{5.47}$$

Therefore,

$$\frac{D\mathbf{v}_i}{Dt} = \sum_{j=1}^{N} V_j \frac{\sigma_j}{\rho_j} \nabla_i W_{ij} + \frac{\sigma_i}{\rho_i^2} \sum_{j=1}^{N} V_j \rho_j \nabla_i W_{ij} + \frac{\mathbf{f}_i}{\rho_i}, \tag{5.48}$$

and with the simplification we have

$$\frac{Dv_i}{Dt} = \sum_j m_j \left(\frac{\sigma_i}{\rho_i^2} + \frac{\sigma_j}{\rho_j^2}\right) \nabla_i W_{ij} + \frac{\mathbf{f}_i}{\rho_i}. \tag{5.49}$$

The symmetric formulations Eq.5.46 and Eq.5.49 are preferred. Eq.5.49 is applied in this thesis. The momentum equation can be split due to Eq.5.27 to get separate equations for the pressure and the deviatoric stresses. The following parts of the thesis uses the pressure evaluations.

5.2.5 Pressure evaluation

The WCSPH evaluates pressure of compressible fluid by state equation. The use of different types of state equations was studied in [273]. The study showed that different state equations have weak influence on numerical results. The method is explicit, simple, and efficient. It is able to simulate accurately a number of problems, however WCSPH tends to face the noisy pressure field, negative pressure field at area, particle clustering,

and requires time step restriction due to explicit formulation [274].

ISPH is an alternative method where the fluid density is constant throughout the simulation. Hence, it is considered accurate and free from pressure noise. However, it might get unstable if the particles are strongly distorted. ISPH unfortunately needs iterative solving scheme for the implicit links between the pressure and the velocities leading to heavy computational cost [275, 276]. In our study, ISPH is not applied and will not be further discussed.

WCSPH Monaghan [209] introduced an equation of state for simulating water flow

$$p = \left(\left(\frac{\rho}{\rho_0} \right)^{\gamma} - 1 \right) B, \tag{5.50}$$

where ρ_0 is a reference density. The reference pressure B and γ are empirically chosen for seawater as $B \approx 3.047 \cdot 10^8 Pa$ and $\gamma \approx 7$. This equation has also been named Tait's equation. In this study, $\gamma = 7$ is in use following Monaghan [209]. As the equation of state is used, the above reference pressure B leads to unfeasible time step limit since the Courant number restricts the time step size to ensure the stable response of the discrete approach. To limit the disturbance of the pressure force, the maximum time step size is constrained by the spacial resolution (h_s kernel length) and the reciprocal speed of sound $1/c_s$

$$\Delta t \approx \frac{h_s}{c_s}. \tag{5.51}$$

Since

$$\frac{\delta\rho}{\rho} \approx \frac{v^2}{c_s^2} \tag{5.52}$$

where v is the maximum speed of the fluid, so we can ensure $|\delta\rho|/\rho \approx 0.01$ if $v/c_s < 0.1$. The pressure and the speed of sound is related by

$$p = \frac{c_s^2 \rho_0}{\gamma}. \tag{5.53}$$

Thus,

$$B = c_s^2 \frac{\rho_0}{\gamma} \tag{5.54}$$

with small relative density variation. Due to the high reported value of B, the $Courant - Friedrichs - Lewy(CFL)$ restriction requires a more practical value for c_s.

Monaghan used an artificial compressibility to reduce speed of sound and to reduce the time step restriction by considering fluid incompressible as the Mach number kept small,

$M \approx 0.1$. The maximum speed of sound is given by

$$c_s = 10 v_{max}, \tag{5.55}$$

to keep Mach number below the limit. v_{max} is the maximum fluid velocity depending on considering simulation. According to Torricelli's law, for a given water column height H, v_{max} can be estimated according to

$$v_{max}^2 = 2gH \tag{5.56}$$

Therefore, one gets the employed reference pressure

$$B = \frac{100 v_{max}^2 \rho_0}{\gamma} \tag{5.57}$$

The equation of state is used herein throughout this thesis.

5.2.6 Boundary conditions

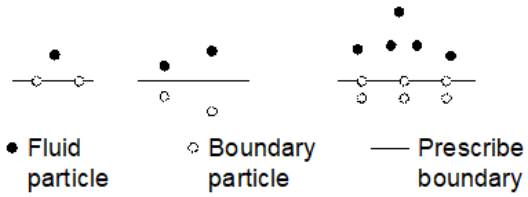

Figure 5.5: Basic boundary concepts

Repulsive boundary forces. Fig.5.5 illustrates three basic boundary methods used in SPH algorithm. The repulsive boundary is proposed by Monaghan [209] based on the solid points treated as an extra class of particle. Theses boundary particles' locations are initiated in the particle distribution process. The boundary particles exert a boundary force on the approaching fluid particles and prevent them penetrating the boundary. The repulsive force depends on the distance between the fluid particles and the boundary one and the amount of force are proportional to the distance between them. The method has advantages in its applicability for variety of forces and the the particle are prevented effectively from penetrating the boundary. However, the areas near the boundary always experience particle deficiency compared to the free surface. In addition, the repulsive force make the interpolation of surface forces and application of boundary condition (i.e. no-slip) difficult.

Ghost particles. The arbitrary particles referred as ghost particles that are created by mirroring the fluid particle approaching boundary lines are located on the other side of the boundary lines. The arbitrary particles possess the same properties as the

approaching fluid particles and they are treated as the regular particles. It is handle to applied the no-slip or free slip boundary conditions with this method. Free-slip condition is obtained by assigning the ghost particles 'velocity tangentially to the boundary or switching the direction of the tangential velocity to achieve no-slip condition. The approach has a compatible results with the repulsive boundary, the major difference between the two method is the boundary only considers the number of particles as they are required. This is specially advantageous for large domains. On the other hand, the method faces challenges as the boundary has complex geometries or has particle interaction among multiple classes. In addition, the generation of ghost particle every time step requiring more computational effort. Another ghost particle utilises the prescribed fixed boundary is the fixed boundary particle method [277] fixes the resolution of the boundary particles and evaluate their properties at the corresponding mirror position inside the fluid domain.

Fixed particles. The boundary is represented by multiple rows of particles ensuring the full kernel support for the moving particles near boundary. The boundary particles are computed every time step as the fluid particle, however, their accelerations are not updated so that their positions remain unchanged under the computational process. The method has advantage in the application of the free-slip boundary condition and the prescribed motion of the moving boundaries. A disadvantage relates to the total number of particle in simulation that includes the boundary particles. It might be negligible as the number of moving particles outweigh the number of boundary particles. The spurious pressure field is another disadvantage of the method due to the reduction of fluid particles in the support area of focal particles near boundary.

Choice of boundary is dependent on the problem. In this thesis, the fixed particles approach is chosen due to it simplicity and flexibility. The pressure and the density of the fluid particles at the wall are different in the above boundary methods. Since the fluid particles'properties are interpolated from its neighbouring particles within the fluid domain, the pressure at the boundary can be computed from the forces at the boundary over a certain reference length. As the ghost or fixed particles boundary approaches are applied, the pressure and density of the fluid particles are computed using the fluid neighbouring particles within the fluid domain and the boundary particles. The ghost particles approach mirror the fluid particles near boundary thus the neighbouring fluid particles are included in the estimation of the fluid particle in the vicinity of the boundary. This lead to the dependence of the pressure on the properties of the fluid particles. Fixed boundary particles possess their own properties. Thus, the computational process includes both the fluid particles and the boundary particles within the support domain.

5.2.7 Time integration

The time step plays an important role in stability of the numerical scheme. An appropriately chosen time step can make the numerical scheme work and the larger time step might lead to a wrong answer and the interruption of simulation. There are a number of time integration schemes available, where the equation of motion is integrated through time using Verlet scheme, two-stage Symplectic method, or variable time step.

Verlet scheme. The Verlet scheme is split into two parts, the advantage of the method is that it does not require multiple calculations for each step, i.e. predictor and corrector. The variables are updated in the next time step from the previous solutions with

$$\begin{aligned} \mathbf{v}_i^{n+1} &= \mathbf{v}_i^{n-1} + 2\Delta t \frac{d\mathbf{v}_i}{dt} \\ \mathbf{r}_i^{n+1} &= \mathbf{r}_i^n + \Delta t \mathbf{v}_i^n + 0.5\Delta t^2 \frac{d\mathbf{v}_i}{dt} \\ \rho_i^{n+1} &= \rho_i^{n-1} + 2\Delta t \frac{d\rho_i}{dt}, \end{aligned} \tag{5.58}$$

where subscript n represents for the time step.

To stop the divergence of integrated values, every N_s steps (≈ 50), the variables are calculated using

$$\begin{aligned} \mathbf{v}_i^{n+1} &= \mathbf{v}_i^{n-1} + \Delta t \frac{d\mathbf{v}_i}{dt} \\ \mathbf{r}_i^{n+1} &= \mathbf{r}_i^n + \Delta t \mathbf{v}_i^n + 0.5\Delta t^2 \frac{d\mathbf{v}_i}{dt} \\ \rho_i^{n+1} &= \rho_i^n + \Delta t \frac{d\rho_i}{dt}, \end{aligned} \tag{5.59}$$

For cases in which the numerical stabilities are an issue, the frequency of N_s can increase to ≈ 10, the predictor-corrector time integration scheme should be used, for instance Symplectic scheme.

Symplectic scheme Symplectic time integration algorithm is applied in this paper. The corrected velocity is calculated from the position and the density at the middle of the time step as follow:

$$\begin{aligned} \mathbf{r}_i^{n+\frac{1}{2}} &= \mathbf{r}_i^n + \frac{\Delta t}{2} \frac{d\mathbf{r}_i^n}{dt}, \\ \rho_i^{n+\frac{1}{2}} &= \rho_i^n + \frac{\Delta t}{2} \frac{d\rho_i^n}{dt} \end{aligned} \tag{5.60}$$

where the pressure $p_i^{n+\frac{1}{2}}$ is calculated using the equation of state above. The subscript n denotes the time step. Then, the field properties are calculated at the next time step according to

$$\begin{aligned} \mathbf{v}_i^{n+1} &= \mathbf{v}_i^{n+\frac{1}{2}} + \Delta t \frac{d\mathbf{v}_i^{n+\frac{1}{2}}}{dt} \\ \mathbf{r}_i^{n+1} &= \mathbf{r}_i^n + \Delta t \mathbf{v}_i^{n+\frac{1}{2}}, \end{aligned} \tag{5.61}$$

and the updated value of density $d\rho_i^{n+1}/dt$ is calculated by the value of $\mathbf{v}_i^{n+1}$ and $\mathbf{r}_i^{n+1}$

[208].

Variable time step. A variable time step Δt is required with the explicit time integration schemes where the time step depends on the CFL condition. Monaghan [278] suggested a variable time step Δt with

$$\begin{aligned} \Delta t &= CFL \cdot min(\Delta t_f, \Delta t_{cv}) \\ \Delta t_f &= min_i(\sqrt{h/|f_i|}) \\ \Delta t_{cv} &= min_i \frac{h}{c_s + max_j \left| \frac{h \mathbf{v}_{ij} \cdot \mathbf{r}_{ij}}{(r_{ab}^2) + \eta^2} \right|} \end{aligned} \tag{5.62}$$

in which Δt_f bases on the force per unit mass ($|f_i|$) and Δt_{cv} combines the Courant and the viscous time step.

5.3 Application of SPH to free surface flows

Water is an incompressible fluid. Hence, it is required that the velocity of sound is large enough to restrict density fluctuation smaller than 0.01. The equation of state given by Batchelor [279] was modified to achieve a smaller speed of sound. This section describes the numerical scheme that is applied within DualSPHysics code. The governing equations, the density correction and stabilization schemes, and the boundary condition are included.

Navier-Stokes equations are applied to govern the hydrodynamics systems. In SPH, Navier-Stokes equations are applied within Newtonian fluid which has a linear relationship between deformation and tension. Hence, the WCSPH means the fluid is defined as compressible rather than incompressible to allow the use of Equation of state to speed up calculations.

5.3.1 Governing equations

The discrete form of the continuity and the momentum equations are given by

$$\frac{D\rho_i}{Dt} = \sum_{j=1}^{N} m_j \left(\mathbf{v}_i - \mathbf{v}_j\right) \nabla_i W_{ij}, \tag{5.63}$$

$$\frac{D\mathbf{v}_i}{Dt} = \sum_{j=1}^{N} m_j \left(\frac{p_j}{\rho_j^2} + \frac{p_i}{\rho_i^2} \right) \nabla_i W_{ij} + \frac{f_i}{\rho_i}. \tag{5.64}$$

The external volumetric force $f_i = \rho_i \mathbf{g}$ in this study is the gravity force where g is the vector of gravitational acceleration, hence

$$\frac{D\mathbf{v}_i}{Dt} = \sum_{j=1}^{N} m_j \left(\frac{p_j}{\rho_j^2} + \frac{p_i}{\rho_i^2} \right) \nabla_i W_{ij} + \mathbf{g}. \tag{5.65}$$

In WCSPH, the accurate equation of state ([279]) was modified to give a smaller speed of sound used in the pressure equation:

$$p_i = B \left(\left(\frac{\rho_i}{\rho_o} \right)^{\gamma} - 1 \right) \tag{5.66}$$

where, $\gamma = 7$ in case of water; p_i is the pressure of particle $'i'$; ρ_0 is the reference density, which is approximately 1000 kg/m^3; ρ_i is the particle density from the continuity equation; $B = c_0^2 \rho_0 / \gamma$ is the maximum limit of the density with c_0 as the speed of sound at the reference density. The choice of c_0 ensures the weakly-compressible regime in which the density fluctuation is within 1%. The density variation in fluid flow is $\approx M^2$, where M is the Mach number ([209]). If $\Delta\rho \approx 0.01\rho_0$, $M = max_t(||\vec{u}||)/c_0 \leq 0.1$, where $max_t(||\vec{u}||)$ is the maximum intensity of the velocity expected in the flow time evolution. Hence, the first constrain for the speed of sound is $c_0 \geq 10 max_t(||\vec{u}||)$. For gravity wave simulation, the wave celerity might be larger than the fluid flow velocity, thus other constrain of the speed of sound results from the wave celerity, $c_w^2 = gtanh(kd)/k$ where d is the still water depth, k is the wave number. When $kd \to 0$, the wave celerity becomes $c_w^2 = \sqrt{gd}$. Choosing $c_0 = 10\sqrt{gd}$ leads to the condition of the speed of sound $c_0 \geq 10 Max(\sqrt{gd}, max_t(||\vec{u}||))$ ([280, 281]). To provide uniform particle distribution and a regular pressure field, δ-Plus-SPH scheme is derived ([282]) using a quasi-Lagrangian approach. In this study, this approach is not applied since the main purpose is the variation of the pressure in the flow field rather than the stability of the particle pressure.

5.3.2 Artificial viscosity

The artificial viscosity term has been added in the momentum equation acting as an atomic force. This term creates a repulsive force when two particles approach to prevent penetration and a pulling force when two particles recede from each other [208]. The momentum equation has the following form

$$\frac{D\mathbf{v}_i}{Dt} = -\sum_{j=1}^{N} m_j \left(\frac{P_j}{\rho_j^2} + \frac{P_j}{\rho_i^2} + \Pi_{ij} \right) \nabla_i W_{ij} + \mathbf{g} \tag{5.67}$$

The viscous force term Π_{ij} has the general form:

$$\Pi_{ij} = \begin{cases} \frac{-\alpha\overline{c_{ij}}\mu_{ij}+\beta\mu_{ij}^2}{\overline{\rho_{ij}}}; \mathbf{v}_{ij}.\mathbf{r}_{ij} < 0; \\ 0; \mathbf{v}_{ij}.\mathbf{r}_{ij} > 0. \end{cases} \tag{5.68}$$

where, ρ and P are the density and pressure, $\mathbf{g}$ is the gravitational acceleration. i and j are the particle indices and m is the mass of particles. $\mathbf{r}_{ij} = \mathbf{r}_i - \mathbf{r}_j$ and $\mathbf{v}_{ij} = \mathbf{v}_i - \mathbf{v}_j$. $\mu_{ij} = h\mathbf{v}_{ij}.\mathbf{r}_{ij}/(\mathbf{r}_{ij}^2 + \eta^2)$ and $\overline{c_{ij}} = 0.5(c_i + c_j)$ is the mean speed of sound, $\eta = 0.01h^2$. $\overline{\rho_{ij}} = 0.5(\rho_i + \rho_j)$ and W_{ij} is the kernel function. The value of $\alpha = 0.01$ and $\beta = 0$ have proven to give the best results in the validation of wave flumes to study wave propagation and wave loading exerted onto structures [211].

5.3.3 Kernel function

The kernel function is a function of the ratio $R_s = r/h$, where $r = |\mathbf{r}_{ij}|$ is the distance between particle $'i'$ and particle $'j'$, while h is the smoothing length, specifying the controlled area around particle $'i'$ in which the number of neighboring particles are calculated. In this study, the Quintic kernel function is chosen:

$$W(R_s, h_s) = \alpha_d \left(1 - \frac{R_s}{2}\right)^4 (2R_s + 1); \qquad 0 \leq R_s \leq 2 \tag{5.69}$$

with α_d equals to $7/4\pi h_s^2$ in two-dimensional simulations.

5.3.4 Time stepping algorithm

Symplectic time integration algorithm is applied in this thesis. The corrected velocity is calculated from the position and the density at the middle of the time step as follow:

$$\begin{aligned} \mathbf{r}_i^{n+\frac{1}{2}} &= \mathbf{r}_i^n + \tfrac{\Delta t}{2}\tfrac{d\mathbf{r}_i^n}{dt}, \\ \rho_i^{n+\frac{1}{2}} &= \rho_i^n + \tfrac{\Delta t}{2}\tfrac{d\rho_i^n}{dt} \end{aligned} \tag{5.70}$$

where the pressure $p_i^{n+\frac{1}{2}}$ is calculated using the equation of state above. The subscript n denotes the time step. Then, the field properties are calculated at the next time step according to

$$\begin{aligned} \mathbf{v}_i^{n+1} &= \mathbf{v}_i^{n+\frac{1}{2}} + \Delta t\tfrac{d\mathbf{v}_i^{n+\frac{1}{2}}}{dt} \\ \mathbf{r}_i^{n+1} &= \mathbf{r}_i^n + \Delta t\mathbf{v}_i^{n+\frac{1}{2}}, \end{aligned} \tag{5.71}$$

and the updated value of density $d\rho_i^{n+1}/dt$ is calculated by the value of $\mathbf{v}_i^{n+1}$ and $\mathbf{r}_i^{n+1}$.

5.3.5 Boundary condition

We use Dynamic Boundary Condition (DBC) which is available in the DualSPHysics code ([220]). The boundary particles satisfy the fundamental equations, however, they are forced to remain at the fixed positions. Thus the boundary particles can automatically generate a repulsive force on their neighboring fluid particles resulting from the change of their density when the fluid particles approach them.

The wall particles are imposed zero acceleration

$$\mathbf{a}_i = 0. \tag{5.72}$$

The moving walls can be assigned an initial velocity v_i to the dedicated value $\tilde{v}_{wall}$ or the time dependence motion $\tilde{v}_{wall(t)}$. Therefore, the boundary position are updated from an integration of the prescribed velocities. The motions of the moving object are interpolated from the neighboring particles by summarizing the properties of the surface boundary particles. The boundary particle k experiences a force per unit mass

$$\mathbf{f}_k = \sum \mathbf{f}_{ki} \tag{5.73}$$

where $\mathbf{f}_{ki}$ is the force per unit mass by the fluid particle i on the boundary particle k that reads

$$m_k \mathbf{f}_{ki} = -m_i \mathbf{f}_{ik} \tag{5.74}$$

The position of the whole moving structure is defined by

$$M_b \frac{d\mathbf{V}_b}{dt} = \sum_{k \in BPs} m_k \mathbf{f}_k \tag{5.75}$$

$$I_b \frac{d\mathbf{\Omega}_b}{dt} = \sum_{k \in BPs} m_k (\mathbf{r}_k - \mathbf{R}_0) \times \mathbf{f}_k \tag{5.76}$$

in which M_b is the mass of the body, I_b is the moment of inertia, V_b is the velocity of the body, Ω_b is the rotational velocity, and R_0 is the centre of mass. The V and Ω are calculated at the beginning of the next time step, then each boundary particle k has a velocity distributed by

$$\mathbf{v}_k = \mathbf{V}_b + \mathbf{\Omega}_b \times (\mathbf{r}_k - \mathbf{R}_0) \tag{5.77}$$

Finally, the position of the moving particles are computed using the above velocity.

5.3.6 Wave-maker theory

The waves of long crested type are created by the motion of the wave maker. The wave maker can be a flap which is hinged at the bottom of the wave tank or it can be a piston at one end of the numerical wave flume. To generate a prescribed wave height, the displacement of the wave maker is assigned at the beginning of the simulation. The wave height and the wave maker displacement has a relation which is derived by Biésel [283] and by Madsen [284]. The following sections will discuss the transfer function that express the above relation for a piston-type wave maker.

First order regular wave

The relation function is derived on the assumption that the fluid is irrotational, incompressible, and that there is a constant pressure at the free surface. The Biésel function [283] relates the first order Stokes wave with the stroke of the piston type wave maker as follows. First, the surface profile of monochromatic sinusoidal wave propagating at infinite distance from the wave maker on horizontal direction is

$$\eta(x) = \frac{H}{2} cos(\omega t - \kappa x + \phi) \tag{5.78}$$

where H is the wave height, x is the distance from the wave maker and ϕ is the initial phase. $\omega = 2\pi/T$ is the angular frequency and $\kappa = 2\pi/L$ is the wave number with T equals to the wave period and L is the wave length. The choice of initial phase ϕ is a random number in the range $(0, 2\pi)$.

In far-field area, the Biesel function relates the wave height to the wave-maker stroke by equation

$$\frac{H}{S_0} = \frac{2sinh^2(\kappa d)}{sinh(\kappa d)cosh(\kappa d) + \kappa d} \tag{5.79}$$

where S_0 is the piston stroke. While the stroke is computed, the piston motion is generated by

$$e_t(t) = \frac{S_0}{2} sin(\omega t + \phi) \tag{5.80}$$

Second order regular wave

The stroke of the wave maker is similar to Eq.5.80 above, where $H/S_0 = m_1$,

$$m_1 = \frac{H}{S_0} = \frac{2sinh^2(\kappa d)}{sinh(\kappa d)cosh(\kappa d) + \kappa d} \tag{5.81}$$

The second term is presented to simulate the second order Stokes wave

$$e_2(t) = \left[\left(\frac{H^2}{32d}\right)\left(\frac{3cosh(kd)}{sinh^3(kd)}\right) - \frac{2}{m_1}\right] sin(2\omega t + 2\phi) \tag{5.82}$$

Therefore, the time series of the motion of the wave maker is

$$e(t) = \frac{S_0}{2} sin(\omega t + \phi) + \left[\left(\frac{H^2}{32d}\right)\left(\frac{3cosh(\kappa d)}{sinh^3(\kappa d)}\right) - \frac{2}{m_1}\right] sin(2\omega t + 2\phi) \tag{5.83}$$

The limitation of the application follows the condition of $HL^2/d^3 < 8\pi^2/3$.

Irregular wave

The real ocean condition observes the random sea state, thus the simulation of irregular wave is applied in DualSPHysics using the method of Liu *et.al* [285]. The wave spectra is chosen from the beginning of the simulation, then the Biesel transfer function is applied to each component. The procedure is summarised as follows

- Choosing of wave spectrum from its characteristics, such as peak frequency, spectrum shape, etc.

- Calculating the spectrum parts $N_s (N_s > 50)$ in the interval (f_{start}, f_{end}). The value of the amplitude of the interval S_n are smaller than those assumed for the peak frequency f_p. For instance, $S_n(f_{start}) < 0.01 S_n(f_p)$ and $S_n(f_{end}) < 0.01 S_n(f_p)$.

- The frequency band width is $\Delta f = (f_{stop} - f_{end})/N$. There are N_s linear waves.

- Each constitutive wave properties are computed so that the angular frequency ω_i, amplitude a_i and initial phase ϕ_i (random between 0 and π)

$$\omega_i = 2\pi f_i \tag{5.84}$$

$$a_i = \sqrt{2 S_n(f_i)\Delta f} = H_i/2 \tag{5.85}$$

- The stroke of each component is calculated using the transfer function in Eq.5.79.

$$\frac{H_i}{S_{0,i}} = \frac{2sinh^2(\kappa_i d)}{sinh(\kappa_i d)cosh(\kappa_i d) + \kappa_i d} \tag{5.86}$$

- The final time series of the displacement of the piston is given by

$$e(t) = \sum_{i=1}^{N} \frac{S_{0,i}}{2} sin(\omega_i t + \phi_i) \tag{5.87}$$

Jonswap and Pierson-Moskowitz spectra are applied in DualSPHysics code [220]. The change of the random seed in the code will obtain different phase σ_i, thus generating different irregular wave time series with same significant wave height (H) and peak period (T_p).

In order to avoid the wave reflection and to prolong the simulation, the right boundary of the domain has a passive beach absorption. The dissipating beach is straightforward and easy to apply. [212] shows that the beach provides good dissipation results compared with the passive wave absorption. In this work, we use a dissipating beach because of its simplicity.

5.4 Validation of SPH with exact large-amplitude regular waves

To investigate the behaviour of flow beneath the numerically generated wave, a steady wave propagating over still water in a two-dimensional wave flume is numerically modeled. DualSPHysics which is an SPH code has been used in this research to generate the non-linear waves. The DualSPHysics code was first introduced in 2011 [220] and the latest version DualSPHysics 5.0 released in 2021 includes the basic examples of SPHysics and added new features. This code has been used in wave simulation [210, 211, 286] and the simulated results have shown a good agreement with experimental tests. We first simulate a numerical wave train using DualSPHysics and then study the flow properties within the fluid domain over one wave length. The velocity and pressure fields are investigated and the variation of these are validated against recently obtained exact results from the full non-linear Euler equations [87].

The aim of this thesis is to verify the velocity profile and the pressure variation inside the fluid domain over one wave length obtained from a numerically simulated SPH model with some exact qualitative results (i.e. increasing/decreasing trend or constant value of a flow field) from a fully non-linear Euler equation for water wave model. A numerical wave flume has been modeled and a regular wave train is created by the horizontal displacement of a wave paddle on one side of the flume. A passive beach is used to dissipate the energy of the wave on the other side. The extracted numerical results are compared with some recently available exact results from a non-linear steady water wave model based on the Euler equations for irrotational flow. The flow properties under wave crests, wave troughs, and along the distance from the wave crest to the wave trough over one wave length are investigated. The horizontal and vertical velocity components and the pressure in the fluid domain agree well with the analytical results.

5.4.1 Numerical simulation

Computational domain

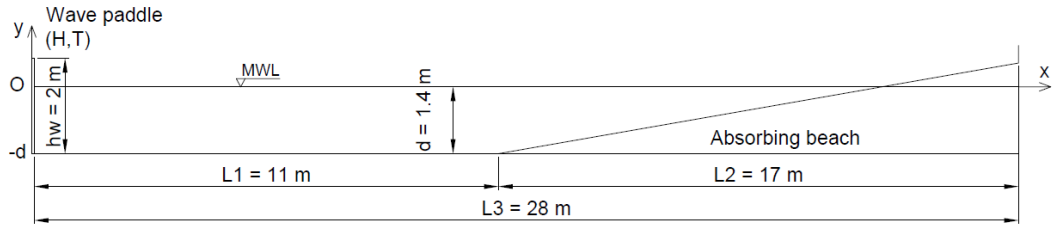

Figure 5.6: Sketch of numerical wave flume.

Fig.5.6 shows the dimensions of the wave flume. A wave paddle on the left-hand side creates a non-linear wave, its height (h_W) is 2 m. The flatbed length is $L1 = 11$ m. The beach on the right-hand side is $L2 = 17$ m long and the total length of the wave flume is $L3 = 28$ m. The beach on the right-hand side acts as a passive wave absorption. Its slope is 1:10. The water depth d is 1.4 m, in comparison with the wave height ($H = 0.2$ m) and the wave period ($T = 1.3$ s), the wave falls into the deep water wave condition. This assumption fits the conclusion of [2] in which the Stokes wave is suitable for modelling deep water small amplitudes waves. A viscous damping zone ([287]) is not considered in the present case since it was not implemented at the numerical model at this stage. Moreover, the main purpose of this study focuses on the flow properties; hence the choice of absorbing beach is for simplicity.

The resolution of the model (i.e. the inter-particle distance) decides the total simulation time and it affects the wave height interpolation in following part of the research. In case of wave generation simulation, [212] studied five different resolutions and the authors have suggested that the ratio of the wave height to the distance between particles (dp) should be higher than 10. A finer resolution will not substantially improve the model accuracy. In the next section, simulation results with three different inter-particle distance $dp = 0.005m, dp = 0.01m$, and $dp = 0.02m$ are examined. Based on these studies, we choose the initial distance among particles and the CFL coefficient for this research.

The simulation has been performed using DualSPHysics code on GPU-CPU, NVIDIA GPU card Quadro M4000. The computational capacity is 5.2, 13 cores, 8GB memory.

5.4.2 Results and discussions

To study the flow properties, it is first necessary to examine whether the waves can be successfully generated and to determine the positions of the wave crest and the wave

trough in the numerical wave tank.

Wave generation

Fig.5.7 shows the wave generated at t = 16.78s. The phenomenon of wave height decaying along the length of the flume is discussed in ([212, 217, 219, 288]). The instability of the pressure field, the boundary condition and the kernel function properties considered are the main reasons for this wave height decay. Despite this discrepancy, we use such a wave in this paper over the region where the wave height is almost constant. We aim to study the flow properties under surface waves, thus we investigate these properties under the wave crest and the wave trough within one wave length. There are three crests and three troughs on the region with flat-bed which are presented in Table 5.1. The flow properties will be discussed further in the following sections.

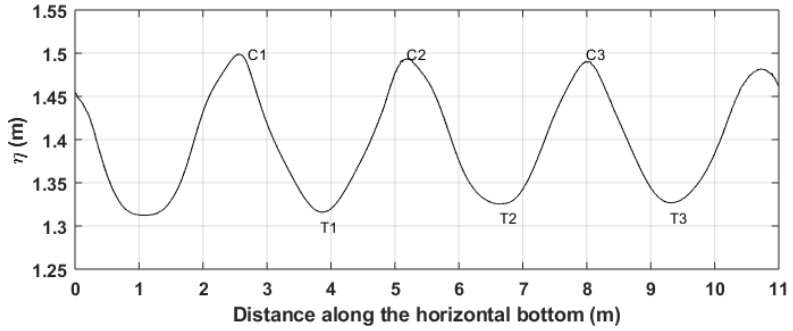

Figure 5.7: The surface elevation for regular wave at $t = 16.78s$.

Crest	x-position (m)	Trough	x-direction (m)
C1	2.56	T1	3.84r
C2	5.18	T2	6.64
C3	7.98	T3	9.30

Table 5.1: Wave crest and wave trough positions.

Convergence study

The purpose of this section is to examine the effect of distance between particles on flow properties including velocity and pressure field. The simulations are set up with different initial distances among the particles and a constant CFL number to examine the effect of the initial distances. Three different resolutions $dp = 0.005m$, $dp = 0.01m$ and $dp = 0.02m$ are considered. The first simulation with ($dp = 0.005m$) takes 25 hours to complete while the second and the third one with $dp = 0.01m$ and $0.02m$ takes 3.9 hours and 36 mins, respectively.

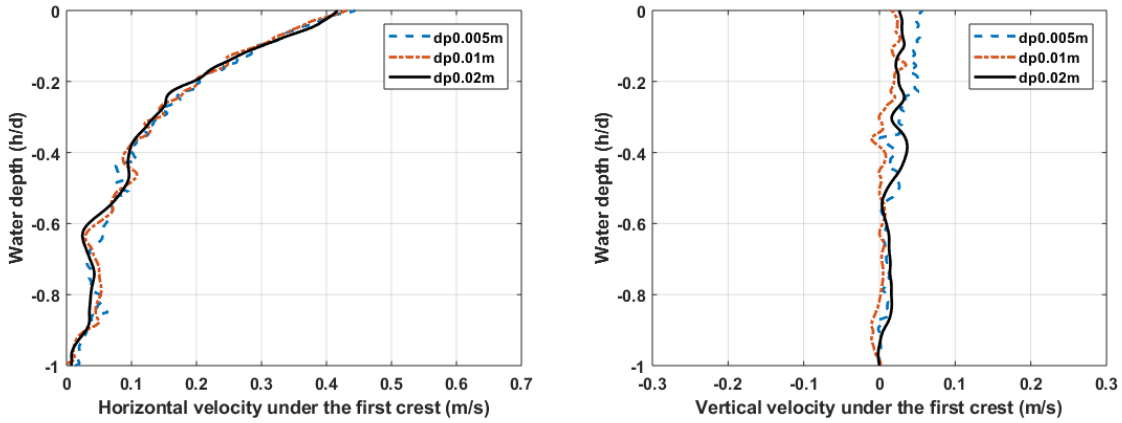

(a) (b)

Figure 5.8: Velocity with three different initial distance among particles dp=0.005m, dp=0.01m and dp=0.02m under C1.

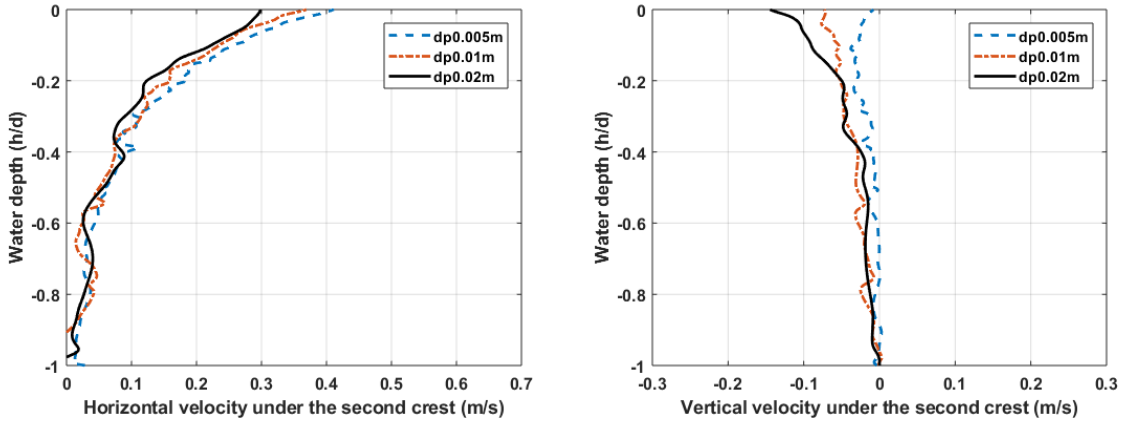

(a) (b)

Figure 5.9: Velocity with three different initial distance among particles dp=0.005m, dp=0.01m and dp=0.02m under C2.

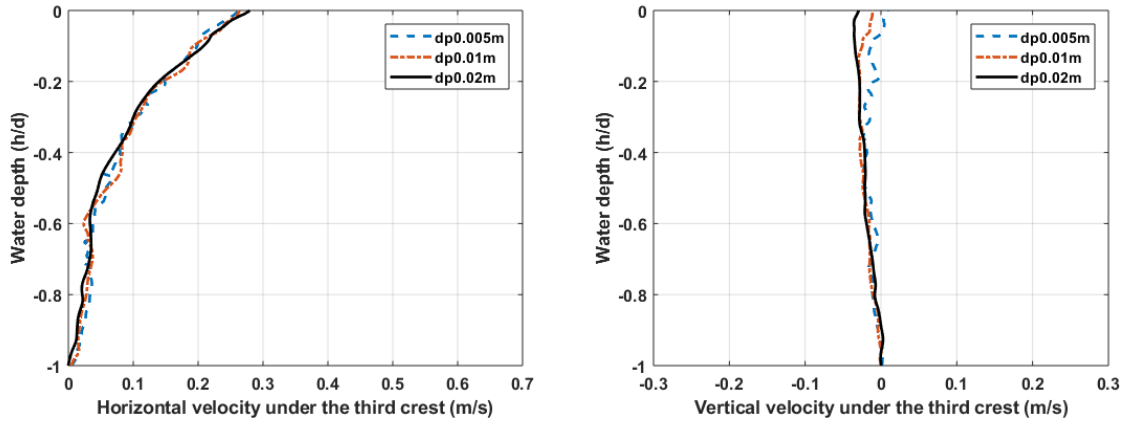

(a) (b)

Figure 5.10: Velocity with three different initial distance among particles dp=0.005m, dp=0.01m and dp=0.02m under C3.

The horizontal and vertical velocity profiles under the three crests are shown in Fig.5.8 to Fig.5.10. In Fig.5.8, the horizontal velocity under the wave crest C1 for the three wave simulations are quite similar, however, the profiles of vertical velocity under the crest exhibit some differences from each other. At locations near the free surface, the horizontal velocity decreases from $0.4m/s$ at C1 to $0.3m/s$ at C3. Horizontal velocity also reduces as we move away from the wave paddle. However, this is possibly related to a similar reason accounting for the spurious decrease in wave height as discussed in Section 5.4.2. Regarding the vertical component of the velocity under the three crests, which fluctuate around $0m/s$ over the depth of the water, no significant differences have been observed.

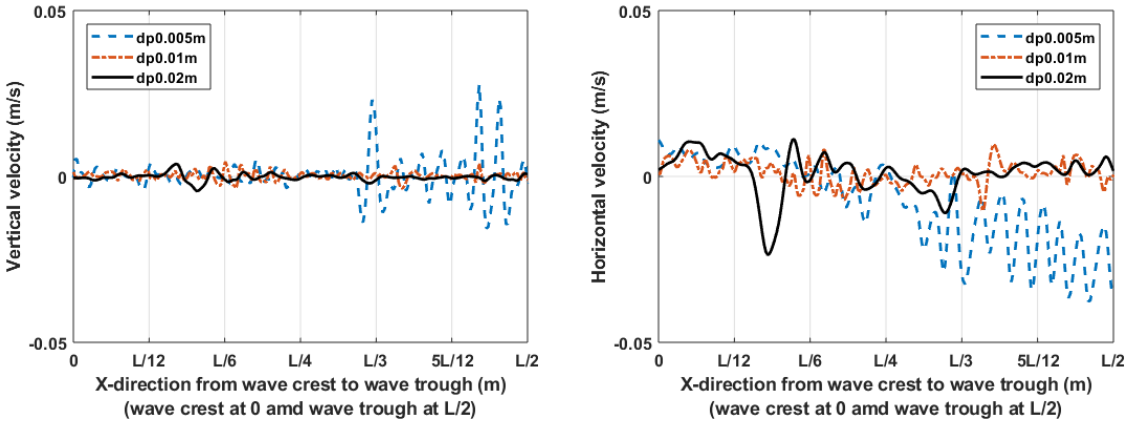

(a) (b)

Figure 5.11: Velocity variation in horizontal direction at sea bed elevation with three different initial distance among particles dp=0.005m, dp=0.01m and dp=0.02m.

Next we study the variation of horizontal and vertical velocity components along the bottom boundary from the point under the first wave crest to the first wave trough. The horizontal and vertical velocities are plotted in Fig.5.11. There are different trends observed in both cases. The vertical velocity varies slightly around $0m/s$, as shown in Fig.5.11(a). With $dp = 0.005m$ simulations show a large fluctuation at positions close to the point under the wave trough. Fig.5.11(b) reveals a significant fluctuation in horizontal velocity field. The fluctuations are due to numerical effects near the boundary as discussed previously. Even though there are fluctuation in the horizontal velocity field observed in 5.11(b) for the simulation with $dp = 0.005m$, a decreasing trend in the amplitude of the horizontal velocity is seen. The other two simulations (with $dp = 0.01m$ and $dp = 0.02m$) are unable to capture this trend. The horizontal velocity at the flat bed has been proved to be monotonically decreasing from the point under a wave crest to the point under a wave trough [289], however Fig.5.11(b) is unable to represent the analytical conclusion clearly. These results further support the idea of unstable velocity field near the boundaries for SPH.

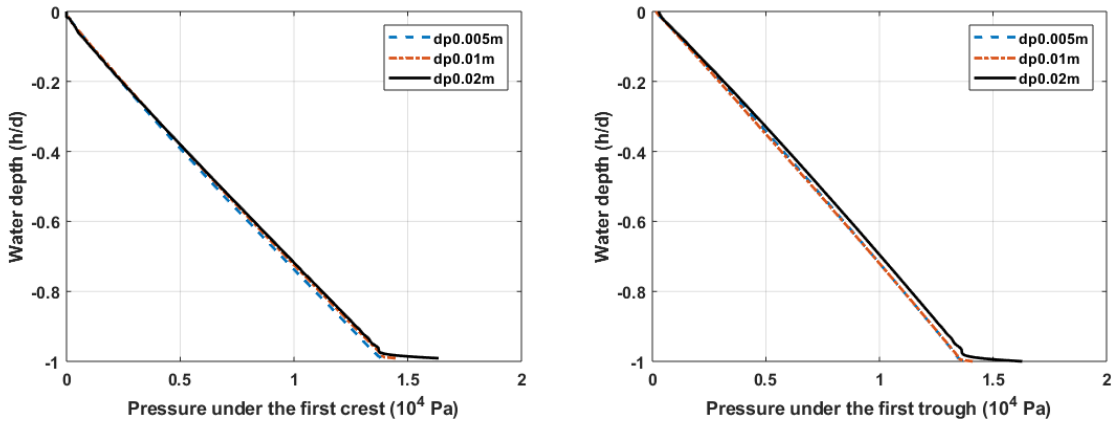

(a) (b)

Figure 5.12: Pressure with three different initial distance among particles dp=0.005m, dp=0.01m and dp=0.02m.

Fig.5.12 shows the variation of total pressure under the first wave, along the crestline and the troughline. Simulations with $dp = 0.005m$ and $dp = 0.01m$ describe a similar pressure profile. It is observed from Fig.5.12 that for the simulation with $dp = 0.02m$, the pressure rises sharply near the flat bed. The sharp increase in pressure seen in Fig.5.12 might be due to the boundary effects in SPH simulation.

Taken together, these results suggest that the initial conditions for this study are sufficient. The next section, therefore, moves on to discuss the variation of flow properties under the generated surface waves in terms of velocity and pressure field over one wave length and compare with the existing exact results.

In this study, the wave height is $0.2m$ and the chosen distance between particles is $0.005m$, thus the ratio (H/dp) is 40. The CFL number of 0.1 has been chosen for stability reasons. Moreover, the ratio of the still water level to the distance between particles (d/dp) is 280 ensuring no inaccuracies in the initial setup.

Variation of horizontal velocity

Fig.5.13(a) shows the horizontal velocity under the wave crests while Fig.5.13b describes those under the wave trough. The velocity distributions agree with previous studies of [288]; the maximum values of horizontal velocity are located at the free surface and the minimum ones are at the bottom. The horizontal velocity along the depth in Fig.5.13(a) follows Eq.2.60 in which the horizontal velocity decrease with the depth. On the other hand, the horizontal velocity under the wave trough is negative and decreases from the flat bed to the surface.

The variation of the horizontal velocity in the propagating direction of the wave is shown in Fig.5.14. The crest line is at 0 and the trough line is at L/2, where L is the length of the wave. It is clearly seen from Fig.5.14 that the velocity changes sign at a unique point [122], thus the velocity from L/4 to L/2 is smaller than 0. Then, a decreasing trend from the point under the crest to the point under the trough is seen which has been predicted from theoretical results (Eq.2.60). In addition, a considerable variation of the velocity is observed in the vicinity of the point directly under the trough. One possible cause of this is the effect of boundary condition which is mentioned in [219, 290].

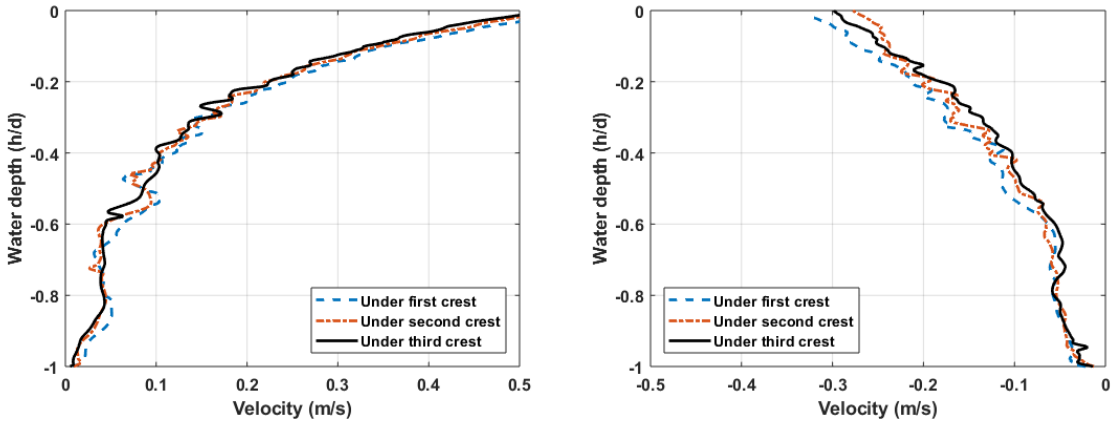

(a) Horizontal velocity under crest

(b) Horizontal velocity under trough

Figure 5.13: Comparison of the horizontal velocity profile as a function of the normalised water depth h/d.

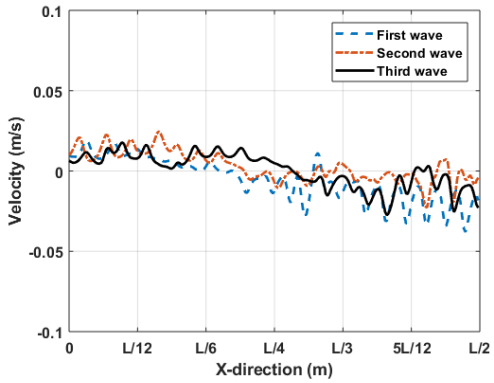

Figure 5.14: Comparison of the velocity profile at the bottom from the wave crest to the wave trough.

Variation of vertical velocity

The vertical velocity profiles are plotted in Fig.5.15(a) and Fig.5.15(b). Fig.5.15(a) shows the variation of the velocity under the wave crest. The vertical component fluctuates more near the free surface. The fluctuation is stronger at the crest line (Fig.5.15(a)) than at the trough line (Fig.5.15(b)). Moreover, the velocity under the third crest is more stable than the first two crest, hence the variation of the vertical velocity might depend on the distance from the wave paddle. This phenomenon is not so clearly seen for the case under the wave trough. The vertical velocities under the wave trough have the same pattern and they fluctuate more in the vicinity of the free surface than in deeper regions.

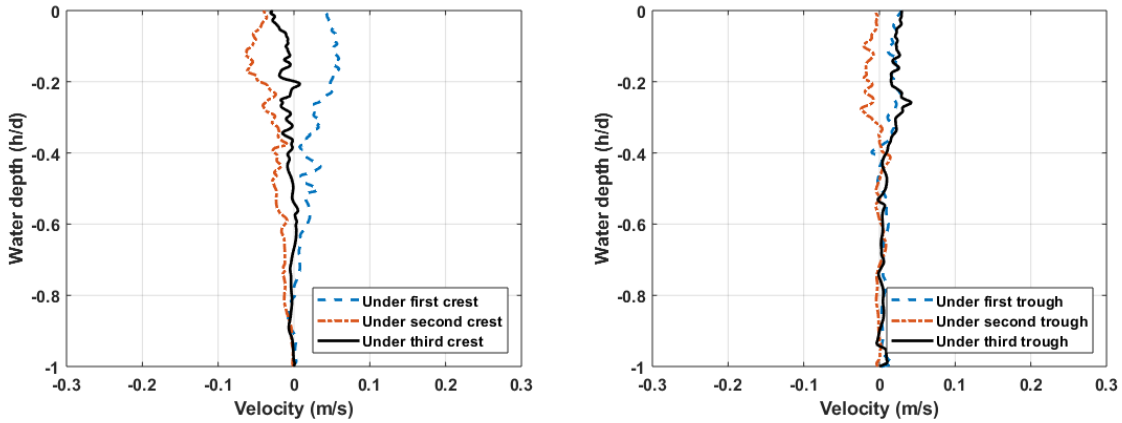

(a) Vertical velocity under crest

(b) Vertical velocity under trough

Figure 5.15: Comparison of the vertical velocity profile as a function of the normalised water depth h/d.

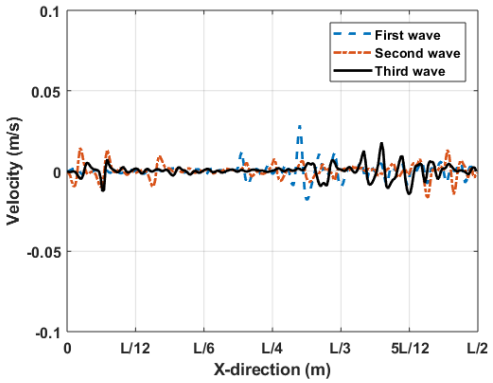

Figure 5.16: Comparison of the velocity profile at the bottom from the wave crest to the wave trough.

Along the propagating direction of the wave, the vertical velocity on the flat bed is more stable than the horizontal components, as shown in Fig.5.16. Fig.5.16 shows the variation of the vertical velocity along x-direction in the range of $-0.02m/s$ to $0.02m/s$. Fluctuations are greater for the point on the bed near the wave trough than near the wave crest. This may result from the compression of the particles under the wave trough leading to an unstable pressure region, hence unstable pressure field affects the velocity of the particles. Note that for the simulation considered the vertical velocity on the flat bed should be identically zero (as expected from the exact results).

Variation of pressure

The pressure distribution under three crests and troughs are shown in Fig.5.17 and Fig.5.18 respectively. The pressure strictly decreases from the bottom depth to the free surface. It is difficult to conclude that the maximum pressure is at the point directly under the wave crest [87] based on Fig.5.17 only, however the pressure shows a downward trend along the flat bed (though numerical fluctuations are unavoidable) from the wave crest to the wave trough in Fig.5.18. Hence, the points of maximum pressure are located at the bottom depth and under the crests. These findings confirm the qualitative success of the numerical simulation comparing with the exact results from the non-linear water wave model governed by the full non-linear Euler equations.

A good agreement was globally observed between numerical results and analytical results in Eq.2.60 and Eq.2.61. The velocity profile distributions along the depth of the water obtained with the numerical model were globally similar to the analytical inequalities. The similar trends were observed throughout the pressure field.

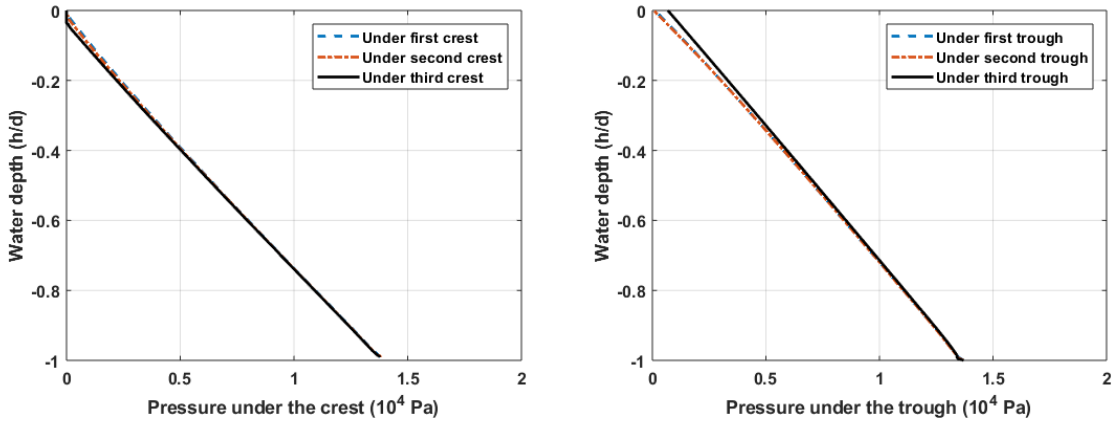

(a) (b)

Figure 5.17: Comparison of the pressure profile as a function of the normalised water depth h/d.

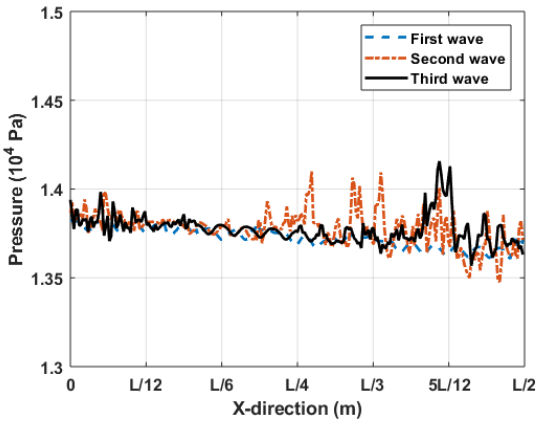

Figure 5.18: Comparison of the pressure profile at the bottom from the wave crest to the wave trough.

An SPH model is used to simulate the regular wave train in a numerical wave flume. To achieve this verification, the velocity profiles under wave crests and wave troughs are examined. Similarly, the pressure along straight lines under wave crests and wave troughs are studied. The numerical simulation results match the trend closely with the exact qualitative results available from the non-linear water wave theory confirming the success of the simulation carried out.

Some fluctuations in velocity and pressure profiles near the boundary close to the bed and at the surface have been observed which will require some attention and improvement in the numerical model. The numerical results show that SPH can be used to simulate regular waves.

6 Solitary wave-structure interaction for FOWTs

6.1 Introduction

In the previous chapters, a coupled FOWT model has been considered for studying the dynamic response of FOWT. The model has been subjected to large-amplitude waves, large-amplitude wave-current interaction, and small-amplitude steady solitary waves. Solitary wave-structure interaction is investigated in this chapter. The free surface profile of the waves deviate from a small amplitude stable form. The modified free surface due to the solitary wave-structure interaction is captured using a SPH numerical wave tank. The wave kinematics under the modified free surface are calculated using finite element method. The FOWT responses due to the effect of solitary wave-structure interaction is analysed.

6.2 Solitary wave-structure interaction effects on flow kinematics

The solitary wave kinematics can be directly exacted from the analytical formulations in chapter 4. However, the solitary wave-structure interaction effects can not be modelled by the analytical equations. Hence, it requires another approach to calculate the fluid kinematics modified by the interaction. Since the physical tests are out of the scope in this work, a numerical scheme is proposed to compute the fluid kinematics from the non-linear free surface generated by the wave approaching the floating structures.

As the solitary wave approaches the structure, the free surface distorts, and thus the flow kinematics change accordingly under the modified free surface. The theoretical equations are no longer adequate to compute flow kinematics since the derived equations are applicable only for the undisturbed free surface profiles. The proposed method in this thesis utilizes the advantage of the SPH method to capture non-linear free surface

profiles for computing the wave kinematics.

6.2.1 Numerical model for solitary wave

Due to the interaction of the wave and the structure, the water climbs up onto the structure and thus, the surface profile is different from the steady free surface provided by the solitary waves theories. Existing studies do not consider the interaction of the solitary waves-structure phenomenon; therefore, our study bridges this gap. A small-scale model is conducted using SPH. The structure is scaled by the water depth to obtain a similar scaling law to the analytical method. In the SPH model, a solitary wave interacts with scaled structure, and the free surface is captured when a hump of the water interacts with the structure. It is worth noting that there is no breaking wave in the numerical model. Due to the interaction, the elevated surface is captured as an input parameter for our approach to compute the fluid kinematics. Therefore, the recomputed fluid kinematics that account for the interaction of the solitary waves and the structure are used to investigate the FOWT responses.

For the purpose of analysis, the structure is fixed in the wave tank at a position shown in Fig.6.1.

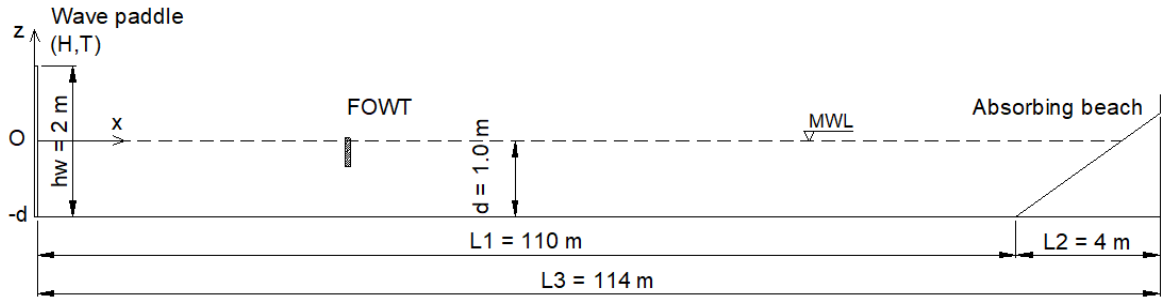

Figure 6.1: Sketch of numerical wave tank.

In this study, all dimensions are scaled according to the physical still water depth $d = 320m$. Therefore, the numerical mean water depth is $d = 1$ m and the solitary wave amplitude is $\eta/d = 0.1$ m. The wave paddle length is $h_w = 2$ m, located on the left of the numerical wave tank. The flatbed length and the beach length are 110 m and 4 m, respectively. The beach is chosen as the passive wave absorber for simplicity.

The solitary wave is generated using the KdV model provided in the DualSPHysics code [220]. The overall FOWT structure is modelled as a rectangular with a width of 0.04 m and a height of 0.375 m. Scaled FOWT is located at $x = 30$ m from the wave paddle. The initial distance between particles is $dp = 0.02$ m, leading to total of 279408 particles in the tank.

The simulation has been performed using DualSPHysics code [220] on GPU-CPU, NVIDIA GPU card Quadro M4000, 13 cores, 8GB memory. The total simulation duration is 30 s and it takes about 9 hours for completing the simulation.

6.2.2 Solitary wave-structure interaction effects on flow kinematics

As the solitary wave profile is modified due to the presence of the structure, the fluid kinematics tend to change. The FOWT interacts with the incoming wave, and thus the wave imposes pressure onto the whole FOWT structure, especially to its submerged parts. In this section, the FOWT responses are analysed, and its movements due to the solitary wave and to the modified-shape solitary wave are compared.

The non-dimensionalized solitary wave height is assumed as $\eta/d = 0.1$ and the non-dimensionalized characteristic wavelength is $L_c/d = 15$. Hence, the analytical solutions require a rescaling calculation in advance. Recall that the length variables, the velocities, and the pressure are scaled with the mean water depth h, by $\sqrt{gh}$, and by ρgh, respectively. The wave properties are shown in Table 6.1 where "Without interaction" are the analytical results without the structure, and "With interaction" are the numerical solutions with the presence of the structure, resulting from the SPH free surface. It is worth noting that the difference in the free surface is not the only variant between the two cases. Due to the modification of the free surface, the flow kinematics change as well.

Table 6.1: Solitary wave properties.

Case	Wave height (m)	Characteristic wave length (m)	Wave speed (m/s)
Without interaction	32.0	9600	56.0285
With interaction	38.4	9600	56.0285

Since the response of the FOWT to solitary waves is short-period, the impact of the wave is similar to impulse load window with considerable wave energy and phase speed.

Fig.6.2 illustrates the change in water elevation due to the presence of the structure. As the wave approaches the structure, there is an increase in the wave's amplitude and thus, the flow kinematics changes accordingly. The velocity profiles on the surface are shown in Fig.6.3, the horizontal velocity at the vicinity of the structure increase dramatically. The vertical velocity also rises sharply because of the structure.

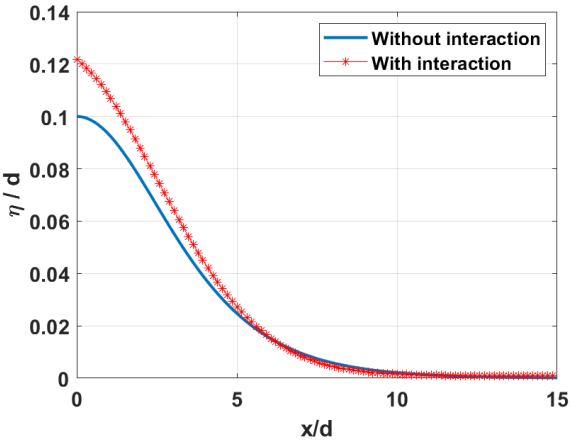

Figure 6.2: Free surface profile.

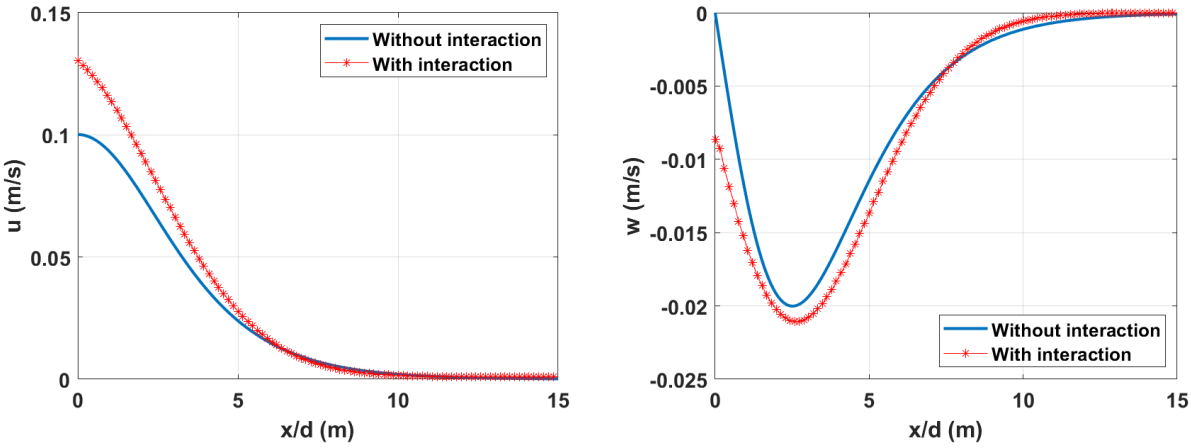

(a) (b)

Figure 6.3: Velocity profiles on the surface.

A similar phenomenon can be observed for the velocity profiles under the free surface in Fig.6.4. Interestingly, the maximum value of the horizontal velocity is not exactly under the crest. It is also worth noting that the vertical velocity near the surface is significantly larger than the analytical results provided by Clamond. The findings confirm our hypothesis regarding the modification of the flow field and the increase in flow velocities due to the structure.

Based on the results from this section, a fluid flow is generated to investigate the impact of the solitary wave-structure interaction. Since a solitary wave is a single wave with significant wave height, the flow impact is transient. The flow is generated with flow properties attached to each node. The interpolation method used in the chapter 2 is applied herein. In the next section, the response of the FOWT are studied in detail.

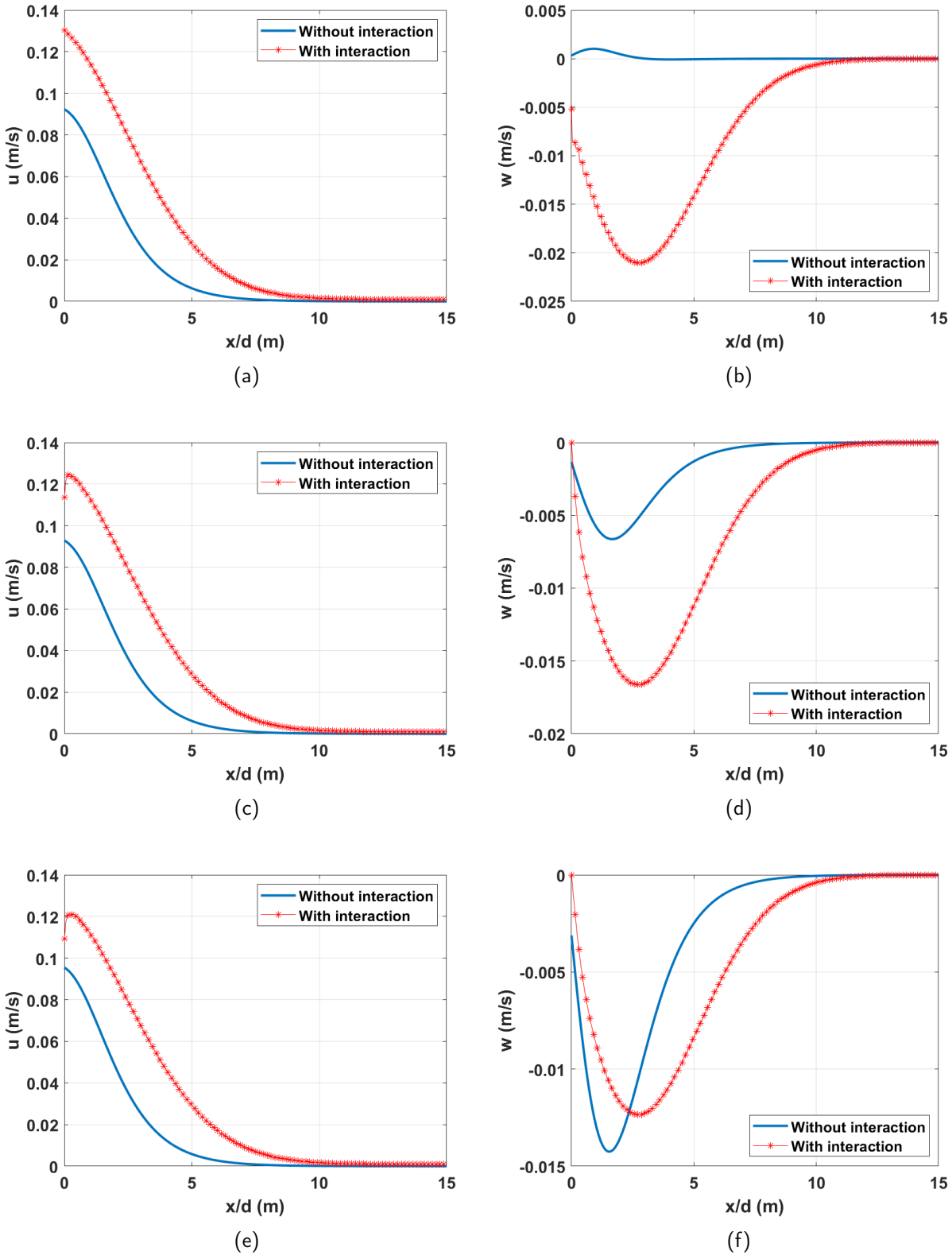

Figure 6.4: Velocity profiles along various streamlines.

6.3 Dynamic response of FOWT to solitary waves

Fig.6.5 shows the displacement of the structure to the (with and without interaction) cases. Due to the long wavelength, the FOWT at first settles down to the equilibrium at about 500s. When the wave approaches the structure, it generates a large hydrodynamic force and thus the structure accelerates. Although the solitary wave is considered a single wave, its large amplitude and energy can significantly impact a floating structure like a FOWT. Herein, the "Without interaction" refers to the simulation that takes the analytical solutions for the free surface without the FOWT into account. The "With interaction" results are the solutions obtained using the free surface generated from the SPH model that considers the wave-structure interaction. It is expected that using the wave-structure interaction water profile will affect the FOWT stronger than the former wave without the presence of FOWT.

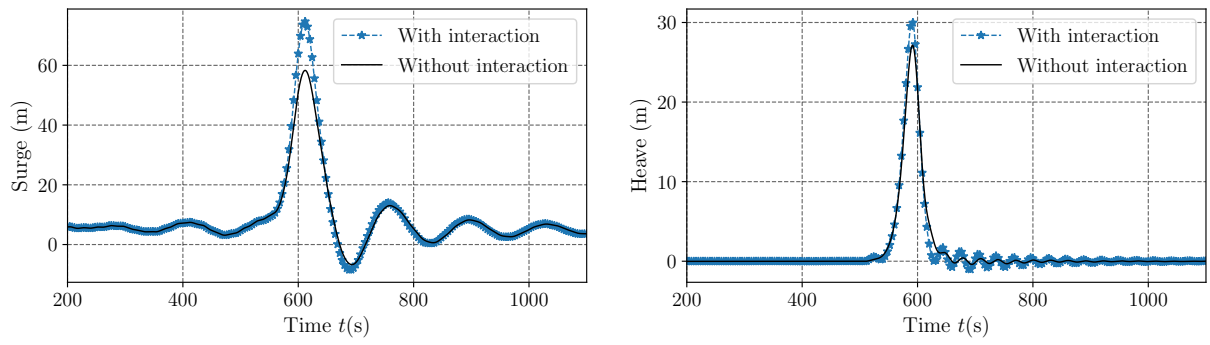

(a) (b)

Figure 6.5: FOWT response in surge and heave.

In Fig.6.5, the surge displacement of the FOWT is significantly increased due to the wave-structure interaction. The FOWT is dragged further downstream, by about 15m, compared to the case when no interaction is considered. This might result from larger hydrodynamic forces caused by the increase of fluid velocities. There is also an increase of the maximum heave response in Fig.6.5, by approximately 3 m. The results show that the result without interaction underestimates the impact of the solitary waves on the FOWT.

Fig.6.6 compares remaining FOWT displacements between the two approaches with and without solitary wave-structure interaction. The wave-structure impact on the out of plane motion (i.e. sway and roll displacement) seems negligible. However, the wave-structure interaction impact has a pronounced effect on the pitch, and the sway motions. As the crest approaches, the maximum pitch value for the case with interaction is almost doubled that of the case without interaction. In addition, the maximum and

the minimum yaw are both larger with interaction than the values computed for the case without interaction.

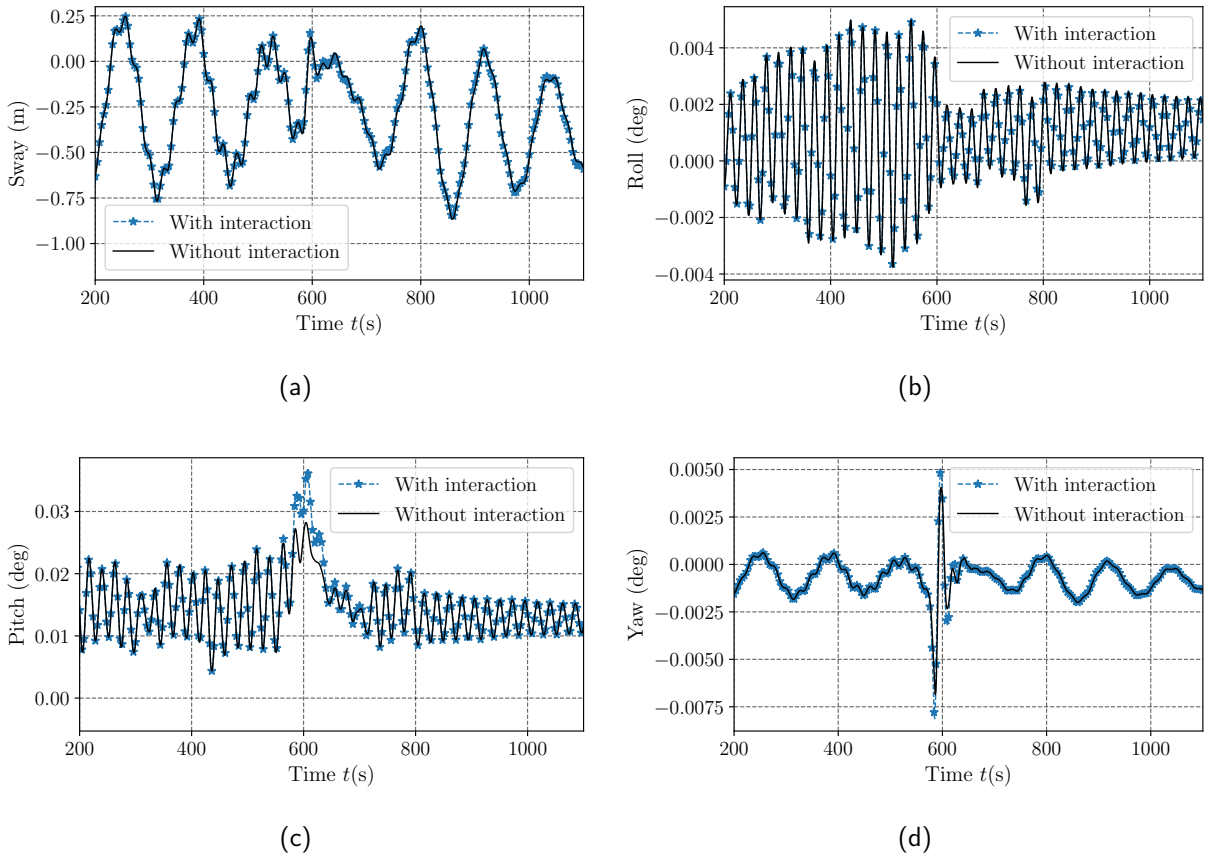

Figure 6.6: FOWT responses.

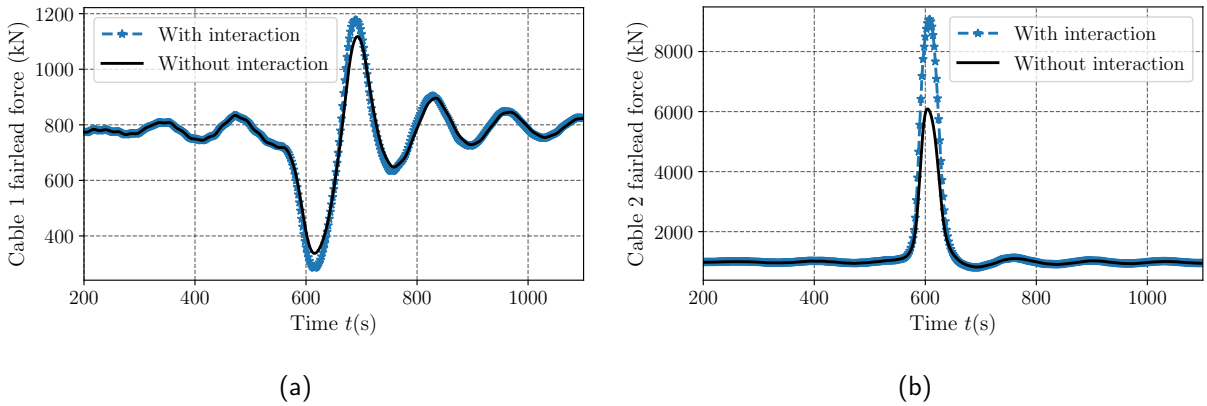

Figure 6.7: Cable fairlead forces.

Fig.6.7 presents the mooring forces. Since cable two and cable three are symmetrical about the x-coordinate, only the fairlead force of cable two is shown here for brevity. The fairlead forces rise generally in both cables for the wave-structure interaction free

surface case, particularly in cable two. The cable two fairlead force increase 1.5 times when interaction is considered. The significant increase in surge and heave motions might be the direct cause of this phenomenon. Moreover, the force in cable one also rises. It is interesting because cable one is in line with the incoming waves. A possible reason for that is the increase in the pitch and yaw motions of the spar.

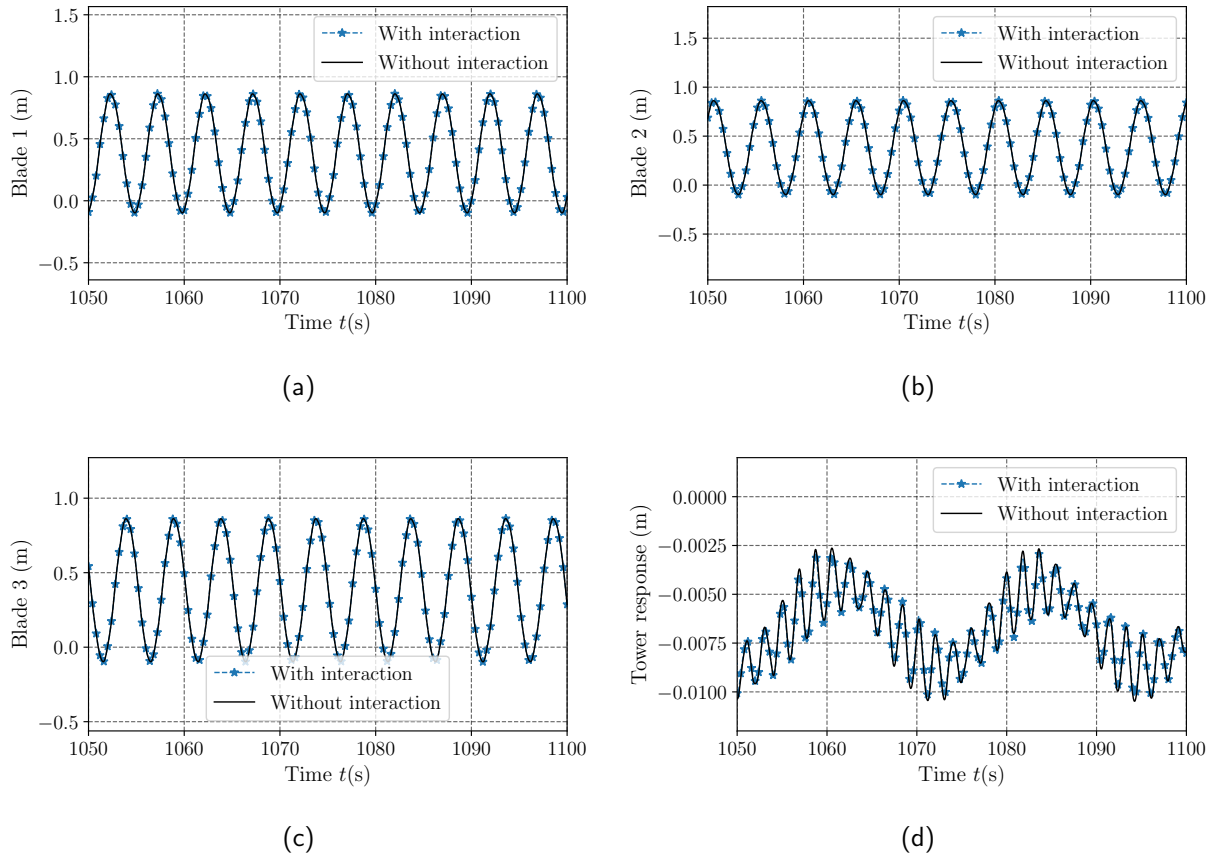

Figure 6.8: Blades' responses and tower response.

Fig.6.8 shows the blade and tower responses for both cases (with and without interaction) considered. The responses in blades and the tower motions are unaffected which means that the solitary waves or the wave-structure interaction have negligible impact on the blade and tower responses.

Nevertheless, it should be noted that the blade responses are the relative edge-wise displacement, and the tower response is side-to-side displacement in the rotor plane. Therefore, the results are not accounted for the total displacement of the blades and the tower displacement. The heave response of the spar shows a significant influence in the vertical direction which can also generated a dramatic impact on the total displacement of the blades and tower.

7 Conclusions

7.1 Summary and Conclusions

This chapter summarises the conclusions that may be drawn from the work presented in this thesis. In this thesis, large-amplitude non-linear waves have been investigated for the hydro-dynamic response of FOWTs. Particular emphasis was laid on applying the large-amplitude waves to and studying the solitary wave-structure impact on FOWTs.

The FOWT was modelled using the Euler-Lagrangian approach as a multi-degree-of-freedom (MDOF) system under wind and wave loadings. A coupled MDOF model was developed including the interaction between the blades-nacelle-tower-platform-mooring system. The dynamic model of the mooring system was also integrated.

A formulation large-amplitude non-linear wave theory has been developed to investigate the dynamic response of FOWT. The numerical model provided in this thesis solves the water wave based on the fully non-linear governing equations using the numerical continuum method for fixed mean depth of water obtaining a family of waves with the same wavelength. The large-amplitude waves simulated have asymmetrical non-linear surface profiles about the mean water level. In addition, the numerical solutions reveal a sensitive relation between the wave amplitude and the wave period on the bifurcation diagram. As shown in Chapter 2, a slight change in the wave period could significantly change the wave height. Increase in the wave height of up to 5 m were observed when the wave period was changed by only a small amount of 0.1 s (see Table 2.2). For a same wave period, the large-amplitude wave theory can generate a larger wave amplitude, e.g. even double the linear wave amplitude (shown in Fig.2.4). The numerical results also reveal the ability of the model to simulate large amplitude waves propagating over still water regions with/without the arbitrary underlying current. The developed wave period-wave amplitude relation provides the engineers and ocean scientists with a new form of information for non-linear waves for the purpose of application. For waves on the bifurcating curve, the amplitude of the waves is sensitive to the wave period. Hence, a cautious approach must be used to avoid detrimental effect of resonance as the non-linear wave period is near the natural period of the system. The large-amplitude wave

theory has not been used to compute the dynamic response of FOWT as the rigorous proof of existence of such waves is only very recent. To compute the fluid acceleration, formulations have been derived using the Euler equations. The flow accelerations are calculated using the modified height function value or by the flow pressure. It was found that the non-linear wave possesses larger values fluid kinematics near the free surface, especially for the waves with large amplitude. The non-linear waves have considerable effect on the floating platform and mooring cables. The FOWT vertical response experiences an offset from mean position, possibly due to the surrounding fluid. Heave and surge responses are strongly impacted by the use of the large-amplitude wave theory. Increases in the surge motion of about 20% in the peak response and a peak-to-peak increase of up to 50% were observed when the FOWT was subjected to large-amplitude waves (see Fig.2.36 and 2.38). A similar changes were observed in the heave motion. As a result, there is a dramatic increase in cable forces regardless of the cable layout. Both peak response and peak-to-peak response increased due to the large-amplitude waves (shown in Fig.2.40, 2.49, and 2.50).

As the surface waves and underlying current coexist in reality, a quantitative study of the FOWT responses in an environment with large-amplitude waves-uniform underlying current was carried out and compared with response from the linear waves-uniform current. The current directions were considered in favourable and adverse direction with respect to the incoming waves. Since the current profiles were assumed to be uniformly distributed along the depth of the water, the large-amplitude waves kinematics were modified with the current strength. Due to the additional effect of the current, the flow kinematics possessed a significant horizontal velocity compared to that from the non-linear waves alone. The numerical results show that the large-amplitude waves-current effects has substantial effect on the horizontal and vertical displacements of the FOWT, i.e. particularly in the vertical and horizontal motions of the platform. The overall structure had a large horizontal displacement due to the presence of the current in the flow. The position of the FOWT displaced by 15 m further downstream when the favourable current is present (as shown in Fig.3.6(a,c,e)). In addition, the cable fairlead forces were affected dramatically due to the presence of the current. The current imposed a large offset force on the cable and modified the period of the force time history. The maximum cable force increased by up to 20% more than that for the case where only wave is acting. Moreover, the FOWT responses depend on the correlation between the wave amplitude and current strength. For a small amplitude wave, the current had a visible impact on the FOWT responses. On the other hand, for the same current strength, the responses of FOWT would be influenced by the wave.

The dynamic response of FOWT to stable small-amplitude solitary waves were also investigated in this thesis. The KdV wave kinematics solutions were computed analyti-

cally using the re-normalization approach. However, the results from the existing theory showed numerical inaccuracies particularly for arbitray surfaces. Hence, an alternative approach has been proposed to compute the wave kinematics, i.e. a FEM approach. In this thesis, the proposed model overcame the instabilities of the re-normalization method at the vicinity of the free surface and it computed exactly the wave kinematics within the fluid domain. The solitary waves kinematic of two wave heights are applied to the numerical FOWT model in this thesis. The results showed critical impulse responses and a relatively short duration of response of the FOWT structure. Moreover, the cables forces consist of a single significant impulse and generally were of relatively short duration, as illustrated in Chapter 4.

The SPH method (a Lagrangian approach in fluid dynamics) was applied to study wave generation in a numerical wave tank. First of all, a nonlinear wave was recreated in the numerical wave tank and the fluid kinematics were analysed qualitatively and validated with analytical results. Then, the numerical wave kinematics under the wave crest, the wave trough, and at the bed are compared with the results from the exact non-linear wave theory, showing a good agreement between the SPH wave and analytical solutions. The SPH model has proved its ability to simulate the non-linear interaction of wave and structure. The advantages of SPH in capturing the non-linear free surface was utilized to investigate the changes of the fluid kinematics due to the solitary wave and structure interaction in this thesis.

The analytical solution of solitary waves could not account for the interaction between the solitary waves and the FOWT structure. However, it was found that the FOWT responses were significantly affected when the wave-structure interactions were taken into account. A hybrid approach was proposed to utilise the advantages of SPH to simulate and calculate the flow kinematics of a solitary wave interacting with the FOWT structure. There is a noticeable difference in the wave kinematics under a stable solitary wave and due to the solitary wave-structure interaction. Interestingly, the difference of the free surface can be captured by the hybrid approach utilising the monitored non-linear free surface from the SPH simulation. Using the extracted free surface from SPH simulations, the fluid kinematics are computed for the whole fluid domain from the free surface to the bottom depth by solving the Laplace equation for the vertical velocity component. A FEM was employed to solve the Laplace equation. The hydrodynamic forces on FOWT were computed using Morrison's equation. As the interaction between solitary wave and the structure was taken into account, there was obvious evidence of the increase of the FOWT responses, notably the surge and the heave motions, compared to the FOWT responses to the stable solitary wave without interaction. Peak increase of up to 30% and 20% were observed in surge and heave motion, respectively (see Fig.6.5). The solitary wave-structure interaction also generated more significant FOWT

responses than the steady solitary wave in pitch and yaw displacement. Nevertheless, the interaction has no or very little effect on the out of plane motions, for instance, sway and roll. The fairlead forces accordingly increased as a result of the FOWT motion. The magnitude of the force depended on the relative position of the cable in the mooring system; for instance, cable two had been more significantly impacted than cable one since it points upstream. As the wave-structure interaction was taken into account, cable two's fairlead force increased by about 1.5 times, shown in Fig.6.7. Interestingly, the force of cable one also had a slight increase. This could have resulted from the rise in the surge and pitch motions. The finding in this study confirmed the impact of wave-structure interaction effects on the FOWT structure. The FOWT responses were generally more significant as the wave-structure interaction was taken into account. The conclusion is that if the stable form of the solitary waves are used for analysis, the FOWT responses would be underestimated.

7.2 Recommendations for Further Research

The results provided in this thesis has led to some valuable conclusions on the application of large-amplitude waves in analysing the dynamic response of FOWTs. However, it has also uncovered many areas that require additional study. The objective of this section is to identify and discuss the need for further research in these areas.

The FOWT structural dynamic models developed in this thesis could be extended. Basu et al. [291] showed the impact of grid-induced vibrations on the mechanical/structural vibrations of the turbine. A future study including the generator, the electrical and mechanical sub-systems could be examined further. Moreover, installing vibration control devices in wind turbines would be of great interest in determining the effect of control during operation and on power production. Active structural control of wind turbines [34] and actuator control of wind turbine blades are potential area of research [233].

Offshore winds are more substantial in force and less turbulent so that the wind energy industry focuses on offshore development. However, the harsh offshore conditions make accessibility and maintenance difficult for offshore wind farms. A study investigating the application of the irregular large-amplitude wave loading, and its interaction with the current and the aerodynamic loads to offshore wind turbines would be relevant research direction. However, there is a fundamental gap in the knowledge with regard to irregular large-amplitude waves and their effect on FOWT. This is a promising area for future research.

The vortex-induced-motions is another area of extension that could be examined further to account for the vertical hydrodynamic loads. There is sparse literature on this topic

and more studies are required in both dynamics and control of vortex-induced-motions in FOWTs [292, 293].

8 Publications

Publications

Nguyen H.X., Chen L., Basu B. (2021). *"Structural responses of spar-type floating offshore wind turbines under large-amplitude regular waves considering wave frequency-amplitude relation"*, submitted.

Nguyen H.X., Basu B. (2021). *"Study of spar-type floating offshore wind turbines response to large-amplitude regular waves and uniform current effects"*, in preparation.

Nguyen H.X., Basu B. (2021). *"Overtopping effects of solitary waves on dynamic response of spar-type floating offshore wind turbines"*, in preparation.

Nguyen H.X., Dinh V.N, Basu B. (2021). *"A comparison of SPH simulation with exact results from a nonlinear water wave model"*, Ocean Systems Engineering, An International Journal, 10.12989/ose.2021.11.2.185.

Conferences / Presentations

Nguyen H.X., Basu B., Dinh V.N. (2019). *"Smoothed Particles Hydrodynamic for wave generation. Beyond the discrete: iterative methods from the continuum perspective"*. Workshop poster.

Dinh V.N., Nguyen H.X., (2019) *"Design of an Offshore Wind farm layout: Design of an Offshore Wind farm layout"*. In: Randolph M., Doan D., Tang A., Bui M., Dinh V. (eds) Proceedings of the 1st Vietnam Symposium on Advances in Offshore Engineering. VSOE 2018. Lecture Notes in Civil Engineering, vol 18. Springer, Singapore. *https* : $//doi.org/10.1007/978 - 981 - 13 - 2306 - 5\_31$.

Nguyen H.X., Basu B., Dinh V.N. (2019) *"Numerical Investigation of Wave-Current Interaction by Using Smoothed Particle Hydrodynamics"*. In: Randolph M., Doan D., Tang A., Bui M., Dinh V. (eds) Proceedings of the 1st Vietnam Symposium on Advances in Offshore Engineering. VSOE 2018. Lecture Notes in Civil Engineering, vol 18. Springer, Singapore. *https* : $//doi.org/10.1007/978 - 981 - 13 - 2306 - 5\_43$

Bibliography

[1] Van Nguyen Dinh and Biswajit Basu. On the modeling of spar-type floating offshore wind turbines. In *Key Engineering Materials*, volume 569, pages 636–643. Trans Tech Publ, 2013.

[2] Adrian Constantin. *Nonlinear water waves with applications to wave-current interactions and tsunamis*. SIAM, 2011.

[3] Bernard Le Méhauté. *An introduction to hydrodynamics and water waves*. Springer Science & Business Media, 1976.

[4] Asian Co-benefits Partnership White Paper 2018. Quantifying Co-benefits in Asia: Methods and Applications, 2018. [Online; accessed 28-April-2019].

[5] International Energy Agency. World enery investment 2021. `https://www.iea.org/reports/world-energy-investment-2021/executive-summary`, 2021. [Online; accessed November 11, 2021].

[6] Global Wind Energy Council. Global wind report. `https://gwec.net/global-wind-report-2021/`, 2021. [Online; accessed November 11, 2021].

[7] Jason Jonkman, Sandy Butterfield, Walter Musial, and George Scott. Definition of a 5-MW reference wind turbine for offshore system development (No. NREL/TP-500-38060). Technical report, National Renewable Energy Lab.(NREL), Golden, CO (United States), 2009.

[8] Hywind Scotland. World's first floating wind farm best performer in UK, 2018. [Online; accessed 13-October-2021].

[9] Jason Mark Jonkman. *Dynamics modeling and loads analysis of an offshore floating wind turbine*. PhD thesis, University of Colorado at Boulder, 2007.

[10] Jason Jonkman. Definition of the floating system for phase iv of oc3 (No. NREL/TP-500-47535). Technical report, National Renewable Energy Lab.(NREL), Golden, CO (United States), 2010.

[11] Ju Gao and Bert Sweetman. Design optimization of hull size for spar-based floating offshore wind turbines. *Journal of Ocean Engineering and Marine Energy*, 4(3):217–229, 2018.

[12] Amy N Robertson and Jason M Jonkman. Loads analysis of several offshore floating wind turbine concepts. In *The Twenty-first International Offshore and Polar Engineering Conference*. OnePetro, 2011.

[13] Simon-Philippe Breton and Geir Moe. Status, plans and technologies for offshore wind turbines in Europe and North America. *Renewable Energy*, 34(3):646–654, 2009.

[14] C M Wang, T Utsunomiya, S C Wee, and Y S Choo. Research on floating wind turbines: a literature survey. *The IES Journal Part A: Civil & Structural Engineering*, 3(4):267–277, 2010.

[15] Sandy Butterfield, Walt Musial, Jason Jonkman, and Paul Sclavounos. Engineering challenges for floating offshore wind turbines (No. NREL/CP-500-38776). Technical report, National Renewable Energy Lab.(NREL), Golden, CO (United States), 2007.

[16] Jason M Jonkman. Dynamics of offshore floating wind turbines—model development and verification. *Wind Energy: An International Journal for Progress and Applications in Wind Power Conversion Technology*, 12(5):459–492, 2009.

[17] Gordon Stewart and Michael Muskulus. A review and comparison of floating offshore wind turbine model experiments. *Energy Procedia*, 94:227–231, 2016.

[18] Mareike Leimeister, Athanasios Kolios, and Maurizio Collu. Critical review of floating support structures for offshore wind farm deployment. In *Journal of Physics: Conference Series*, volume 1104, page 012007. IOP Publishing, 2018.

[19] First Edition, J M J Journée, and W W Massie. *Offshore Hydromechanics*. Delft University of Technology, 2001.

[20] Kai-Tung Ma, Yong Luo, Chi-Tat Thomas Kwan, and Yongyan Wu. *Mooring system engineering for offshore structures*. Gulf Professional Publishing, 2019.

[21] Denis Matha, Markus Schlipf, Andrew Cordle, Ricardo Pereira, and Jason Jonkman. Challenges in simulation of aerodynamics, hydrodynamics, and mooring-line dynamics of floating offshore wind turbines. Technical report, National Renewable Energy Lab.(NREL), Golden, CO (United States), 2011.

[22] Hidekazu Matsukuma and Tomoaki Utsunomiya. Motion analysis of a floating offshore wind turbine considering rotor-rotation. *The IES Journal Part A: Civil & Structural Engineering*, 1(4):268–279, 2008.

[23] Lei Wang and Bert Sweetman. Simulation of large-amplitude motion of floating wind turbines using conservation of momentum. *Ocean Engineering*, 42:155–164, 2012.

[24] Lei Wang and Bert Sweetman. Multibody dynamics of floating wind turbines with large-amplitude motion. *Applied Ocean Research*, 43:1–10, 2013.

[25] Frank Sandner, David Schlipf, Denis Matha, Robert Seifried, and Po Wen Cheng. Reduced nonlinear model of a spar-mounted floating wind turbine. 2012.

[26] Frank Sandner. *Reduced model design of a floating wind turbine*. PhD thesis, University of Stuttgart, Germany, 2012.

[27] Gireesh Kumar V Ramachandran, Henrik Bredmose, Jens Nørkær Sørensen, and Jørgen Juncher Jensen. Fully coupled three-dimensional dynamic response of a tension-leg platform floating wind turbine in waves and wind. *Journal of Offshore Mechanics and Arctic Engineering*, 136(2), 2014.

[28] Van-Nguyen Dinh, Biswajit Basu, and Soren R K Nielsen. Impact of spar-nacelle-blade coupling on the edgewise response of floating offshore wind turbines. *Coupled Syst. Mech*, 2(3):231–253, 2013.

[29] Mohammed Khair Hamdan Al-Solihat. *Dynamics modeling, simulation and analysis of a floating offshore wind turbine*. PhD thesis, McGill University, 2017.

[30] Lin Chen, Biswajit Basu, and Søren R K Nielsen. A coupled finite difference mooring dynamics model for floating offshore wind turbine analysis. *Ocean Engineering*, 162:304–315, 2018.

[31] Lin Chen and Biswajit Basu. Wave-current interaction effects on structural responses of floating offshore wind turbines. *Wind Energy*, 22(2):327–339, 2019.

[32] Van-Nguyen Dinh, Biswajit Basu, and Satish Nagarajaiah. Semi-active control of vibrations of spar type floating offshore wind turbines. *Smart Struct Syst*, 18(4): 683–705, 2016.

[33] Saptarshi Sarkar and Breiffni Fitzgerald. Vibration control of spar-type floating offshore wind turbine towers using a tuned mass-damper-inerter. *Structural Control and Health Monitoring*, 27(1):e2471, 2020.

[34] Saptarshi Sarkar. *Individual blade pitch control strategies for spar-type floating offshore wind turbines*. PhD thesis, Trinity College Dublin, 2020.

[35] J Jonkman and W Musial. Offshore code comparison collaboration (OC3) for IEA task 23 offshore wind technology and deployment. *Contract*, 303:275–3000, 2010.

[36] Andrew Cordle and Jason Jonkman. State of the art in floating wind turbine design tools. In *The twenty-first international offshore and polar engineering conference*. OnePetro, 2011.

[37] Odd Faltinsen. *Sea loads on ships and offshore structures*, volume 1. Cambridge University Press, 1993.

[38] R K Jain. A simple method of calculating the equivalent stiffnesses in mooring cables. *Applied Ocean Research*, 2(3):139–142, 1980.

[39] M S Triantafyllou. *Cable mechanics with marine applications*. PhD thesis, Department of Ocean Engineering, Massachusetts Institute of Technology, Cambridge, MA, USA, 1990.

[40] Michael Isaacson and John Baldwin. Moored structures in waves and currents. *Canadian Journal of Civil Engineering*, 23(2):418–430, 1996.

[41] H J J Van den Boom. Dynamic behaviour of mooring lines. In *BOSS Conference*, volume 1, pages 359–368, 1985.

[42] E Kreuzer and U Wilke. Dynamics of mooring systems in ocean engineering. *Archive of Applied Mechanics*, 73(3):270–281, 2003.

[43] Bradley Jason Buckham. *Dynamics modelling of low-tension tethers for submerged remotely operated vehicles*. PhD thesis, University of Victoria, USA, 2003.

[44] Marco Masciola, Jason Jonkman, and Amy Robertson. Extending the capabilities of the mooring analysis program: A survey of dynamic mooring line theories for integration into fast. In *International Conference on Offshore Mechanics and Arctic Engineering*, volume 45530, page V09AT09A032. American Society of Mechanical Engineers, 2014.

[45] E R Jefferys and M H Patel. On the dynamics of taut mooring systems. *Engineering Structures*, 4(1):37–43, 1982.

[46] Brad Buckham, Frederick R Driscoll, and Meyer Nahon. Development of a finite element cable model for use in low-tension dynamics simulation. *J. Appl. Mech.*, 71(4):476–485, 2004.

[47] Martin O L Hansen. *Aerodynamics of wind turbines*. Routledge, 2015.

[48] James F Manwell, Jon G McGowan, and Anthony L Rogers. *Wind energy explained: theory, design and application*. John Wiley & Sons, 2010.

[49] Nicholas Haritos. Introduction to the analysis and design of offshore structures–an overview. *Electronic Journal of Structural Engineering*, 7(Special Issue: Loading on Structures):55–65, 2007.

[50] Subrata Chakrabarti. *Handbook of Offshore Engineering (2-volume set)*. Elsevier, 2005.

[51] Thanh Dam Pham and Hyunkyoung Shin. A new conceptual design and dynamic analysis of a spar-type offshore wind turbine combined with a moonpool. *Energies*, 12(19):3737, 2019.

[52] Henrik Bredmose, F Lemmer, M Borg, A Pegalajar-Jurado, Robert Flemming Mikkelsen, T Stoklund Larsen, T Fjelstrup, Wenye Yu, Anders Kjær Lomholt, and L Boehm. The Triple Spar campaign: Model tests of a 10MW floating wind turbine with waves, wind and pitch control. *Energy Procedia*, 137:58–76, 2017.

[53] Madjid Karimirad and Torgeir Moan. Feasibility of the application of a spar-type wind turbine at a moderate water depth. *Energy Procedia*, 24:340–350, 2012.

[54] Tomoaki Utsunomiya, Tomoki Sato, Hidekazu Matsukuma, and Kiyokazu Yago. Experimental validation for motion of a spar-type floating offshore wind turbine using 1/22.5 scale model. In *ASME 2009 28th International Conference on Ocean, Offshore and Arctic Engineering*, pages 951–959. American Society of Mechanical Engineers Digital Collection, 2009.

[55] Hyunkyoung Shin, Pham Thanh Dam, Kwang Jin Jung, Jinseob Song, Chaewhan Rim, and Taeyoung Chung. Model test of new floating offshore wind turbine platforms. *International Journal of Naval Architecture and Ocean Engineering*, 5 (2):199–209, 2013.

[56] Hyunkyoung Shin, Wooseob Lee, Kwangjin Jung, and Jungtae Kim. Model test and simulation of modified spar type floating offshore wind turbine with three catenary mooring lines. *Journal of Renewable and Sustainable Energy*, 6(4): 042009, 2014.

[57] Long Meng, Yan-ping He, Yong-sheng Zhao, Jie Yang, He Yang, Zhao-long Han, Long Yu, Wen-gang Mao, and Wei-kang Du. Dynamic response of 6MW spar type floating offshore wind turbine by experiment and numerical analyses. *China Ocean Engineering*, 34(5):608–620, 2020.

[58] Giuseppe Roberto Tomasicchio, Felice D'Alessandro, Alberto Maria Avossa, Luigia Riefolo, Elena Musci, Francesco Ricciardelli, and Diego Vicinanza. Experimental modelling of the dynamic behaviour of a spar buoy wind turbine. *Renewable Energy*, 127:412–432, 2018.

[59] Zhenqing Liu, Yuangang Tu, Wei Wang, and Guowei Qian. Numerical analysis of a catenary mooring system attached by clump masses for improving the wave-resistance ability of a spar buoy-type floating offshore wind turbine. *Applied Sciences*, 9(6):1075, 2019.

[60] Sara Russo, Pasquale Contestabile, Andrea Bardazzi, Elisa Leone, Gregorio Iglesias, Giuseppe R Tomasicchio, and Diego Vicinanza. Dynamic loads and response of a spar buoy wind turbine with pitch-controlled rotating blades: An experimental study. *Energies*, 14(12):3598, 2021.

[61] Karsten M Kopperstad, Rajan Kumar, and Kourosh Shoele. Aerodynamic characterization of barge and spar type floating offshore wind turbines at different sea states. *Wind Energy*, 23(11):2087–2112, 2020.

[62] Daniela Pantusa, Antonio Francone, and Giuseppe Roberto Tomasicchio. Floating Offshore Renewable Energy Farms. A Life-Cycle Cost Analysis at Brindisi, Italy. *Energies*, 13(22):6150, 2020.

[63] Tom Salic, Jean Frédéric Charpentier, Mohamed Benbouzid, and Marc Le Boulluec. Control strategies for floating offshore wind turbine: challenges and trends. *Electronics*, 8(10):1185, 2019.

[64] Xue Xu and Narakorn Srinil. Dynamic response analysis of spar-type floating wind turbines and mooring lines with uncoupled vs coupled models. In *International Conference on Offshore Mechanics and Arctic Engineering*, volume 56574, page V009T09A062. American Society of Mechanical Engineers, 2015.

[65] Madjid Karimirad, Quentin Meissonnier, Zhen Gao, and Torgeir Moan. Hydroelastic code-to-code comparison for a tension leg spar-type floating wind turbine. *Marine Structures*, 24(4):412–435, 2011.

[66] Kun Xu, Min Zhang, Yanlin Shao, Zhen Gao, and Torgeir Moan. Effect of wave nonlinearity on fatigue damage and extreme responses of a semi-submersible floating wind turbine. *Applied Ocean Research*, 91:101879, 2019.

[67] N Tran, N Y Sergiienko, B S Cazzolato, B Ding, M H Ghayesh, and M Arjomandi. The impact of pitch-surge coupling on the performance of a submerged cylindrical wave energy converter. *Applied Ocean Research*, 104:102377, 2020.

[68] Yupeng Ren, Xingbei Xu, Guohui Xu, and Zhiqin Liu. Measurement and calculation of particle trajectory of liquefied soil under wave action. *Applied Ocean Research*, 101:102202, 2020.

[69] Iftekhar Anam and Jose M Roesset. Effect of nonlinear wave kinematics on dynamic response of spars. *Journal of Engineering Mechanics*, 128(9):925–934, 2002.

[70] George G Stokes. On the theory of oscillatory waves. *Transactions of the Cambridge Philosophical Society*, 1880.

[71] Motohiko Umeyama. Eulerian–Lagrangian analysis for particle velocities and trajectories in a pure wave motion using particle image velocimetry. *Philosophical Transactions of the Royal Society A: Mathematical, Physical and Engineering Sciences*, 370(1964):1687–1702, 2012.

[72] Nekrasov Aleksandr Ivanovich. On steady waves. *Izvestia Ivanovo-Voznesensk. Politekhn. Inst.*, 3:52–65, 1921.

[73] Tullio Levi-Civita. Determinazione rigorosa delle onde irrotazionali periodiche in acqua profonda. *Rend. Accad. Lincei*, 33:141–150, 1924.

[74] Dirk J Struik. Détermination rigoureuse des ondes irrotationelles périodiques dans un canal à profondeur finie. *Mathematische Annalen*, 95(1):595–634, 1926.

[75] Yu P Krasovskii. On the theory of steady-state waves of finite amplitude. *USSR Computational Mathematics and Mathematical Physics*, 1(4):996–1018, 1962.

[76] G Keady and J Norbury. On the existence theory for irrotational water waves. In *Mathematical Proceedings of the Cambridge Philosophical Society*, volume 83, pages 137–157. Cambridge University Press, 1978.

[77] John Francis Toland. On the existence of a wave of greatest height and Stokes's conjecture. *Proceedings of the Royal Society of London. A. Mathematical and Physical Sciences*, 363(1715):469–485, 1978.

[78] J B McLeod. The Stokes and Krasovskii Conjectures for the wave of greatest height. Technical report, Wisconsin Univ-Madison Mathematics Research Center, 1980.

[79] J Bryce McLeod. The Stokes and Krasovskii conjectures for the wave of greatest height. *Studies in Applied Mathematics*, 98(4):311–333, 1997.

[80] René Gouyon. Contributions à la théorie des houles. In *Annales de la Faculté des sciences de Toulouse: Mathématiques*, volume 22, pages 1–55, 1958.

[81] Eberhard Zeidler. Existenzbeweis für permanente kapillar-schwerewellen mit allgemeinen wirbelverteilungen. *Archive for Rational Mechanics and Analysis*, 50 (1):34–72, 1973.

[82] Charles J Amick and John F Toland. On solitary water-waves of finite amplitude. *Archive for Rational Mechanics and Analysis*, 76(1):9–95, 1981.

[83] F I Gonzalez, E D Cokelet, J F R Gower, and M R Mulhern. SLAR and in-situ observations of wave-current interaction on the Columbia River Bar. In *The ocean surface*, pages 303–310. Springer, 1985.

[84] P H Kemp and R R Simons. The interaction between waves and a turbulent current: waves propagating with the current. *Journal of Fluid Mechanics*, 116: 227–250, 1982.

[85] C Swan, I P Cummins, and R L James. An experimental study of two-dimensional surface water waves propagating on depth-varying currents. Part 1. Regular waves. *Journal of Fluid Mechanics*, 428:273, 2001.

[86] G P Thomas. Wave–current interactions: an experimental and numerical study. Part 2. Nonlinear waves. *Journal of Fluid Mechanics*, 216:505–536, 1990.

[87] Adrian Constantin and Walter Strauss. Exact steady periodic water waves with vorticity. *Communications on Pure and Applied Mathematics*, 57(4):481–527, 2004.

[88] Joy Ko and Walter Strauss. Effect of vorticity on steady water waves. *Journal of Fluid Mechanics*, 608:197–215, 2008.

[89] Joy Ko and Walter Strauss. Large-amplitude steady rotational water waves. *European Journal of Mechanics-B/Fluids*, 27(2):96–109, 2008.

[90] Adrian Constantin, Mats Ehrnström, and Erik Wahlén. Symmetry of steady periodic gravity water waves with vorticity. *Duke Mathematical Journal*, 140(3): 591–603, 2007.

[91] Adrian Constantin and Joachim Escher. Symmetry of steady periodic surface water waves with vorticity. *Journal of Fluid Mechanics*, 498:171–181, 2004.

[92] Adrian Constantin and Joachim Escher. Symmetry of steady deep-water waves with vorticity. *European Journal of Applied Mathematics*, 15(6):755–768, 2004.

[93] Adrian Constantin and Walter A Strauss. Stability properties of steady water waves with vorticity. *Communications on Pure and Applied Mathematics: A Journal Issued by the Courant Institute of Mathematical Sciences*, 60(6):911–950, 2007.

[94] Adrian Constantin and Joachim Escher. Analyticity of periodic traveling free surface water waves with vorticity. *Annals of Mathematics*, pages 559–568, 2011.

[95] David Henry. Analyticity of the free surface for periodic travelling capillary-gravity water waves with vorticity. *Journal of Mathematical Fluid Mechanics*, 14(2):249–254, 2012.

[96] David Henry. Analyticity of the streamlines for periodic travelling free surface capillary-gravity water waves with vorticity. *SIAM Journal on Mathematical Analysis*, 42(6):3103–3111, 2010.

[97] Bogdan-Vasile Matioc. Analyticity of the streamlines for periodic traveling water waves with bounded vorticity. *International Mathematics Research Notices*, 2011 (17):3858–3871, 2011.

[98] Bogdan-Vasile Matioc. On the regularity of deep-water waves with general vorticity distributions. *Quarterly of Applied Mathematics*, 70(2):393–405, 2012.

[99] Geoffrey R Burton and John F Toland. Surface waves on steady perfect-fluid flows with vorticity. *Communications on Pure and Applied Mathematics*, 64(7): 975–1007, 2011.

[100] Adrian Constantin and Walter Strauss. Rotational steady water waves near stagnation. *Philosophical Transactions of the Royal Society A: Mathematical, Physical and Engineering Sciences*, 365(1858):2227–2239, 2007.

[101] Adrian Constantin and Walter Strauss. Periodic traveling gravity water waves with discontinuous vorticity. *Archive for Rational Mechanics and Analysis*, 202 (1):133–175, 2011.

[102] Adrian Constantin and Eugen Varvaruca. Steady periodic water waves with constant vorticity: regularity and local bifurcation. *Archive for Rational Mechanics and Analysis*, 199(1):33–67, 2011.

[103] M Lilli and JF Toland. Waves on a steady stream with vorticity. *Perspectives in Partial Differential Equations, Harmonic Analysis and Applications: A Volume in Honor of Vladimir G. Maz'ya's 70th Birthday*, 79:266, 2008.

[104] Erik Wahlén. Steady periodic capillary-gravity waves with vorticity. *SIAM Journal on Mathematical Analysis*, 38(3):921–943, 2006.

[105] Samuel Walsh. Steady periodic gravity waves with surface tension. *arXiv preprint arXiv:0911.1375*, 2009.

[106] David Henry. Steady periodic waves bifurcating for fixed-depth rotational flows. *Quarterly of Applied Mathematics*, 71(3):455–487, 2013.

[107] David Henry. Large amplitude steady periodic waves for fixed-depth rotational flows. *Communications in Partial Differential Equations*, 38(6):1015–1037, 2013.

[108] Adrian Constantin, Konstantinos Kalimeris, and Otmar Scherzer. A penalization method for calculating the flow beneath traveling water waves of large amplitude. *SIAM Journal on Applied Mathematics*, 75(4):1513–1535, 2015.

[109] D Amann and K Kalimeris. A numerical continuation approach for computing water waves of large wave height. *European Journal of Mechanics-B/Fluids*, 67: 314–328, 2018.

[110] K Kalimeris. Asymptotic expansions for steady periodic water waves in flows with constant vorticity. *Nonlinear Analysis: Real World Applications*, 37:182–212, 2017.

[111] Konstantinos Kalimeris. Analytical approximation and numerical simulations for periodic travelling water waves. *Philosophical Transactions of the Royal Society A: Mathematical, Physical and Engineering Sciences*, 376(2111):20170093, 2018.

[112] Hsien-Kuo Chang and Liang-Sheng Ho. Highly nonlinear interactions between a gravity wave and a current of constant vorticity. *Journal of the Chinese Institute of Engineers*, 18(2):169–183, 1995.

[113] Youngok Kang and Jean-Marc Vanden-Broeck. Gravity-capillary waves in the presence of constant vorticity. *European Journal of Mechanics-B/Fluids*, 19(2): 253–268, 2000.

[114] Hisashi Okamoto. *The mathematical theory of permanent progressive water-waves*, volume 20. World Scientific, 2001.

[115] A F Teles Da Silva and D H Peregrine. Steep, steady surface waves on water of finite depth with constant vorticity. *Journal of Fluid Mechanics*, 195:281–302, 1988.

[116] J-M Vanden-Broeck. Periodic waves with constant vorticity in water of infinite depth. *IMA Journal of Applied Mathematics*, 56(3):207–217, 1996.

[117] G P Thomas and G Klopman. Wave-current interactions in the near shore region. *International series on Advances in Fluid Mechanics*, 10:255–319, 1997.

[118] Sergey A Dyachenko and Vera Mikyoung Hur. Stokes waves with constant vorticity: I. Numerical computation. *Studies in Applied Mathematics*, 142(2):162–189, 2019.

[119] André Nachbin and Roberto Ribeiro-Junior. A boundary integral formulation for particle trajectories in Stokes waves. *Discrete & Continuous Dynamical Systems*, 34(8):3135, 2014.

[120] Roberto Ribeiro, Paul A Milewski, and André Nachbin. Flow structure beneath rotational water waves with stagnation points. *Journal of Fluid Mechanics*, 812: 792–814, 2017.

[121] Biswajit Basu. Irrotational two-dimensional free-surface steady water flows over a flat bed with underlying currents. *Nonlinear Analysis: Theory, Methods & Applications*, 147:110–124, 2016.

[122] Adrian Constantin. The trajectories of particles in Stokes waves. *Inventiones Mathematicae*, 166(3):523–535, 2006.

[123] Adrian Constantin and Walter Strauss. Exact periodic traveling water waves with vorticity. *Comptes Rendus Mathematique*, 335(10):797–800, 2002.

[124] Biswajit Basu. On the existence of two-dimensional irrotational water waves over finite depth with uniform current. *Applicable Analysis*, 97(14):2523–2532, 2018.

[125] Lin Chen and Biswajit Basu. Numerical investigations of two-dimensional irrotational water waves over finite depth with uniform current. *Applicable Analysis*, pages 1–9, 2019.

[126] Lin Chen and Biswajit Basu. Numerical continuation method for large-amplitude steady water waves on depth-varying currents in flows with fixed mean water depth. *Applied Ocean Research*, 111:102631, 2021.

[127] Marie Louise Dubreil-Jacotin. *Sur la détermination rigoureuse des ondes permanentes périodiques d'ampleur finie*. PhD thesis, Gauthier-Villars, 1934.

[128] M S Longuet-Higgins and R W Stewart. Changes in the form of short gravity waves on long waves and tidal currents. *Journal of Fluid Mechanics*, 8(4):565–583, 1960.

[129] Michael S Longuet-Higgins and R W Stewart. The changes in amplitude of short gravity waves on steady non-uniform currents. *Journal of Fluid Mechanics*, 10(4): 529–549, 1961.

[130] Robert A Dalrymple. A finite amplitude wave on a linear shear current. *Journal of Geophysical Research*, 79(30):4498–4504, 1974.

[131] Robert A Dalrymple. Water waves on a bilinear shear current. *Coastal Engineering*, pages 626–641, 1975.

[132] Robert A Dalrymple. A numerical model for periodic finite amplitude waves on a rotational fluid. *Journal of Computational Physics*, 24(1):29–42, 1977.

[133] B Liao, G Dong, Y Ma, and J L Gao. Linear-shear-current modified Schrödinger equation for gravity waves in finite water depth. *Physical Review E*, 96(4):043111, 2017.

[134] B Liao, Y Ma, X Ma, and G Dong. Experimental study on the evolution of Peregrine breather with uniform-depth adverse currents. *Physical Review E*, 97 (5):053102, 2018.

[135] Y Ma, G Dong, M Perlin, X Ma, and G Wang. Experimental investigation on the evolution of the modulation instability with dissipation. *Journal of Fluid Mechanics*, 711:101–121, 2012.

[136] Yuxiang Ma, Xiaozhou Ma, Marc Perlin, and Guohai Dong. Extreme waves generated by modulational instability on adverse currents. *Physics of Fluids*, 25(11): 114109, 2013.

[137] Qin Chen, Per A Madsen, Hemming A Schäffer, and David R Basco. Wave-current interaction based on an enhanced Boussinesq approach. *Coastal Engineering*, 33 (1):11–39, 1998.

[138] Yu Hsiao, Chung-Liang Tsai, Yen-Lung Chen, Han-Lun Wu, and Shih-Chun Hsiao. Simulation of wave-current interaction with a sinusoidal bottom using OpenFOAM. *Applied Ocean Research*, 94:101998, 2020.

[139] James T Kirby. A note on linear surface wave-current interaction over slowly varying topography. *Journal of Geophysical Research: Oceans*, 89(C1):745–747, 1984.

[140] G P Thomas. Wave-current interactions: an experimental and numerical study. Part 1. Linear waves. *Journal of Fluid Mechanics*, 110:457–474, 1981.

[141] Chi C Tung and Norden E Huang. Influence of current on statistical properties of waves. *Journal of the Waterways, Harbors and Coastal Engineering Division*, 100(4):267–278, 1974.

[142] Norden E Huang, Davidson T Chen, Chi-Chao Tung, and James R Smith. Interactions between steady won-uniform currents and gravity waves with applications for current measurements. *Journal of Physical Oceanography*, 2(4):420–431, 1972.

[143] T S Hedges and B W Lee. The equivalent uniform current in wave-current computations. *Coastal Engineering*, 16(3):301–311, 1992.

[144] Richard L Soulsby, L Hamm, G Klopman, D Myrhaug, R R Simons, and G P Thomas. Wave-current interaction within and outside the bottom boundary layer. *Coastal Engineering*, 21(1-3):41–69, 1993.

[145] H L Tolman. The influence of unsteady depths and currents of tides on wind-wave propagation in shelf seas. *Journal of Physical Oceanography*, 20(8):1166–1174, 1990.

[146] Hendrik L Tolman. Effects of tides and storm surges on North Sea wind waves. *Journal of Physical Oceanography*, 21(6):766–781, 1991.

[147] Hendrik L Tolman. A third-generation model for wind waves on slowly varying, unsteady, and inhomogeneous depths and currents. *Journal of Physical Oceanography*, 21(6):782–797, 1991.

[148] R Burrows and T S Hedges. The influence of currents on ocean wave climates. *Coastal Engineering*, 9(3):247–260, 1985.

[149] T S Hedges. Combinations of waves and currents: an introduction. *Proceedings of the Institution of Civil Engineers*, 82(3):567–585, 1987.

[150] J Wolf. The analysis of bottom pressure and current data for waves. In *Seventh International Conference on Electronic Engineering in Oceanography - Technology Transfer from Research to Industry*, pages 165–172. IET, 1997.

[151] J Wolf and D Prandle. Some observations of wave–current interaction. *Coastal Engineering*, 37(3-4):471–485, 1999.

[152] H Peters and H Boonstra. Fatigue loading on a single pile platform due to combined action of waves and currents. In *Vol 3. Structures*. Intl. Conference on Behaviour of Offshore Structures (BOSS '88), 1988.

[153] Johan M Peeringa. Fatigue loading on a 5MW offshore wind turbine due to the combined action of waves and current. In *Journal of Physics: Conference Series*, volume 524, page 012093. IOP Publishing, 2014.

[154] Josh Davidson and John V Ringwood. Mathematical modelling of mooring systems for wave energy converters—A review. *Energies*, 10(5):666, 2017.

[155] Det Norske Veritas. Dnv-os-j101:'offshore standard: Design of offshore wind turbine structures'. *Det Norske Veritas AS*, 2013.

[156] Matthew Hall, Brad Buckham, and Curran Crawford. Evaluating the importance of mooring line model fidelity in floating offshore wind turbine simulations. *Wind Energy*, 17(12):1835–1853, 2014.

[157] José Azcona, David Palacio, Xabier Munduate, Leo González, and Tor Anders Nygaard. Impact of mooring lines dynamics on the fatigue and ultimate loads of three offshore floating wind turbines computed with IEC 61400-3 guideline. *Wind Energy*, 20(5):797–813, 2017.

[158] J W Leonard and R A Young. Coupled response of compliant offshore platforms. *Engineering Structures*, 7(2):74–84, 1985.

[159] T S Hedges. Some effects of currents on wave spectra. In *Proceedings of the First Indian Conference in Ocean Engineering*, volume 1, pages 30–35, 1981.

[160] Terence S Hedges, Kostas Anastasiou, and David Gabriel. Interaction of random waves and currents. *Journal of Waterway, Port, Coastal, and Ocean Engineering*, 111(2):275–288, 1985.

[161] Ronald J Lai, Steven R Long, and Norden E Huang. Laboratory studies of wave-current interaction: Kinematics of the strong interaction. *Journal of Geophysical Research: Oceans*, 94(C11):16201–16214, 1989.

[162] C Guedes Soares and H De Pablo. Experimental study of the transformation of wave spectra by a uniform current. *Ocean Engineering*, 33(3-4):293–310, 2006.

[163] M C Silva, M A Vitola, P T T Esperança, S H Sphaier, and C A Levi. Numerical simulations of wave–current flow in an ocean basin. *Applied Ocean Research*, 61: 32–41, 2016.

[164] Nabil M Ismail. Wave-current models for design of marine structures. *Journal of Waterway, Port, Coastal, and Ocean Engineering*, 110(4):432–447, 1984.

[165] N Haritos. Modeling the response of TLP structures to environmental loading. *Journal of Wind Engineering and Industrial Aerodynamics*, 44(1-3):2475–2485, 1992.

[166] N Barltrop, K S Varyani, A Grant, D Clelland, and X P Pham. Investigation into wave—current interactions in marine current turbines. *Proceedings of the Institution of Mechanical Engineers, Part A: Journal of Power and Energy*, 221 (2):233–242, 2007.

[167] T A de Jesus Henriques, S C Tedds, A Botsari, G Najafian, T S Hedges, C J Sutcliffe, Ieuan Owen, and R J Poole. The effects of wave–current interaction on the performance of a model horizontal axis tidal turbine. *International Journal of Marine Energy*, 8:17–35, 2014.

[168] Lin Chen and Biswajit Basu. Fatigue load estimation of a spar-type floating offshore wind turbine considering wave-current interactions. *International Journal of Fatigue*, 116:421–428, 2018.

[169] Jeffrey Alan Simmen and P G Saffman. Steady deep-water waves on a linear shear current. *Studies in Applied Mathematics*, 73(1):35–57, 1985.

[170] Adrian Constantin. Dispersion relations for periodic traveling water waves in flows with discontinuous vorticity. *Communications on Pure & Applied Analysis*, 11(4): 1397, 2012.

[171] Calin Iulian Martin. Dispersion relations for periodic water waves with surface tension and discontinuous vorticity. *Discrete & Continuous Dynamical Systems*, 34(8):3109, 2014.

[172] Calin Iulian Martin. Dispersion relations for gravity water flows with two rotational layers. *European Journal of Mechanics-B/Fluids*, 50:9–18, 2015.

[173] Walter Strauss. Steady water waves. *Bulletin of the American Mathematical Society*, 47(4):671–694, 2010.

[174] Adrian Constantin and Joachim Escher. Particle trajectories in solitary water waves. *Bulletin of the American Mathematical Society*, 44(3):423–431, 2007.

[175] Biswajit Basu. Estimation of wave heights from pressure data at the bed in the presence of uniform underlying currents. *Nonlinear Analysis*, 156:82–89, 2017.

[176] Biswajit Basu. Wave height estimates from pressure and velocity data at an intermediate depth in the presence of uniform currents. *Philosophical Transactions of the Royal Society A: Mathematical, Physical and Engineering Sciences*, 376 (2111):20170087, 2018.

[177] Biswajit Basu. Solitary water waves propagating on an underlying uniform current over a finite depth. *Nonlinear Analysis*, 172:25–35, 2018.

[178] Biswajit Basu and Calin I Martin. An alternative approach to study irrotational periodic gravity water waves. *Zeitschrift für angewandte Mathematik und Physik*, 72(4):1–15, 2021.

[179] NOAA's National Weather Service. Pacific Tsunami Warning Center FAQ. `http://ptwc.weather.gov/faq.php`, 2014. [Online; accessed March 3, 2014].

[180] Commonwealth of Australia Bureau of Meteorology. Tsunami Facts and Information. `http://www.bom.gov.au/tsunami/info/`, 2014. [Online; accessed March 3, 2014].

[181] Costas E Synolakis and Emile A Okal. 1992–2002: perspective on a decade of post-tsunami surveys. In *Tsunamis*, pages 1–29. Springer, 2005.

[182] Hong-jian Cao and De-cheng Wan. RANS-VOF solver for solitary wave run-up on a circular cylinder. *China Ocean Engineering*, 29(2):183–196, 2015.

[183] Se-Min Jeong, Ji-In Park, and Jong-Chun Park. Numerical simulation of 2-D solitary wave run-up over various slopes using a particle-based method. *Water*, 11(3):462, 2019.

[184] George T Yates and Kuan-Hsiung Wang. Solitary wave scattering by a vertical cylinder: experimental study. In *The Fourth International Offshore and Polar Engineering Conference*. OnePetro, 1994.

[185] Ming Zhao, Liang Cheng, and Bin Teng. Numerical simulation of solitary wave scattering by a circular cylinder array. *Ocean Engineering*, 34(3-4):489–499, 2007.

[186] Lei Li, Jingxin Zhang, Jack M Chen, and Xuanyu Zhao. Experimental study of solitary wave interaction with vertical structures. In *The 28th International Ocean and Polar Engineering Conference*. International Society of Offshore and Polar Engineers, 2018.

[187] Chih-Hua Chang. Interaction of a solitary wave with vertical fully/partially submerged circular cylinders with/without a hollow zone. *Journal of Marine Science and Engineering*, 8(12):1022, 2020.

[188] BZ Zhou, GX Wu, and QC Meng. Interactions of fully nonlinear solitary wave with a freely floating vertical cylinder. *Engineering Analysis with Boundary Elements*, 69:119–131, 2016.

[189] Junnan Cui, Sheng Dong, Zhifeng Wang, Xinyu Han, and Miao Yu. Experimental research on internal solitary waves interacting with moored floating structures. *Marine Structures*, 67:102641, 2019.

[190] Shuqun Cai, Xiaomin Long, and Zijun Gan. A method to estimate the forces exerted by internal solitons on cylindrical piles. *Ocean Engineering*, 30(5):673–689, 2003.

[191] Shuqun Cai, Xiaomin Long, and Shengan Wang. Forces and torques exerted by internal solitons in shear flows on cylindrical piles. *Applied Ocean Research*, 30 (1):72–77, 2008.

[192] H Q Zhang and J C Li. Wave loading on floating platforms by internal solitary waves. In *New trends in fluid mechanics research*, pages 304–307. Springer, 2007.

[193] Wenhao Huang, Yunxiang You, and Wei Li. Predicting internal solitary wave loads on spar platforms. In *Offshore Technology Conference*. Offshore Technology Conference, 2015.

[194] Xu Wang and Ji-Fu Zhou. Numerical and experimental study on the scale effect of internal solitary wave loads on spar platforms. *International Journal of Naval Architecture and Ocean Engineering*, 12:569–577, 2020.

[195] Bastiaan Buchner. *Green water on ship-type offshore structures*. PhD thesis, Delft University of Technology Delft, The Netherlands, 2002.

[196] M Greco. *A Two-dimensional Study of Green-water Loading*. PhD thesis, Norwegian University of Science and Technology, Trondheim, Norwegian, 2001.

[197] J V Hernández-Fontes. *An analytical and experimental study of shipping water evolution and related vertical loading*. PhD thesis, COPPE, Federal University of Rio de Janeiro, Brazil, 2018.

[198] M Greco, G Colicchio, and O M Faltinsen. Shipping of water on a two-dimensional structure. part 2. *Journal of Fluid Mechanics*, 581:371–399, 2007.

[199] M Greco, O M Faltinsen, and M Landrini. Shipping of water on a two-dimensional structure. *Journal of Fluid Mechanics*, 525:309–332, 2005.

[200] Bas Buchner. The impact of green water on FPSO design. In *Offshore technology conference*. OnePetro, 1995.

[201] Daniel F C Silva, Alvaro L G A Coutinho, and Paulo T T Esperança. Green water loads on FPSOs exposed to beam and quartering seas, part I: Experimental tests. *Ocean Engineering*, 140:419–433, 2017.

[202] Katsuji Tanizawa, Hiroshi Sawada, Kunihiro Hoshino, and Masaru Tsujimoto. Visualization of shipping water on running ship foredeck in regular head seas. In *The Fourteenth International Offshore and Polar Engineering Conference*. OnePetro, 2004.

[203] Jassiel V H Fontes, Irving D Hernández, Edgar Mendoza, Rodolfo Silva, Eliana Brandão da Silva, Matheus Rocha de Sousa, José Gonzaga, Raíssa SF Kamezaki, Lizeth Torres, and Paulo T T Esperança. On the evolution of different types of green water events. *Water*, 13(9):1148, 2021.

[204] Jassiel V Hernández-Fontes, Irving D Hernández, Edgar Mendoza, and Rodolfo Silva. Green water evolution on a fixed structure induced by incoming wave trains. *Mechanics Based Design of Structures and Machines*, pages 1–29, 2020.

[205] Jassiel V Hernández-Fontes, Paulo de Tarso T Esperança, Juan F Bárcenas Graniel, Sergio H Sphaier, and Rodolfo Silva. Green water on a fixed structure due to incident bores: Guidelines and database for model validations regarding flow evolution. *Water*, 11(12):2584, 2019.

[206] Jassiel V Hernández-Fontes, Marcelo A Vitola, T Esperança Paulo de Tarso, and Sergio H Sphaier. Analytical convolution model for shipping water evolution on a fixed structure. *Applied Ocean Research*, 82:415–429, 2019.

[207] Irving D Hernández, Jassiel V Hernández-Fontes, Marcelo A Vitola, Monica C Silva, and Paulo T T Esperança. Water elevation measurements using binary image analysis for 2d hydrodynamic experiments. *Ocean Engineering*, 157:325–338, 2018.

[208] Joe J Monaghan. Smoothed particle hydrodynamics. *Reports on Progress in Physics*, 68(8):1703, 2005.

[209] Joe J Monaghan. Simulating free surface flows with SPH. *Journal of Computational Physics*, 110(2):399–406, 1994.

[210] Corrado Altomare, Alejandro J C Crespo, B D Rogers, J M Domínguez, X Gironella, and M Gómez-Gesteira. Numerical modelling of armour block sea breakwater with smoothed particle hydrodynamics. *Computers & Structures*, 130: 34–45, 2014.

[211] Corrado Altomare, Alejandro JC Crespo, Jose M Domínguez, Moncho Gómez-Gesteira, Tomohiro Suzuki, and Toon Verwaest. Applicability of smoothed particle hydrodynamics for estimation of sea wave impact on coastal structures. *Coastal Engineering*, 96:1–12, 2015.

[212] C Altomare, J M Domínguez, A J C Crespo, J González-Cao, T Suzuki, M Gómez-Gesteira, and P Troch. Long-crested wave generation and absorption for SPH-based DualSPHysics model. *Coastal Engineering*, 127:37–54, 2017.

[213] S Adami, X Y Hu, and Nikolaus A Adams. A generalized wall boundary condition for smoothed particle hydrodynamics. *Journal of Computational Physics*, 231 (21):7057–7075, 2012.

[214] Andrea Colagrossi and Maurizio Landrini. Numerical simulation of interfacial flows by smoothed particle hydrodynamics. *Journal of Computational Physics*, 191(2): 448–475, 2003.

[215] Ricardo B Canelas, Jose M Domínguez, Alejandro J C Crespo, Moncho Gómez-Gesteira, and Rui M L Ferreira. A Smooth Particle Hydrodynamics discretization for the modelling of free surface flows and rigid body dynamics. *International Journal for Numerical Methods in Fluids*, 78(9):581–593, 2015.

[216] Ricardo B Canelas, Alejandro J C Crespo, Jose M Domínguez, Rui M L Ferreira, and Moncho Gómez-Gesteira. SPH–DCDEM model for arbitrary geometries in free surface solid–fluid flows. *Computer Physics Communications*, 202:131–140, 2016.

[217] Pourya Omidvar, Hossein Norouzi, and Ahad Zarghami. Smoothed particle hydrodynamics for water wave propagation in a channel. *International Journal of Modern Physics C*, 26(08):1550085, 2015.

[218] Pourya Omidvar, Peter K Stansby, and Benedict D Rogers. SPH for 3D floating bodies using variable mass particle distribution. *International Journal for Numerical Methods in Fluids*, 72(4):427–452, 2013.

[219] Jiang Chang, Shu-xue Liu, and Jin-xuan Li. A study of the stability properties in simulation of wave propagation with SPH method. *China Ocean Engineering*, 31 (2):173–182, 2017.

[220] Alejandro JC Crespo, José M Domínguez, Benedict D Rogers, Moncho Gómez-Gesteira, S Longshaw, R Canelas, R Vacondio, A Barreiro, and O García-Feal. DualSPHysics: Open-source parallel CFD solver based on Smoothed Particle Hydrodynamics (SPH). *Computer Physics Communications*, 187:204–216, 2015.

[221] Tim Verbrugghe, José Manuel Domínguez, Alejandro J C Crespo, Corrado Altomare, Vicky Stratigaki, Peter Troch, and Andreas Kortenhaus. Coupling methodology for smoothed particle hydrodynamics modelling of non-linear wave-structure interactions. *Coastal Engineering*, 138:184–198, 2018.

[222] Henry David and Silvia Sastre-Gomez. Steady periodic water waves bifurcating for fixed-depth rotational flows with discontinuous vorticity. *Differential and Integral Equations*, 31(1/2):1–26, 2018.

[223] Mateusz Kluczek and Calin Iulian Martin. Dispersion relations for fixed mean-depth flows with two discontinuities in vorticity. *Nonlinear Analysis*, 181:62–86, 2019.

[224] Paschalis Karageorgis. Dispersion relation for water waves with non-constant vorticity. *European Journal of Mechanics-B/Fluids*, 34:7–12, 2012.

[225] James T Kirby and Tsung-Muh Chen. Surface waves on vertically sheared flows: approximate dispersion relations. *Journal of Geophysical Research: Oceans*, 94 (C1):1013–1027, 1989.

[226] Simen Å Ellingsen and Yan Li. Approximate dispersion relations for waves on arbitrary shear flows. *Journal of Geophysical Research: Oceans*, 122(12):9889–9905, 2017.

[227] Gaël Guennebaud and Benoit Jacob. Eigen. *URl: http://eigen. tuxfamily. org*, 2010.

[228] Adrian Constantin and Walter Strauss. Pressure beneath a Stokes wave. *Communications on Pure and Applied Mathematics*, 63(4):533–557, 2010.

[229] John H Michell. Xliv. the highest waves in water. *The London, Edinburgh, and Dublin Philosophical Magazine and Journal of Science*, 36(222):430–437, 1893.

[230] John Fenton. A ninth-order solution for the solitary wave. *J. Fluid Mech*, 53(2): 257–271, 1972.

[231] Leonard W Schwartz. Computer extension and analytic continuation of Stokes' expansion for gravity waves. *Journal of Fluid Mechanics*, 62(3):553–578, 1974.

[232] D C Quarton. The evolution of wind turbine design analysis—a twenty year progress review. *Wind Energy: An International Journal for Progress and Applications in Wind Power Conversion Technology*, 1(S1):5–24, 1998.

[233] A Staino, B Basu, and Søren R K Nielsen. Actuator control of edgewise vibrations in wind turbine blades. *Journal of Sound and Vibration*, 331(6):1233–1256, 2012.

[234] A Staino and B Basu. Dynamics and control of vibrations in wind turbines with variable rotor speed. *Engineering Structures*, 56:58–67, 2013.

[235] Andrea Staino and Biswajit Basu. Emerging trends in vibration control of wind turbines: a focus on a dual control strategy. *Philosophical Transactions of the Royal Society A: Mathematical, Physical and Engineering Sciences*, 373(2035): 20140069, 2015.

[236] John Arrigan, Vikram Pakrashi, Biswajit Basu, and Satish Nagarajaiah. Control of flapwise vibrations in wind turbine blades using semi-active tuned mass dampers. *Structural Control and Health Monitoring*, 18(8):840–851, 2011.

[237] Breiffni Fitzgerald, Biswajit Basu, and Søren R K Nielsen. Active tuned mass dampers for control of in-plane vibrations of wind turbine blades. *Structural Control and Health Monitoring*, 20(12):1377–1396, 2013.

[238] Breiffni Fitzgerald and B Basu. Cable connected active tuned mass dampers for control of in-plane vibrations of wind turbine blades. *Journal of Sound and Vibration*, 333(23):5980–6004, 2014.

[239] MATLAB. *version 7.10.0 (R2010a)*. The MathWorks Inc., Natick, Massachusetts, 2010.

[240] J R Morison, J W Johnson, and S A Schaaf. The force exerted by surface waves on piles. *Journal of Petroleum Technology*, 2(05):149–154, 1950.

[241] Zili Zhang, Biswajit Basu, and Søren R K Nielsen. Tuned liquid column dampers for mitigation of edgewise vibrations in rotating wind turbine blades. *Structural Control and Health Monitoring*, 22(3):500–517, 2015.

[242] A A Tjavaras. *The dynamics of Highly Extensible Cables*. PhD thesis, Massachusetts Institute of Technology (USA), 1996.

[243] A A Tjavaras, Q Zhu, Y Liu, M S Triantafyllou, and D K P Yue. The mechanics of highly-extensible cables. *Journal of Sound and Vibration*, 213(4):709–737, 1998.

[244] J I Gobat and M A Grosenbaugh. Time-domain numerical simulation of ocean cable structures. *Ocean Engineering*, 33(10):1373–1400, 2006.

[245] L Chen and B Basu. Development of an open-source simulation tool for mooring systems. *CERI-ITRN 2018, the Univeristy of Dublin, Ireland*, pages 823–828, 2018.

[246] Matthew Hall and Andrew Goupee. Validation of a lumped-mass mooring line model with DeepCwind semisubmersible model test data. *Ocean Engineering*, 104:590–603, 2015.

[247] William H Press. *The art of scientific computing*. Cambridge University Press, 1992.

[248] William C Webster. Mooring-induced damping. *Ocean Engineering*, 22(6):571–591, 1995.

[249] J Gobat. *The Dynamics of Geometrically Compliant Mooring Systems*. PhD thesis, Massachusets Institute of Technology and Woods Hole Oceanographic Institution, 2003.

[250] Adrian Constantin. Exact travelling periodic water waves in two-dimensional irrotational flows. In *Nonlinear water waves*, pages 1–82. Springer, 2016.

[251] S Barth. Description of the relation of wind, wave and current characteristics at the offshore wind farm Egmond aan Zee (OWEZ) location in 2006 (ECN-E-07-104). *Report by ECN, Energy research Centre of the Netherlands, Netherlands*, 2008.

[252] Didier Clamond. Steady finite-amplitude waves on a horizontal seabed of arbitrary depth. *Journal of Fluid Mechanics*, 398:45–60, 1999.

[253] J Lighthill. Waves in fluids. *Cambridge University Press*, 1978.

[254] J J Stoker. *Water Waves. The Mathematical Theory with Applications*. Interscience Publ Inc., New York, 1957.

[255] Walter Craig and Peter Sternberg. Symmetry of solitary waves: Solitary waves. *Communications in Partial Differential Equations*, 13(5):603–633, 1988.

[256] Charles J Amick. Bounds for water waves. *Archive for Rational Mechanics and Analysis*, 99(2):91–114, 1987.

[257] Pavel I Plotnikov. A proof of the Stokes conjecture in the theory of surface waves. *Studies in Applied Mathematics*, 108(2):217–244, 2002.

[258] Didier Clamond. Cnoidal-type surface waves in deep water. *Journal of Fluid Mechanics*, 489:101–120, 2003.

[259] Didier Clamond and Denys Dutykh. Fast accurate computation of the fully nonlinear solitary surface gravity waves. *Computers & fluids*, 84:35–38, 2013.

[260] D J Kordeweg and G de Vries. On the change of form of long waves advancing in a rectangular channel, and a new type of long stationary wave. *Phil. Mag*, 39: 422–443, 1895.

[261] Milton Abromowitz and Irene A Stegun. *Handbook of mathematical functions*. NBS (now NIST).

[262] Robert G Dean and Robert A Dalrymple. *Water wave mechanics for engineers and scientists*, volume 2. world scientific publishing Co Inc, 1991.

[263] Denys Dutykh and Didier Clamond. Efficient computation of steady solitary gravity waves. *Wave Motion*, 51(1):86–99, 2014.

[264] Mitsuhiro Tanaka. The stability of solitary waves. *The Physics of fluids*, 29(3): 650–655, 1986.

[265] Eugene Isaacson and Herbert Bishop Keller. *Analysis of numerical methods*. Courier Corporation, 2012.

[266] Lloyd N Trefethen and David Bau III. *Numerical linear algebra*, volume 50. Siam, 1997.

[267] Vladimir I Petviashvili. Equation of an extraordinary soliton. *Fizika plazmy*, 2: 469–472, 1976.

[268] Andrea Colagrossi, Matteo Antuono, and David Le Touzé. Theoretical considerations on the free-surface role in the smoothed-particle-hydrodynamics model. *Physical Review E*, 79(5):056701, 2009.

[269] Gui-Rong Liu and Moubin B Liu. *Smoothed Particle Hydrodynamics: A meshfree particle method*. World Scientific, 2003.

[270] Joseph J Monaghan and John C Lattanzio. A refined particle method for astrophysical problems. *Astronomy and Astrophysics*, 149:135–143, 1985.

[271] Holger Wendland. Piecewise polynomial, positive definite and compactly supported radial functions of minimal degree. *Advances in Computational Mathematics*, 4(1):389–396, 1995.

[272] Jonathan Feldman. *Dynamic refinement and boundary contact forces in Smoothed Particle Hydrodynamics with applications in fluid flow problems*. PhD thesis, Swansea University, 2006.

[273] DIEGO Molteni, Andrea Colagrossi, and Giuseppina Colicchio. On the use of an alternative water state equation in SPH. In *Proc. SPHERIC, 2nd International Workshop*. Citeseer, 2007.

[274] J W Swegle, D L Hicks, and S W Attaway. Smoothed particle hydrodynamics stability analysis. *Journal of Computational Physics*, 116(1):123–134, 1995.

[275] E-S Lee, Charles Moulinec, Rui Xu, Damien Violeau, Dominique Laurence, and Peter Stansby. Comparisons of weakly compressible and truly incompressible algorithms for the SPH mesh free particle method. *Journal of Computational Physics*, 227(18):8417–8436, 2008.

[276] Rui Xu, Peter Stansby, and Dominique Laurence. Accuracy and stability in incompressible SPH (ISPH) based on the projection method and a new approach. *Journal of Computational Physics*, 228(18):6703–6725, 2009.

[277] Salvatore Marrone, MAGD Antuono, A Colagrossi, G Colicchio, D Le Touzé, and G Graziani. δ-SPH model for simulating violent impact flows. *Computer Methods in Applied Mechanics and Engineering*, 200(13-16):1526–1542, 2011.

[278] J J Monaghan and A Kos. Solitary waves on a cretan beach. *Journal of Waterway, Port, Coastal, and Ocean Engineering*, 125(3):145–155, 1999.

[279] George Keith Batchelor. *An introduction to fluid dynamics*. Cambridge University Press, 2000.

[280] Matteo Antuono, Andrea Colagrossi, Salvatore Marrone, and Claudio Lugni. Propagation of gravity waves through an SPH scheme with numerical diffusive terms. *Computer Physics Communications*, 182(4):866–877, 2011.

[281] S Marrone. *Enhanced SPH modeling of free-surface flows with large deformations*. PhD thesis, University of Rome La Sapienza, Rome, Italy, 2012.

[282] P N Sun, A Colagrossi, S Marrone, M Antuono, and A-M Zhang. A consistent approach to particle shifting in the δ-Plus-SPH model. *Computer Methods in Applied Mechanics and Engineering*, 348:912–934, 2019.

[283] F Biésel and F Suquet. Les appareils générateurs de houle en laboratoire. *La houille blanche*, (2):147–165, 1951.

[284] Ole Secher Madsen. On the generation of long waves. *Journal of Geophysical Research*, 76(36):8672–8683, 1971.

[285] Zhou Liu and Peter Frigaard. *Generation and analysis of random waves*. Aalborg Universitet, 1999.

[286] Alejandro C Crespo, Jose M Dominguez, Anxo Barreiro, Moncho Gómez-Gesteira, and Benedict D Rogers. GPUs, a new tool of acceleration in CFD: efficiency and reliability on smoothed particle hydrodynamics methods. *PloS one*, 6(6):e20685, 2011.

[287] A-man Zhang, Peng-nan Sun, Fu-ren Ming, and A Colagrossi. Smoothed particle hydrodynamics and its applications in fluid-structure interactions. *Journal of Hydrodynamics, Ser. B*, 29(2):187–216, 2017.

[288] SJ Lind, Rui Xu, PK Stansby, and Benedict D Rogers. Incompressible smoothed particle hydrodynamics for free-surface flows: A generalised diffusion-based algorithm for stability and validations for impulsive flows and propagating waves. *Journal of Computational Physics*, 231(4):1499–1523, 2012.

[289] Adrian Constantin. Mean velocities in a Stokes wave. *Archive for Rational Mechanics and Analysis*, pages 1–11, 2013.

[290] Pourya Omidvar, Peter K Stansby, and Benedict D Rogers. Wave body interaction in 2D using smoothed particle hydrodynamics (SPH) with variable particle mass. *International Journal for Numerical Methods in Fluids*, 68(6):686–705, 2012.

[291] Biswajit Basu, Andrea Staino, and Malabika Basu. Role of flexible alternating current transmission systems devices in mitigating grid fault-induced vibration of wind turbines. *Wind Energy*, 17(7):1017–1033, 2014.

[292] Daniel W Carlson and Yahya Modarres-Sadeghi. Vortex-induced vibration of spar platforms for floating offshore wind turbines. *Wind Energy*, 21(11):1169–1176, 2018.

[293] Fei Duan, Zhiqiang Hu, and Jin Wang. Investigation of the VIMs of a spar-type FOWT using a model test method. *Journal of Renewable and Sustainable energy*, 8(6):063301, 2016.

[294] Young W Kwon and Hyochoong Bang. *The finite element method using MATLAB*. CRC press, 2018.

A1 Appendix

A1.1 Generalized matrices

A1.1.1 Generalized mass matrix

$$M_{structuralmass} = \begin{bmatrix} M_{11} & 0 & 0 & M_{14} & 0 & M_{16} & M_{17} & M_{18} & 0 & 0 \\ 0 & M_{22} & 0 & M_{24} & 0 & M_{26} & M_{27} & M_{28} & 0 & 0 \\ 0 & 0 & M_{33} & M_{34} & 0 & M_{36} & M_{37} & M_{38} & 0 & 0 \\ M_{41} & M_{42} & M_{43} & M_{44} & 0 & 0 & 0 & 0 & 0 & 0 \\ 0 & 0 & 0 & 0 & M_{55} & 0 & 0 & 0 & 0 & 0 \\ M_{61} & M_{62} & M_{63} & 0 & 0 & M_{66} & 0 & 0 & 0 & 0 \\ M_{71} & M_{72} & M_{73} & 0 & 0 & 0 & M_{77} & 0 & 0 & 0 \\ M_{81} & M_{82} & M_{83} & 0 & 0 & 0 & 0 & M_{8,8} & 0 & 0 \\ 0 & 0 & 0 & 0 & 0 & 0 & 0 & 0 & M_{99} & 0 \\ 0 & 0 & 0 & 0 & 0 & 0 & 0 & 0 & 0 & M_{1010} \end{bmatrix} \tag{A1.1}$$

The matrix elements in Eq.A1.1 are expressed by

$$M_{11} = M_{b,e} \tag{A1.2a}$$
$$M_{22} = M_{b,e} \tag{A1.2b}$$
$$M_{33} = M_{b,e} \tag{A1.2c}$$
$$M_{44} = M_{t,e} \tag{A1.2d}$$
$$M_{55} = M_s \tag{A1.2e}$$
$$M_{66} = M_s \tag{A1.2f}$$
$$M_{77} = M_s \tag{A1.2g}$$
$$M_{88} = I_{s,1} + M_s * d(d = 0) \tag{A1.2h}$$
$$M_{99} = I_{s,2} + M_s * d(d = 0) \tag{A1.2i}$$
$$M_{1010} = I_{s,3}, \tag{A1.2j}$$

where, M_s is the spar mass, $I_{s,1}, I_{s,2}, I_{s,3}$ are the mass moment of inertia of the spar. d

is the distance from the depth of spar reference point to the depth of the mass centre $M_{t,e} = \int_0^{h_t} \mu_t \phi_t^2(z_t) dz_t$ is the tower modal mass. $M_{b,e} = \int_0^R \mu_b \phi_b^2 dr$ is the blade modal mass. The total mass of each blade is $M_b = \int_0^R \mu_b(r) dr$. $M_{t,1} = \int_0^{h_t} \mu_t \phi_t(z_t) dz_t$ is tower mass weighted by the mode shape, $M_n = M_{nac} + M_{rotor}$ is the nacelle and rotor mass. The nacelle mass center to tower top is denoted by $l_m = (1.9, 0, 1.75)$, the rotor mass center to tower top is denoted by $l_r = (-5.0191, 0, 1.96)$.

The term $h_{tc,1} = \int_0^{h_t} \mu_t \phi_t(z_t) dz_t / M_{t,1}$ is the mass center of $M_{t,1}$; $h_{tc} = \int_0^{h_t} \mu_t z_t dz_t / M_t$ is the tower mass center, I_t is the tower moment of inertia about its mass center in roll and pitch directions. The first mode shape of the tower side-to-side vibration is denoted by $\phi_t(z_t)$ where z_t is the tower axis upward originating from tower base. Hence, the tower lateral deformation is denoted as $\phi_t(z_t) q_4(t)$. The tower height is denoted as h_t measured from the base of the tower and tower mass per unit height is denoted as $\mu_t(z_t)$. Note that the mode shape function ϕ_t is normalized so that $\phi_t(h_t) = 1$, which is thus omitted in the following parts. The total tower mass is $M_t = \int_0^{h_t} \mu_t dz_t$.

$$\mathbf{M}_{timevarying} = \begin{bmatrix} 0 & 0 & 0 & M_{14} & 0 & M_{16} & M_{17} & M_{18} & 0 & 0 \\ 0 & 0 & 0 & M_{24} & 0 & M_{26} & M_{27} & M_{28} & 0 & 0 \\ 0 & 0 & 0 & M_{34} & 0 & M_{36} & M_{37} & M_{38} & 0 & 0 \\ M_{41} & M_{42} & M_{43} & 0 & 0 & 0 & 0 & 0 & 0 & 0 \\ 0 & 0 & 0 & 0 & 0 & 0 & 0 & 0 & 0 & 0 \\ M_{61} & M_{62} & M_{63} & 0 & 0 & 0 & 0 & 0 & 0 & 0 \\ M_{71} & M_{72} & M_{73} & 0 & 0 & 0 & 0 & 0 & 0 & 0 \\ M_{81} & M_{82} & M_{83} & 0 & 0 & 0 & 0 & 0 & 0 & 0 \\ 0 & 0 & 0 & 0 & 0 & 0 & 0 & 0 & 0 & 0 \\ 0 & 0 & 0 & 0 & 0 & 0 & 0 & 0 & 0 & 0 \end{bmatrix} \tag{A1.3}$$

where, the blade weighted masses are computed by

$$M_{ij} = -M_{b,1} cos\Psi_j, i = 4, 6, j = 1, 2, 3, \tag{A1.4a}$$

$$M_{7j} = -M_{b,1} sin\Psi_j, j = 1, 2, 3, \tag{A1.4b}$$

$$M_{8j} = hM_{4j}, j = 1, 2, 3. \tag{A1.4c}$$

The blade mass weighted by the mode shape is given as $M_{b,1} = \int_0^R \mu_b(r) \phi_b(r) dr$.

$$\mathbf{M}_{spar.lumpedmass} = \begin{bmatrix} M_{55} & 0 & 0 & 0 & M_{59} & 0 \\ 0 & M_{66} & 0 & M_{68} & 0 & M_{610} \\ 0 & 0 & M_{77} & 0 & M_{79} & 0 \\ 0 & M_{86} & 0 & M_{88} & 0 & 0 \\ M_{95} & 0 & M_{97} & 0 & M_{99} & 0 \\ 0 & M_{106} & 0 & 0 & 0 & M_{1010} \end{bmatrix} \tag{A1.5}$$

where, the lumped nacelle mass, rotor mass, and tower mass are taken with respect to the spar reference point. The matrix elements are given as follows

$$M_{55} = M_n + M_n + M_t, \tag{A1.6a}$$

$$M_{66} = M_n + M_n + M_t, \tag{A1.6b}$$

$$M_{77} = M_n + M_n + M_t, \tag{A1.6c}$$

$$M_{88} = M_{nac}(l_m(3) + h)^2 + M_{nac}l_m^2(2) + M_r(l_r(3) + h)^2 + M_r l_r^2(2) + M_t(h - h_t + h_{tc,1}) + I_{nac}(1), \tag{A1.6d}$$

$$M_{99} = M_{nac}(l_m(3) + h)^2 + M_{nac}l_m^2(1) + M_r(l_r(3) + h)^2 + M_r l_r^2(1) + M_t(h - h_t + h_{tc,1}) + I_{nac}(2), \tag{A1.6e}$$

$$M_{1010} = I_{nac}(3) + M_r l_r^2(1) + M_r l_r^2(2), \tag{A1.6f}$$

$$M_{68} = -M_{nac}(l_m(3) + h)^2 - M_r(l_r(3) + h)^2 - M_t(h - h_t + h_{tc,1}), \tag{A1.6g}$$

$$M_{86} = M_{68}, \tag{A1.6h}$$

$$M_{59} = M_{nac}(l_m(3) + h) + M_r(l_r(3) + h) + M_t(h - h_t + h_{tc,1}), \tag{A1.6i}$$

$$M_{95} = M_{59}, \tag{A1.6j}$$

$$M_{610} = M_{nac}l_m(1) + M_r l_r(1), \tag{A1.6k}$$

$$M_{106} = M_{610}, \tag{A1.6l}$$

$$M_{79} = -M_{nac}l_m(1) - M_r l_r(1), \tag{A1.6m}$$

$$M_{97} = M_{79}, \tag{A1.6n}$$

where, $h = e_t + d_G$, e_t is the elevation of the tower top, d_G is the depth of the centre of spar.

Added mass coefficient

$$\mathbf{M}_{spar.addedmass} = \begin{bmatrix} M_{55} & 0 & 0 & 0 & M_{59} & 0 \\ 0 & M_{66} & 0 & M_{68} & 0 & 0 \\ 0 & 0 & 0 & 0 & 0 & 0 \\ 0 & M_{86} & 0 & M_{88} & 0 & 0 \\ M_{95} & 0 & 0 & 0 & M_{99} & 0 \\ 0 & 0 & 0 & 0 & 0 & 0 \end{bmatrix} \tag{A1.7}$$

$$M_{55} = \sum_{i=1}^{N} C_{s,a} \frac{\rho\pi}{4} dz d_s^2(z_i), \tag{A1.8a}$$

$$M_{66} = \sum_{i=1}^{N} C_{s,a} \frac{\rho\pi}{4} dz d_s^2(z_i), \tag{A1.8b}$$

$$M_{59} = \sum_{i=1}^{N} C_{s,a} \frac{\rho\pi}{4} dz (z_i - z_G) d_s^2(z_i), \tag{A1.8c}$$

$$M_{95} = M_{59}, \tag{A1.8d}$$

$$M_{68} = -\sum_{i=1}^{N} C_{s,a} \frac{\rho\pi}{4} dz (z_i - z_G) d_s^2(z_i), \tag{A1.8e}$$

$$M_{86} = M_{68}, \tag{A1.8f}$$

$$M_{88} = \sum_{i=1}^{N} C_{s,a} \frac{\rho\pi}{4} dz (z_i - z_G)^2 d_s^2(z_i), \tag{A1.8g}$$

$$M_{99} = \sum_{i=1}^{N} C_{s,a} \frac{\rho\pi}{4} dz (z_i - z_G)^2 d_s^2(z_i), \tag{A1.8h}$$

where, $d_s(z_i)$ is the diameter of the spar at z_i; d_z is the height of the $i-$th segment is constant in our study. Note that the heave motions are not considered in the added mass matrix since the Morison equation does not account for the vertical component.

The mass matrix is finally given as follows

$$\mathbf{M} = \begin{bmatrix} M_{11} & 0 & 0 & M_{14} & 0 & M_{16} & M_{17} & M_{18} & 0 & 0 \\ 0 & M_{22} & 0 & M_{24} & 0 & M_{26} & M_{27} & M_{28} & 0 & 0 \\ 0 & 0 & M_{33} & M_{34} & 0 & M_{36} & M_{37} & M_{38} & 0 & 0 \\ M_{41} & M_{42} & M_{43} & M_{44} & 0 & M_{46} & 0 & M_{48} & 0 & 0 \\ 0 & 0 & 0 & 0 & M_{55} & 0 & 0 & 0 & M_{59} & 0 \\ M_{61} & M_{62} & M_{63} & M_{64} & 0 & M_{66} & 0 & M_{68} & 0 & M_{610} \\ M_{71} & M_{72} & M_{73} & 0 & 0 & 0 & M_{77} & 0 & M_{79} & 0 \\ M_{81} & M_{82} & M_{83} & M_{84} & 0 & M_{86} & 0 & M_{88} & 0 & 0 \\ 0 & 0 & 0 & 0 & M_{95} & 0 & M_{97} & 0 & M_{99} & 0 \\ 0 & 0 & 0 & 0 & 0 & M_{106} & 0 & 0 & 0 & M_{1010} \end{bmatrix} \tag{A1.9}$$

A1.1.2 Generalized damping matrix

The general damping matrix is given by

$$\mathbf{C} = \begin{bmatrix} 0 & 0 & 0 & \\ 0 & 0 & 0 & \\ 0 & 0 & 0 & \\ -2\Omega M_{71} & -2\Omega M_{72} & -2\Omega M_{73} & \\ 0 & 0 & 0 & \\ -2\Omega M_{71} & -2\Omega M_{72} & -2\Omega M_{73} & \mathbf{0}_{10\times 7} \\ 2\Omega M_{41} & 2\Omega M_{42} & 2\Omega M_{43} & \\ 2\Omega h M_{71} & 2\Omega h M_{72} & 2\Omega h M_{73} & \\ 0 & 0 & 0 & \\ 0 & 0 & 0 & \end{bmatrix} \tag{A1.10}$$

where, $\mathbf{0}_{10\times7}$ denotes a zero matrix of size 10×7. The time invariant damping matrix is diagonal with the nonzero components are given in the following expressions by

$$\mathbf{C}_{timeinvariant} = \begin{bmatrix} C_{11} & 0 & 0 & 0 & 0 & 0 & 0 & 0 & 0 & 0 \\ 0 & C_{22} & 0 & 0 & 0 & 0 & 0 & 0 & 0 & 0 \\ 0 & 0 & C_{33} & 0 & 0 & 0 & 0 & 0 & 0 & 0 \\ 0 & 0 & 0 & C_{44} & 0 & 0 & 0 & 0 & 0 & 0 \\ 0 & 0 & 0 & 0 & C_{55} & 0 & 0 & 0 & 0 & 0 \\ 0 & 0 & 0 & 0 & 0 & C_{66} & 0 & 0 & 0 & 0 \\ 0 & 0 & 0 & 0 & 0 & 0 & C_{77} & 0 & 0 & 0 \\ 0 & 0 & 0 & 0 & 0 & 0 & 0 & 0 & 0 & 0 \\ 0 & 0 & 0 & 0 & 0 & 0 & 0 & 0 & 0 & 0 \\ 0 & 0 & 0 & 0 & 0 & 0 & 0 & 0 & 0 & C_{1010} \end{bmatrix} \tag{A1.11}$$

$$C_{ii} = C_b, i = 1, 2, 3, \tag{A1.12a}$$

$$C_{44} = C_n + C_t, \tag{A1.12b}$$

$$C_{55} = 1e5, \tag{A1.12c}$$

$$C_{66} = 1e5, \tag{A1.12d}$$

$$C_{77} = 1.3e5, \tag{A1.12e}$$

$$C_{1010} = 1.3e7, \tag{A1.12f}$$

where, C_b is the blade damping coefficient, C_t is the tower damping coefficient, C_n is the nacelle damping coefficient, and C_s is the additional damping coefficient of the spar from additional damping in FAST input file: NRELOffshrBsline5MW-OC3Hywind-HydroDyn.dat.

The time varying damping matrix is obtained from the unit velocity at the blade and

the damping forces are generated at the spar as follows

$$\mathbf{C}_{timevarying} = \begin{bmatrix} 0 & 0 & 0 & \\ 0 & 0 & 0 & \\ 0 & 0 & 0 & \\ C_{41} & C_{42} & C_{43} & \\ 0 & 0 & 0 & \\ C_{61} & C_{62} & C_{63} & \mathbf{0}_{10\times 7} \\ C_{71} & C_{72} & C_{73} & \\ C_{81} & C_{82} & C_{83} & \\ 0 & 0 & 0 & \\ 0 & 0 & 0 & \end{bmatrix} \tag{A1.13}$$

where,

$$C_{ii} = 2\Omega M_{b,1} sin\Psi_j \Omega, i = 4, 6, j = 1, 2, 3, \tag{A1.14a}$$

$$C_{7j} = -2\Omega M_{b,1} cos\Psi_j \Omega, j = 1, 2, 3, \tag{A1.14b}$$

$$C_{8j} = -2h\Omega M_{b,1} sin\Psi_j \Omega, j = 1, 2, 3. \tag{A1.14c}$$

A1.1.3 Generalized stiffness matrix

It is worth to note that the only non-zero elements in the stiffness matrix correspond to the tower stiffness, the diagonal elements for the blade mode shape and the blade related elements. The spar restoring stiffness elements $K_{ii}(i = 7, 8, 9, 10)$ are provide from the NREL Offshore Baseline 5MW-OC3 Hywind Hydrodynamic model (provided in NRELOffshrBsline5MW-OC3Hywind-HydroDyn.dat).

The time invariant stiffness matrix is obtained as

$$\mathbf{K}_{timeinvariant} = \begin{bmatrix} 0 & 0 & 0 & 0 & 0 & 0 & 0 & 0 & 0 & 0 \\ 0 & 0 & 0 & 0 & 0 & 0 & 0 & 0 & 0 & 0 \\ 0 & 0 & 0 & 0 & 0 & 0 & 0 & 0 & 0 & 0 \\ 0 & 0 & 0 & K_{44} & 0 & 0 & 0 & 0 & 0 & 0 \\ 0 & 0 & 0 & 0 & 0 & 0 & 0 & 0 & 0 & 0 \\ 0 & 0 & 0 & 0 & 0 & 0 & 0 & 0 & 0 & 0 \\ 0 & 0 & 0 & 0 & 0 & 0 & K_{77} & 0 & 0 & 0 \\ 0 & 0 & 0 & 0 & 0 & 0 & 0 & K_{88} & 0 & 0 \\ 0 & 0 & 0 & 0 & 0 & 0 & 0 & 0 & K_{99} & 0 \\ 0 & 0 & 0 & 0 & 0 & 0 & 0 & 0 & 0 & K_{1010} \end{bmatrix} \tag{A1.15}$$

where,

$$K_{44} = k_{t,e}, \tag{A1.16a}$$
$$K_{77} = \rho_w g \pi d_{wpa}^2/4, \tag{A1.16b}$$
$$K_{88} = \rho_w g((h_B - h_G)V_s + \pi d_{wpa}^4/64), \tag{A1.16c}$$
$$K_{99} = K_{88}, \tag{A1.16d}$$
$$K_{1010} = 98340000. \tag{A1.16e}$$

In Eq.A1.16, $k_{t,e}$ is the tower modal stiffness. d_{wpa}, which is the spar diameter at water plane area, equals to the taper top diameter of the spar. The tower modal stiffness, $k_{t,e}$, is given by

$$k_{t,e} = \int_0^{h_t} \alpha_t \left(\frac{d^2\phi_t}{d^2z}\right)^2 dz. \tag{A1.17}$$

Similarly, the time-varying stiffness matrix is also obtained with the temporal components are illustrated as

$$\mathbf{K}_{timevarying} = \begin{bmatrix} K_{11} & 0 & 0 & 0 & \\ 0 & K_{22} & 0 & 0 & \\ 0 & 0 & K_{33} & 0 & \\ K_{41} & K_{42} & K_{43} & 0 & \\ 0 & 0 & 0 & 0 & \mathbf{0}_{10\times 6} \\ K_{61} & K_{62} & K_{63} & 0 & \\ K_{71} & K_{72} & K_{73} & 0 & \\ K_{81} & K_{82} & K_{83} & 0 & \\ 0 & 0 & 0 & 0 & \\ 0 & 0 & 0 & 0 & \end{bmatrix}, \tag{A1.18}$$

where,

$$K_{ii} = k_{b,e} + k_{b,c} - \Omega^2 M_{b,e} + k_{bi,g}, i = 1, 2, 3, \tag{A1.19a}$$
$$K_{ij} = -\Omega^2 M_{ij}, i = 4, 6, 7, 8, j = 1, 2, 3. \tag{A1.19b}$$

The term $k_{bi,g}(i = 1, 2, 3)$ are the blade stiffness arising from gravity with

$$k_{b,e} = \omega_b^2 M_{b,e}, \tag{A1.20a}$$
$$k_{bi,g} = -g cos\Psi_i \int_0^R \left[\int_r^R \mu_b(\tau) d\tau\right] \left(\frac{d\phi_b}{dr}\right)^2 dr, \tag{A1.20b}$$
$$k_{b,c} = \Omega^2 \int_0^R \left[\int_r^R \mu_b(\tau)\tau d\tau\right] \left(\frac{d\phi_b}{dr}\right)^2 dr, \tag{A1.20c}$$

where, $k_{b,e}$ is the blade modal stiffness. The tower distributed bending stiffness is denoted as $\alpha_t(z_t)$ and z_t is the tower axis upward originating from tower base. The generalized stiffness coefficients for all the blades are the same because the blades are assumed to be identical.

Note that the buoyancy force contributes to the hydrostatic restoring stiffness, hence

$$\mathbf{K} = \begin{bmatrix} K_{11} & 0 & 0 & 0 & 0 & 0 & 0 & 0 & 0 & 0 \\ 0 & K_{22} & 0 & 0 & 0 & 0 & 0 & 0 & 0 & 0 \\ 0 & 0 & K_{33} & 0 & 0 & 0 & 0 & 0 & 0 & 0 \\ K_{41} & K_{42} & K_{43} & K_{44} & 0 & 0 & 0 & 0 & 0 & 0 \\ 0 & 0 & 0 & 0 & 0 & 0 & 0 & 0 & 0 & 0 \\ K_{61} & K_{62} & K_{63} & 0 & 0 & 0 & 0 & 0 & 0 & 0 \\ K_{71} & K_{72} & K_{73} & 0 & 0 & 0 & K_{77} & 0 & 0 & 0 \\ K_{81} & K_{82} & K_{83} & 0 & 0 & 0 & 0 & K_{88} & 0 & 0 \\ 0 & 0 & 0 & 0 & 0 & 0 & 0 & 0 & K_{99} & 0 \\ 0 & 0 & 0 & 0 & 0 & 0 & 0 & 0 & 0 & K_{1010} \end{bmatrix} \tag{A1.21}$$

with K_{77}, K_{88}, and K_{99} are the element from the adding stiffness matrix.

A1.1.4 Generalized forces

The detail of the general force vector are given as follows

$$F_1 = f_{w,1} + f_{g,1}, \tag{A1.22a}$$
$$F_2 = f_{w,2} + f_{g,2}, \tag{A1.22b}$$
$$F_3 = f_{w,3} + f_{g,3}, \tag{A1.22c}$$
$$F_4 = f_{w,4}, \tag{A1.22d}$$
$$F_5 = f_{w,5} + f_{m,5} + f_{d,5} + f_{i,5}, \tag{A1.22e}$$
$$F_6 = f_{w,6} + f_{m,6} + f_{d,6} + f_{i,6}, \tag{A1.22f}$$
$$F_7 = f_{w,7} + f_{g,7} + f_{m,7} + f_{b,7} + f_{i,7}, \tag{A1.22g}$$
$$F_8 = f_{w,8} + f_{m,8} + f_{d,8} + f_{i,8}, \tag{A1.22h}$$
$$F_9 = f_{w,9} + f_{g,9} + f_{m,9} + f_{d,9} + f_{i,9}, \tag{A1.22i}$$
$$F_{10} = f_{m,10}, \tag{A1.22j}$$

with $\mathbf{f}_b$ is equal the spar hydrostatic load.

A1.1.5 Eigen analysis of the FOWT structure

The solution of equation of motion for natural frequencies and normal modes requires a special reduced from of the equation of motion. If there is no damping and no applied loading, the equation of motion in matrix form reduces to

$$[M]\{\ddot{u}\} + [K]\{u\} = 0, \tag{A1.23}$$

where, $[M]$ is the mass matrix, and $[K]$ is the stiffness matrix. The above equation is the equation of motion for undamped free vibration. A harmonic solution of the form $\{u\} = \{\phi\}sin\omega t$ is assumed to solve the quation of motion, in which $\{\phi\}$ is the eigenvector or mode shape, ω is the circular natural frequency. The harminic form of the solution physically means that all the degrees of freedom of the vibrating structure move in a synchoronous manner. The structural configuration does not change its basic shape during motion but the amplitude.

If differentiation fo the assumed harmonic solution is performed, and substituted into the equation of motion, the follwoing is obtained

$$-\omega[M]\{\phi\}sin\omega t + [K]\{\phi\}sin\omega t = 0, \tag{A1.24}$$

which after simplifying becomes

$$([K] - \omega^2[M])\{\phi\} = 0, \tag{A1.25}$$

thus, non-trivial solution ($\{\phi\}$) is obtained with

$$det([K] - \omega^2[M]) = 0 \tag{A1.26}$$

at a set of discrete eigenvalues ω_i^2. There is an eigenvector $\{\phi_i\}$ which satisfies Eq. and corresponds to each eigenvalue. The $i-$th eigenvalue ω_i^2 is related to the $i-$th natural frequency as follows:

$$f_i = \frac{\omega_i}{2\pi}, \tag{A1.27}$$

hence,

$$T_i = 1/f_i. \tag{A1.28}$$

Mass and stiffness matrices

The mass matrix of the overall structure and the stiffness matrix are calculated in this section. It is worth to note that the mass matrix is determined by the real mass of the spar, nacelle, hub and tower while the stiffness matrix is calculated with respect to the

hydrostatic stiffness of the spar in heave, roll, pitch, yaw and to the mooring system in surge and sway directions.

Firstly, the mass matrix is calculated with respect to the center of mass of the system. The centre of mass of spar is at -89.9155 m. The centre of mass of the whole system is at (-1.3918E-2, 1.1132E-2, -78.0013). Calculating the mass of the spar with respect to the centre of the system, we get

$$\mathbf{M}_{spar} = \begin{bmatrix} m & 0 & 0 & 0 & 0 & 0 \\ 0 & m & 0 & & 0 & 0 \\ 0 & 0 & m & 0 & 0 & 0 \\ 0 & 0 & 0 & I_{XX} + m * d^2 & 0 & 0 \\ 0 & 0 & 0 & 0 & I_{YY} + m * d^2 & 0 \\ 0 & 0 & 0 & 0 & 0 & I_{ZZ} + m * d^2 \end{bmatrix} \tag{A1.29}$$

whereas, m is the mass of the spar, I_{XX}, I_{YY}, I_{ZZ} are moment of inertia about the spar centre of mass, $d = z_{centreofmassofsystem} - z_{centreofmassofspar}$.

Mass of superstructure is lumped to the centre of mass of the system, which has been detailed in previous section, Section A1.1.1. Added mass matrix considers the effect of surrounding water is also given in Section A1.1.1.

To sum up, the overall mass matrix of the system is given as follow

$$[M]_{system} = [M]_{spar-structural-mass} + [M]_{spar-added-mass} + [M]_{lumpedmass}. \tag{A1.30}$$

Stiffness matrix is a diagonal matrix which is detailed as follow

$$[K]_{system} = [K]_{hydrostatic} + [K]_{mooring}, \tag{A1.31}$$

with

$$\mathbf{K}_m = \begin{bmatrix} 4.118E4 & 0 & 0 & 0 & -2.906E6 & 0 \\ 0 & 4.118E4 & 0 & 2.906E6 & 0 & 0 \\ 0 & 0 & 1.194E4 & 0 & 0 & 0 \\ 0 & 2.906E6 & 0 & 3.108E8 & 0 & 0 \\ -2.906E6 & 0 & 0 & 0 & 3.108E8 & 0 \\ 0 & 0 & 0 & 0 & 0 & 1.156E7 \end{bmatrix} \tag{A1.32}$$

We have to consider the impact of the restoring effects of body weight. Hence an

additional term is added to roll and pitch direction as following

$$K_{4,4} = K_{5,5} = \left(h_B V_s + \frac{\pi D_0^2}{64} \right) \rho_w g - mgh_G, \tag{A1.33}$$

with m is mass of spar, h_G is the vertical distance from the centre of the system to the still water level. The hydrostatic stiffness matrix becomes

$$\mathbf{K}_r = \begin{bmatrix} 0 & 0 & 0 & 0 & & 0 \\ 0 & 0 & 0 & & 0 & 0 \\ 0 & 0 & 3.335E5 & 0 & 0 & 0 \\ 0 & & 0 & 1.5758E9 & 0 & 0 \\ 0 & 0 & 0 & 0 & 1.5758E9 & 0 \\ 0 & 0 & 0 & 0 & 0 & 0 \end{bmatrix} \tag{A1.34}$$

The system stiffness matrix is given by

$$\mathbf{K} = \begin{bmatrix} 4.118E4 & 0 & 0 & 0 & & 0 \\ 0 & 4.118E4 & 0 & & 0 & 0 \\ 0 & 0 & 3.335E5 & 0 & 0 & 0 \\ 0 & & 0 & 1.5758E9 & 0 & 0 \\ 0 & 0 & 0 & 0 & 1.5758E9 & 0 \\ 0 & 0 & 0 & 0 & 0 & 9.834E7 \end{bmatrix} \tag{A1.35}$$

Natural period of FOWT structure

The natural frequency of the system are listed in reference OC3 report [10]. The FOWT model natural periods are very close to the published model in reference.

Motion mode	Natural period from ref (s)	Natural frequency from ref (Hz)	Natural period computed (s)	Natural frequency computed (Hz)
Surge	125.8	0.0079	124.455	0.0080
Sway	124.9	0.008	124.455	0.0080
Heave	30.9	0.032	30.8978	0.0324
Pitch	30.0	0.033	30.1134	0.0332
Roll	30.0	0.033	30.1134	0.0332
Yaw	8.3	0.12	8.2516	0.1212

A1.2 Finite element method using MATLAB

The Finite Element Method is a package applied as Matlab toolbox for solving Partial Differential Equation. The method is widely applicable in various problems from the structural analysis to the heat transfer problems. The numerical scheme is described clearly in the book [294] and a selected part is described in the following part including integral estimation and triangular mesh method. Finally, Matlab code used to compute the vertical velocity in a half wave length is provided.

A1.2.1 Governing equation

Laplace's equation is

$$\nabla^2 w = 0 \tag{A1.36}$$

and the Poisson's equation is given as

$$\nabla^2 w = g \tag{A1.37}$$

It can be seen that the Poisson's equation is more general than the Laplace's equation, the solving procedure for Possion's equation is formulated in the following part.

In two dimensional domain, the Poisson's equation states

$$\frac{\partial^2 w}{\partial x^2} + \frac{\partial^2 w}{\partial y^2} = g(x, z) \text{ in } \Omega. \tag{A1.38}$$

The boundaries conditions are

$$u = \bar{u} \text{ on } \Gamma_e \tag{A1.39}$$

and

$$\frac{\partial u}{\partial n} = \bar{q} \text{ on } \Gamma_n \tag{A1.40}$$

where $\bar{u}$ and $\bar{q}$ represent known variable and flux boundary conditions. $\mathbf{n}$ is the normal vector pointing outward at the boundary. Γ_e and Γ_n are the boundaries for essential and natural boundary conditions. The well-posed problem holds

$$\Gamma_e \cup \Gamma_n = \mathbf{\Gamma} \tag{A1.41}$$

and

$$\mathbf{\Gamma_e} \cap \Gamma_n = \emptyset, \tag{A1.42}$$

where $\cup$ and $\cap$ are sum and intersecton, respectively. $\mathbf{\Gamma}$ is the total boundary of the domain Ω.

The weighted residual of the differential equation and boundary condition is integrated as

$$I = \int_{\Omega} f \left(\frac{\partial^2 w}{\partial x^2} + \frac{\partial^2 w}{\partial z^2} - g(x,y) \right) d\Omega - \int_{\Gamma_e} f \frac{\partial u}{\partial n} d\Gamma. \tag{A1.43}$$

The *weak formulation* is introduced by applying integration by part. The objective of the derivation is to reduce the order of the differentiation within the integral.

The first term of the integration is

$$\int_{\Omega} f \frac{\partial^2 w}{\partial x^2} d\Omega. \tag{A1.44}$$

It is rewritten as

$$\int_{z_1}^{z_2} \left(\int_{x_1}^{x_2} f \frac{\partial^2 f}{\partial x^2} dx \right) dz, \tag{A1.45}$$

where z_1 and z_2 are the minimum and the maximum of the domain in z-axis. Integration by part with respect to x, one obtains

$$- \int_{z_1}^{z_2} \int_{x_1}^{x_2} \frac{\partial f}{\partial x} \frac{\partial u}{\partial x} dx dz + \int_{z_1}^{z_2} \left[f \frac{\partial u}{\partial x} \right]_{x_1}^{x_2} dz, \tag{A1.46}$$

rewriting the expression

$$- \int_{\Omega} \frac{\partial f}{\partial x} \frac{\partial u}{\partial x} d\Omega + \int_{\Gamma_2} f \frac{\partial u}{\partial x} n_x d\Gamma - \int_{\Gamma_1} f \frac{\partial u}{\partial x} n_x d\Gamma, \tag{A1.47}$$

where n_x is the x-component of the unit normal vector assumed to be positive in the outward direction. The two boundary integrals is combined thus

$$- \int_{\Omega} \frac{\partial f}{\partial x} \frac{\partial u}{\partial x} d\Omega + \oint_{\Gamma} f \frac{\partial w}{\partial x} n_x d\Gamma, \tag{A1.48}$$

where the boundary integral is in the counter-clockwise direction.

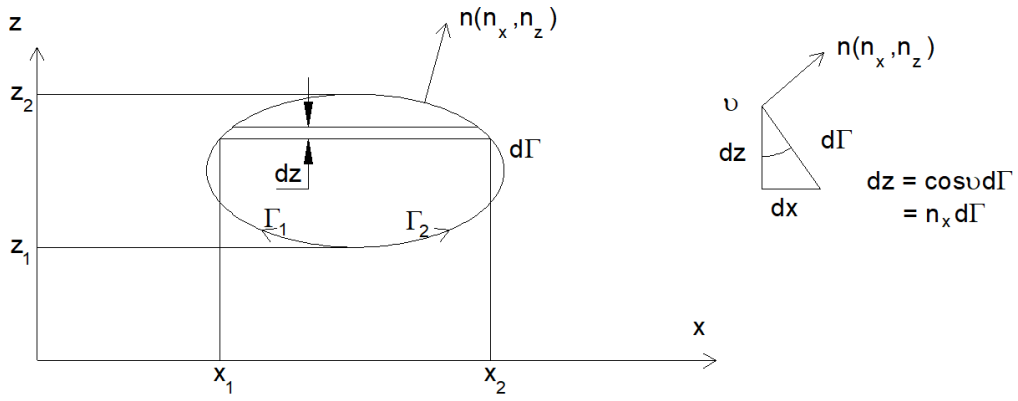

Figure A1.1: Computational domain.

The second term of the integration A1.43 is

$$-\int_{\Omega}\frac{\partial f}{\partial z}\frac{\partial w}{\partial z}d\Omega+\oint_{\Gamma}f\frac{\partial w}{\partial z}n_z d\Gamma. \tag{A1.49}$$

Adding two terms, Eq.A1.48 and Eq.A1.49, one yields

$$\int_{\Omega}f\left(\frac{\partial^2 w}{\partial x^2}+\frac{\partial^2 w}{\partial z^2}\right)d\Omega=-\int_{\Omega}\left(\frac{\partial f}{\partial x}\frac{\partial u}{\partial x}+\frac{\partial f}{\partial z}\frac{\partial w}{\partial z}\right)d\Omega+\oint_{\Gamma}f\left(\frac{\partial w}{\partial x}n_x+\frac{\partial w}{\partial z}n_z\right)d\Gamma, \tag{A1.50}$$

where $\oint$ is the line integral around a close boundary. The boundary integral can be written as

$$\frac{\partial w}{\partial n}=\frac{\partial w}{\partial x}n_x+\frac{\partial w}{\partial z}n_z \tag{A1.51}$$

Eq.A1.50 can be rewritten as

$$\int_{\Omega}f\left(\frac{\partial^2 w}{\partial x^2}+\frac{\partial^2 w}{\partial z^2}\right)d\Omega=-\int_{\Omega}\left(\frac{\partial f}{\partial x}\frac{\partial u}{\partial x}+\frac{\partial f}{\partial z}\frac{\partial w}{\partial z}\right)d\Omega+\oint_{\Gamma}f\frac{\partial w}{\partial n}d\Gamma. \tag{A1.52}$$

Substituting Eq.A1.52 to Eq.A1.43, the integral becomes

$$I=-\int_{\Omega}\left(\frac{\partial f}{\partial x}\frac{\partial u}{\partial x}+\frac{\partial f}{\partial z}\frac{\partial w}{\partial z}\right)d\Omega-\int_{\Omega}fg(x,y)d\Omega+\oint_{\Gamma}f\frac{\partial w}{\partial n}d\Gamma. \tag{A1.53}$$

The first term is a matrix term. The second and the third term are a vector term. In physical application, the second term denotes a source or sink within the domain while the third term represents the flux through the natural boundary.

A1.2.2 Discretization

The domain is discretised using the two-dimensional three nodes triangular element or linear triangular elements. There is three nodes at the vertices of the triangle. The variable interpolation within the element is linear in x and z as

$$w=a_1+a_2x+a_3z \tag{A1.54}$$

or

$$w=\begin{bmatrix}1 & x & z\end{bmatrix}\begin{bmatrix}a_1\\a_2\\a_3\end{bmatrix}, \tag{A1.55}$$

in which a_i is the constant to be determined. The interpolation function in Eq.A1.52 is the nodal variable. Substituting the coordinate of each node, one obtains

$$\begin{bmatrix} w_1 \\ w_2 \\ w_3 \end{bmatrix} = \begin{bmatrix} 1 & x_1 & z_1 \\ 1 & x_2 & z_2 \\ 1 & x_3 & z_3 \end{bmatrix} \begin{bmatrix} a_1 \\ a_2 \\ a_3 \end{bmatrix}, \tag{A1.56}$$

where x_i and z_i are the coordinates of node i while w_i is the nodal variable. Therefore, we find a_i by

$$\begin{bmatrix} a_1 \\ a_2 \\ a_3 \end{bmatrix} = \frac{1}{2A} \begin{bmatrix} x_2z_3 - x_3z_2 & x_3z_1 - x_1z_3 & x_1z_2 - x_2z_1 \\ z_2 - z_3 & z_3 - z_1 & z_1 - z_2 \\ x_3 - x_2 & x_1 - x_3 & x_2 - x_1 \end{bmatrix} \begin{bmatrix} w_1 \\ w_2 \\ w_3 \end{bmatrix}, \tag{A1.57}$$

where,

$$A = \frac{1}{2}\det \begin{bmatrix} 1 & x_1 & z_1 \\ 1 & x_2 & z_2 \\ 1 & x_3 & z_3 \end{bmatrix} \tag{A1.58}$$

Magnitude of A is the area of the linear triangular element and its value sign positive as the element node is numbered counter-clockwise direction and vice versa. The element nodal sequence must follow the same direction for every element in the discretised domain.

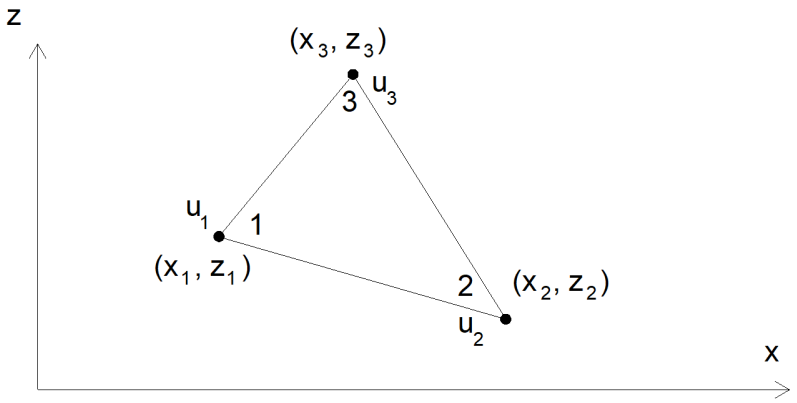

Figure A1.2: Three nodes triangular element.

Substituting a_i back to Eq.A1.52, the nodal variable is given by

$$u = H_1(x, y)u_1 + H_2(x, y)u_2 + H_3(x, y)u_3, \tag{A1.59}$$

where, $H_i(x, y)$ is the shape function given as

$$H_1 = \frac{1}{2A}\left[(x_2z_3 - x_3z_2) + (z_2 - z_3)\,x + (x_3 - x_2)\,z\right] \tag{A1.60}$$

$$H_2 = \frac{1}{2A}\left[(x_3 z_1 - x_1 z_3) + (z_3 - z_1)\, x + (x_1 - x_3)\, z\right] \tag{A1.61}$$

$$H_3 = \frac{1}{2A}\left[(x_1 z_2 - x_2 z_1) + (z_1 - z_2)\, x + (x_2 - x_1)\, z\right] \tag{A1.62}$$

The shape function fulfils the conditions

$$H_i(x_j, z_j) = \delta_{ij}, \tag{A1.63}$$

and

$$\sum_{i=1}^{3} H_i = 1, \tag{A1.64}$$

where, δ_{ij} is the *Kronecker delta* function, given as follows

$$\delta_{ij} = \begin{Bmatrix} 1 & if & i = j \\ 0 & if & i \neq j \end{Bmatrix} \tag{A1.65}$$

The wave domain is discretized into a number of triangular elements. The curve boundary is approximated by a piecewise linear boundary the finer resolution for closer approximation of the actual boundary using the linear triangular elements.

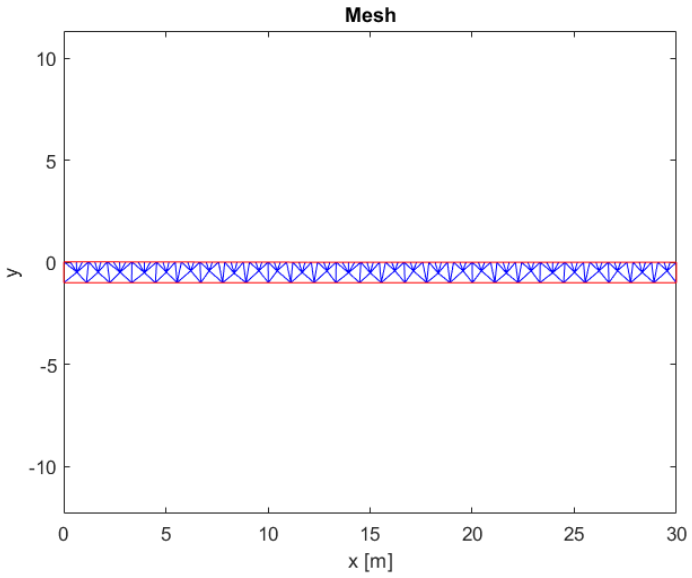

Figure A1.3: Two-dimensional domain mesh.

For a single triangular element, the elements of the matrix is derived as

$$
\begin{aligned}
[K^e] &= \int_{\Omega^e} \left(\frac{\partial f}{\partial x}\frac{\partial w}{\partial x} + \frac{\partial f}{\partial z}\frac{\partial w}{\partial z} \right) d\Omega \\
&= \int_{\Omega^e} \left(\begin{bmatrix} \frac{\partial H_1}{\partial x} \\ \frac{\partial H_2}{\partial x} \\ \frac{\partial H_3}{\partial x} \end{bmatrix} \begin{bmatrix} \frac{\partial H_1}{\partial x} & \frac{\partial H_2}{\partial x} & \frac{\partial H_3}{\partial x} \end{bmatrix} + \begin{bmatrix} \frac{\partial H_1}{\partial z} \\ \frac{\partial H_2}{\partial z} \\ \frac{\partial H_3}{\partial z} \end{bmatrix} \begin{bmatrix} \frac{\partial H_1}{\partial z} & \frac{\partial H_2}{\partial z} & \frac{\partial H_3}{\partial z} \end{bmatrix} \right) d\Omega
\end{aligned} \tag{A1.66}
$$

where, Ω^e is the element domain. Substituting the shape function, Eq.A1.63-A1.65, into the element matrix in Eq.A1.66, one obtains

$$
[K^e] = \begin{bmatrix} k_{11} & k_{12} & k_{13} \\ k_{21} & k_{22} & k_{23} \\ k_{31} & k_{32} & k_{33} \end{bmatrix}, \tag{A1.67}
$$

where,

$$k_{11} = \frac{1}{4A}[(x_3 - x_2)^2 + (z_2 - z_3)^2], \tag{A1.68}$$

$$k_{12} = \frac{1}{4A}[(x_3 - x_2)(x_1 - x_3) + (z_2 - z_3)(z_3 - z_1)], \tag{A1.69}$$

$$k_{13} = \frac{1}{4A}[(x_3 - x_2)(x_2 - x_1) + (z_2 - z_3)(z_1 - z_2)], \tag{A1.70}$$

$$k_{21} = k_{12}, \tag{A1.71}$$

$$k_{22} = \frac{1}{4A}[(x_1 - x_3)^2 + (z_3 - z_1)^2], \tag{A1.72}$$

$$k_{23} = \frac{1}{4A}[(x_1 - x_3)(x_2 - x_1) + (z_3 - z_1)(z_1 - z_2)], \tag{A1.73}$$

$$k_{31} = k_{13}, \tag{A1.74}$$

$$k_{32} = k_{23}, \tag{A1.75}$$

$$k_{33} = \frac{1}{4A}[(x_2 - x_1)^2 + (z_1 - z_2)^2], \tag{A1.76}$$

The integrand in Eq.A1.66 is constant since $\frac{\partial H_i}{\partial x}$ and $\frac{\partial H_i}{\partial z}$ are constant. The results are given in Eq.A1.68 to Eq.A1.76.

The second term in Eq.A1.53 is

$$\oint_{\Omega} f(x, z)\Omega. \tag{A1.77}$$

The computation of this integral over each element yields

$$\oint_{\Omega^e} \begin{bmatrix} H_1 \\ H_2 \\ H_3 \end{bmatrix} f(x, z)\Gamma. \tag{A1.78}$$

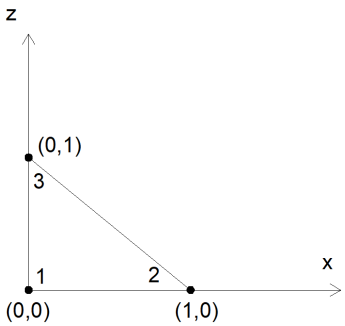

Figure A1.4: Triangular domain of one element.

In this thesis, the problem is a value problem. the function $g(x, z) = 0$ due to the value of the vertical velocity at boundary.